UNIVERSITÀ DEGLI STUDI DI SALERNO

DIPARTIMENTO DI CHIMICA E BIOLOGIA
˝ADOLFO ZAMBELLIˋ

PHD THESIS IN
CHEMICAL, BIOLOGICAL AND ENVIRONMENTAL SCIENCES

Properties and Applications of Nanoporous-Crystalline Polymers

TUTOR
PROF. PAOLA RIZZO

PhD STUDENT
Antonietta COZZOLINO
[8801800002]

CO-TUTORS
PROF. GAETANO GUERRA
PROF. CHRISTOPHE DANIEL

COORDINATOR
PROF. CLAUDIO PELLECCHIA

XXXV CYCLE – 2019-2022

ABSTRACT

Nanoporous-crystalline (NC) forms, i.e. crystalline structure presenting nanocavities or nanochannels inside the crystalline lattice, are possible only for two polymers, both commercially available: syndiotactic polystyrene (sPS) and poly(2,6-dimethyl-1,4-phenylene) oxide (PPO). In particular, the two NC phases of sPS, named delta (δ) and epsilon (ε), showing pores as cavities or channels, are well described and characterized in literature since 1994 and 2007, respectively; whereas, as for PPO, evidences of the formation of NC phases have been established only in 2011.

NC phases present several features which make them interesting for many industrial fields, for instance they can absorb suitable guest molecules, even at low activity from water and air, making them useful for applications such as air and water purification and/or molecular sensors. Moreover, the capability to absorb suitable guest molecules inside the NC lattice, leading to the formation of co-crystalline (CC) phases, can open the possibility of applications of these CC polymeric materials, in many different fields depending on the chemical nature of the guest molecule, as for instance fluorescence, photoreactivity, magnetism, ferroelectricity and antimicrobial.

The present Ph.D. thesis aimed to investigate on new properties as well as on possible applications of these peculiar thermoplastic polymers, and the goals achieved are reported as follows.

Firstly, WAXD and FTIR measurements have shown the formation of two well-separated NC (and CC) forms of PPO, named alpha (α) and beta (β). The NC α and β forms not only exhibit different chain packing but also slightly different chain conformations (***c*** = 5.28 and 5.47 Å, respectively). Additionally, the α-form is favored by hydrophobic (with solubility lower than 0.11 mmol per 100 mL of water) and bulky guest molecules (with molecular volumes higher than 230 $Å^3$) while the β-form (being characterized by a higher chain periodicity) is favored by hydrophilic (with solubility higher than 2 mmol per 100 mL of water) and small guest molecules (with molecular volumes lower than 149 $Å^3$).

Another important aspect which has been point out is the strong influence of the crystalline phase orientation of NC PPO α phase with respect to the film plane on guest molecules diffusivity. In particular, NC PPO films exhibit higher diffusivity of the pollutant perchloroethylene (PCE) from vapors (5.6×10^{-10} cm^2 s^{-1}) as well as from aqueous solutions (2.1×10^{-10} cm^2 s^{-1}) when the orientation of the NC α phase is

preferentially perpendicular to the film plane ($c_\perp$ orientation). Specifically, diffusivity values are higher than for films with $c_{//}$ orientation (1.5×10^{-11} cm^2 s^{-1}) and much higher than for NC sPS films (6.7×10^{-12} cm^2 s^{-1}). Moreover, guest uptakes for NC $c_\perp$ PPO films, when expressed as mass of guest per polymer volume, are also much higher than for NC PPO powders and aerogels. This advantage becomes very important considering that for most purification processes the limiting factor is the volume of the absorbent material.

Furthermore, it has been also found that guest diffusivity values of PCE on NC PPO films presenting high surface area (up to 620 m^2 g^{-1}) are even much higher than for $c_\perp$ oriented NC PPO films, both for sorption from vapor phase (3.3×10^{-9} cm^2 s^{-1}) and from diluted aqueous solutions (3.8×10^{-10} cm^2 s^{-1}). These features make NC PPO films (especially with high surface area) particularly suitable for air and water purification.

In addition, preliminary results about potential gas sensors made with PPO films/coatings have been reported. Two approaches have been proposed based on the transduction methods: electrical and optical. About electrical approach, a potential gas indicator based on a metal insulator semiconductor has been proposed. This device presents a PPO coating (≈1μm) as dielectric material between two metal contacts (Au, gold). When it is exposed to different gases (i.e., methyl ethyl ketone and carbon tetrachloride), a diverse response pattern has been achieved, therefore a discrimination among volatile chemicals seems to be possible. As concern optical approach, PPO films containing 1–2 wt% of the fluorophore umbelliferone has been tested in saturated chloroform vapours. Once exposed to these vapours, fluorescence rapidly turned on within the first minutes thanks to the solvation effect provided by the polar vapours. Such vapochromic response has appeared also to be reversible after many cycles. The whole set of data has suggested that PPO films/coatings could be very suitable for developing new advanced materials for detection of harmful volatile organic compound vapours.

Furthermore, sorption of carboxylic acids in NC phases of axially oriented sPS phases has been explored. The main results which have been observed are that ε sPS phases can host hydrogen-bonded molecules to form a “polymer” into the crystalline channels (i.e., with the dicarboxylic adipic acid). This could be particularly interesting for films exhibiting the $c_\perp$ orientation, in which the crystalline channels and hence the hydrogen-bonded “linear polymers” are preferentially perpendicular to the film plane. This procedure could possibly lead to formation of isolated semiconductive linear polymers perpendicular to the plane of insulating sPS films for new membranes with electrical properties.

Finally, the phenomenon of crystallization associated to the unusual induction of axial orientation in sPS unstretched fibers has been also observed. Different guests (as pure solvent or in aqueous diluted solutions) have been tested finding that they are able to induce crystallization in CC phases associated to high degree of axial orientation (in the range $0.7 < f_c < 0.8$). This high degree of axial orientation can be also completely retained after guest removal leading to NC phases. The occurring of axial orientation improves mechanical property of sPS fibers and hence could be notably relevant from an industrial point of view.

Moreover, axially oriented CC sPS fibers including natural antimicrobial guest molecules (i.e., eugenol, carvacrol and thymol), have been also studied during time. They present a slow and controlled release in air at room temperature; this long-term antimicrobial release makes them usable for months in many biomedical applications where the inhibition of microorganisms' growth is crucial.

CONTENTS

CHAPTER 1

CHAPTER 2

CHAPTER 3

CHAPTER 4

CHAPTER 5

INTRODUCTION

Co-crystalline (CC) forms between a polymeric host and low-molecular-mass (guest) molecules are known for many polymers.[1–5] For most host polymers, CC phases are formed only with a very limited number of guest molecules due to specific host-guest interactions. The removal of guest molecules from CC phases usually generates amorphous or dense crystalline phases.[3,4,6–8] Exceptions to this general rule are two important thermoplastic polymers: syndiotactic polystyrene (sPS) and poly(2,6-dimethyl-1,4-phenylene oxide) (PPO). Both are able to form not only CC phases with a large number of low-molecular-mass molecules but by using simple extraction procedures nanoporous crystalline (NC) phases can be obtained. These NC phases show spatially ordered pores with identical size and hence the crystalline density is lower than those of corresponding amorphous phases.

Particularly, two NC phases for sPS, named delta (δ)[9–11] and epsilon (ε),[12] showing pores as cavities or channels, are well described and characterized in literature. As for PPO, evidences on the formation of co-crystals with many guests have been well known in the literature from decades, but only in 2011 the nanoporous nature of PPO crystalline phases was established.[13]

These polymers are commercially available and the presence of simple processing conditions (low pressure and temperature) and processing techniques (both from melt and solutions)[14] can lead to a large variety of morphologies, like fibers, sheets, films, membranes, foams, gels and aerogels.[15–19] They present also several features which make them interesting materials to be applied in many industrial fields. Firstly, the identical cavities of these NC polymers allow molecular selectivity[20–26] comparable to those of NC inorganic and organometallic materials.

Additionally, NC phases can absorb guest molecules, even at low activity, from air as well as from water,[23] and this can be particularly relevant for many applications, such as air and water purification, molecular separation as well as molecular sensors.[27–35] Moreover, the sorption of suitable guests in the crystalline phases can open the possibility of applications of CC polymeric samples, depending on the nature of the molecules, into many different fields, including fluorescence, photoreactivity, magnetism, ferroelectricity and antimicrobial.[36–44] Another remarkable characteristic is that by using different crystallization procedures, the orientation of both host polymeric and guest molecules into the CC phases can be easily realized.[45]

The aim of the present Ph.D. thesis is the investigation on new properties as well as trying to establish possible applications of these innovative NC polymers, inducing a substantial advance in the scientific literature about them.

In detail, this thesis is divided into Part I and Part II which are related to advances in the study on PPO and sPS, respectively. At the end of each part, general concluding remarks are there reported.

Part I has been sectioned into three chapters. In the first chapter, a significant progress in the characterization of NC forms of PPO, named alpha (α) and beta (β), has been achieved. In particular, guests leading to CC (and NC) α or β forms of PPO and the molecular features behind their formation are described.

In the second chapter, sorption properties of NC PPO samples, prevailingly films, are investigated in order to check their possible application for air and water purification.

Then, in the third chapter, taking into account the extraordinary ability of NC PPO phases in terms of sorption, the investigation about PPO films for developing gas sensors is carried out.

The Part II moves the attention to CC sPS phases, and it is subdivided into two chapters (fourth and fifth, respectively).

In the fourth chapter, the possibility of inclusion of carboxylic acids, especially with long aliphatic chains, to form linear hydrogen bonded aggregates in sPS crystalline epsilon channels is described.

Finally at the end, the fifth chapter of this thesis details about a very unusual phenomenon of both crystallization as well as axial orientation in sPS unstretched fibers by different guests. Some of these guests, which are able to induce axial orientation in sPS unoriented fibers, present also antimicrobial activity, so, in addition, antimicrobial guest release from these axially oriented CC sPS fibers has been as well investigated.

REFERENCES

(1) El Hasri, S.; Ray, B.; Thierry, A.; Guenet, J.-M. Solvent-Induced Organization of Amorphous Isotactic Polystyrene. *Macromolecules* **2004**, *37* (11), 4124–4129. https://doi.org/10.1021/ma049701x.

(2) Tarallo, O.; Esposito, G.; Passarelli, U.; Petraccone, V. A Clathrate Form of Syndiotactic Poly(*p* -Methylstyrene) Containing Two Different Types of Cavities. *Macromolecules* **2007**, *40* (15), 5471–5478. https://doi.org/10.1021/ma070523s.

(3) Dasgupta, D.; Malik, S.; Thierry, A.; Guenet, J. M.; Nandi, A. K. Thermodynamics, Morphology, and Structure of the Poly(Vinylidene Fluoride)−Ethyl Acetoacetate System. *Macromolecules* **2006**, *39* (18), 6110–6114. https://doi.org/10.1021/ma0610921.

(4) Daniel, C.; Vitillo, J. G.; Fasano, G.; Guerra, G. Aerogels and Polymorphism of Isotactic Poly(4-Methyl-Pentene-1). *ACS Appl. Mater. Interfaces* **2011**, *3* (4), 969–977. https://doi.org/10.1021/am200107w.

(5) Rizzo, P.; Ianniello, G.; Venditto, V.; Tarallo, O.; Guerra, G. Poly(L -Lactic Acid): Uniplanar Orientation in Cocrystalline Films and Structure of the Cocrystalline Form with Cyclopentanone. *Macromolecules* **2015**, *48* (20), 7513–7520. https://doi.org/10.1021/acs.macromol.5b00908.

(6) Atkins, E. D. T.; Isaac, D. H.; Keller, A.; Miyasaka, K. Analysis of Anomalous X-Ray Diffraction Effects of Isotactic Polystyrene Gels and Its Implications for Chain Conformation and Isomeric Homogeneity. *J. Polym. Sci. Polym. Phys. Ed.* **1977**, *15* (2), 211–226. https://doi.org/10.1002/pol.1977.180150202.

(7) Paternostre, L.; Damman, P.; Dosière, M. Polymorphism and Crystal Morphology of Poly(Ethylene Oxide)−2-Methyl Resorcinol Supramolecular Complexes. *Macromolecules* **1999**, *32* (1), 153–161. https://doi.org/10.1021/ma9809839.

(8) Marubayashi, H.; Asai, S.; Sumita, M. Complex Crystal Formation of Poly(L -Lactide) with Solvent Molecules. *Macromolecules* **2012**, *45* (3), 1384–1397. https://doi.org/10.1021/ma202324g.

(9) De Rosa, C.; Guerra, G.; Petraccone, V.; Pirozzi, B. Crystal Structure of the Emptied Clathrate Form (δ_eForm) of Syndiotactic Polystyrene. *Macromolecules* **1997**, *30* (14), 4147–4152. https://doi.org/10.1021/ma970061q.

(10) Tarallo, O.; Petraccone, V.; R. Albunia, A.; Daniel, C.; Guerra, G. Monoclinic and Triclinic δ-Clathrates of Syndiotactic Polystyrene. *Macromolecules* **2010**, *43* (20), 8549–8558. https://doi.org/10.1021/ma1013513.

(11) Acocella, M. R.; Rizzo, P.; Daniel, C.; Tarallo, O.; Guerra, G. Nanoporous Triclinic δ Modification of Syndiotactic Polystyrene. *Polymer* **2015**, *63*, 230–236. https://doi.org/10.1016/j.polymer.2015.02.058.

(12) Petraccone, V.; Ruiz de Ballesteros, O.; Tarallo, O.; Rizzo, P.; Guerra, G. Nanoporous Polymer Crystals with Cavities and Channels. *Chem. Mater.* **2008**, *20* (11), 3663–3668. https://doi.org/10.1021/cm800462h.

(13) Daniel, C.; Longo, S.; Fasano, G.; Vitillo, J. G.; Guerra, G. Nanoporous Crystalline Phases of Poly(2,6-Dimethyl-1,4-Phenylene)Oxide. *Chem. Mater.* **2011**, *23* (13), 3195–3200. https://doi.org/10.1021/cm200546r.

(14) Joseph, A. M.; Nagendra, B.; Shaiju, P.; Surendran, K. P.; Gowd, E. B. Aerogels of Hierarchically Porous Syndiotactic Polystyrene with a Dielectric Constant near to Air. *J. Mater. Chem. C* **2018**, *6* (2), 360–368. https://doi.org/10.1039/C7TC05102F.

(15) Daniel, C.; Longo, S.; Ricciardi, R.; Reverchon, E.; Guerra, G. Monolithic Nanoporous Crystalline Aerogels. *Macromol. Rapid Commun.* **2013**, *34* (15), 1194–1207. https://doi.org/10.1002/marc.201300260.

(16) Mochizuki, J.; Sano, T.; Tokami, T.; Itagaki, H. Decisive Properties of Solvent Able to Form Gels with Syndiotactic Polystyrene. *Polymer* **2015**, *67*, 118–127. https://doi.org/10.1016/j.polymer.2015.04.042.

(17) Cheng, Y.-W.; Wang, C. Solvent-Induced Crystallization of Electrospun Syndiotactic Polystyrene Nanofibers and Its Reversible Desorption/Sorption of Volatile Organic Vapors. *J. Polym. Res.* **2016**, *23* (11), 234. https://doi.org/10.1007/s10965-016-1130-2.

(18) Raut, P.; Liang, W.; Chen, Y.-M.; Zhu, Y.; Jana, S. C. Syndiotactic Polystyrene-Based Ionogel Membranes for High Temperature Electrochemical Applications. *ACS Appl. Mater. Interfaces* **2017**, *9* (36), 30933–30942. https://doi.org/10.1021/acsami.7b09155.

(19) Itagaki, H.; Sano, T.; Okabe, T.; Sano, S.; Ebihara, H.; Tomono, F.; Dohra, H. Polymerization of Aniline in Tubular Cavities of the Crystalline Phase of Syndiotactic Polystyrene: Proposal of a Preparation Method of Sophisticated Polymer Composites. *ACS Macro Lett.* **2017**, *6* (10), 1099–1103. https://doi.org/10.1021/acsmacrolett.7b00661.

(20) Guerra, G.; Milano, G.; Venditto, V.; Musto, P.; De Rosa, C.; Cavallo, L. Thermoplastic Molecular Sieves. *Chem. Mater.* **2000**, *12* (2), 363–368. https://doi.org/10.1021/cm991064f.

(21) Mahesh, K. P. O.; Sivakumar, M.; Yamamoto, Y.; Tsujita, Y.; Yoshimizu, H.; Okamoto, S. Structure and Properties of the Mesophase of Syndiotactic Polystyrene. *J. Membr. Sci.* **2005**, *262* (1–2), 11–19. https://doi.org/10.1016/j.memsci.2005.04.002.

(22) Tarallo, O.; Auriemma, F.; de Ballesteros, O. R.; Di Girolamo, R.; Diletto, C.; Malafronte, A.; De Rosa, C. The Role of Shape and Size of Guest Molecules in the Formation of Clathrates and Intercalates of Syndiotactic Polystyrene. *Macromol. Chem. Phys.* **2013**, *214* (17), 1901–1911. https://doi.org/10.1002/macp.201300071.

(23) Larobina, D.; Sanguigno, L.; Venditto, V.; Guerra, G.; Mensitieri, G. Gas Sorption and Transport in Syndiotactic Polystyrene with Nanoporous Crystalline Phase. *Polymer* **2004**, *45* (2), 429–436. https://doi.org/10.1016/j.polymer.2003.11.009.

(24) Uda, Y.; Kaneko, F.; Kawaguchi, T. Selective Guest Uptake from Solvent Mixtures in the Clathrate Phase of Syndiotactic Polystyrene. *Macromol. Rapid Commun.* **2004**, *25* (22), 1900–1904. https://doi.org/10.1002/marc.200400328.

(25) Tanigami, K.; Ishii, D.; Nakaoki, T.; Stroeve, P. Characterization of Toluene and 2-Methylnaphthalene Transport Separated by Syndiotactic Polystyrene Having Various Crystalline Forms. *Polym. J.* **2013**, *45* (11), 1135–1139. https://doi.org/10.1038/pj.2013.44.

(26) Kobayashi, H.; Urakawa, O.; Kaneko, F.; Inoue, T. Dynamics of Polar Aromatic Molecules Confined in a Nanocavity of δ-Phase of Syndiotactic Polystyrene as Studied by Dielectric Spectroscopy. *Chem. Phys.* **2016**, *479*, 122–128. https://doi.org/10.1016/j.chemphys.2016.07.021.

(27) Albunia, A. R.; Minucci, T.; Guerra, G. Ethylene Removal by Sorption from Polymeric Crystalline Frameworks. *J. Mater. Chem.* **2008**, *18* (9), 1046. https://doi.org/10.1039/b715144f.

(28) Venditto, V.; Pellegrino, M.; Califano, R.; Guerra, G.; Daniel, C.; Ambrosio, L.; Borriello, A. Monolithic Polymeric Aerogels with VOCs Sorbent Nanoporous Crystalline and Water Sorbent Amorphous Phases. *ACS Appl. Mater. Interfaces* **2015**, *7* (2), 1318–1326. https://doi.org/10.1021/am507116e.

(29) Daniel, C.; Antico, P.; Yamaguchi, H.; Kogure, M.; Guerra, G. Microporous-Crystalline Microfibers by Eco-Friendly Guests: An Efficient Tool for Sorption of Volatile Organic Pollutants. *Microporous Mesoporous Mater.* **2016**, *232*, 205–210. https://doi.org/10.1016/j.micromeso.2016.06.028.

(30) Daniel, C.; Antico, P.; Guerra, G. Etched Fibers of Syndiotactic Polystyrene with Nanoporous-Crystalline Phases. *Macromolecules* **2018**, *51* (15), 6138–6148. https://doi.org/10.1021/acs.macromol.8b01044.

(31) Galizia, M.; Daniel, C.; Fasano, G.; Guerra, G.; Mensitieri, G. Gas Sorption and Diffusion in Amorphous and Semicrystalline Nanoporous Poly(2,6-Dimethyl-1,4-Phenylene)Oxide. *Macromolecules* **2012**, *45* (8), 3604–3615. https://doi.org/10.1021/ma3000626.

(32) Galizia, M.; Daniel, C.; Guerra, G.; Mensitieri, G. Solubility and Diffusivity of Low Molecular Weight Compounds in Semi-Crystalline Poly-(2,6-Dimethyl-1,4-Phenylene)Oxide: The Role of the Crystalline Phase. *J. Membr. Sci.* **2013**, *443*, 100–106. https://doi.org/10.1016/j.memsci.2013.04.070.

(33) Figueroa-Gerstenmaier, S.; Daniel, C.; Milano, G.; Guerra, G.; Zavorotynska, O.; Vitillo, J. G.; Zecchina, A.; Spoto, G. Storage of Hydrogen as a Guest of a Nanoporous Polymeric Crystalline Phase. *Phys. Chem. Chem. Phys.* **2010**, *12* (20), 5369. https://doi.org/10.1039/b923173k.

(34) Pilla, P.; Cusano, A.; Cutolo, A.; Giordano, M.; Mensitieri, G.; Rizzo, P.; Sanguigno, L.; Venditto, V.; Guerra, G. Molecular Sensing by Nanoporous Crystalline Polymers. *Sensors* **2009**, *9* (12), 9816–9857. https://doi.org/10.3390/s91209816.

(35) Lova, P.; Bastianini, C.; Giusto, P.; Patrini, M.; Rizzo, P.; Guerra, G.; Iodice, M.; Soci, C.; Comoretto, D. Label-Free Vapor Selectivity in Poly(*p* -Phenylene Oxide) Photonic Crystal Sensors. *ACS Appl. Mater. Interfaces* **2016**, *8* (46), 31941–31950. https://doi.org/10.1021/acsami.6b10809.

(36) Uda, Y.; Kaneko, F.; Tanigaki, N.; Kawaguchi, T. The First Example of a Polymer-Crystal–Organic-Dye Composite Material: The Clathrate Phase of Syndiotactic Polystyrene with Azulene. *Adv. Mater.* **2005**, *17* (15), 1846–1850. https://doi.org/10.1002/adma.200500396.

(37) Anna De Girolamo Del Mauro; Maurizio Carotenuto; Vincenzo Venditto; Vittorio Petraccone; Marco Scoponi; Gaetano Guerra. Fluorescence of Syndiotactic Polystyrene/Trimethylbenzene Clathrate and Intercalate Co-Crystals. *Chem Mater* **2007**, *19* (24), 6041–6046. https://doi.org/10.1021/cm071483+.

(38) Albunia, A. R.; Rizzo, P.; Coppola, M.; De Pascale, M.; Guerra, G. Azobenzene Isomerization in Polymer Co-Crystalline Phases. *Polymer* **2012**, *53* (13), 2727–2735. https://doi.org/10.1016/j.polymer.2012.04.015.

(39) Albunia, A. R.; D'Aniello, C.; Guerra, G.; Gatteschi, D.; Mannini, M.; Sorace, L. Ordering Magnetic Molecules within Nanoporous Crystalline Polymers. *Chem. Mater.* **2009**, *21* (20), 4750–4752. https://doi.org/10.1021/cm902158k.

(40) Daniel, C.; Rufolo, C.; Bobba, F.; Scarfato, A.; Cucolo, A. M.; Guerra, G. Ferroelectric Co-Crystalline Polymers. *J. Mater. Chem.* **2011**, *21* (47), 19074. https://doi.org/10.1039/c1jm13282b.

(41) Albunia, A. R.; Rizzo, P.; Ianniello, G.; Rufolo, C.; Guerra, G. Syndiotactic Polystyrene Films with a Cocrystalline Phase Including Carvacrol Guest Molecules. *J. Polym. Sci. Part B Polym. Phys.* **2014**, *52* (9), 657–665. https://doi.org/10.1002/polb.23464.

(42) Golla, M.; Nagendra, B.; Daniel, C.; Rizzo, P.; Guerra, G. Isolated and Aggregated Carvacrol Guest Molecules in Cocrystalline Poly(2,6-Dimethyl-1,4-Phenylene)Oxide Films. *Polym. J.* **2021**, *53* (10), 1093–1100. https://doi.org/10.1038/s41428-021-00511-0.

(43) Albunia, A. R.; Guerra, G. Spectroscopic Investigation of Guest–Guest Interactions in the Nanoporous-Crystalline δ and ε Forms of Syndiotactic Polystyrene. *J. Phys. Chem. C* **2014**, *118* (22), 11774–11783. https://doi.org/10.1021/jp502679d.

(44) Rizzo, P.; Cozzolino, A.; Guerra, G. Chemical Stabilization of Hexanal Molecules by Inclusion as Guests of Nanoporous-Crystalline Syndiotactic Polystyrene Crystals. *Macromolecules* **2019**, *52* (6), 2255–2264. https://doi.org/10.1021/acs.macromol.8b02168.

(45) Guerra, G.; Daniel, C.; Rizzo, P.; Tarallo, O. Advanced Materials Based on Polymer Cocrystalline Forms. *J. Polym. Sci. Part B Polym. Phys.* **2012**, *50* (5), 305–322. https://doi.org/10.1002/polb.23035.

PART I

Results and Discussion about advances in the study on Poly(2,6-dimethyl-1,4-phenylene)oxide

CHAPTER 1
Nanoporous Crystalline alfa and beta phases of PPO

In this chapter, WAXD and FTIR characterizations of NC forms of PPO are shown. In particular, guests leading to co-crystalline (CC) and nanoporous crystalline (NC) α or β forms of PPO as well as the molecular features (i.e., solubility and molecular volume parameters) behind their formation are here analyzed.

1.1 Structural features on Nanoporous Crystalline PPO forms

It is known that PPO is a commercial thermoplastic polymer,[1–4] commonly available in the amorphous state and it is able to crystallize with low-molecular-mass molecules leading to CC forms.[5–7] However, only recently, it has been found that, after guest-extraction processes, PPO with NC phases can be easily obtained.[8–14]

As for NC phases of PPO, regardless of the polymer morphology (powders,[8] films,[9,13] or aerogels[12]), the existence of a continuum[14] of NC modifications has been suggested by WAXD patterns.

In this section, experimental evidences, mainly based on WAXD and FTIR measurements, show instead the formation of two well-separated NC forms, hereafter named α and β, which not only exhibit different chain packing but also slightly different chain conformations.

1.1.1 Guests leading to crystalline α-forms

The WAXD pattern, as taken with the X-ray beam parallel to the film plane (EDGE pattern), of a PPO film cast from carbon tetrachloride (CCl_4) solution is shown in Figure 1.1a. The presence of diffraction arcs centered on the equator of the pattern indicates that chain axes of the crystalline phase present an orientation preferentially parallel to the film plane ($c_{//}$ orientation).[14] The degree of planar orientation as evaluated by an azimuthal scan of the 001 reflection ($\chi_{(001)}$) of the EDGE pattern of Figure 1.1a is close to 0.6.

Equatorial profiles of EDGE patterns (like the one of Figure 1.1a) of PPO cast films from CCl_4, 1,1,1-trichloroethane (TCA), and 1,1,2-trichloroethylene (TCE) solutions, with a guest content of ∼11, ∼9, ∼12 wt%, evaluated by TGA measurements, are shown in Figure 1.2a-c, respectively. The diffraction profiles of the three CC films exhibit similar $2\theta_{CuK\alpha}$ values for the observed reflections. However, as generally expected for polymer CC phases,[15,16] variations in relative intensity of the observed peaks (mainly for low $2\theta_{CuK\alpha}$ reflections), depending on the chemical structure of the guest molecules, are observed. The WAXD EDGE pattern of the cast PPO film after CCl_4 removal by supercritical carbon dioxide ($scCO_2$) extraction is shown in Figure 1.1b. It is apparent that guest extraction does not change substantially the position of the diffraction arcs, neither their shape, clearly indicating the maintenance of a similar degree of $c_{//}$ orientation.

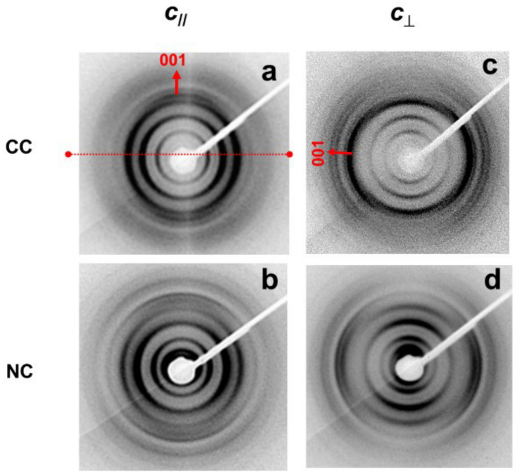

Figure 1.1 WAXD patterns, as taken with the X-ray beam parallel to the film plane (EDGE patterns), of CC PPO films (a,c) obtained by casting from CCl_4 solution (a) or by crystallization of the amorphous film by BE sorption (b) and of the respective α NC PPO films (b,d) obtained after CCl_4 (b) and BE (d) removal by $scCO_2$ extraction. The dashed red line in (a) shows the direction of equatorial profiles.

To get a more quantitative information, equatorial profiles of EDGE patterns, like the one shown in Figure 1.1b, for PPO cast films from CCl_4, TCA, and TCE solutions, after complete guest removal by $scCO_2$ extraction, are shown in Figure 1.2a′-c′, respectively. It is apparent that, as a consequence of guest extraction, the WAXD patterns of the three films become nearly identical to each other ($2\theta_{CuK\alpha}$ values of the main diffraction peaks and the corresponding Miller indexes, as proposed in ref [14], are collected in Table 1.1). This indicates the formation of a same NC phase starting from three different CC phases. It is also worth noting that the WAXD pattern of the NC films exhibits, with respect to the patterns of all considered CC forms, increased intensity of the 100 reflection and (to a lower extent) of the 010 reflection as well as a decreased intensity of the 310 reflection. EDGE patterns like those of Figure 1.1 also allow an accurate evaluation of the position of the meridional peak (001, at $2\theta_{CuK\alpha} = 16.8°$) and hence of the ***c*** periodicity, which is nearly 5.3 Å for the CC forms with CCl_4 (Figure 1.1a), TCA, and TCE, as well as for the corresponding NC forms (Figure 1.1b).

A strictly similar behavior is observed for other PPO CC films exhibiting c// orientation, like those obtained by casting from chlorobenzene (CB), 1,2-dichloro-benzene (*o*-DCB), 1,2,4-trichlorobenzene (TCB), toluene (TOL), and *o*-xylene ($2\theta_{CuK\alpha}$ values of the main diffraction peaks are collected in Table 1.1).

As for films obtained by guest-induced crystallization of amorphous PPO films, which exhibit a c⊥ orientation rather than the c// orientation,[14] the EDGE patterns show equatorial reflections centered along the meridian of the pattern (Figure 1.1c,d).

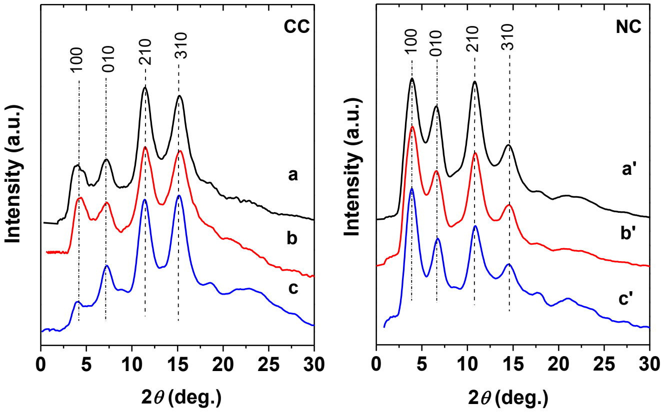

Figure 1.2 Equatorial profiles of EDGE WAXD patterns, like those of Figure 1.1, for PPO films: CC (a−c) as obtained by casting from CCl_4 (a), TCA (b), and TCE solutions (c); α NC (a′−c′) as obtained after $scCO_2$ extraction of CCl_4 (a′), TCA (b′), and TCE (c′) from cast films.

FTIR spectra of all the NC films of Table 1.1 are compared in Figure 1.3 with a spectrum (curve l) of an amorphous PPO film, for the spectral ranges 840−740 and 500−400 cm^{-1}. The presence of FTIR peaks associated with a crystalline phase is immediately apparent, as already reported in literature.[9,12] Moreover, all considered NC films of Table 1.1 present identical FTIR peak positions (828, 773, 495, and 414 cm^{-1}).

The whole set of WAXD and FTIR data clearly indicate the formation of a same NC form, by guest removal from many different CC phases. This NC form, which is characterized by a chain conformation with ***c*** periodicity of 5.28 ± 0.01 Å, will be named hereafter as α-form. Based on an average of the data of Table 1.1, an orthorhombic unit cell with a = 19.7 Å; b = 12.4 Å; c = 5.28 Å can be also derived. Density values of the NC films of Table 1.1, measured by floatation method, are rather similar (0.988 ± 0.004) and definitely smaller than the density of PPO amorphous films (1.043 ± 0.002).

The density of the NC α-form, as obtained by plotting measured densities versus degrees of crystallinity (as evaluated by FTIR spectra), and by extrapolating to 100% of crystallinity, is close to 0.93 g/cm^3.

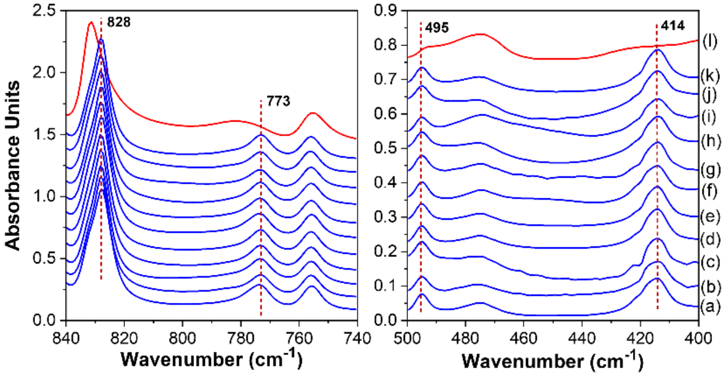

Figure 1.3 FTIR spectra of PPO films: α NC as obtained by scCO$_2$ extraction from CC films with different guests: (a) CCl$_4$, (b) TCA, (c) TCE, (d) CB, (e) *o*-DCB, (f) TCB, (g) *o*-xylene, (h) TOL, (i) carvone, (j) limonene, and (k) BE; amorphous (l).

Table 1.1 Miller indexes and $2\theta_{CuK\alpha}$ positions of the observed reflections for α NC films as obtained by guest removal from the corresponding co-crystalline films.

Guest	***$2\theta_{CuK\alpha}$ (deg), α nanoporous-crystalline films***													***c (Å)***	***orientation***	***Density (g/cm^3)***
	100	**010**	**200**	**210**	**310**	**001**	**011**	**211**	**301**	**221**	**321**	**131**	**331**			
CCl_4	4.5	7.1	-	11.2	15.0	16.8	18.1	20.4	21.3	23.9	-	27.6	30.2	5.27	$c_{//}$	0.982
TCA	4.5	7.2	-	11.2	15.0	16.7	18.1	20.3	21.3	23.9	-	27.6	30.1	5.30	$c_{//}$	0.990
TCE	4.5	7.2	-	11.3	15.0	16.7	18.2	-	21.5	23.9	-	27.6	30.2	5.30	$c_{//}$	0.995
CB	4.5	7.0	-	11.2	14.9	16.7	18.0	-	21.3	-	25.9	27.6	30.2	5.30	$c_{//}$	0.990
o-DCB	4.5	7.1	-	11.2	14.9	16.8	18.0	-	21.4	23.8	25.8	27.5	30.1	5.27	$c_{//}$	0.985
TCB	4.5	7.2	9.1	11.3	15.0	16.8	18.1	20.5	21.5	23.9	25.9	27.4	30.1	5.27	$c_{//}$	0.990
TOL	4.5	7.0	9.1	11.2	15.0	16.7	18.1	20.3	21.3	23.9	-	27.5	30.3	5.30	$c_{//}$	0.994
o-Xylene	4.5	7.2	-	11.3	14.9	16.7	18.1	-	21.6	23.9	25.8	27.4	-	5.30	$c_{//}$	0.992
Carvone*	4.5	7.1	9.0	11.3	15.1	16.8	18.1	20.5	21.5	24.0	25.8	27.5	30.3	5.27	$c_{\perp}$	0.982
Limonene*	4.6	7.1	9.1	11.3	15.1	16.7	18.1	20.4	21.4	24.0	-	27.4	30.3	5.29	$c_{\perp}$	0.992
BE*	4.5	7.1	9.0	11.2	-	16.8	18.2	-	21.4	23.9	25.8	27.6	30.1	5.27	$c_{\perp}$	0.982

Note: Precursor co-crystalline films were generally prepared by casting from solution or, for guests labeled with *, by guest-induced crystallization on amorphous films.

1.1.2 Guests leading to crystalline β-forms

WAXD EDGE patterns of a PPO film cast from benzene solution, before and after benzene extraction by $scCO_2$, are shown in Figure 1.4a and b, respectively. As discussed for Figure 1.1a and b, the presence of the 001 diffraction arcs centered on the equator of the pattern indicates the occurrence of $c_{//}$ orientation. The degree of planar orientation for both CC and NC films are close to $\chi_{(001)} = 0.5$. Equatorial profiles of EDGE patterns, like the one shown in Figure 1.4a, for PPO cast films from benzene, chloroform ($CHCl_3$) and for an amorphous film as crystallized by methyl ethyl ketone (MEK) sorption, with a guest content of ∼15, 13, 10 wt% by TGA measurements, are shown in Figure 1.5a-c, respectively. As already observed in the previous section, depending on the chemical nature of the guest molecules, variations in relative intensity of the peaks (mainly at low $2\theta_{CuK\alpha}$ values) are observed.[15,16]

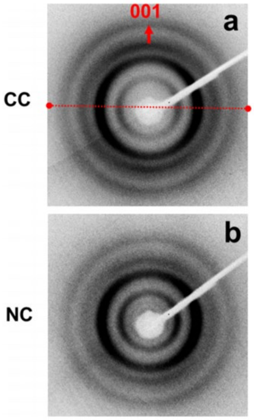

Figure 1.4 WAXD patterns, as taken with the X-ray beam parallel to the film plane (EDGE patterns) of CC PPO film obtained by cast from benzene solution (a) and of the corresponding NC β PPO film obtained after benzene removal by $scCO_2$ extraction (b). The dashed red line in (a) shows the direction of equatorial profiles.

Equatorial profiles of EDGE patterns, like the one shown in Figure 1.4b, for PPO CC films with benzene, $CHCl_3$, and MEK, after complete guest removal by $scCO_2$ extraction, are shown in Figure 1.5a′-c′, respectively. It is apparent that, as a consequence of guest extraction, the WAXD patterns of the three films become nearly identical to each other ($2\theta_{CuK\alpha}$ values of the main diffraction peaks and the corresponding Miller indexes, as proposed in ref[14], are collected in Table 1.2), for the CC films with benzene, $CHCl_3$, and MEK as well as for the CC film with hexanal. This indicates the formation of a same NC phase starting from three different CC phases. It is also worth noting that WAXD patterns of the NC films exhibit, with respect to patterns of all the considered CC forms, increased intensity of the equatorial *hk0* reflections (at $2\theta_{CuK\alpha}$ = 5.2°, 7.7° and 12.7°) with respect to first layer line *hk1* reflections (at $2\theta_{CuK\alpha}$ = 16.2° and 21.5°).

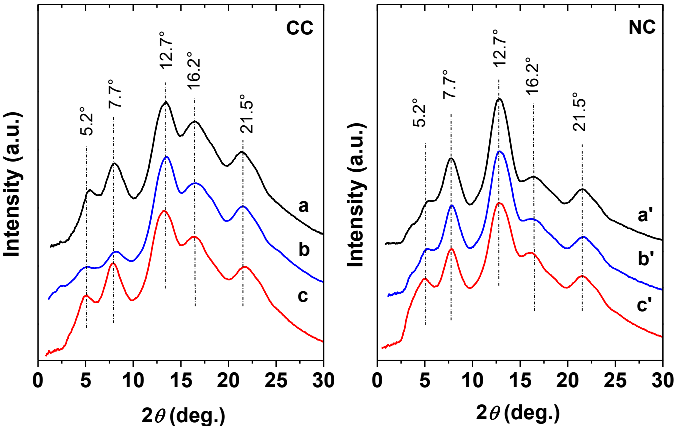

Figure 1.5 Equatorial profiles of EDGE WAXD patterns for PPO films: (a−c) CC β as obtained by casting in benzene (a), $CHCl_3$ (b) and by crystallization of amorphous film as induced by MEK sorption (c); (a′−c′) NC β as obtained after guest extraction by $scCO_2$ from CC films with benzene (a′), $CHCl_3$ (b′) and MEK (c′).

EDGE patterns like those of Figure 1.4 also allow an accurate evaluation of the position of the meridional peak (001, at $2\theta_{CuK\alpha}$ = 16.2°) and hence of the ***c*** periodicity, which is 5.47 ± 0.02 Å for the CC forms with benzene, $CHCl_3$, and MEK, as well as for the corresponding NC forms. This ***c*** periodicity is definitely higher than the ***c*** periodicity of the NC α-form of the previous section (5.28 Å).

The FTIR spectra of all NC films of Table 1.2 are compared in Figure 1.6 with a spectrum (curve e) of an amorphous PPO film, for the spectral ranges 840−740 and 500−400 cm^{-1}. The presence of FTIR peaks associated with a crystalline phase is immediately apparent, as already reported in literature.[9,12] Moreover, all the considered NC films of Table 1.2 present identical FTIR peak positions (826, 777, 495, and 418 cm^{-1}). Three of these crystalline FTIR peaks are definitely shifted with respect to those of the NC α-form of the previous section (828, 773, and 414 cm^{-1}).

The whole set of WAXD and FTIR data of this section clearly indicates the formation, starting from many different CC forms, of a same NC form, different from the NC α-form, which will be hereafter named as NC β-form, which is characterized by a chain conformation with ***c*** periodicity of 5.47 ± 0.02 Å.

Density values (by floatation method) of the NC films of Table 1.2 are rather similar (1.014 ± 0.009) and definitely smaller than the density of PPO amorphous films (1.043 ± 0.002). The density of the NC β-form, as obtained by plotting measured densities versus degrees of crystallinity (as evaluated by FTIR spectra), and by extrapolating to 100% of crystallinity, is close to 0.95 g/cm^3.

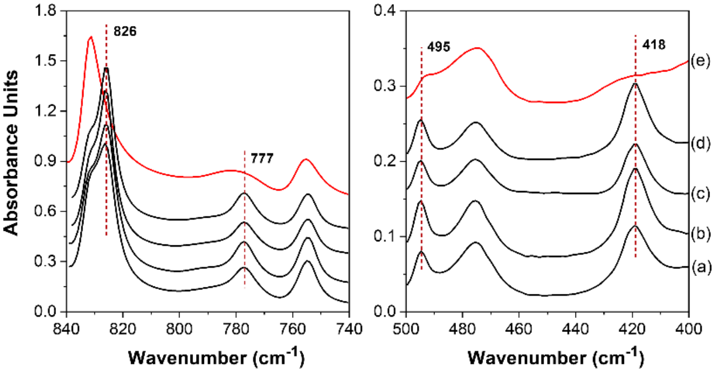

Figure 1.6 FTIR spectra of PPO films: (a−d) NC β as obtained after $scCO_2$ extraction from CC films, as prepared by casting from benzene (a) or $CHCl_3$ (b) solutions or from immersion of an amorphous film in liquid hexanal (c), and MEK (d); (e) amorphous.

Table 1.2 $2\theta_{CuK\alpha}$ positions and layer lines of the observed reflections for β NC films as obtained by guest removal from the corresponding co-crystalline films.

Guest	*$2\theta_{CuK\alpha}$ (deg.), β nanoporous-crystalline films*					*c (Å)*	*Preparation technique*	*Density (g/cm^3) (±0.005)*
	hk0	*hk0*	*hk0*	*001*	*hk1*			
Benzene	5.2	7.7	12.7	16.2	21.5	5.48	Solution casting	0.982
$CHCl_3$	5.2	7.8	12.8	16.1	21.5	5.50		0.990
MEK	5.1	7.7	12.8	16.2	21.4	5.47	Crystallization of amorphous film	0.995
Hexanal	5.1	7.6	12.8	16.2	21.4	5.45		0.982

Note: Density values were obtained by floatation method.

1.1.3 Guests leading to α or β forms depending on crystallization conditions

Regardless of the considered crystallization conditions, all guest molecules of previous sections (1.1.1 and 1.1.2) lead to PPO films with α and β NC forms, respectively.

However, there are also some guest molecules which lead, depending on crystallization conditions, to CC and NC films exhibiting α or β phases. This is shown, for instance, for CC films with methyl benzoate (MB) and corresponding NC films, whose equatorial profiles of EDGE diffraction patterns are shown in Figure 1.7. WAXD patterns of a PPO

CC film as cast at 60 °C from MB 1 wt% solution (with an MB content nearly equal to ~12 wt%, Figure 1.7a) and of the corresponding NC film (Figure 1.7a′), exhibit typical 100, 010, 210 and 310 reflections of the NC α form (see Table 1.1). WAXD patterns of a PPO CC film as crystallized by immersion of an amorphous film at room temperature in MB for 2 min (Figure 1.7b), and of the corresponding NC film (Figure 1.7b′) show, on the contrary, the diffraction peaks of the β-form (see Table 1.2).

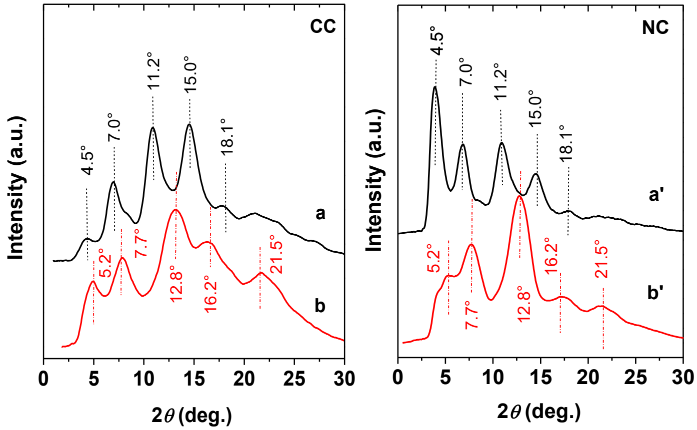

Figure 1.7 Equatorial profiles of EDGE WAXD patterns of PPO films: CC (a) and NC (a′), by casting from MB solution at 60 °C, exhibiting the diffraction peaks of the α-form; CC (b) and NC (b′), by crystallization of an amorphous film by immersion in MB at 20 °C, exhibiting the diffraction peaks of the β-form.

The formation of α and β NC forms is confirmed by ***c*** periodicities of 5.25 and 5.47 Å (as derived by the 001 reflection on the same EDGE patterns) for films casted from MB and for films crystallized by immersion in MB, respectively.

The achievement of α and β NC forms, by using the same guest molecule (MB) and changing the crystallization procedures (cast films or guest-induced crystallizations), is clearly confirmed by the FTIR spectra of the two NC films, as obtained by MB solution casting and by MB induced crystallization of an amorphous film, which are shown in Figure 1.8 by curves (a) and (b), respectively. In fact, the FTIR spectrum (a) shows the peaks at 828, 773, and 414 cm^{-1} typical of the α-form, whereas the FTIR spectrum (b) instead shows the peaks at 826, 777, and 418 cm^{-1} typical of the β-form.

For suitable guests, it is also possible to obtain NC α or β forms, for a same kind of crystallization procedure, by using only small changes in the crystallization temperature. For instance, the FTIR spectra (c) and (d) of Figure 1.8 correspond to amorphous films as crystallized by immersion in acetone at temperatures close to 60 and 50 °C, respectively.

Based on the positions of the crystalline peaks, it is immediately apparent that the blue-colored (a) and (c) spectra correspond to the NC α-form, whereas the black-colored (b) and (d) spectra correspond to the NC β-form.

Additionally, as can be easily observed, the FTIR spectrum of fully amorphous PPO samples (curve l of Figure 1.3; curve e of Figure 1.5) in the 840−400 cm^{-1} region is markedly different from those of both semicrystalline PPO samples (curves a-k of Figure 1.3; curves a-d of Figure 1.5). In particular, in the 500−400 cm^{-1} region, the semicrystalline samples display sharp FTIR bands which are negligible in the amorphous PPO, and the sharp band at 831 cm^{-1} becomes, in semicrystalline PPO samples, the shoulder of a new band located at a lower wavenumber. For an easier comparison, the most important FTIR peak positions for amorphous and NC PPO films are reported in Table 1.3.

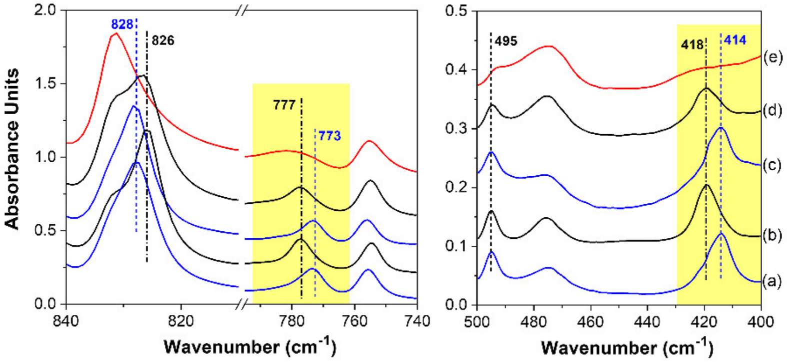

Figure 1.8 FTIR spectra of NC PPO films obtained after $scCO_2$ extraction of (a) films cast from MB solution at 60 °C; (b) films crystallized by immersion of an amorphous film in liquid MB at 20 °C; (c,d) films crystallized by immersion of amorphous films in acetone at 60 °C (c) or at 50 °C (d). For the sake of comparison, the FTIR spectrum of a fully amorphous PPO film is shown in (e). Blue and black colors correspond to spectra typical of α and β forms, respectively.

Table 1.3 FTIR peak positions for PPO chains only in the amorphous phase (1st column), only in the NC α-form (2nd column), only in the NC β-form (3rd column).

FTIR peak positions		
amorphous	**α-form**	**β-form**
831	828	826
781	773	777
755	756	756
491	495	495
	414	418

1.2 Molecular features behind formation of alfa and beta phases of PPO

PPO can be easily crystallized by solution casting method as well as by sorption of guest molecules in amorphous samples,[8,17–21] as shown in the previous section (1.1).

In particular, two completely different classes of CC forms with low-molecular-mass guest molecules can be observed: Class i and Class ii. The CC forms of Class i are formed only with few specific guests (α-pinene, tetralin, and decalin), exhibit regular polymer helices, and give rise to highly ordered CC phases.[5,7] The CC forms of Class ii are, instead, formed with many guests and exhibit different chain conformations and less ordered crystalline phases.[8,20–22]

The CC forms of Class ii, moreover, can be divided into two subclasses which are named α and β with different values of the chain periodicities ($\boldsymbol{c}$ = 0.528 nm and $\boldsymbol{c}$ = 0.547 nm) and different polymer packing (with main equatorial reflections at $2\theta_{CuK\alpha} \approx 4.5°$, 7.0°, 11.2°, 15.0°, and 5.2°, 7.7°, 12.7°, respectively),[8,20] as shown previously. After guest removal, the CC phases of Class i become amorphous,[5,7] while the CC phases of Class ii can produce two different NC forms, i.e., crystalline forms with a density lower than that of the corresponding amorphous phase.

In the present section, guest molecular features determining the formation of α or β crystalline PPO phases are explored.

1.2.1 Solubility parameter

WAXD patterns of the NC PPO films (with thickness in the range 40–70 μm), as obtained by casting from 1.5 wt% polymer solutions in many different solvents, followed by guest removal by immersion in acetonitrile (ACN) for 2 hours, are shown in Figure 1.9. The patterns of Figure 1.9 clearly show that the crystalline phases obtained from the polymer solutions in *p*-xylene (A) and 1,3-dichlorobenzene (B) exhibit *hk0* diffraction peaks at $2\theta_{CuK\alpha} \approx 7.1°$, 11.3°, 15.0° typical of the α-form, while the crystalline phases obtained with perchloroethylene (D), ethylbenzene (E), 1,2-dichloropropane (F), and 1,4-dioxane (G) exhibit the *hk0* diffraction peaks at $2\theta_{CuK\alpha} \approx 7.7°$, 12.8° typical of the β-form. The WAXD pattern of the film obtained by casting from *m*-xylene solution (C) shows diffraction peaks of both α and β crystalline forms.

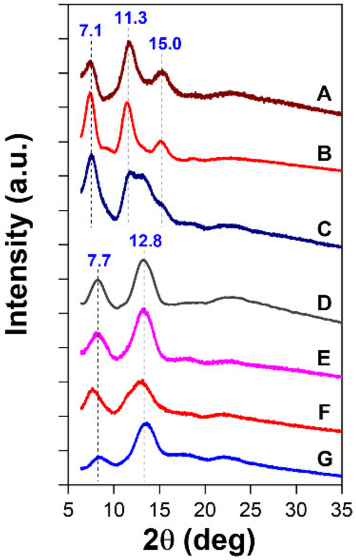

Figure 1.9 WAXD patterns of NC PPO films as obtained by solution casting, followed by guest extraction by ACN: A) *p*-xylene, B) 1,3-dichlorobenzene, C) *m*-xylene, D) perchloroethylene, E) ethylbenzene, F) 1,2-dichloropropane, and G) 1,4-dioxane.

This information is confirmed by FTIR spectra of the same films of Figure 1.9, which are reported in Figure 1.10, for the spectral range 800–400 cm^{-1}.

In fact, Figure 1.10A,B show absorbance peaks typical of the α-form (at 773 and 414 cm^{-1}), while the spectra of Figure 1.10D-G show absorbance peaks typical of the β-form (at 777 and 418 cm^{-1}).

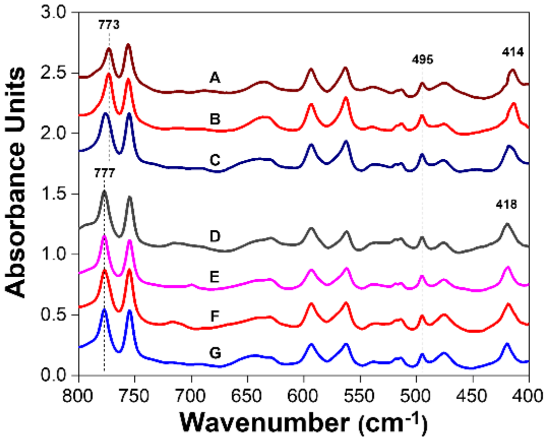

Figure 1.10 FTIR spectra of PPO films as obtained by solution casting, followed by guest extraction by ACN: A) *p*-xylene, B) 1,3-dichlorobenzene, C) *m*-xylene, D) perchloroethylene, E) ethylbenzene, F) 1,2-dichloropropane, and G) 1,4-dioxane.

The crystalline forms (α or β) of films as crystallized by sorption of the same solvents in amorphous PPO films were also established by WAXD and FTIR measurements, like those of Figures 1.9 and 1.10, respectively.

Table 1.4 collects in its last column the crystalline forms (α or β) of all films characterized in this study together with those already reported in the literature.[8,18,20,23–25]

In Table 1.4, the guest molecules are ordered on the basis of their Hildebrand solubility parameter (*δ*, second column) while the used crystallization methods are indicated in the fourth column. The Hildebrand solubility parameter[26] *δ* generally provides a numerical estimate of the degree of interaction between materials. It can be a good indication of how capable they are to form a solution (i.e. solubility), particularly for nonpolar materials such as many polymers. Materials with similar values of *δ* are likely to be miscible.

Table 1.4 Solubility parameter (*δ*) of the guest molecules vs corresponding crystalline phases of PPO.

Guest Molecules	**Solubility Parameter ($MPa^{1/2}$)**	**Reference for crystal form**	**Preparation technique**	**Crystal form**
Diethyl ether	15.64	present analysis	GIC	β-form
1,1,1-Trichloroethane	17.45	Nagendra *et al.*, 2019,[20] & 2021[23]	casting & GIC	α-form
m-Xylene	17.70	present analysis	casting & GIC	Mixed
p-Xylene	17.70	present analysis	casting & GIC	α-form
CCl_4	17.81	Nagendra *et al.*, 2019,[20] & 2021[23]	casting & GIC	α-form
Limonene	17.82	Nagendra *et al.*, 2019,[20] & 2021[25]	casting & GIC	α-form
Ethyl benzene	17.86	present analysis	casting & GIC	β-form
Mesitylene	18.01	Golla *et al.*, 2020[24] & Nagendra *et al.*, 2021[23]	casting & GIC	α-form
o-Xylene	18.09	Nagendra *et al.*, 2019,[20] & 2021[23]	casting & GIC	α-form
Ethyl acetate	18.15	present analysis	GIC	β-form
Toluene	18.16	Nagendra *et al.*, 2019,[20] & 2021[23]	casting & GIC	α-form
Benzene	18.50	Nagendra *et al.*, 2019,[20]	casting	β-form
Hexanal	18.73	Nagendra *et al.*, 2019,[20]	GIC	β-form
1,2-dichloropropane	18.92	present analysis	casting & GIC	β-form
$CHCl_3$	18.94	Nagendra *et al.*, 2019,[20]	casting	β-form
Trichloroethylene	19.01	Nagendra *et al.*, 2019,[20]	casting	α-form
Methyl ethyl ketone	19.05	Nagendra *et al.*, 2019,[20]	GIC	β-form
Dibenzyl ether	19.13	Nagendra *et al.*, 2019,[20] & 2021[23]	casting & GIC	α-form
Methyl benzoate	19.45	Nagendra *et al.*, 2019,[20] & 2021[23]	casting & GIC	β-form
Tetrahydrofuran	19.46	present analysis	GIC	β-form
Chlorobenzene	19.58	Nagendra *et al.*, 2019,[20] & 2021[23]	casting & GIC	α-form
1,2-Dichloroethane	19.88	Nagendra *et al.*, 2021[25]	casting & GIC	β-form
Carvone	19.90	Nagendra *et al.*, 2021[25] & 2021[23]	casting & GIC	α-form
Eugenol	20.03	present analysis & Nagendra *et al.*, 2021[23]	casting& GIC	α-form
Perchloroethylene	20.28	present analysis	casting & GIC	β-form
1,4-Dioxane	20.46	present analysis	casting & GIC	β-form
1,2-dichlorobenzene	20.47	Nagendra *et al.*, 2019,[20] & 2021[23]	casting & GIC	α-form
Carbon disulfide	20.50	Toi *et al.*, 1982[27]	casting	β-form
1,3- dichlorobenzene	20.52	present analysis	casting & GIC	α-form
Carvacrol	20.70	Golla *et al.*, 2021[28]	GIC	α-form
1,2,4- trichlorobenzene	21.31	Nagendra *et al.*, 2019,[20] & 2021[23]	casting & GIC	α-form

GIC: Guest Induced Crystallization on amorphous film.

The fourth column of Table 1.4 clearly shows that the structure of the obtained crystalline forms does not depend on the crystallization method but only on the chemical nature of the guest used for polymer co-crystallization. Moreover, Table 1.4 shows the absence of any correlation between the structure of the CC forms (α or β) and the δ solubility parameter of the guest, which is generally expected to be relevant for host-guest co-crystallizations.

1.2.2 Molecular volume and water solubility parameters

Based on the crystallization data of Table 1.4, possible correlations between the structural and physical properties of the considered guests and the achievement of the α and β forms were then investigated. It was found that the best correlations occur with molecular volume and solubility in water (collected from the literature),[29,30] as shown in Tables 1.5 and 1.6, respectively.

In detail, Table 1.5 shows that all the considered guests with molecular volumes higher than 230 Å^3 and lower than 149 Å^3 lead to the α and β forms, respectively. As for the guest molecular volume, it is worth adding that it also has a key role in determining the orientation (with crystalline chain axis being preferentially parallel or perpendicular to the film plane)[31] of PPO films.[23]

Table 1.6 shows that all guests whose solubility is lower than 0.11 mmol per 100 mL of water and higher than 2 mmol per 100 mL of water lead to the α and β forms, respectively.

In summary, the data in Tables 1.5 and 1.6 show that, independently of the crystallization method, the α-form is favored by hydrophobic and bulky guest molecules while the hydrophilic and small guest molecules favor the β-form. Hence, more hydrophilic and smaller guest molecules favor the formation of the CC and NC crystalline β-forms, which are characterized by a higher chain periodicity.[20]

For many guests seems to be apparent a co-operation between guest molecular volume and hydrophobicity nature in forming one crystalline form (α or β) instead of the other one.

Table 1.5 Guest molecular volume vs corresponding crystalline forms.

Guest Molecules	Guest molecular volume ($Å^3$)	Crystal form
Dibenzyl ether	315.8	α-form
Limonene	269.0	
Carvone	259.9	
Eugenol	257.3	
Carvacrol	255.3	
Mesitylene	231.0	
Methyl benzoate	208.6	β-form
1,2,4-trichlorobenzene	206.4	α-form
m-Xylene	205.0	mixed
p-Xylene	204.8	α-form
Hexanal	204.1	β-form
Ethyl benzene	203.5	β-form
o-Xylene	200.4	α-form
1,3-dichlorobenzene	189.6	α-form
1,2-dichlorobenzene	187.8	α-form
Toluene	175.9	α-form
Diethyl ether	172.6	β-form
Perchloroethylene	169.8	β-form
Chlorobenzene	168.4	α-form
TCA	167.8	α-form
1,2-dichloropropane	162.3	β-form
Ethyl acetate	162.2	β-form
CCl_4	160.7	α-form
trichloroethylene	149.4	α-form
Methyl ethyl ketone	148.7	β-form
Benzene	148.1	
1,4-Dioxane	141.6	
Tetrahydrofuran	135.0	
$CHCl_3$	133.1	
DCA	131.5	
Carbon disulfide	99.8	

Table 1.6 Guest solubility in 100 mL of water vs corresponding crystalline forms.

Guest Molecules	Guest solubility in 100 mL of water at 25 °C (mmol)	Crystal form
Limonene	0.010	α-form
Dibenzyl ether	0.020	
1,2,4-Trichlorobenzene	0.027	
Mesitylene	0.040	
1,3-dichlorobenzene	0.084	
1,2-dichlorobenzene	0.106	
perchloroethylene	0.124	β-form
o-Xylene	0.152	α-form
m-Xylene	0.150	Mixed
p-Xylene	0.154	α-form
Ethyl benzene	0.159	β-form
Chlorobenzene	0.439	α-form
CCl_4	0.526	α-form
Toluene	0.564	α-form
Carvacrol	0.832	α-form
Carvone	0.865	α-form
TCA	0.967	α-form
trichloroethylene	0.974	α-form
Eugenol	1.498	α-form
Methyl benzoate	1.491	β-form
Benzene	2.304	
1,2-dichloropropane	2.478	
Carbon disulfide	2.836	
Hexanal	4.992	
$CHCl_3$	6.701	
DCA	8.700	
Diethyl ether	81.62	
Methyl ethyl ketone	323.1	
Ethyl acetate	92.1	
Tetrahydrofuran	686	
1,4-Dioxane	1140	

1.3 Conclusions

WAXD and FTIR measurements show the formation of two well-separated NC forms of PPO, named α and β, which are obtained by guest removal by two well-separated families of CC forms. Most of the used guest molecules lead only to α or β CC and NC forms, independently of the crystallization procedure (solution casting and solvent-induced crystallization of amorphous films) and can be considered α or β guests of PPO. For few guest molecules (MB, acetone) α or β CC and NC forms are obtained depending on the crystallization conditions.

As for the NC α form, the inclusion of low-molecular-mass molecules as guest of the crystalline phase (rather than absorbed in the amorphous phase, as generally observed for polymers) is associated with decrease and increase of intensity of 100 and 310 reflections, respectively. As for the NC β form, the inclusion of low-molecular-mass molecules as guests of the crystalline phase is associated with decrease and increase of intensity of equatorial *hk0* and first layer line *hk1* reflections, respectively.

NC (and CC) α and β forms not only exhibit different chain packing but also slightly different chain conformations ($\boldsymbol{c}$ = 5.28 and 5.47 Å, respectively).

Additionally, independently of the two considered crystallization methods, the α-form is favored by hydrophobic and bulky guest molecules while the β-form (being characterized by a higher chain periodicity) is favored by hydrophilic and small guest molecules.

In detail, all the considered guests with molecular volumes higher than 230 Å^3 and lower than 149 Å^3 lead to the α and β forms, respectively. Moreover, all guests with solubility lower than 0.11 mmol per 100 mL of water and higher than 2 mmol per 100 mL of water lead to the α and β forms, respectively.

REFERENCES

(1) Guerra, G.; De Rosa, C.; Vitagliano, V. M.; Petraccone, V.; Corradini, P. Effects of Blending on the Polymorphic Behavior of Melt-Crystallized Syndiotactic Polystyrene. *J. Polym. Sci. Part B Polym. Phys.* **1991**, *29* (3), 265–271. https://doi.org/10.1002/polb.1991.090290301.

(2) Aguilar-Vega, M.; Paul, D. R. Gas Transport Properties of Polyphenylene Ethers. *J. Polym. Sci. Part B Polym. Phys.* **1993**, *31* (11), 1577–1589. https://doi.org/10.1002/polb.1993.090311114.

(3) Tsujita, Y. Gas Sorption and Permeation of Glassy Polymers with Microvoids. *Prog. Polym. Sci.* **2003**, *28* (9), 1377–1401. https://doi.org/10.1016/S0079-6700(03)00048-0.

(4) Minelli, M.; De Angelis, M. G.; Sarti, G. C. Predictive Calculations of Gas Solubility and Permeability in Glassy Polymeric Membranes: An Overview. *Front. Chem. Sci. Eng.* **2017**, *11* (3), 405–413. https://doi.org/10.1007/s11705-017-1615-5.

(5) Horikiri, S. Single Crystals of Poly(2,6-Dimethylphenylene Oxide). *J. Polym. Sci. Part -2 Polym. Phys.* **1972**, *10* (6), 1167–1170. https://doi.org/10.1002/pol.1972.160100618.

(6) Ilinitch, O. M.; Semin, G. L.; Chertova, M. V.; Zamaraev, K. I. Novel Polymeric Membranes for Separation of Hydrocarbons. *J. Membr. Sci.* **1992**, *66* (1), 1–8. https://doi.org/10.1016/0376-7388(92)80085-X.

(7) Tarallo, O.; Petraccone, V.; Daniel, C.; Fasano, G.; Rizzo, P.; Guerra, G. A Chiral Co-Crystalline Form of Poly(2,6-Dimethyl-1,4-Phenylene)Oxide (PPO). *J. Mater. Chem.* **2012**, *22* (23), 11672. https://doi.org/10.1039/c2jm30907f.

(8) Daniel, C.; Longo, S.; Fasano, G.; Vitillo, J. G.; Guerra, G. Nanoporous Crystalline Phases of Poly(2,6-Dimethyl-1,4-Phenylene)Oxide. *Chem. Mater.* **2011**, *23* (13), 3195–3200. https://doi.org/10.1021/cm200546r.

(9) Galizia, M.; Daniel, C.; Fasano, G.; Guerra, G.; Mensitieri, G. Gas Sorption and Diffusion in Amorphous and Semicrystalline Nanoporous Poly(2,6-Dimethyl-1,4-Phenylene)Oxide. *Macromolecules* **2012**, *45* (8), 3604–3615. https://doi.org/10.1021/ma3000626.

(10) Daniel, C.; Zhovner, D.; Guerra, G. Thermal Stability of Nanoporous Crystalline and Amorphous Phases of Poly(2,6-Dimethyl-1,4-Phenylene) Oxide. *Macromolecules* **2013**, *46* (2), 449–454. https://doi.org/10.1021/ma302227q.

(11) Galizia, M.; Daniel, C.; Guerra, G.; Mensitieri, G. Solubility and Diffusivity of Low Molecular Weight Compounds in Semi-Crystalline Poly-(2,6-Dimethyl-1,4-Phenylene)Oxide: The Role of the Crystalline Phase. *J. Membr. Sci.* **2013**, *443*, 100–106. https://doi.org/10.1016/j.memsci.2013.04.070.

(12) Daniel, C.; Pellegrino, M.; Venditto, V.; Aurucci, S.; Guerra, G. Nanoporous-Crystalline Poly(2,6-Dimethyl-1,4-Phenylene)Oxide (PPO) Aerogels. *Polymer* **2016**, *105*, 96–103. https://doi.org/10.1016/j.polymer.2016.10.017.

(13) Lova, P.; Bastianini, C.; Giusto, P.; Patrini, M.; Rizzo, P.; Guerra, G.; Iodice, M.; Soci, C.; Comoretto, D. Label-Free Vapor Selectivity in Poly(*p* -Phenylene Oxide) Photonic Crystal Sensors. *ACS Appl. Mater. Interfaces* **2016**, *8* (46), 31941–31950. https://doi.org/10.1021/acsami.6b10809.

(14) Rizzo, P.; Gallo, C.; Vitale, V.; Tarallo, O.; Guerra, G. Nanoporous-Crystalline Films of PPO with Parallel and Perpendicular Polymer Chain Orientations. *Polymer* **2019**, *167*, 193–201. https://doi.org/10.1016/j.polymer.2019.01.073.

(15) De Rosa, C.; Guerra, G.; Petraccone, V.; Pirozzi, B. Crystal Structure of the Emptied Clathrate Form (δ_eForm) of Syndiotactic Polystyrene. *Macromolecules* **1997**, *30* (14), 4147–4152. https://doi.org/10.1021/ma970061q.

(16) Guerra, G.; Daniel, C.; Rizzo, P.; Tarallo, O. Advanced Materials Based on Polymer Cocrystalline Forms. *J. Polym. Sci. Part B Polym. Phys.* **2012**, *50* (5), 305–322. https://doi.org/10.1002/polb.23035.

(17) Alentiev, A.; Drioli, E.; Gokzhaev, M.; Golemme, G.; Ilinich, O.; Lapkin, A.; Volkov, V.; Yampolskii, Yu. Gas Permeation Properties of Phenylene Oxide Polymers. *J. Membr. Sci.* **1998**, *138* (1), 99–107. https://doi.org/10.1016/S0376-7388(97)00219-6.

(18) Khulbe, K. X-Ray Diffraction Analysis of Dense PPO Membranes. *J. Membr. Sci.* **2000**, *170* (1), 81–89. https://doi.org/10.1016/S0376-7388(99)00365-8.

(19) Sterescu, D. M.; Stamatialis, D. F.; Mendes, E.; Kruse, J.; Rätzke, K.; Faupel, F.; Wessling, M. Boltorn-Modified Poly(2,6-Dimethyl-1,4-Phenylene Oxide) Gas Separation Membranes. *Macromolecules* **2007**, *40* (15), 5400–5410. https://doi.org/10.1021/ma070772g.

(20) Nagendra, B.; Cozzolino, A.; Daniel, C.; Rizzo, P.; Guerra, G.; Auriemma, F.; De Rosa, C.; D'Alterio, M. C.; Tarallo, O.; Nuzzo, A. Two Nanoporous Crystalline Forms of Poly(2,6-Dimethyl-1,4-Phenylene)Oxide and Related Co-Crystalline Forms. *Macromolecules* **2019**, *52* (24), 9646–9656. https://doi.org/10.1021/acs.macromol.9b01911.

(21) Alentiev, A. Y.; Levin, I. S.; Buzin, M. I.; Belov, N. A.; Nikiforov, R. Y.; Chirkov, S. V.; Blagodatskikh, I. V.; Kechekyan, A. S.; Kechekyan, P. A.; Bekeshev, V. G.; Ryzhikh, V. E.; Yampolskii, Yu. P. Gas Transport Parameters, Density and Free Volume of Nanocrystalline Poly-2,6-Dimethylphenylene Oxide. *Polymer* **2021**, *226*, 123804. https://doi.org/10.1016/j.polymer.2021.123804.

(22) Golla, M.; Nagendra, B.; Fierro, F.; Rizzo, P.; Daniel, C.; Guerra, G. Axially Oriented Nanoporous Crystalline Phases of Poly(2,6-Dimethyl-1,4-Phenylene)Oxide. *ACS Appl. Polym. Mater.* **2020**, *2* (8), 3518–3524. https://doi.org/10.1021/acsapm.0c00532.

(23) Nagendra, B.; Golla, M.; Gallo, C.; Daniel, C.; Rizzo, P.; Guerra, G.; Baldino, L.; Reverchon, E. Mechanisms Determining Different Planar Orientations in PPO Films Crystallized by Guest Sorption. *Polymer* **2021**, *235*, 124242. https://doi.org/10.1016/j.polymer.2021.124242.

(24) Golla, M.; Nagendra, B.; Daniel, C.; Rizzo, P.; Guerra, G. Axial Orientation of Co-Crystalline Phases of Poly(2,6-Dimethyl-1,4-Phenylene)Oxide Films. *Polymers* **2020**, *12* (10), 2394. https://doi.org/10.3390/polym12102394.

(25) Nagendra, B.; Golla, M.; Daniel, C.; Rizzo, P.; Guerra, G. Melting of Nanoporous-Crystalline and Co-Crystalline Solution Cast Films of Poly(2,6-Dimethyl-1,4-Phenylene) Oxide. *Polymer* **2021**, *228*, 123935. https://doi.org/10.1016/j.polymer.2021.123935.

(26) Hansen, C. M. *Hansen Solubility Parameters: A User's Handbook, Second Edition*, 0 ed.; CRC Press, 2007. https://doi.org/10.1201/9781420006834.

(27) Toi, K.; Morel, G.; Paul, D. R. Gas Sorption and Transport in Poly(Phenylene Oxide) and Comparisons with Other Glassy Polymers. *J. Appl. Polym. Sci.* **1982**, *27* (8), 2997–3005. https://doi.org/10.1002/app.1982.070270823.

(28) Golla, M.; Nagendra, B.; Daniel, C.; Rizzo, P.; Guerra, G. Isolated and Aggregated Carvacrol Guest Molecules in Cocrystalline Poly(2,6-Dimethyl-1,4-Phenylene)Oxide Films. *Polym. J.* **2021**, *53* (10), 1093–1100. https://doi.org/10.1038/s41428-021-00511-0.

(29) Schneider, G. M. A. L. Horvath: Halogenated Hydrocarbons. Solubility - Miscibility with Water, Marcel Dekker, Inc., New York, Basel 1982. 889 Seiten, Preis: 310 SFr. *Berichte Bunsenges. Für Phys. Chem.* **1983**, *87* (3), 289–289. https://doi.org/10.1002/bbpc.19830870329.

(30) Yalkowsky, S. H.; He, Y.; Jain, P. *Handbook of Aqueous Solubility Data*, 0 ed.; CRC Press, 2016. https://doi.org/10.1201/EBK1439802458.

(31) Rizzo, P.; Gallo, C.; Vitale, V.; Tarallo, O.; Guerra, G. Nanoporous-Crystalline Films of PPO with Parallel and Perpendicular Polymer Chain Orientations. *Polymer* **2019**, *167*, 193–201. https://doi.org/10.1016/j.polymer.2019.01.073.

CHAPTER 2

Nanoporous Crystalline PPO films for air and water purification

In this chapter, sorption properties of NC PPO samples are investigated in order to prove if they could be suitable for applications such as air and water purification. In particular, sorption tests from vapour phase as well as from aqueous solutions are performed considering the pollutant perchloroethylene (PCE).

The presence of PCE in air and groundwater is due to anthropogenic sources (e.g. industrial discharges from manufacturing activities, solid waste landfill, etc.)[1,2] and results in alteration of the natural environment. Treatment methods for PCE pollution control consist mainly of conventional phase separation techniques (e.g., adsorption processes,[2–4] electrokinetic technologies)[5–7] and methods which destroy the contaminants (e.g., chemical oxidation/reduction,[8–10] bioremediation).[11,12] As concern the latter one, production of less harmful products is the main disadvantage which should be carefully considered for its practical application.

Adsorption treatments of contaminated air/groundwater are widely used, and they have a good potential as pollutant remediation method. As the adsorption phenomena take place, the pollutant is immobilized into the barrier, avoiding leaching and precipitation phenomena. Many adsorbent materials could be used as permeable barrier and the passive character (no energy input is required), high efficiency and relatively low operating and maintenance cost in the long-term are the principal advantages of this technique.

So, NC samples of PPO (and sPS for comparison) in different morphologies (i.e., aerogels, powders, films) have been tested as permeable barrier for PCE remediation from air as well as from water.

2.1 Perchloroethylene sorption from air

About sorption capacity of NC samples of PPO, compared to that of NC samples of sPS, it was found that for most guest molecules (e.g., small gas molecules,[13] benzene,[14] decane[15]) the sorption capacity of PPO is higher than for sPS. However, for some molecules whose fitting with the crystalline cavities of sPS is particularly favorable (e.g., for 1,2-dichloroethane), guest sorption is higher for NC sPS samples.[16]

This generally higher sorption capacity of NC PPO samples is mainly due to its high free-volume amorphous phase, which is also nanoporous[17–20] although with a guest sorption capacity (for low guest concentrations) being generally smaller than for the corresponding NC phases.[14,15]

Moreover, largely different kinetics of guest sorption occur for samples exhibiting different morphologies. In particular, the highest guest sorption kinetics are obtained for NC aerogels[21] and rather similar sorption kinetics are observed for NC microfibers or etched fibers.[22] Definitely slower kinetics are instead observed for NC films,[21] with reduction of apparent diffusivities of many orders of magnitude.[23]

In the present section, the sorption behavior of PCE, a common pollutant,[2,8] in NC PPO samples is explored. A significant comparison with sPS samples is also reported.

2.1.1 Diffusivity in NC aerogels

WAXD patterns of PPO aerogels obtained by solvent extraction with $scCO_2$ from gels prepared in carbon tetrachloride (CCl_4) and in methyl benzoate (MB) are shown in Figure 2.1a and b, respectively. The WAXD pattern of Figure 2.1a displays diffraction peaks at $2\theta_{CuK\alpha}$ = 4.5°, 7.1°, 11.1°, 15.0°, 18.0° and 21.4° typical of the NC α-form[24] while the WAXD pattern of Figure 2.1b displays diffraction peaks at $2\theta_{CuK\alpha}$ = 5.2°, 7.4°, 12.5° and 21.1° typical of the NC β-form.[24]

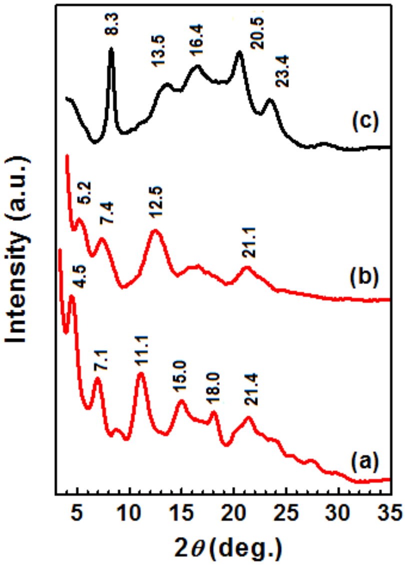

Figure 2.1 WAXD patterns of PPO (curves a and b) and sPS (curve c) aerogels obtained by solvent extraction with $scCO_2$ of PPO gels prepared in CCl_4 (a, α-form of PPO), MB (b, β-form of PPO) and of a sPS gel prepared in DCE (c, δ-form of sPS).

The WAXD pattern of a sPS aerogel obtained by solvent extraction with $scCO_2$ from a gel prepared in 1,2-dichloroethane (DCE) is shown in Figure 2.1c and exhibits the diffraction peaks at $2\theta_{CuK\alpha}$ = 8.3°, 13.5°, 16.4°, 20.5° and 23.4°, typical of the NC δ-form.[25]

Degrees of crystallinity of the aerogels of Figure 2.1, as evaluated by subtraction of the diffraction halo of a fully amorphous PPO sample, are in the range 40–50%. These values well agree with those obtained by DSC and FTIR methods for PPO and sPS aerogels, respectively.

BET surface area (SA_{BET}) values, as evaluated by N_2 sorption measurements at 77 K for the three types of aerogels are reported in 4th column of Table 2.1. In agreement with literature,[15,23] SA_{BET} values for NC PPO aerogels are much higher than for NC sPS aerogels.

This result can be possibly explained by the occurrence for PPO of a high-free-volume amorphous phase.[17–19] As for PPO, it is also worth noting that the NC β-form aerogel exhibits a surface area higher than the NC α-form aerogel.[15]

As for NC aerogels of sPS, it is very well established that surface area mainly depends on the nature of the crystalline phase. In fact, the highest SA values are observed for the nanoporous δ-form (SA = ~270–290 m^2/g) while a lower value for the nanoporous ε aerogels (SA = ~230 m^2/g).[26] Hence is not surprising that also for PPO there is a dependence of SA_{BET} on the α or β crystalline form.

Gravimetric sorption of PCE in aerogels, which exhibit NC phases of PPO and sPS, was investigated at T = 35 °C and for p/p_0 in the range 0.01–0.04 (Figure 2.2).

Sorption isotherms (Figure 2.2a) show that the sPS aerogel presents a PCE sorption capacity slightly higher than for both PPO aerogels. For instance, at $(p/p_0) = 0.01$ the PCE equilibrium uptake for the sPS aerogel is ≈12.25 wt% while the uptake for PPO α-form and PPO β-form aerogels is ≈9.15 wt% and ≈9.75 wt%, respectively.

PCE sorption kinetics at T = 35 °C and $p/p_0 = 0.01$ (Figure 2.2b) show that PCE sorption is fast for all the considered aerogels, due to the presence of porosity ($P \approx 90\%$) which allows fast diffusivities. Based on the initial slopes of the curves (inset of Figure 2.2b) apparent diffusivities are reported in the last column of Table 2.1. The higher diffusivities of PPO aerogels are well rationalized by their higher surface area (4th column of Table 2.1).

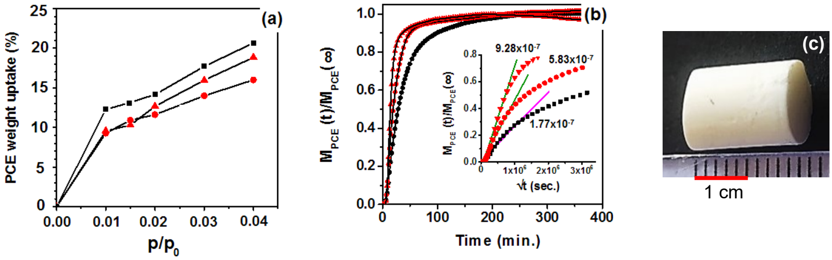

Figure 2.2 Gravimetric uptake of PCE at 35 °C and for $0.04 \geq p/p_0 \geq 0.01$ in NC aerogels: PPO α-form (●), PPO β-form (▲) and sPS δ-form (■). (a) Sorption isotherms; (b) Sorption kinetics for $p/p_0 = 0.01$, reported as $M_{PCE}(t)/M_{PCE}(\infty)$ vs time, where $M_{PCE}(\infty)$ is the PCE equilibrium weight uptake; (c) a photograph of a PPO aerogel, with a density $\rho = 0.1$ g/cm^3. The inset in (b) shows $M_{PCE}(t)/M_{PCE}(\infty)$ data vs square root of time, which have been used to evaluate apparent diffusivity values of the last column of Table 2.1 (rows 1–3).

Table 2.1 Density, BET surface area, PCE uptake and diffusivity values (at 35 °C for $p/p_0 = 0.01$) for aerogels and films.

	NC sample	*Density (g cm^{-3})*	*SA_{BET} (m^2 g^{-1})*	*g_{PCE}/g_{poly} (%)*	*g_{PCE}/V_{poly} (g/100 mL)*	*D_{abs} (cm^2 s^{-1})*
Aerogels	δ form sPS	0.1	270	12.2	1.2	$D_{\delta sPS}$
	α form PPO	0.1	521	9.1	0.91	$D_{\delta sPS}\times 11$
	β form PPO	0.1	630	9.7	0.97	$D_{\delta sPS}\times 27$
Films	δ form sPS	1.01	< 4	0.5	0.5	1.2×10^{-12}
	Tenax amorphous	1.09	< 4	1.2	1.2	1.4×10^{-11}
	α form PPO, $c_{//}$	0.99	< 4	4.8	4.8	1.4×10^{-11}
	α form PPO, $c_{\perp}$	0.98	< 4	9.6	9.5	5.6×10^{-10}

2.1.2 Diffusivity in NC films

WAXD patterns, taken by a powder diffractometer, of PPO and sPS films with thickness in the range 40–60 μm, being used for sorption measurements, are shown in Figure 2.3. In particular, a WAXD pattern of a fully amorphous PPO film, as obtained by casting from a 1.5 wt% chloroform ($CHCl_3$) solution at T = 60 °C, is shown in Figure 2.3a while WAXD patterns of NC PPO films, as obtained by casting from a 1 wt% CCl_4 solution and by immersion of an amorphous PPO film in carvone, are shown in Figure 2.3b and c, respectively.

Both PPO films exhibit the NC α-form and the large differences observed in the diffraction patterns are only due to different orientations of crystalline phases with respect to the film plane. In particular, the diffraction patterns of Figure 2.3b,c are typical of α crystalline phases with an orientation of their chain axes being preferentially perpendicular and parallel to the film plane ($c_{\perp}$ and $c_{//}$ orientations),[27] respectively.

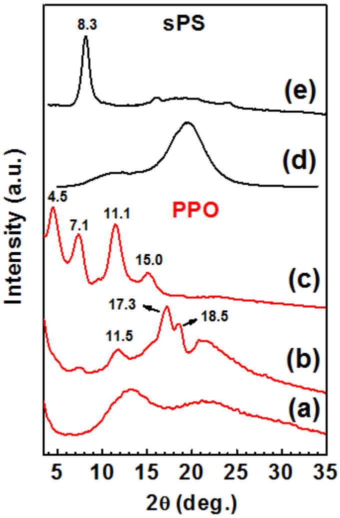

Figure 2.3 WAXD patterns of films with thickness in the range 40–60 µm: a) amorphous PPO, b) α-form PPO obtained by immersion of amorphous PPO film in carvone ($c_{\perp}$ orientation); c) α-form PPO obtained by casting from a 1 wt% CCl_4 solution ($c_{//}$ orientation); d) amorphous sPS; e) δ-form sPS obtained by casting form a 1 wt% $CHCl_3$ solution ($a_{//}c_{//}$ orientation).

The degree of $c_{//}$ and $c_{\perp}$ orientations of the PPO films, as evaluated by the intensity of azimuthal distribution of 001 reflection,[27] is +0.4 and –0.23, respectively.

The degree of crystallinity of the two NC PPO films with $c_{\perp}$ and $c_{//}$ orientations, as evaluated by the DSC method, are 56% and 47%, respectively.

The WAXD pattern of a NC δ-form sPS film, as obtained by casting from 1 wt% chloroform solution at room temperature, is shown in Figure 2.3e.

Differently from the diffraction pattern of the δ-form sPS aerogel (curve c of Figure 2.1), the δ-form sPS film (curve e of Figure 2.3) presents a prevalence of the (010) diffraction peak at $2\theta_{CuK\alpha} = \sim 8.3°$. This diffraction pattern is typical of δ-form films exhibiting the so-called $a_{//}c_{//}$ orientation, i.e., with *ac* layers of alternated enantiomorphous helices being preferentially parallel to the film plane.[28] A WAXD pattern of a fully amorphous melt-extruded sPS film is shown, for comparison, in Figure 2.3d.

For all films of Figure 2.3, gravimetric uptakes of PCE after 12h at T = 35 °C and for p/p_0 in the range 0.01–0.04, are compared in Figure 2.4a. For the same films, PCE sorption kinetics at T = 35 °C and $p/p_0 = 0.01$ are shown in Figure 2.4b. It is well apparent a high guest diffusivity of NC PPO films with $c_{\perp}$ orientation respect to the film showing parallel orientation as well as to PPO amorphous film and sPS samples.

Surprisingly, by considering the guest mass uptake per mass of polymer (Figure 2.5a), NC PPO films with $c_{\perp}$ orientation exhibit a sorption kinetic similar to that one of NC PPO powders and only slightly slower than for NC PPO aerogels. Completely different is the behavior of NC sPS samples (black curves in Figure 2.5a), with sorption kinetics being very fast for aerogels, slow for powders and very slow for films. Experiments were performed also considering the benchmark adsorbent poly(2,6-diphenyl-1,4-phenylene)oxide (Tenax) samples, whose guest uptake (blue curves in Figure 2.5a) is much smaller than for all PPO samples (red curves in Figure 2.5a).

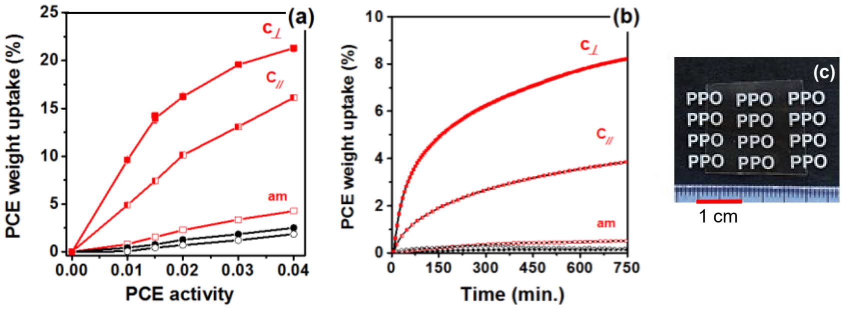

Figure 2.4 Gravimetric sorption measurements of PCE at 35 °C and for $0.04 \geq p/p_0 \geq 0.01$ in films with thickness in the range 40–60 μm: (■, NC α-form PPO, with $c_{\perp}$ orientation); (◧, NC α-form PPO, with $c_{//}$ orientation); (□, amorphous PPO); (●, NC δ-form sPS); (○, amorphous sPS). (a) PCE uptake after 12h; (b) Sorption kinetics for $p/p_0 = 0.01$, reported as PCE wt% uptake vs time; (c) photograph of a transparent PPO film exhibiting $c_{\perp}$ orientation, with a density $\rho = 0.986$ g/cm^3.

By considering the guest mass uptake per volume of polymer (Figure 2.5b), which is generally the quantity more relevant for industrial applications, the sorption behavior of NC PPO films, mainly of those with $c_{\perp}$ orientation, becomes even more impressive. For instance, at $p/p_0 = 0.01$ after 12h, the PCE uptake in the NC $c_{\perp}$ PPO film (9.5 g/100 mL) is nearly 3.7 and 10 times higher than for NC PPO powder and aerogel, respectively, as well as nearly 26 times higher than for the benchmark Tenax powder.[29–31]

To determine diffusivities of PCE in the films, Fick's plots have been prepared, by assuming that the equilibrium PCE uptake ($M_{PCE}(\infty)$) does not depend on the orientation of the crystalline phase ($M_{PCE}(\infty,c//) = M_{PCE}(\infty,c\perp)$).

As for sPS and Tenax films, because the guest uptake is extremely slow, it can be assumed that $M_{PCE}(\infty)$ is equal to the equilibrium sorption of the corresponding powder samples.

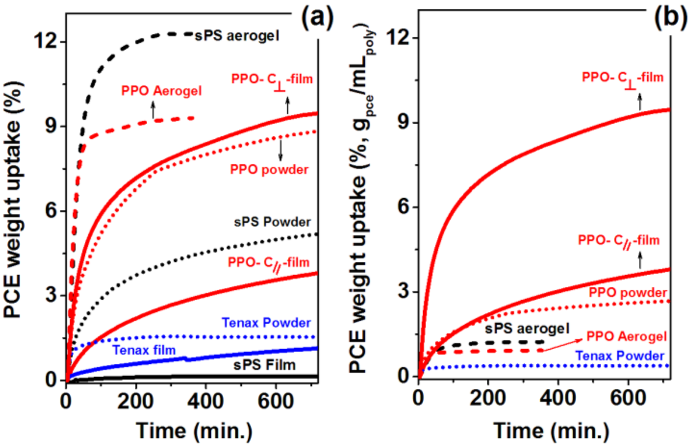

Figure 2.5 PCE sorption kinetics for $p/p_0 = 0.01$ at 35 °C, as measured for δ-form NC sPS (black symbols), α-form NC PPO (red symbols) and Tenax (blue symbols) samples. The PCE uptake is expressed as: (a) mass of guest per mass of polymer; (b) mass of guest per volume of polymer.

Diffusivities of PCE at $p/p_0 = 0.01$, as obtained by fitting by means of Fick's model, are listed in the last column of Table 2.1. For the δ-form sPS film, the diffusivity (1.2×10^{-12} $cm^2\ s^{-1}$) is of the same order of magnitude of those measured for the transport of $CHCl_3$ at low vapor pressure (at T = 56 °C, P = 5 Torr, and $D_{abs} = 0.86 \times 10^{-12}$ $cm^2\ s^{-1}$)[32] and for DCE from 50 ppm aqueous solution ($D_{abs} = 0.68 \times 10^{-12}$ $cm^2\ s^{-1}$ for a δ-form film with $a_{//}c_{//}$ orientation).[28]

Diffusivities as evaluated for PPO films are much higher than for the NC sPS film and strongly dependent on the orientation of chain axes of the NC phases. In particular, the PCE diffusivity at $p/p_0 = 0.01$ in the PPO film with $c_{\perp}$ orientation (Figure 2.5, red symbols) is nearly 40 times higher than for the film with $c_{//}$ orientation as well as for a film prepared from the benchmark adsorbent Tenax (Figure 2.5, blue symbols) and nearly five hundred times higher than for the NC sPS film (Figure 2.5, black symbols).

In this respect, it is worth noting that variations of guest diffusivity with the orientation of NC phases were already observed for sPS films, but with smaller differences. In fact, for sPS, the ratio between maximum and minimum diffusivity corresponding to different planar orientations is only in the range 5–8 for sorption of DCE,[28,33] ethylene[34] and carbon dioxide.[35]

As for NC PPO films, this ratio between maximum and minimum diffusivity depending on different planar orientations is even higher (nearly 40 times).

The particularly high guest diffusivity of NC PPO films with $c_\perp$ orientation clearly suggest that the empty space of the NC α-form of PPO is organized as channels being parallel to the crystalline chain axes. This hypothesis was already suggested by infrared linear dichroism studies on benzene guest orientation in axially oriented NC PPO films.[36,37]

2.2 Perchloroethylene sorption in NC PPO films from water

The study in the previous section (2.1) has shown that PCE uptake from vapor phase for NC PPO films is generally much higher than for NC sPS films,[38] due to the higher permeability of its high free volume amorphous phase.[17,39,40] The same study has shown that the control of planar orientation[27,41–43] is extremely relevant for kinetics of guest uptake for NC PPO films. In particular, NC PPO films exhibiting an orientation of the crystalline chain axes[27] preferentially perpendicular to the film surface show diffusivities much higher than for films with orientation of the crystalline chain axes preferentially parallel to the film surface (at vapour activity $p/p_0 = 0.01$, $D_{c\perp}/D_{c//} \approx 40$).[38]

In this section, uptakes of the same pollutant (PCE) from diluted aqueous solutions, i.e., in relevant conditions for groundwater decontamination, for NC PPO films have been investigated. Aim of the present analysis is to establish if the PCE uptake from water can be maximized by controlling the planar orientation of the crystalline phase, confirming the data obtained for sorption from air (i.e., vapour phase).

2.2.1 Influence of crystalline phase orientations

WAXD EDGE patterns of two NC PPO films, as crystallized by room temperature immersion of an amorphous PPO in liquid *p*-xylene and benzyl ether (followed by guest removal by ACN) are shown in Figure 2.6A and B, respectively. Corresponding diffraction profiles along equatorial and meridional directions of the 2D patterns are shown on the right part of Figure 2.6. For both films, the presence of diffraction peaks at $2\theta_{CuK\alpha} \approx 4.5°$, 7.1°, 11.3° and 15.0° indicate the presence of the NC α-form.[24] WAXD patterns of Figure 2.6A,B show *hk0* diffraction arcs centered along the equator and the meridian and indicate the occurrence of $c_{//}$ and $c_\perp$ orientation, respectively.[27]

The degree of orientation, as evaluated by the EDGE patterns of Figure 2.6, by considering azimuthal profiles of the 001 diffraction arc, is close to +0.20 and –0.25, for NC PPO α-form films with $c_{//}$ and $c_\perp$ orientations, respectively (f_{001} in the first column of Table 2.2). If the guest removal procedure is conducted by $scCO_2$ extraction rather than by ACN sorption/desorption at room temperature, the WAXD patterns are similar to those of Figure 2.6, with nearly unaltered degrees of planar orientation.

The degree of crystallinity of the considered NC films, as evaluated by DSC, is indicated in 4th column of Table 2.2 and is rather similar for the considered semicrystalline films. The degree of crystallinity is also poorly dependent on the film extraction procedure ($scCO_2$ or ACN). Also informative are the film density values, as obtained by the floatation method (5th column of Table 2.2), which for NC films are definitely lower than for the amorphous PPO films. These differences are again essentially independent of the two considered extraction methods ($scCO_2$ or ACN).

PCE uptake experiments were conducted considering a 50 ppm aqueous solution (aqueous solubility of 150 mg/L), this concentration could be considered a real case of groundwater pollution.[10]

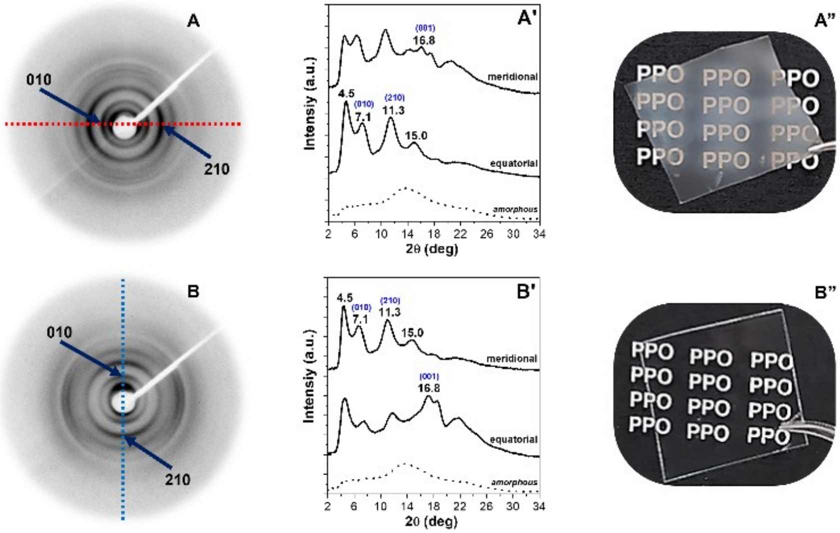

Figure 2.6 WAXD patterns of NC PPO α-form films with different orientations of their crystalline phases, as induced by sorption/desorption of different guest molecules in an amorphous film: (A, A′) $c_{//}$ orientation, crystallization induced by *p*-xylene; (B, B′) $c_{\perp}$ orientation, crystallization induced by BE; (A, B) WAXD patterns as collected by sending the X-ray beam parallel to the film plane (EDGE patterns). (A′, B′) Diffraction profiles as collected along equator and meridian of the EDGE patterns. Black dotted curves show the WAXD pattern of the starting unoriented amorphous PPO film. Red and blue dotted lines show equator and meridian in the WAXD patterns, respectively. (A″, B″) Photographs of the NC PPO α-form films with different orientations (and opacity).

For the NC and amorphous PPO films of Table 2.2, PCE uptake from dilute aqueous solutions was studied by evaluating the absorbance of FTIR guest peaks. FTIR spectra in the range 820–720 cm^{-1} after three different times of immersion in a 50 ppm aqueous

PCE solution, for the NC films with $c_{//}$ and $c_{\perp}$ orientations and for the starting amorphous film are shown in Figure 2.7A,B and C, respectively. It is well evident the presence of the FTIR peaks at 800 and 777 cm^{-1} related to the pollutant PCE.[44]

PCE sorption kinetics, as derived by FTIR spectra like those of Figure 2.7, by using the 800 cm^{-1} guest peak, are shown in Figure 2.8. In particular, Figure 2.8A mainly compares PCE uptake from the starting amorphous film (curve a) and for two NC films having a similar thickness (≈60 μm) but opposite kind of crystalline phase orientation ($c_{//}$ for curve b and $c_{\perp}$ for curve c). As already shown in the previous section (2.1), it is well evident that the PCE uptake from dilute aqueous solutions is much higher for the NC films than for the amorphous film, confirming data obtained for sorption from vapour phase.

Additionally, pollutant uptake is particularly fast for NC PPO films with $c_{\perp}$ orientations. For instance, after 24h of film immersion in water, PCE uptake is close to 2.5 wt% for the amorphous film (black squares) while it is much higher for the NC films: 6 wt% and 14 wt% for films with $c_{//}$ (blue circles) and $c_{\perp}$ orientations (red triangles), respectively.

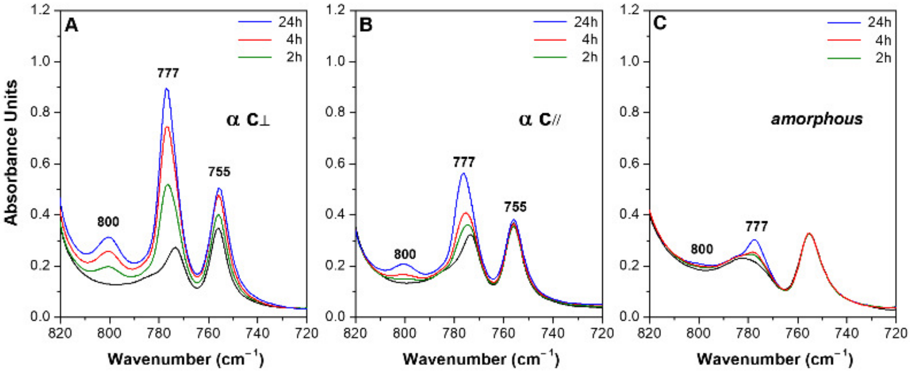

Figure 2.7 FTIR spectra in the range 820–720 cm^{-1} of PPO films after different times of immersion in 50 ppm PCE aqueous solution: (A) NC PPO α-form film with $c_{\perp}$ orientation; (B) NC PPO α-form film with $c_{//}$ orientation; (C) PPO amorphous film. FTIR spectra are collected after 2 h (green lines), 4 h (red lines) and 24 h (blue lines) of sorption. FTIR spectra of the starting films are also reported (black lines). FTIR peaks at 800 and 777 cm^{-1} are due to the PCE guest.

PCE sorption kinetics, as measured for three α-form NC PPO films of largely different thickness, all exhibiting a similar degree of $c_{\perp}$ orientation ($f_c \approx -0.3$), are shown in Figure 2.8B. These films were obtained by crystallization of amorphous films by immersion in a 50/50 wt/wt limonene/carvone solution at room temperature for 24h. Of course, kinetics of guest sorption are faster for thinner films. Corresponding guest diffusivities are evaluated by the Fick's model, considering equilibrium PCE uptake after long-term sorption, as described in the following section (and reported in Table 2.2).

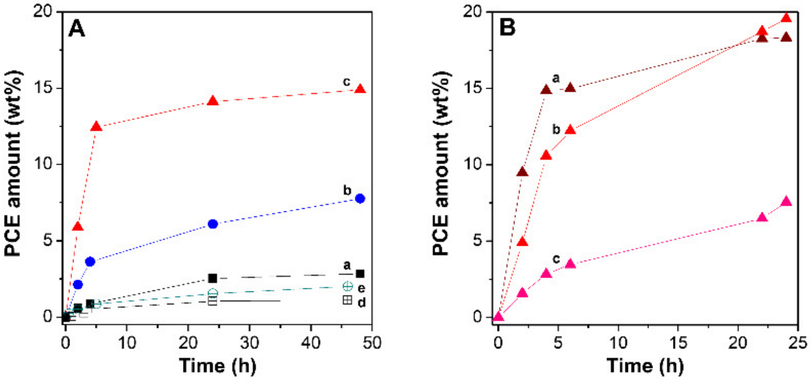

Figure 2.8 PCE sorption kinetics at room temperature from 50 ppm aqueous solutions, for polymer films: A) amorphous PPO (a); NC PPO α-form with $c_{//}$ orientation (b); NC PPO α-form with $c_{\perp}$ orientation (c); amorphous sPS, with thickness of 40 µm (d); NC sPS δ-form, with thickness of 40 µm (e). B) NC PPO α-form films with $c_{\perp}$ orientation, all prepared by a same procedure (immersion of an amorphous film in limonene/carvone 50/50 wt% solution) and with largely different thickness: 30 µm (a); 60 µm (b); 150 µm (c).

2.2.2 Long-term sorption experiments

To better discriminate between kinetic and thermodynamic features of the observed phenomena, long term sorption experiments (up to 500h) were also conducted. Figure 2.9 shows that, for the fully amorphous film, the PCE uptake is lower than 3 wt% after 24h but gradually increases up to nearly 11 wt% after 500h of sorption. As for the considered NC films, although kinetics are largely different depending on crystalline phase orientation, after 500h the guest uptake is in the narrow range 14–15 wt%, thus showing a nearly equal equilibrium guest uptake. This poor dependence of the equilibrium guest uptake on the crystalline phase orientation well agrees with the similar content of NC α phase (degree of crystallinity reported in the 4th column of Table 2.2). Sorption kinetics of Figure 2.8A and B, by using as equilibrium uptake the maximum values taken from Figure 2.9, are shown as Fick's plots in Figure 2.10A and B, respectively. Fick's plots allow determining diffusivity values of PCE from 50 ppm aqueous solutions, which are indicated close to the interpolation lines and collected in the last column of Table 2.2.

It is immediately apparent the much higher diffusivity of the NC films with $c_{\perp}$ orientation, with respect to NC films with $c_{//}$ orientation and of amorphous films, being reduced of nearly 14 and 88 times, respectively (Figure 2.10A).

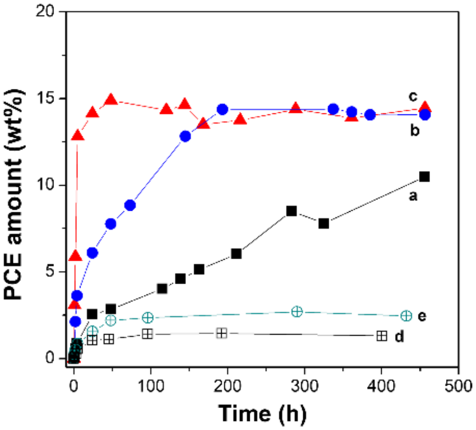

Figure 2.9 Long term PCE uptake at room temperature from 50 ppm aqueous solutions, for different polymer films: a) amorphous PPO (black squares); (b,c) NC PPO α-form film with $c_{//}$ orientation (b, blue circles) or with $c_{\perp}$ orientation (c, red triangles); d) amorphous sPS (crossed squares); e) NC δ-form sPS film (crossed circles).

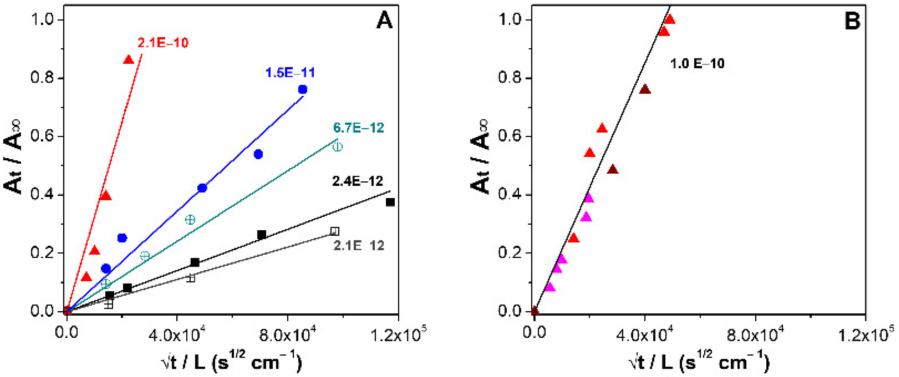

Figure 2.10 Fick's plot for kinetics of sorption of PCE from 50 ppm aqueous solutions at room temperature. A_∞ and A_t are the absorbance of the FTIR peak of PCE at 800 cm^{-1}, maximum value and at a given immersion time (t), respectively. L is the film thickness. Diffusivity values, calculated on the basis of the slopes of the linear interpolations and expressed as cm^2/s, are indicated close to the lines. A) for different polymer films: (black squares) amorphous PPO; (blue circles) NC PPO α-form with $c_{//}$ orientation; (red triangles) NC PPO α-form with $c_{\perp}$ orientation; (crossed squares) amorphous sPS; (crossed circles) NC δ-form sPS. B) NC PPO α-form films with $c_{\perp}$ orientation, all prepared by a same procedure (immersion of an amorphous film in liquid limonene/carvone 50/50 wt% solution) and with different thickness: (brown triangles) 30 µm; (red triangles) 60 µm; (magenta triangles) 150 µm.

This strong dependence of sorption kinetics on the crystalline phase orientation, already observed for PCE sorption from vapor phase,[38] indicates the presence of anisotropic guest diffusion pathways[45] with higher diffusivity in the direction parallel to the polymer host chain axes. This can suggest the presence for the α PPO phase of crystalline channels being parallel to the polymer chain axes, as observed for the crystalline structure of the ε-form of sPS.[46] The possible occurrence of crystalline channels parallel to the polymer chain axes was already suggested on the basis of *n*-decane sorption data in NC PPO aerogels[15] as well as based on the parallelism of guest phenyl rings with respect to the polymer host chain axes, as proved by linear dichroism measurements on infrared guest (benzene and toluene) peaks, for axially oriented PPO α phases.[37,47]

Table 2.2 Kind and degree of orientation, preparation method, thickness, degree of crystallinity ($X_{c,DSC}$) and density of the main PPO films used in the present study. The last column reports diffusivity values as obtained by Fick's plots based on absorption of PCE from 50 ppm aqueous solutions (Figure 2.10).

Planar orientation, Degree of orientation, Crystalline form	*Guest inducing crystallization*	*Thickness (μm)*	$X_{c,DSC}$ *(%)*	*Density (g cm^{-3})*	*Diffusivity (cm^2 s^{-1})*
$c_{//}$, f_{001}= +0.2$_0$ α-form	*p*-Xylene	60	45	0.996	1.5 × 10^{-11}
$c_{\perp}$, f_{001}= −0.2$_5$ α-form	Benzyl ether	60	43	0.992	2.1 × 10^{-10}
$c_{\perp}$, f_{001}= −0.3$_0$ α-form	Limonene/carvone 50/50 by wt	30	43	0.987	
$c_{\perp}$, f_{001}= −0.3$_0$ α-form	Limonene/carvone 50/50 by wt	60	43	0.987	1.0 × 10^{-10}
$c_{\perp}$, f_{001}= −0.3$_0$ α-form	Limonene/carvone 50/50 by wt	150	43	0.987	
Amorphous	Cast at 60 °C from $CHCl_3$ solution	60	--	1.04	2.4 × 10^{-12}

2.2.3 Comparison with sorption by NC sPS films

Sorption kinetics of PCE from 50 ppm aqueous solutions, relative to amorphous (crossed squares) and NC δ-form (crossed circles) sPS films, are also shown in Figures 2.8A and 2.9. Equilibrium PCE uptake is nearly 1.3 and 2.4 wt% from amorphous and NC sPS films, respectively. This confirms that guest sorption ability of NC PPO films is much higher than for NC sPS films.[38]

Fick's plots for sorption kinetics for amorphous and NC δ-form sPS films are shown in Figure 2.10A and allow calculating diffusivity values of 2.1×10^{-12} and 6.7×10^{-12} cm^2/s, respectively, very similar to those observed for sorption study from DCE 50 ppm aqueous solution ($D_{abs} = 0.68 \times 10^{-12}$ cm^2 s^{-1}). These values are nearly 100 and 30 times smaller than for the NC PPO α-form film with $c_{\perp}$ orientation.

It is worth adding that, although enormous guest sorption differences occur for films, NC PPO and NC sPS aerogels exhibit similar guest sorption behavior.[38] This is probably due to the low and high free-volume of the amorphous phases of sPS and PPO films,[17,39,40] respectively.

2.3 Perchloroethylene (PCE) sorption in high surface area PPO films

As shown previously (section 2.1), PCE uptakes are particularly fast for sPS and PPO NC aerogels and for PPO NC powders because of their high surface area (in the ranges 200−350 and 500−750 $m^2\ g^{-1}$ for sPS and PPO, respectively). However, because of their low density (typically in the range 0.01−0.2 $g\ cm^{-3}$), aerogels show high values of pollutant uptake per unit mass but much poorer pollutant uptake per unit volume. Moreover, PPO powders, which generally can be packed in absorption systems only up to an apparent density of 0.3 $g\ cm^{-3}$, also present the disadvantage of difficult handling, as always occurs for fine particles. Much more handleable are of course self-supporting polymer films, which exhibit negligible surface area (<4 $m^2\ g^{-1}$), as generally occurs for polymer films and even for NC polymers. Additionally, irrespective of their negligible surface area, NC PPO films can reach very fast guest uptakes by using crystallization procedures leading to orientation of the chain axes of the NC phases being preferentially perpendicular to the film plane ($c_{\perp}$ orientation),[27] as shown also in section 2.2.

In this section, NC PPO films with surface area even higher than 600 $m^2\ g^{-1}$ are presented and their pollutant uptakes from air as well as from water are described.

2.3.1 Procedures leading to high surface area NC PPO films

Preparation methods of NC PPO films, whose surface area is high and unexpectedly comparable to those of NC PPO aerogels, is described below. These methods require fast guest uptakes up to their limit value and fast guest-induced crystallization (GIC) in amorphous films, followed by guest extraction by exchange with a more volatile guest.

The kinetics of sorption at 30 °C of carvone from an amorphous PPO film, having a thickness of nearly 20 μm, is shown by filled circles in Figure 2.11a. It is apparent that in less than 10 min a limit uptake value of nearly 85 wt% is reached.

The degree of crystallinity and SA_{BET} of the NC PPO films as obtained by rapid guest removal from the films (by ACN sorption/desorption), after different sorption times, are shown in Figure 2.11b and c, respectively. It is apparent that both high degrees of crystallinity (higher than 40%) and high SA_{BET} (close to 500 $m^2\ g^{-1}$) are reached only by guest extraction from films with very high guest content (≈85 wt%). This preparation procedure for high-SA NC films leads to an increase of film thickness of nearly 3 times with a complete loss of film transmittance.

The slower kinetics of sorption of carvone at a lower temperature (~4 °C), in a PPO amorphous film of the same thickness, is shown as red squares in Figure 2.11a. The limit carvone uptake value is nearly 80 wt%, i.e., not far from the value reached by sorption at 30 °C, but the sorption time needed to reach this limit value is much longer (close to 1000 min). The degree of crystallinity and SA_{BET} of the NC PPO films as obtained by rapid guest removal from the films (by ACN sorption/desorption), after different sorption times at ~4 °C, are shown as red symbols in Figure 2.11b and c, respectively.

It is apparent that while degrees of crystallinity can be high (up to nearly 40%), the SA_{BET} of the obtained NC films is always negligible. This preparation procedure of NC films with negligible SA_{BET} leads to an increase of film thickness of 2.0–2.2 times with substantial maintenance of film transmittance. Figure 2.11a and c clearly show that to obtain high-SA films, besides large guest uptakes from amorphous PPO films also fast kinetics of guest sorption and of GIC are needed.

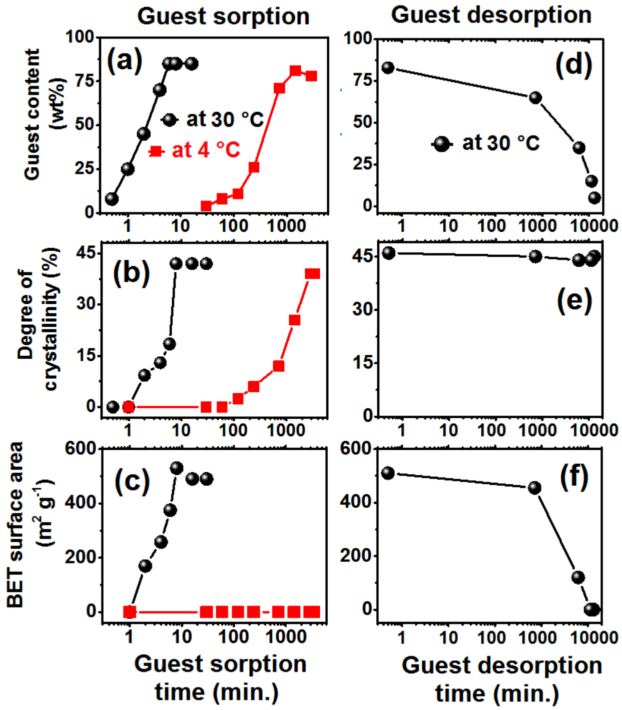

Figure 2.11 (a–c) Carvone uptake from 20 μm amorphous PPO films: at 30 °C (black circles) and at 4 °C (red squares): (a) kinetics of sorption, (b) degree of crystallinity, and (c) SA_{BET} of the NC PPO films as obtained by rapid carvone removal from the films, after different sorption times. (d–f) Carvone desorption from a 20 μm amorphous PPO films after carvone uptake close to the limit value (85 wt%): (d) kinetics of desorption at 30 °C in air, (e) degree of crystallinity, and (f) SA_{BET} of the NC PPO films as obtained by rapid carvone removal from the films, after different desorption times.

The kinetics of desorption (at 30 °C) of carvone from the PPO film, which has reached the limit carvone uptake value (85 wt%), is shown in Figure 2.11d.

The degrees of crystallinity and SA_{BET} of the NC PPO films as obtained by rapid guest removal from the films (by sorption/desorption of ACN), after different desorption times, are shown in Figure 2.11e and f, respectively. It is apparent that while degrees of crystallinity are high (close to 45%), independent of desorption time, the SA_{BET} of the obtained NC films markedly decreases with desorption.

For instance, if the guest extraction procedure is conducted on films whose residual guest content is decreased from 85 wt% to 35 wt%, the SA_{BET} correspondingly decreases from nearly 510 m^2 g^{-1} down to nearly 100 m^2 g^{-1}.

Analogous studies of crystallization of thicker amorphous PPO films (of nearly 100 μm) as induced by sorption of carvone are also highly informative. For these thick films, GIC at 30 °C leads to high crystallinity but to negligible surface area. To obtain high-SA films from 100 μm thick amorphous films, higher temperatures of guest sorption are needed. For instance, at T_{GIC} = 80 °C, films with surface area close to 500 m^2 g^{-1} are obtained.

In summary, preparation procedures leading to high-SA PPO films require a guest sorption step in amorphous films leading to fast co-crystallization, followed by a guest desorption step leading to NC phases. The guest sorption step requires a high guest content, both in the crystalline and in the amorphous phase (the overall content generally being in the range 70−90 wt%) as well as a fast co-crystallization with the polymer, leading to high degree of crystallinity. The following guest desorption step requires exchange procedures with a temporary guest (e.g., ACN or carbon dioxide) for CC films with high guest content and high degree of crystallinity.

The NC PPO film as obtained by the carvone sorption procedure at ∼4 °C (shown as red squares in Figure 2.11a), exhibits a $c_{\perp}$ oriented NC α-form with a degree of orientation f_c ≈ −0.3 and a degree of crystallinity of nearly 40%. This film is highly transparent, as generally found for PPO films exhibiting $c_{\perp}$ planar orientation of the crystalline chain axis,[48] as shown by the photo of Figure 2.12A. The NC PPO film as obtained by carvone sorption procedure at 30 °C (shown as black circles in Figure 2.11a), exhibits the presence of fully unoriented NC α-form with a similar degree of crystallinity (≈44%). Additionally, its density (0.84 g cm^{-3}) is lower than the $c_{\perp}$ oriented NC α film (0.99 g cm^{-3}) but even lower than for the pure α-form (0.93 g cm^{-3}). This indicates the presence in these films of voids in an amount close to 14 vol%. Correspondingly, as shown by the photo of Figure 2.12B, these films are opaque.

For comparison, a photo of a cylindrical aerogel (Figure 2.12C), with a density of 0.12 g cm^{-3}, exhibiting the NC α-form, with degree of crystallinity close to 55% (as evaluated by DSC) is also shown. SEM images of the three NC α-form samples ($c_\perp$ oriented film, high-SA film, and aerogel) are also shown in Figure 2.12. A fibrillar morphology for both the high SA film and for the aerogel is clearly apparent.

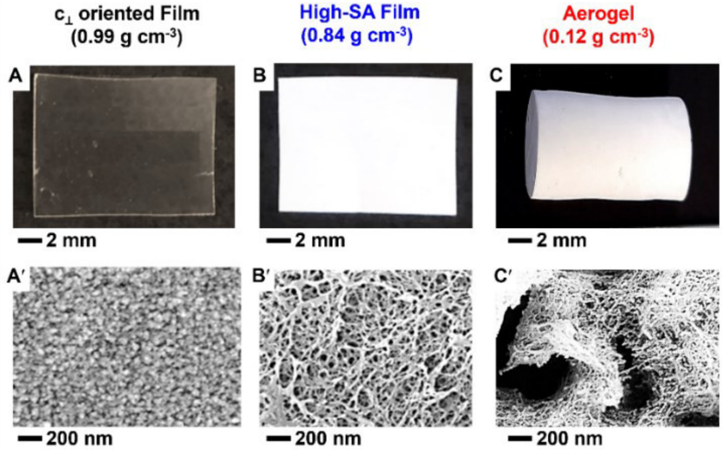

Figure 2.12 Photographs and SEM images for NC α-form PPO samples: (A−A′), $c_\perp$ oriented film; (B−B′) high-SA film; (C−C′) aerogel with porosity P ≈ 90%.

2.3.2 PCE uptake from vapor phase

Sorption kinetics of PCE from vapor phase, at 35 °C and $p/p_0 = 0.01$, are compared in Figure 2.13a-c for different PPO samples. Particularly impressive is the much faster kinetics observed for the high-SA NC film (blue pentagons) with respect to the high diffusivity $c_\perp$ oriented NC film (black circles) and amorphous PPO films (orange stars). For instance, after 25 min of sorption, the guest uptake is negligible for the amorphous PPO film while is close to 3 and 10 wt% for the $c_\perp$ and high-SA NC films, respectively (Figure 2.13b). The large differences between sorption kinetics of the three PPO films is also clearly pointed out by the Fick’s plot in Figure 2.13c, with calculated diffusivities (at 35 °C and $p/p_0 = 0.01$) increasing from 8.2×10^{-12}, 6.7×10^{-10}, and 3.3×10^{-9} cm^2 s^{-1} for amorphous, $c_\perp$ NC, and high-SA NC films, respectively.

Figure 2.13a,b also show that kinetics of PCE sorption from the high-SA film are even faster than for NC powders (green squares) as well as for the NC aerogel (red hexagons).

For instance, after 10 min of vapor sorption, the PCE uptake is nearly 8 wt% while it is only close to 4 wt% for the powder and the aerogel (Figure 2.13b).

Equilibrium uptakes of PCE at 35 °C and for $0.05 \geq p/p_0 \geq 0.01$ are shown in Figure 2.13d. It is clearly apparent that all the NC PPO samples, independently of their morphology, exhibit equilibrium uptakes much higher with respect to the amorphous film. In particular, $c_\perp$ and high-SA NC films present similar equilibrium uptakes for the whole considered activity range. Hence, the high-SA is extremely relevant for sorption kinetics (Figure 2.13a-c) but not relevant for guest equilibrium uptakes (Figure 2.13d).

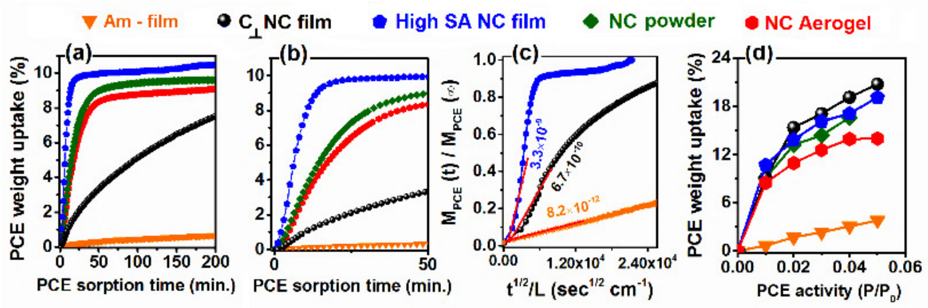

Figure 2.13 PCE sorption tests at 35 °C for different PPO samples: (blue pentagons) high-SA NC film; (green squares) NC powder; (red hexagons) NC aerogel; (black circles) $c_\perp$ NC film; (orange triangles) amorphous film. The considered films have thickness in the range 40−60 μm. (a−c) Sorption kinetics at $p/p_0 = 0.01$: (a) up to 200 min; (b) up to 50 min; (c) Fick's plot for the three PPO films; curves are reported in the normalized form, as $M_{PCE(t)}/M_{PCE(\infty)}$ vs $t^{1/2}/L$. (d) Equilibrium gravimetric PCE uptake for $0.05 \geq p/p_0 \geq 0.01$ for the five PPO samples.

2.3.3 PCE uptake from dilute aqueous solutions

Sorption kinetics of PCE from 50 ppm aqueous solutions, at room temperature (20 °C), are compared in Figure 2.14a-c, for the above-described PPO films. As already observed for sorption from the vapor phase, kinetics of sorption from the high-SA NC film are faster than for the $c_\perp$ film and much faster than for the amorphous film. For instance, after 30 min of sorption, the PCE uptake is nearly 0.3, 1.8, and 5 wt% for films being amorphous, $c_\perp$ NC, and high-SA NC, respectively (Figure 2.14b).

The large differences between sorption kinetics of the three PPO films is also pointed out by Fick's plot of Figure 2.14c, with calculated diffusivities (from 50 ppm aqueous solutions) increasing from 4.2×10^{-12}, 1.3×10^{-10}, and 3.8×10^{-10} cm^2 s^{-1} for amorphous, $c_\perp$ NC, and high-SA NC films, respectively. Hence, the high surface area is relevant for sorption kinetics mainly for short sorption times (Figure 2.14b) although it is not relevant for long-term guest equilibrium uptakes (Figure 2.14a).

It is worth adding that the guest sorption data of Figures 2.13 and 2.14 are expressed as mass of pollutant per mass of the polymer. The faster kinetics observed for high-SA films are also more clearly apparent if the guest uptake is expressed as mass uptake per volume of the polymer, which is more relevant for most purification processes where the limiting factor is the volume of the absorbent material. In this respect, it is worth reminding that while high-SA NC films have a density higher than 0.8 g cm^{-3}, the density of packed NC PPO powder is generally lower than 0.3 g cm^{-3} while for the NC aerogels it is generally lower than 0.2 g cm^{-3}.

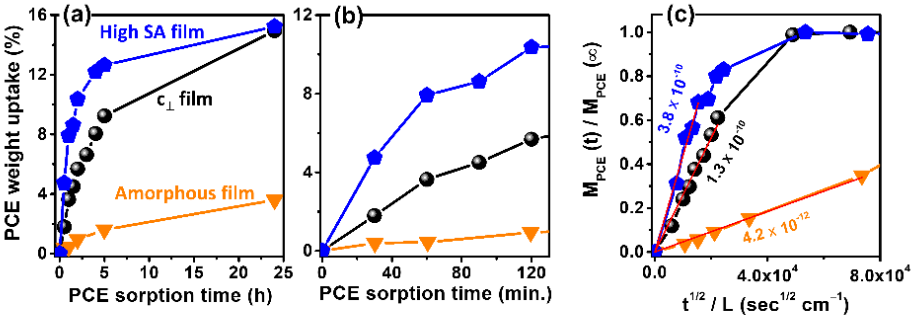

Figure 2.14 (a, b) PCE sorption kinetics from dilute aqueous solutions (50 ppm) at room temperature for different PPO films: (blue pentagons) NC high SA; (black circles) c$_\perp$ NC; (orange triangle) amorphous. PCE sorption kinetics (a) up to 25h and (b) up to 120 min and (c) Fick's plot.

Diffusivity values obtained for PCE sorption for the three different PPO films are collected in Table 2.3. In all cases, the diffusivity of the high-SA NC film is definitely higher than for the high free-volume amorphous film: of nearly 400 and 90 times for PCE sorption from vapor phase at p/p$_0$ = 0.01 at 35 °C and from 50 ppm aqueous solution, respectively.

Table 2.3 PCE Diffusivity as evaluated for sorption kinetics of the three different PPO films.

	PCE sorption			
PPO Films	*At 35 °C from vapor phase (p/p$_0$= 0.01)*		*At 20 °C from a 50 ppm aqueous solution*	
	Diffusivity (cm^2 s^{-1})	*Relative diffusivity*	*Diffusivity (cm^2 s^{-1})*	*Relative diffusivity*
Amorphous	8.2×10^{-12}	1	4.2×10^{-12}	1
c$_\perp$ α NC	6.7×10^{-10}	82	1.3×10^{-10}	31
High-SA α NC	3.3×10^{-9}	402	3.8×10^{-10}	90.5

2.4 Conclusions

In this chapter, kinetics for sorption of a relevant organic pollutant (perchloroethylene, PCE) from vapour phase at low activities ($0.01 \leq p/p_0 \leq 0.04$) as well as from a 50 ppm aqueous solution in different samples being amorphous or exhibiting NC phases are reported.

As concern PCE sorption from vapour phase, NC aerogels of sPS and PPO exhibit similar high guest solubility and fast sorption kinetics. Notwithstanding, guest sorption behavior of sPS and PPO films is instead extremely different. In fact, NC PPO films, mainly when orientation of their NC phases is preferentially perpendicular to the film plane ($c_\perp$ orientation), exhibit much higher guest uptakes with respect to NC sPS films (e.g., 20 times higher for PCE at $p/p_0 = 0.01$).

Guest uptakes for NC PPO films, when expressed as mass of guest per polymer volume, are also much higher than for NC PPO powders and aerogels. For instance, at $p/p_0 = 0.01$ after 12h, the PCE uptake in the NC $c_\perp$ PPO film (9.5 g/100 mL) is nearly 3.7 and 10 times higher than for NC PPO powder and aerogel, respectively.

Moreover, PPO films with $c_\perp$ orientation exhibit diffusivity of organic guest molecules higher (e.g., nearly 40 times, for PCE at $p/p_0 = 0.01$) than for films with orientation of the chain axes being preferentially parallel to the film plane ($c_{//}$ orientation) and much higher (nearly 500 times) than for films exhibiting the NC δ-form of sPS.

PCE sorption experiments were performed also from a 50 ppm aqueous solution in films exhibiting NC phases of both PPO and sPS. Also in this case, equilibrium PCE uptakes and sorption kinetics of the NC films are always higher and faster than for the corresponding amorphous films. Moreover, in agreement with results on sorption of the same pollutant from vapor phase at low activities, equilibrium uptakes are much higher (nearly 10 times, from 50 ppm aqueous solutions) for NC PPO than for NC sPS. The much faster diffusion kinetics of NC PPO films, with respect to NC sPS films, are due to the presence for PPO not only of a NC phase but also of a high free volume amorphous phase.

In the same way, comparing NC PPO films, particularly relevant is the presence of the planar orientation of the α phase. For instance, for PCE sorption from 50 ppm aqueous solutions, NC films with $c_\perp$ orientation exhibit a diffusivity nearly 14 times higher than for NC films with $c_{//}$ orientation and nearly 88 higher than for amorphous PPO films. This strong dependence of sorption kinetics on the crystalline phase planar orientation can be rationalized by anisotropic guest diffusion pathways with higher diffusivity in the direction parallel to the polymer host chain axes.

The much higher guest diffusivity for $c_{\perp}$ oriented NC PPO films, with respect to $c_{//}$ oriented NC PPO films, is in agreement with a recent hypothesis that the empty space of NC forms of PPO is organized as channels being parallel to the crystalline chain axes.

Furthermore, PCE sorption experiments both from vapour phase and aqueous solutions, were also performed considering NC PPO films with high surface area (up to 620 m^2 g^{-1}). The preparation procedure consists of two steps: (i) fast guest-induced co-crystallization of amorphous films, leading to CC films with high guest content, both in the crystalline and in the amorphous phase (70−90 wt%); (ii) guest extraction from these CC films, by exchange with a temporary guest (e.g., acetonitrile or preferably $scCO_2$), eventually leading to highly crystalline NC films, having a density higher than 0.8 g cm^{-3}.

It has been found that guest diffusivity values in the high-SA NC PPO films are much higher even than of the $c_{\perp}$ oriented NC PPO films, for sorption from both vapour phase and diluted aqueous solutions, due to a fibrillar morphology similar to aerogels.

These new films (especially with high-SA) based on a commercial high-performance polymer are expected to find application in PCE remediation as barrier, both from air and water, but these results could be considered general also for many other organic pollutants (e.g., aliphatic and aromatic hydrocarbons or other halogenated hydrocarbons).

REFERENCES

(1) Volpe, A.; Del Moro, G.; Rossetti, S.; Tandoi, V.; Lopez, A. Remediation of PCE-Contaminated Groundwater from an Industrial Site in Southern Italy: A Laboratory-Scale Study. *Process Biochem.* **2007**, *42* (11), 1498–1505. https://doi.org/10.1016/j.procbio.2007.07.017.

(2) Nardo, A. D.; Natale, M. D.; Erto, A.; Musmarra, D.; Bortonea, I. Permeable Reactive Barrier for Groundwater PCE Remediation: The Case Study of a Solid Waste Landfill Pollution. In *Computer Aided Chemical Engineering*; Elsevier, 2010; Vol. 28, pp 1015–1020. https://doi.org/10.1016/S1570-7946(10)28170-1.

(3) Erto, A.; Bortone, I.; Di Nardo, A.; Di Natale, M.; Musmarra, D. Permeable Adsorptive Barrier (PAB) for the Remediation of Groundwater Simultaneously Contaminated by Some Chlorinated Organic Compounds. *J. Environ. Manage.* **2014**, *140*, 111–119. https://doi.org/10.1016/j.jenvman.2014.03.012.

(4) Bortone, I.; Di Nardo, A.; Di Natale, M.; Erto, A.; Musmarra, D.; Santonastaso, G. F. Remediation of an Aquifer Polluted with Dissolved Tetrachloroethylene by an Array of Wells Filled with Activated Carbon. *J. Hazard. Mater.* **2013**, *260*, 914–920. https://doi.org/10.1016/j.jhazmat.2013.06.050.

(5) Chen, S.-S.; Huang, Y.-C.; Kuo, T.-Y. The Remediation of Perchloroethylene Contaminated Groundwater by Nanoscale Iron Reactive Barrier Integrated with Surfactant and Electrokinetics. *Ground Water Monit. Remediat.* **2010**, *30* (4), 90–98. https://doi.org/10.1111/j.1745-6592.2010.01311.x.

(6) Lee, M.; Kang, H.; Do, W. Application of Nonionic Surfactant-Enhanced in Situ Flushing to a Diesel Contaminated Site. *Water Res.* **2005**, *39* (1), 139–146. https://doi.org/10.1016/j.watres.2004.09.012.

(7) Qin, X. S.; Huang, G. H.; Chakma, A.; Chen, B.; Zeng, G. M. Simulation-Based Process Optimization for Surfactant-Enhanced Aquifer Remediation at Heterogeneous DNAPL-Contaminated Sites. *Sci. Total Environ.* **2007**, *381* (1–3), 17–37. https://doi.org/10.1016/j.scitotenv.2007.04.011.

(8) Hirvonen, A.; Tuhkanen, T.; Ettala, M.; Korhonen, S.; Kalliokoski, P. Evaluation of a Field-Scale UV/H2O2-Oxidation System for the Purification of Groundwater Contaminated with PCE. *Environ. Technol.* **1998**, *19* (8), 821–828. https://doi.org/10.1080/09593330.1998.9618696.

(9) Miao, Z.; Gu, X.; Lu, S.; Zang, X.; Wu, X.; Xu, M.; Ndong, L. B. B.; Qiu, Z.; Sui, Q.; Fu, G. Y. Perchloroethylene (PCE) Oxidation by Percarbonate in Fe2+-Catalyzed Aqueous Solution: PCE Performance and Its Removal Mechanism. *Chemosphere* **2015**, *119*, 1120–1125. https://doi.org/10.1016/j.chemosphere.2014.09.065.

(10) Tsai, T. T.; Kao, C. M.; Hong, A. Treatment of Tetrachloroethylene-Contaminated Groundwater by Surfactant-Enhanced Persulfate/BOF Slag Oxidation—A Laboratory Feasibility Study. *J. Hazard. Mater.* **2009**, *171* (1–3), 571–576. https://doi.org/10.1016/j.jhazmat.2009.06.036.

(11) Kao, C. M.; Chen, S. C.; Liu, J. K. Development of a Biobarrier for the Remediation of PCE-Contaminated Aquifer. *Chemosphere* **2001**, *43* (8), 1071–1078. https://doi.org/10.1016/S0045-6535(00)00190-9.

(12) Freedman, D. L.; Gossett, J. M. Biological Reductive Dechlorination of Tetrachloroethylene and Trichloroethylene to Ethylene under Methanogenic Conditions. *Appl. Environ. Microbiol.* **1989**, *55* (9), 2144–2151. https://doi.org/10.1128/aem.55.9.2144-2151.1989.

(13) Galizia, M.; Daniel, C.; Fasano, G.; Guerra, G.; Mensitieri, G. Gas Sorption and Diffusion in Amorphous and Semicrystalline Nanoporous Poly(2,6-Dimethyl-1,4-Phenylene)Oxide. *Macromolecules* **2012**, *45* (8), 3604–3615. https://doi.org/10.1021/ma3000626.

(14) Daniel, C.; Longo, S.; Fasano, G.; Vitillo, J. G.; Guerra, G. Nanoporous Crystalline Phases of Poly(2,6-Dimethyl-1,4-Phenylene)Oxide. *Chem. Mater.* **2011**, *23* (13), 3195–3200. https://doi.org/10.1021/cm200546r.

(15) Daniel, C.; Pellegrino, M.; Venditto, V.; Aurucci, S.; Guerra, G. Nanoporous-Crystalline Poly(2,6-Dimethyl-1,4-Phenylene)Oxide (PPO) Aerogels. *Polymer* **2016**, *105*, 96–103. https://doi.org/10.1016/j.polymer.2016.10.017.

(16) Guerra, G.; Daniel, C.; Rizzo, P.; Tarallo, O. Advanced Materials Based on Polymer Cocrystalline Forms. *J. Polym. Sci. Part B Polym. Phys.* **2012**, *50* (5), 305–322. https://doi.org/10.1002/polb.23035.

(17) Aguilar-Vega, M.; Paul, D. R. Gas Transport Properties of Polyphenylene Ethers. *J. Polym. Sci. Part B Polym. Phys.* **1993**, *31* (11), 1577–1589. https://doi.org/10.1002/polb.1993.090311114.

(18) Tsujita, Y. Gas Sorption and Permeation of Glassy Polymers with Microvoids. *Prog. Polym. Sci.* **2003**, *28* (9), 1377–1401. https://doi.org/10.1016/S0079-6700(03)00048-0.

(19) Minelli, M.; De Angelis, M. G.; Sarti, G. C. Predictive Calculations of Gas Solubility and Permeability in Glassy Polymeric Membranes: An Overview. *Front. Chem. Sci. Eng.* **2017**, *11* (3), 405–413. https://doi.org/10.1007/s11705-017-1615-5.

(20) Shaver, A.; Moon, J. D.; Savacool, D.; Zhang, W.; Narang, G.; Miller, G.; Vondrasek, B.; Lesko, J. J.; Freeman, B. D.; Riffle, J. S.; McGrath, J. E. Poly(2,6-Dimethyl-1,4-Phenylene Oxide) Blends with a Poly(Arylene Ether Ketone) for Gas Separation Membranes. *Polymer* **2017**, *114*, 135–143. https://doi.org/10.1016/j.polymer.2017.02.041.

(21) Daniel, C.; Alfano, D.; Venditto, V.; Cardea, S.; Reverchon, E.; Larobina, D.; Mensitieri, G.; Guerra, G. Aerogels with a Microporous Crystalline Host Phase. *Adv. Mater.* **2005**, *17* (12), 1515–1518. https://doi.org/10.1002/adma.200401762.

(22) Daniel, C.; Antico, P.; Guerra, G. Etched Fibers of Syndiotactic Polystyrene with Nanoporous-Crystalline Phases. *Macromolecules* **2018**, *51* (15), 6138–6148. https://doi.org/10.1021/acs.macromol.8b01044.

(23) Daniel, C.; Sannino, D.; Guerra, G. Syndiotactic Polystyrene Aerogels: Adsorption in Amorphous Pores and Absorption in Crystalline Nanocavities. *Chem. Mater.* **2008**, *20* (2), 577–582. https://doi.org/10.1021/cm702475a.

(24) Nagendra, B.; Cozzolino, A.; Daniel, C.; Rizzo, P.; Guerra, G.; Auriemma, F.; De Rosa, C.; D'Alterio, M. C.; Tarallo, O.; Nuzzo, A. Two Nanoporous Crystalline Forms of Poly(2,6-Dimethyl-1,4-Phenylene)Oxide and Related Co-Crystalline Forms. *Macromolecules* **2019**, *52* (24), 9646–9656. https://doi.org/10.1021/acs.macromol.9b01911.

(25) De Rosa, C.; Guerra, G.; Petraccone, V.; Pirozzi, B. Crystal Structure of the Emptied Clathrate Form (δ_eForm) of Syndiotactic Polystyrene. *Macromolecules* **1997**, *30* (14), 4147–4152. https://doi.org/10.1021/ma970061q.

(26) Daniel, C.; Giudice, S.; Guerra, G. Syndiotatic Polystyrene Aerogels with β, γ, and ε Crystalline Phases. *Chem. Mater.* **2009**, *21* (6), 1028–1034. https://doi.org/10.1021/cm802537g.

(27) Rizzo, P.; Gallo, C.; Vitale, V.; Tarallo, O.; Guerra, G. Nanoporous-Crystalline Films of PPO with Parallel and Perpendicular Polymer Chain Orientations. *Polymer* **2019**, *167*, 193–201. https://doi.org/10.1016/j.polymer.2019.01.073.

(28) Venditto, V.; De Girolamo Del Mauro, A.; Mensitieri, G.; Milano, G.; Musto, P.; Rizzo, P.; Guerra, G. Anisotropic Guest Diffusion in the δ Crystalline Host Phase of Syndiotactic Polystyrene: Transport Kinetics in Films with Three Different Uniplanar Orientations of the Host Phase. *Chem. Mater.* **2006**, *18* (9), 2205–2210. https://doi.org/10.1021/cm051657s.

(29) Helmig, Detlev.; Vierling, Lee. Water Adsorption Capacity of the Solid Adsorbents Tenax TA, Tenax GR, Carbotrap, Carbotrap C, Carbosieve SIII, and Carboxen 569 and Water Management Techniques for the Atmospheric Sampling of Volatile Organic Trace Gases. *Anal. Chem.* **1995**, *67* (23), 4380–4386. https://doi.org/10.1021/ac00119a029.

(30) Gallego, E.; Roca, F. J.; Perales, J. F.; Guardino, X. Comparative Study of the Adsorption Performance of an Active Multi-Sorbent Bed Tube (Carbotrap, Carbopack X, Carboxen 569) and a Radiello® Diffusive Sampler for the Analysis of VOCs. *Talanta* **2011**, *85* (1), 662–672. https://doi.org/10.1016/j.talanta.2011.04.043.

(31) Matsiko, J.; Li, H.; Wang, P.; Sun, H.; Zheng, S.; Wang, D.; Zhang, W.; Hao, Y.; Zuo, P.; Li, Y.; Zhang, Q.; Zhang, J.; Jiang, G. Multivariate Optimization of Tenax TA-Thermal Extraction for Determining Gaseous Phase Organophosphate Esters in Air Samples. *Sci. Rep.* **2019**, *9* (1), 3330. https://doi.org/10.1038/s41598-019-40119-2.

(32) Musto, P.; Mensitieri, G.; Cotugno, S.; Guerra, G.; Venditto, V. Probing by Time-Resolved FTIR Spectroscopy Mass Transport, Molecular Interactions, and Conformational Ordering in

the System Chloroform−Syndiotactic Polystyrene. *Macromolecules* **2002**, *35* (6), 2296–2304. https://doi.org/10.1021/ma011684d.

(33) Albunia, A. R.; Rizzo, P.; Guerra, G. Control of Guest Transport in Polymer Films by Structure and Orientation of Nanoporous-Crystalline Phases. *Polymer* **2013**, *54* (6), 1671–1678. https://doi.org/10.1016/j.polymer.2013.01.027.

(34) Albunia, A. R.; Rizzo, P.; Guerra, G. Polymeric Films with Three Different Orientations of Crystalline-Phase Empty Channels. *Chem. Mater.* **2009**, *21* (14), 3370–3375. https://doi.org/10.1021/cm900968c.

(35) Annunziata, L.; Albunia, A. R.; Venditto, V.; Mensitieri, G.; Guerra, G. Polymer/Gas Clathrates for Gas Storage and Controlled Release. *Macromolecules* **2006**, *39* (26), 9166–9170. https://doi.org/10.1021/ma0618878.

(36) Golla, M.; Nagendra, B.; Rizzo, P.; Daniel, C.; Ruiz de Ballesteros, O.; Guerra, G. Polymorphism of Poly(2,6-Dimethyl-1,4-Phenylene)Oxide in Axially Stretched Films. *Macromolecules* **2020**, *53* (6), 2287–2294. https://doi.org/10.1021/acs.macromol.9b02691.

(37) Golla, M.; Nagendra, B.; Fierro, F.; Rizzo, P.; Daniel, C.; Guerra, G. Axially Oriented Nanoporous Crystalline Phases of Poly(2,6-Dimethyl-1,4-Phenylene)Oxide. *ACS Appl. Polym. Mater.* **2020**, *2* (8), 3518–3524. https://doi.org/10.1021/acsapm.0c00532.

(38) Daniel, C.; Rizzo, P.; Nagendra, B.; Cozzolino, A.; Guerra, G. High Diffusivity Dense Films of a Nanoporous-Crystalline Polymer. *Polymer* **2021**, *229*, 124005. https://doi.org/10.1016/j.polymer.2021.124005.

(39) Alentiev, A.; Drioli, E.; Gokzhaev, M.; Golemme, G.; Ilinich, O.; Lapkin, A.; Volkov, V.; Yampolskii, Yu. Gas Permeation Properties of Phenylene Oxide Polymers. *J. Membr. Sci.* **1998**, *138* (1), 99–107. https://doi.org/10.1016/S0376-7388(97)00219-6.

(40) Khulbe, K. C.; Hamad, F.; Feng, C.; Matsuura, T.; Gumi, T.; Palet, C. Characterization of the Poly(Phenylene Oxide) Dense Membrane Prepared at Different Temperatures. *Sep. Purif. Technol.* **2004**, *36* (1), 53–62. https://doi.org/10.1016/S1383-5866(03)00152-7.

(41) Rizzo, P.; Spatola, A.; De Girolamo Del Mauro, A.; Guerra, G. Polymeric Films with Three Different Uniplanar Crystalline Phase Orientations. *Macromolecules* **2005**, *38* (24), 10089–10094. https://doi.org/10.1021/ma051247p.

(42) Albunia, A. R.; Rizzo, P.; Guerra, G. Polymeric Films with Three Different Orientations of Crystalline-Phase Empty Channels. *Chem. Mater.* **2009**, *21* (14), 3370–3375. https://doi.org/10.1021/cm900968c.

(43) Nagendra, B.; Golla, M.; Gallo, C.; Daniel, C.; Rizzo, P.; Guerra, G.; Baldino, L.; Reverchon, E. Mechanisms Determining Different Planar Orientations in PPO Films Crystallized by Guest Sorption. *Polymer* **2021**, *235*, 124242. https://doi.org/10.1016/j.polymer.2021.124242.

(44) Bernstein, H. J. The Vibrational Spectrum of Tetrachloroethylene. *J. Chem. Phys.* **1950**, *18* (4), 478–481. https://doi.org/10.1063/1.1747664.

(45) Milano, G.; Guerra, G. Understanding at Molecular Level of Nanoporous and Co-Crystalline Materials Based on Syndiotactic Polystyrene. *Prog. Mater. Sci.* **2009**, *54* (1), 68–88. https://doi.org/10.1016/j.pmatsci.2008.07.001.

(46) Petraccone, V.; Ruiz de Ballesteros, O.; Tarallo, O.; Rizzo, P.; Guerra, G. Nanoporous Polymer Crystals with Cavities and Channels. *Chem. Mater.* **2008**, *20* (11), 3663–3668. https://doi.org/10.1021/cm800462h.

(47) Golla, M.; Nagendra, B.; Daniel, C.; Rizzo, P.; Guerra, G. Axial Orientation of Co-Crystalline Phases of Poly(2,6-Dimethyl-1,4-Phenylene)Oxide Films. *Polymers* **2020**, *12* (10), 2394. https://doi.org/10.3390/polym12102394.

(48) Nagendra, B.; Vignola, E.; Daniel, C.; Rizzo, P.; Guerra, G. Dependence on Film Thickness of Guest-Induced c Perpendicular Orientation in PPO Films. *Polymers* **2021**, *13* (24), 4384. https://doi.org/10.3390/polym13244384.

CHAPTER 3

Gas sensors based on PPO films/coatings

Gas sensors are devices that are designed and optimized to have performance criteria such as the ability to detect low concentrations of certain gas analytes in the ppb levels,[1–6] to have short response time,[7–9] and low power consumption, which is related to the temperature of the operating point.[10,11] They have applications ranging from environmental monitoring, food safety monitoring, medical diagnostics, and electronic nose applications.[12,13]

Hence, the detection of volatile organic compounds (VOCs) is nowadays considered one of the key aspects for controlling and limiting their release into the environment.

Various types of gas sensors have been developed that are classified by the transduction methods, which include electrochemical,[14] optical,[15,16] thermoelectrical,[17] electrical,[18,19] and piezoelectric methods.[20]

In this chapter, preliminary studies on NC PPO coatings (≈1 μm thick) and on CC PPO films (≈40 μm thick) are reported. Particularly, the aim of this investigation is to check if they could be considered the operating element for gas sensors with electrical in one case (NC PPO coating) or optical (for CC PPO film) responses. Both approaches (electrical and optical) have been explored considering different VOCs.

3.1 Electrical approach: NC PPO coatings for Metal Insulator Semiconductors

Gas sensors, based on electrically transducers, can be subdivided considering unique device architectures and sensing mechanisms, such as, field-effect transistor-based sensors (i.e., chemFET),[48,49] conductometric sensors,[50] chemiresistive sensors[51–53] and chemicapacitive sensors.[54,55]

Particularly, capacitive measurement under exposure of gases/vapour is relatively new and far more accurate than the resistive one.[54–59] The capacitive measurement is predominantly governed by the change in relative dielectric permittivity (ε_r) of the medium in presence of gases/vapour and is less sensitive to the charge effects.[60]

Materials, such as metal oxide semiconductors (MOSs),[53,61] metal insulator semiconductors (MISs),[55] polymers[62,63] and carbon-based materials[59,64] are generally used as gas sensors depending on the change in electrical properties in the presence/absence of target gases.[65]

Specifically, a "chemicapacitive" sensor (or "chemicapacitor") is a capacitor that has a selectively absorbing material, such as a polymer, as a dielectric. Polymer-based chemicapacitors, in particular, are promising platforms for low-cost, low-power sensors, since unlike most other gas sensors they do not require heating, mechanical excitation, or light sources.

Chemicapacitors use two basic geometries: interdigitated electrodes and parallel-plate configurations. Interdigitated electrodes[62] consist of a single layer of metal deposited on a substrate to form two meshed combs. The absorbent material is then deposited on the top of the combs.

Parallel-plate sensors,[63] instead, consist of a layer of metal deposited on a substrate, followed by a layer of a polymer and finally a second porous layer of metal above the polymer.

Parallel-plate chemicapacitive sensors with absorbent polymer coatings have been successfully used to detect a wide range of volatile gases.[66]

The selectivity of these absorbing polymers results from functional groups that interact weakly with certain target analytes, imparting some degree of preferred interactions. In fact, polymers are selected based on their ability to form stronger reversible hydrogen bonds, van der Waals bonds, and dipole–dipole interactions with some analytes over others.[67]

The amount of target gases (i.e., VOCs), absorbed into a polymer depends not only on the ambient concentration of the VOCs, but also on the chemical properties of both VOCs and polymers.

Typically, for individual parallel-plate capacitors, filled or partially filled with selectively absorbing polymers, when exposed to volatile analytes, the absorption of the chemicals into the polymer film alters the permittivity of the polymers resulting in changes in the capacitance of the sensor elements.[68] Of course, the absorbing property of the polymer is crucial for the developing of the gas sensor.

In the previous chapter (second), the extraordinary ability of PPO in terms of sorption of pollutants from air (and water) even at low activities has been reported.[69,70]

In this section, a very preliminary study on a potential MIS-based gas indicator (in parallel-plate chemicapacitor device) using as dielectric matrix a PPO coating between two layers of metal (i.e., Au), is described. These primary results seem to be very promising, so encouraging to go on deeper in this research.

3.1.1 Sample preparation and characterization

PPO 3 wt% $CHCl_3$ solution was used to form a thin layer on a golden (Au) support by spin coating technique, using the following parameters: 2000 rpm/sec; 1000 rpm; 30 seconds. The resulting PPO coating shows a thickness of nearly 1 µm and a wrinkled surface. Then, an Au contact having dimension 2mm × 2mm × 50nm was deposited on the top of the PPO coating by thermal evaporation technique. This Au layer acts as top contact while the Au support acts as bottom contact. Figure 3.1 shows a schematic (not in scale) of the capacitive sensor device where the PPO coating is the insulator material while Au contacts are the plates of the capacitor.

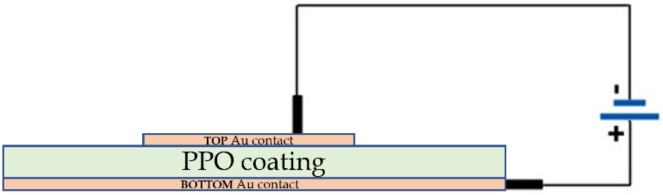

Figure 3.1 Schematic of the capacitive gas device made with a PPO coating (≈1 µm) as insulator material between a top and a bottom Au contacts (not in scale). The electrical driving force is applied on the Au contacts of the capacitor.

This device (Figure 3.1) is an example of a parallel-plate chemicapacitive Metal Insulator Semiconductor (MIS).[55]

The capacitance (C_p) of the sensor device with PPO coating was detected at room temperature in air ambient using a voltage $\Delta V = 100mV$ and it was ≈27 pF. The electrical driving force was applied on the Au contacts of the capacitor (as shown in Figure 3.1).

This device was then ready to be tested by exposure to gases and by recording change in capacitance. Many experiments were done testing different gases, but the results here reported are related only to two VOCs taken as referring models: carbon tetrachloride (CCl_4) and methyl ethyl ketone (MEK). Both VOCs are widely used in industries and they results to be hazardous for human health.[71,72]

PPO coatings in the parallel-plate chemicapacitive MIS-based indicator were characterized by FTIR analysis using PPO films with a higher thickness (≈8 µm), as shown in Figure 3.2. These thicker PPO films were made by spin coating technique on a silicon (Si) wafer using the same parameters applied for the coating on Au contacts (2000 rpm/sec; 1000 rpm; 30 seconds). It is apparent that the PPO film was amorphous[40] as indicated by the presence of the FTIR peak located at 831 cm^{-1} (Figure 3.2a).

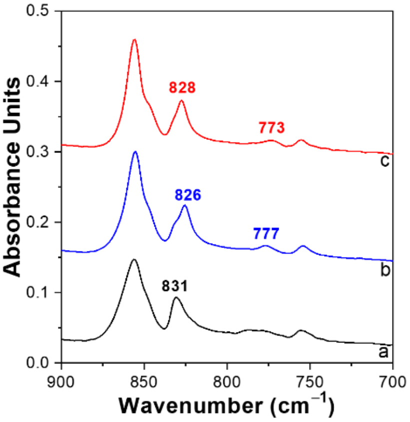

Figure 3.2 FTIR analysis of PPO film (≈8 µm thick) after spin coating technique on Si support: (a) amorphous film by spinning; (b) after exposure of amorphous film to MEK saturated vapours; (c) after exposure of amorphous film to CCl_4 saturated vapours.

These PPO films (≈8 µm thick) were then placed in the following conditions (as used for testing the sensor): hermetically closed chamber of MEK or CCl_4 saturated vapours for 30 min. After that, they were recovered and FTIR measurements were performed. Crystalline peaks were well evident (Figure 3.2b,c). In particular, the PPO films exposed to MEK saturated vapours (Figure 3.2b) is crystalline in β phase[40] (peaks at 826 and 777 cm^{-1}) while for the film exposed to CCl_4 saturated vapours (Figure 3.2c) the α crystalline phase[40] was induced (peaks at 828 and 773 cm^{-1}).

3.1.2 Electrical capacitance response

The MIS-based device made with a PPO coating of nearly 1 µm in a parallel-plate Au capacitor were exposed for 30 min to saturated vapors of CCl_4 or MEK.

Once exposed, the devices were subjected to an electric potential (ΔV = 100 mV) and the capacitance was recorded during time.

In particular, three runs were performed as shown in Figure 3.3 and data about capacitance values are collected in Table 3.1.

In the run I (Figure 3.3A) the capacitance value became higher (from 27 pF to 44 pF) for the device exposed to MEK saturated vapours (sample A, increasing of nearly +63%) while after exposure to CCl_4 saturated vapours there was a decrease of the capacitance value from 27 pF to 18 pF (sample B, decreasing of nearly –33%).

This phenomenon of total capacitive change is mainly due to a change in dielectric permittivity (ε_r) of the insulator material (PPO coating), as soon as the gas sorption starts.

In general, the dielectric ε_r of the medium is defined as the following formula: $\varepsilon_r = \varepsilon_m/\varepsilon_0$; where ε_m is the permittivity of the material and ε_0 is the vacuum permittivity.[73]

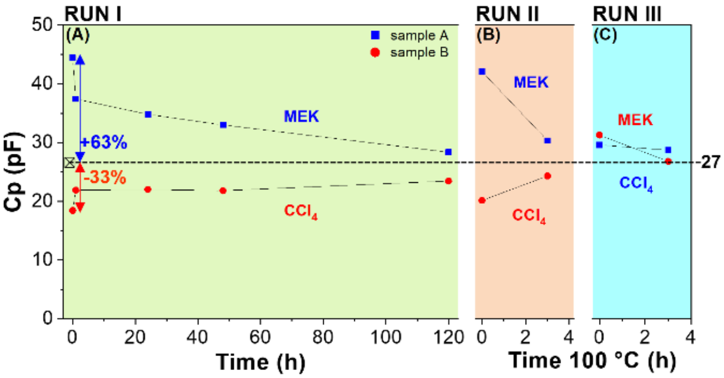

Figure 3.3 Capacitance values at ≈20 °C vs time for two gas indicators: (■) sample A; (●) sample B. The devices were exposed to MEK or CCl_4 saturated vapours for 30 min (run I and II), a reverse response was performed for run III. Once collected, the devices were placed at room temperature ≈20 °C (run I) or heated at 100 °C for 3 hours (run II and III).

When MEK/CCl_4 sorption in the PPO coating starts, a change in this ε_r value occurs, depending not only on the dielectric permittivity of PPO (ε_{PPO}) but also on the dielectric permittivity values of the considered gases (i.e., ε_{MEK} and ε_{CCl4}). The ε_{PPO} value was estimated according to the following formula:

$$\varepsilon_{PPO} = \frac{C_p * d}{\varepsilon_0 * A} \tag{3.1}$$

where C_p is the capacitance of the sensor (≈27 pF), d is the distance between the parallel plates of the capacitor (PPO thickness, ≈1µm), ε_0 is the vacuum permittivity ($8.85 \mathrm{x} 10^{-12}$ Fm^{-1}) and A is the area of the Au top contact (0.04 cm^2).

About dielectric permittivity of MEK an CCl_4, the values were collected by literature and they are 18.4 and 2.2 pFm^{-1} for ε_{MEK}[74] and ε_{CCl4},[75] respectively.

It is also evident (Figure 3.3A) that during time the capacitive values in both devices tends to reach the initial value. This is almost certainly due to the desorption of the gases from the PPO coatings at room temperature (≈20 °C). Consequently, the dielectric ε_r value of the coating was progressively changing while desorption occurred.

In the run II (Figure 3.3B) the sensors were again exposed to the same VOCs saturated vapours, but the desorption was accelerated by inducing a thermal treatment at 100 °C. In fact, it is well evident that the tendence to reach the starting capacitive value is faster than previous (Figure 3.3A, run I). In the run III (Figure 3.3C) a reverse exposure as well as heating treatments at 100 °C were performed. Specifically, the device which was previously exposed to MEK saturated vapours (sample A) was then subjected to CCl_4 saturated vapours, on the contrary for the other device (sample B) which, instead, was exposed to MEK saturated vapours. It is clear that the capacitive change for this experiment behaves in an opposite direction: the sample A shows a decrease (from +30 to +29 pF) while for the sample B there is an increase of capacitive values (from –11 to +15 pF).

Thus, it is well evident that the change in capacitance of the gas indicator is depending on the nature of the VOC absorbed ($\varepsilon_{MEK}/\varepsilon_{CCl4}$) which in turn changes the dielectric permittivity of the insulator material in the device. The diverse response patterns seem to be useful to discriminate the volatile chemicals from each other.

Specifically, the response (*RM*) was calculated as absolute variation, considering the following formula[68]:

$$RM = (C_g - C_p / C_p) \text{ x } 100 \qquad (3.2)$$

where C_p is the initial capacitance of the sensor (≈27 pF) and C_g is the capacitance in presence of tested VOCs.

The response was estimated also taking into account the relative variation $RM' = (C_g - C_{g'} / C_{g'}) \text{ x } 100$, where C_g is the capacitance in presence of tested VOCs at initial time of the run and $C_{g'}$ is the final capacitance of the previous run (exactly before the initial time of the run).

Focusing the attention on the relative variation in the capacitance values between two consecutive runs (*RM'* values of Table 3.1), it is clearly evident that the behavior is similar when the exposure occurs with the same VOC, but it is completely opposite when the same device is exposed to a different gas.

In particular, when the sample A is exposed again to MEK vapors (Figure 3.3B; run II; sample A), the relative capacitive change *RM'* is +50% (roughly lower than the starting value of +63%), but it becomes –3% when the sensor is exposed to CCl_4 vapours (Figure 3.3C; run III; sample A).

The behavior of the other sample is in the opposite direction: when it is exposed again to CCl_4 vapors (Figure 3.3B; run II; sample B), the capacitive change is –13% (sharply lower than the starting value of –33%), but it converts to +29% when the exposure happens with MEK vapours (Figure 3.3C; run III; sample B). It is worth noting that also the *RM* value is almost different in the run II compared to the run I, probably due to a weak damage of the thin PPO layer by the saturated vapours treatments.

Table 3.1 Experimental data concerning the response of the parallel-plate chemicapacitive MIS-based gas indicators coated with a thin PPO layer. C_g is the capacitance of the sensors; *RM* is the absolute variation in the capacitance values; *RM'* is the relative variation in the capacitance values (between two consecutive runs).

VOCs	RUN	Sample	Time	C_g (pF)	*RM* (%)	*RM'* (%)
MEK	I	A	initial	44	+63	+63
			after 1h	37	+37	-
			after 24h	34	+26	-
			after 48h	33	+22	-
			after 120h	28	+4	0
	II	A	initial	42	+56	+50
			after 3h at 100 °C	30	+11	0
	III	B	initial	29	+7	–3
			after 3h at 100 °C	28	+4	-
CCl_4	I	B	initial	18	–33	–33
			after 1h	22	–19	-
			after 24h	22	–19	-
			after 48h	22	–19	-
			after 120h	23	–15	0
	II	B	initial	20	–26	–13
			after 3h at 100 °C	24	–11	0
	III	A	initial	31	+15	+29
			after 3h at 100 °C	27	0	-

Additionally, it is significant to notice that in the parallel-plate chemicapacitive MIS-based gas indicator the PPO layer is amorphous at the beginning. Once exposed to MEK/CCl_4 vapours (Figure 3.3A, run I), crystallinity is induced in the PPO coatings (Figure 3.2B,C). At the second exposure with the same gases (Figure 3.3B, run II), the PPO layer was at that moment crystalline as well as nanoporous, but the capacitive change was almost the same compared to that of the run I where the starting PPO layer was amorphous (see *RM'* values in Table 3.1). This is probably due to the fact that the exposure is performed considering saturated vapours conditions. Certainly, the sorption uptake from amorphous phases is lower than from NC phases,[69,70] especially at low concentration. Then, it is reasonable considering that also the change in capacitance of these gas indicators would be different at low vapour activities. Further studies are needed to better understand if there would be a difference in performances of the potential gas sensor if the nature of the PPO layer is amorphous or nanoporous-crystalline.

3.2 Optical approach: CC PPO films with a fluorescent guest

Sensing devices based on chromogenic characteristics of the designed materials are important references in the literature.[21–27] Particularly, being VOCs uncolored and lacking of fluorescence, the optical-based approach is an indirect tool for their detection taking advantages of the chromogenic properties of certain chromophores or fluorophore species when interact with analytes in the gas phase. Therefore, the design and the fabrication of novel colored and fluorescent materials to detect VOCs exposure with even more sensitivity are highly demanded and investigated.[28–32]

When the solvating activity of the absorbed VOC molecules occurs, a strongly influence on the intensity and/or on the position of the emission band of the active fluorophore can be found. This phenomenon is called vapochromism.[29]

Fluorescent enhancements (i.e., typical OFF-ON responses) are the most preferred since scientifically appealing and more sensitive detection by the naked eye. Polymers act as a supporting highly viscous matrix which is highly permeable to VOCs. In certain cases, viscosity variations during VOCs uptake cause fluorescence variation of the embedded fluorophore due to the variation of their intramolecular motions.[33]

In this section, the combination of the sorption ability of PPO and the fluorescence characteristics of 7-hydroxy coumarin (i.e., umbelliferone) for the detection of VOCs is proposed. More specifically, among the vapours that were demonstrated to effectively interact with PPO,[34] chloroform ($CHCl_3$) has been selected as the volatile contaminant model being considered harmful, irritant and possibly carcinogenic after prolonged exposure.[35]

Umbelliferone has been reported in literature as an efficient fluorescent probe for the detection of Pd(II) in living cells,[36] of pyridine gas in cucurbit[10]uril encapsulations,[37] and, very recently, of SO_2 vapours with high sensitivity and selectivity (<0.2 ppm) when covalently linked to anion-functionalized ionic liquids.[38] Particularly, umbelliferone is a fluorescent molecule characterized by a low quantum yield in non-polar media and in the solid state due to radiationless de-excitation attributed to the proximity effect.[39] When $CHCl_3$ molecules get in contact with umbelliferone, fluorescence raising is therefore expected.

In this section, CC PPO films with umbelliferone have been studied as potential vapochromic gas sensors towards $CHCl_3$ molecules. Another polar VOC like dichloromethane (DCM) has been investigated for comparison.

3.2.1 Sample preparation and characterization

PPO films (≈40 μm of thickness) presenting NC α and β phases were obtained by 1 wt% CCl_4 and benzene solution casting, respectively, and subsequent solvent removal by ACN at room temperature. PPO amorphous films were made by casting of 1.5 wt% $CHCl_3$ solution and subsequent solvent evaporation at 60 °C. These films were characterized by WAXD and FTIR analysis.

WAXD patterns, gathered from a two-dimensional diffractometer (on the left), and the corresponding equatorial diffraction profiles (on the right) are reported on Figure 3.4. For crystalline PPO films, the diffraction peaks at $2\theta_{CuK\alpha} \approx 4.5°$, 7.1°, 11.3° and 15.0° and at $2\theta_{CuK\alpha} \approx 5.2°$, 7.7° and 12.8° indicate the presence of the NC α and β phases,[40] respectively (Figure 3.4A,B). The presence of a diffuse halo, as shown by WAXD patterns and equatorial profile of Figure 3.4C, is instead typical of a fully amorphous material. FTIR spectra of PPO films with diffractograms reported in Figure 3.4, are shown in Figure 3.5; typical peaks at 828, 773, 756 and 414 cm^{-1} for α phase, at 826, 777, 756 and 418 cm^{-1} for β crystalline phase and at 831 and 755 cm^{-1} for amorphous, are apparent and in agreement with the literature.[41]

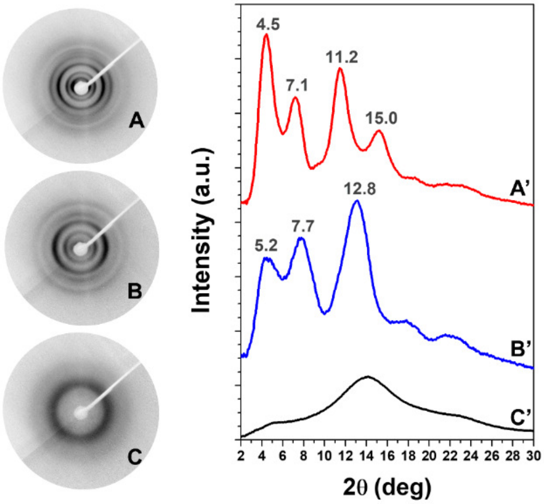

Figure 3.4 WAXD patterns (A–C) and corresponding equatorial intensity profiles (A′–C′) of PPO films presenting: NC α, (A, A′), NC β (B, B′) and amorphous phases (C, C′).

The degree of crystallinity (X_c) for α and β films, as evaluated by FTIR spectroscopy, are ~43% and ~46%, respectively.

FTIR spectra in the wavenumber range of 1850–1500 cm^{-1} are reported in Figure 3.6 for the NC α and β as well as for the amorphous PPO films, before (gray lines) and after immersion in saturated umbelliferone/methanol solution for 30 min (red, blue and black lines), respectively. Umbelliferone FTIR spectrum is also reported for comparison (green line).

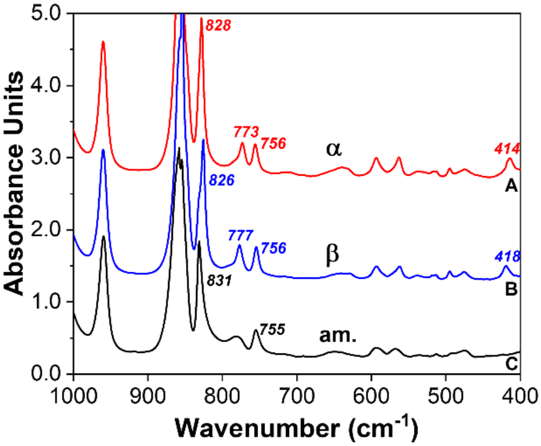

Figure 3.5 FTIR spectra of PPO films presenting: (A) NC α phase (red line); (B) NC β phase (blue line) and (C) amorphous (black line) phase.

The most relevant feature of PPO film spectra is the presence of an extra peak at 1748 cm^{-1}, beside the typical peak at 1705 cm^{-1} of umbelliferone (Figure 3.6).

In agreement with the literature on umbelliferone[42] and with other recent studies on different systems,[43] the peak at 1748 cm^{-1} can be associated to the band of C=O groups of α-pyrone molecules free from hydrogen bonding, while the peak at 1708 cm^{-1} is possibly attributed to the band of C=O groups of umbelliferone involved in intermolecular interactions (mainly intermolecular hydrogen bonds).

Inspection of Figure 3.6 shows that the amount of umbelliferone absorbed in PPO films is higher for CC phases with respect to the amorphous one. Notably, umbelliferone uptake was evaluated by TGA analyses, and it was close to 2.0% and 2.2% for α and β PPO films, respectively, whereas only ~1% for the amorphous sample.

The different distribution of coumarin molecules absorbed in PPO films can be evaluated by analyzing the relative intensities of FTIR peaks at 1748 cm^{-1} and 1708 cm^{-1}. Thus, the unbonded umbelliferone fraction is 25% (~0.5 wt%), 36% (~0.8 wt%) and 70% (~0.7 wt%) of the total molecules present in α, β and amorphous PPO films, respectively. Consequently, the major fraction of molecules interacting via hydrogen bonding are present into the CC α phase (75%, ~1.5).

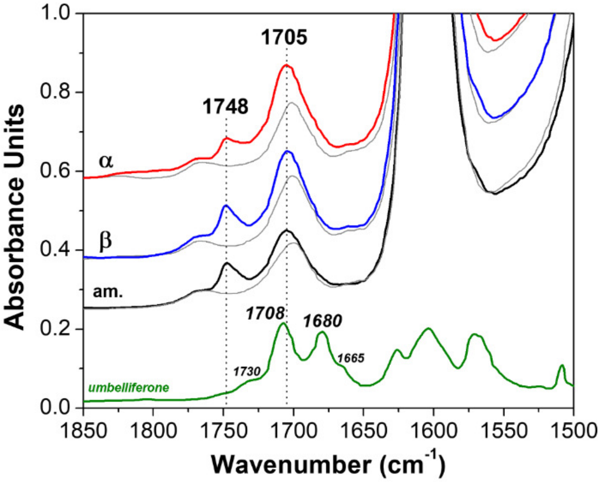

Figure 3.6 FTIR spectra of α (red line), β (blue line) NC as well as of amorphous (black line) films, before (gray lines) and after immersion in umbelliferone/methanol solution for 30 min. Spectrum of umbelliferone is also reported (green line) for comparison.

UV–Vis spectra of PPO films doped with umbelliferone showed the typical absorption band at 330 nm and attributed to the π-π* transition[39] (Figure 3.7). The absorption intensity agrees well with the amount of dye molecules included into the PPO matrix as evaluated from the FTIR spectra, thus confirming the higher uptake of umbelliferone by the NC β and α films.

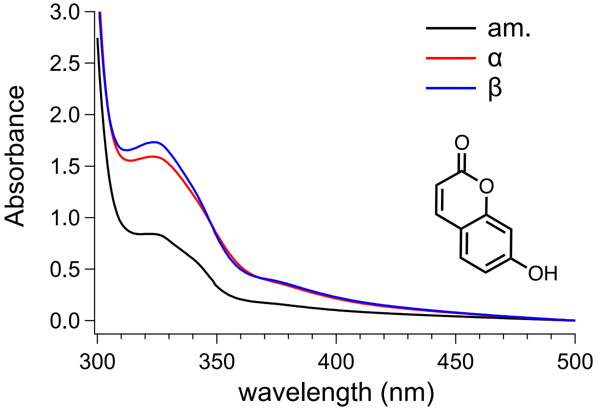

Figure 3.7 UV–Vis spectra of α (red line), β (blue line) as well as of amorphous (black line) PPO films, after immersion in umbelliferone/methanol solution for 30 min. In the inset, the chemical formula of umbelliferone.

The umbelliferone-doped PPO films showed the typical emission behavior of the embedded coumarin with a fluorescence maximum at about 430 nm (Figure 3.8). This peak appeared mostly unaltered by the different nature of the PPO matrix, whereas the

PPO films show a very low quantum yield (Φ_F) of around 1–2%. The fluorescent Φ_F is defined as the ratio of the number of photons emitted to the number of photons absorbed. Notably, quantum yield is independent of instrument settings and describes how efficiently a fluorophore converts the excitation light into fluorescence.[44]

Thus, the Φ_F values of umbelliferone in PPO films indicate that radiationless relaxation pathways are the most occurring phenomena in the solid state.[39,45] It was worth noting that this behavior appeared more pronounced in the α and β PPO films (i.e., Φ_F of 1.1% and 1.4%, respectively, with respect to 1.8% of the amorphous film), where the stronger molecular interaction places the fluorophores in a specific environment and possibly favors fluorescence quenching. As a matter of fact, the lowest Φ_F of 1.1% was calculated for umbelliferone embedded in the NC α phase where the highest content of hydrogen bonded guest molecules (~1.5 wt%) was observed (Table 3.2).

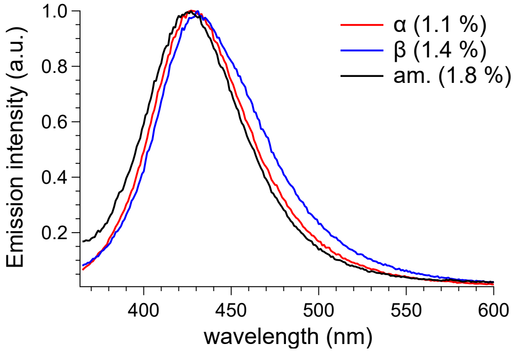

Figure 3.8 Normalized fluorescence spectra of α (red line), β (blue line) as well as of amorphous (black line) PPO films, after immersion in umbelliferone/methanol solution for 30 min (λ_{exc} = 340 nm). In parentheses the emission quantum yield (Φ_F) was reported.

Table 3.2 Amount of coumarin embedded in the α and β crystalline and amorphous phases of the PPO matrix and the derived Φ_F.

PPO film	Hydrogen bonded umbelliferone (wt%)	Φ_F (%)
α	1.5	1.1
β	1.4	1.4
amorphous	0.3	1.8

3.2.2 *Vapochromic fluorescent response*

The umbelliferone/PPO films were therefore exposed to chloroform vapours selected as the volatile contaminant model. Particularly, the fluorescence variation of the films was determined by exposing a 1 cm × 1 cm film to $CHCl_3$ vapours at 20 °C under saturation conditions (schematic of the apparatus used for the vapochromism studies is shown in Figure 3.9).

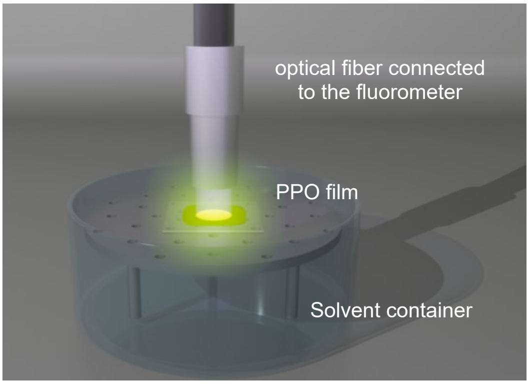

Figure 3.9 Apparatus used for the vapochromism studies.

Fluorescence spectra (λ_{exc} = 340 nm) of the umbelliferone-doped PPO films were collected for 20 min of exposure to $CHCl_3$ vapours and with a time interval of 1 min. For all the umbelliferone/PPO films, an increasing of the emission intensity occurred when the doped films get in contact with the chloroform atmosphere (Figure 3.10).

The maximum fluorescence was recorded after about 20 min of chloroform vapours exposure, and then maintained constant before solvent desorption from the films. Moreover, both shape and fluorescence peak remained unchanged during the experiments as well as the film integrity.

Fluorescence enhancements were addressed to the effective solvent/umbelliferone interactions. More specifically, as soon as PPO films were exposed to chloroform vapours, they start filling the empty nanopores of the polymer matrix, get in contact with the fluorophore molecules that, in turn, increase their emission due to the solvation effect. The "turn-on" effect of fluorescence due to solvation agrees well with Φ_F = 7% of umbelliferone in chloroform and appears faster in case of the PPO α form.[46]

With the aim to determine the possible influence of the α and β nanoporous crystalline or amorphous phases of PPO matrix on the vapochromic response of the included umbelliferone, the fluorescence intensity variation (i.e. $F–F_0/F_0$, Figure 3.11) was determined from the fluorescence maxima shown in Figure 3.10. It should be noted that the fluorescence variation appeared fastest in the case of umbelliferone included in the α form of PPO, whereas the amorphous matrix provided the slowest fluorescence variation (Figure 3.11a).

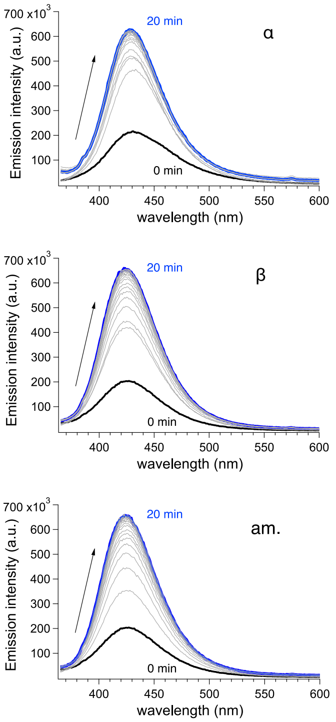

Figure 3.10 Fluorescence spectra of the umbelliferone-doped PPO films collected for 20 min of exposure to $CHCl_3$ and with a time interval of 1 min (λ_{exc} = 340 nm).

Therefore, the umbelliferone/PPO film with the lowest Φ_F and quenched emission showed the most rapid fluorescence enhancements. The umbelliferone fluorophore dispersed in the amorphous phase resulted optically responsive towards $CHCl_3$ vapours as well, but with a slower kinetics being umbelliferone molecules less interacting via H-bonding, as revealed by FTIR experiments (Figure 3.6).

The vapochromic response was also tested by using DCM as VOC, i.e. a chlorinated polar compound that is characterized by a weaker C–H donor strength with respect to chloroform.[47] Notwithstanding the higher vapour pressure of DCM (i.e. 349 mm Hg against 158.4 mm Hg of chloroform), the fluorescence variation was slower for all the umbelliferone/PPO films within the first 2–3 min of exposure, while levelling off after a longer period (Figure 3.11). It was worth noting that the delayed response appeared more evident in the case of umbelliferone included in the α and β forms of PPO, and particularly evidenced for the α one. This phenomenon suggested that the stronger donor C–H behavior of chloroform is the key parameter to accelerate the vapochromic response, being more effective in breaking H-bondings in umbelliferone poorly emissive assemblies.

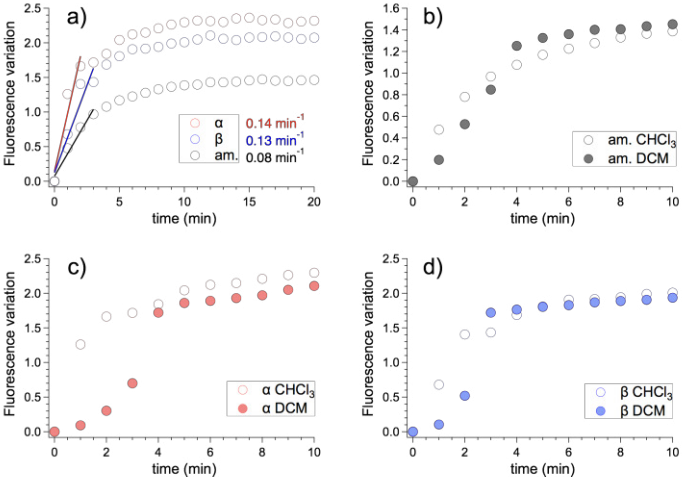

Figure 3.11 Fluorescence intensity variation of the umbelliferone/PPO films in response to the exposure to a) $CHCl_3$ and DCM vapours for b) amorphous, c) α-form and d) β-form of PPO. (λ_{exc} = 340 nm, data were acquired from the intensities of spectra reported in Figure 3.10).

Moreover, since the chloroform/PPO matrix interactions are reversible, the films were dried under vacuum for one night. Φ_F were then repeated and all the umbelliferone/PPO films displayed quantum efficiencies around 1.1–1.3%, i.e., without significant differences among them. Then, a second cycle of exposure to chloroform vapours were performed and the emission enhancement occurred again, thus suggesting a reversible vapochromic response (Figure 3.12).

Although the expected reversible vapochromic features, no significant difference among the fluorescence intensity variations between the CC and amorphous phases of PPO films were detected. Particularly, α and β PPO films still showed the same fluorescence variations coefficients of 0.14–0.13 min^{-1}, whereas for the amorphous it increased from 0.08 to a value similar to that of the β phase in agreement with Φ_F close to 1%.

Fluorescence maximum variations were detailed monitored in order to verify the reversibility of the emission response after successive solvent absorption/desorption cycles. Notably, the vapochromic response appeared affected after the third cycle of chloroform vapours exposure, probably due to the occurrence of a roughened surface that could adversely affect the fluorescence emitted by the film.

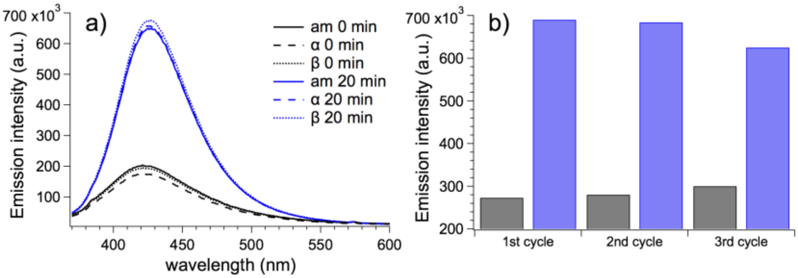

Figure 3.12 a) Fluorescence spectra of the umbelliferone/PPO films in response to the second exposure time to $CHCl_3$ vapours and b) fluorescence intensity of the umbelliferone/α-form PPO film at 0 min (black bars) and 20 min (blue bars) of $CHCl_3$ exposure at different cycles. In all cases, λ_{exc} = 340 nm.

Additionally, FTIR spectra of α (red line), β (blue line) and amorphous (black line) PPO films, before and after the third exposure to chloroform vapours have been performed and compared in Figure 3.13.

The peak at 668 cm^{-1} related to the presence of chloroform is present in all the PPO samples. Furthermore, it is worth noting that the amorphous film (curve C) after exposure to chloroform vapours (dark yellow curve) crystallizes in β phase as pointed out by the peaks at 594, 563, 495 and 418 cm^{-1}.[41]

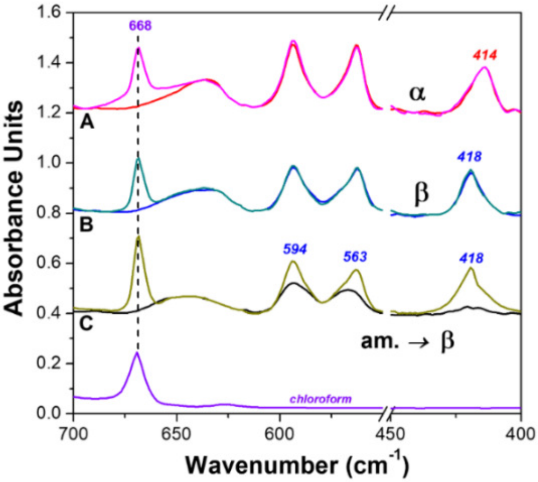

Figure 3.13 FTIR spectra in the wavenumber range 700–400 cm^{-1} of α (red and pink lines), β (blue and light blue lines) NC and of amorphous (black and dark yellow lines) films before and after exposition to chloroform vapours for 20 min. Spectrum of chloroform (violet line) is also reported.

3.3 Conclusions

In this chapter, a very preliminary study on a potential parallel-plate chemicapacitor MIS-based gas sensor, in which the dielectric material is a PPO coating interacting with metal contacts from both sides, has been reported. These primary results are positive and fairly promising because a diverse response pattern is achieved when the electrical indicator is exposed to two different gases (i.e., MEK and CCl_4), therefore it can be used to discriminate the volatile chemicals from each other. Probably, the magnitude of this change in capacitance results from a complex combination of response phenomena that depends on several factors. Analyte adsorption phenomena into the polymer, of course, play a major role in sensor response. The main factors could be as follows: (i) dielectric chemical structure modification from reversible weak interactions with the analyte; (ii) dielectric swelling due to absorption of the analyte which reduce dipole moments within the polymer altering its permittivity and conductivity; (iii) the permittivity of the analyte being absorbed; and (iv) the amount of analyte absorbed into the dielectric. Further studies are needed to better understand and optimize this potential electrical MIS-based gas sensor.

Another aspect here reported is related to the vapochromic response against chloroform vapours in CC and amorphous PPO films containing 1–2 wt% of umbelliferone. The prepared films showed fluorescence maximum at about 430 nm with emission intensities mostly quenched and with minimum Φ_F of around 1% in the NC α and β PPO phases. This phenomenon was possibly addressed to the stronger molecular interactions of the fluorophore via H-bonding occurred in the case of the nanoporous-crystalline confinement that caused intense fluorescence self-quenching. Once exposed to chloroform vapours, fluorescence rapidly turned on within the first minutes for all the umbelliferone-doped PPO films thanks to the solvation effect provided by the polar vapours. Particularly, vapochromism was particularly faster in the case of NC PPO films (0.14–0.13 min^{-1} against 0.08 min^{-1} for the amorphous PPO film) being the fluorescence quenching more effective. Such fluorescence response appeared also reversible for these PPO films up to three cycles, whereas the amorphous sample crystallized into the β form upon chloroform saturated vapours exposure.

The whole set of data suggests that PPO films/coatings can be suitable for developing new advanced materials for optical as well as electrical detection of harmful VOC vapours.

REFERENCES

(1) Hu, J.; Yang, J.; Wang, W.; Xue, Y.; Sun, Y.; Li, P.; Lian, K.; Zhang, W.; Chen, L.; Shi, J.; Chen, Y. Synthesis and Gas Sensing Properties of NiO/SnO2 Hierarchical Structures toward Ppb-Level Acetone Detection. *Mater. Res. Bull.* **2018**, *102*, 294–303. https://doi.org/10.1016/j.materresbull.2018.02.006.

(2) Karmaoui, M.; Leonardi, S. G.; Tobaldi, D. M.; Donato, N.; Pullar, R. C.; Seabra, M. P.; Labrincha, J. A.; Neri, G. Novel Nanosynthesis of In $_2$ O $_3$ and Its Application as a Resistive Gas Sensor for Sevoflurane Anesthetic. *J. Mater. Chem. B* **2015**, *3* (3), 399–407. https://doi.org/10.1039/C4TB01177E.

(3) Li, D.; Tang, Y.; Ao, D.; Xiang, X.; Wang, S.; Zu, X. Ultra-Highly Sensitive and Selective H2S Gas Sensor Based on CuO with Sub-Ppb Detection Limit. *Int. J. Hydrog. Energy* **2019**, *44* (7), 3985–3992. https://doi.org/10.1016/j.ijhydene.2018.12.083.

(4) Na, H.-B.; Zhang, X.-F.; Deng, Z.-P.; Xu, Y.-M.; Huo, L.-H.; Gao, S. Large-Scale Synthesis of Hierarchically Porous ZnO Hollow Tubule for Fast Response to Ppb-Level H $_2$ S Gas. *ACS Appl. Mater. Interfaces* **2019**, *11* (12), 11627–11635. https://doi.org/10.1021/acsami.9b00173.

(5) Zhang, W.; Cheng, X.; Zhang, X.; Xu, Y.; Gao, S.; Zhao, H.; Huo, L. High Selectivity to Ppb-Level HCHO Sensor Based on Mesoporous Tubular SnO2 at Low Temperature. *Sens. Actuators B Chem.* **2017**, *247*, 664–672. https://doi.org/10.1016/j.snb.2017.03.099.

(6) Han, D.; Zhai, L.; Gu, F.; Wang, Z. Highly Sensitive NO2 Gas Sensor of Ppb-Level Detection Based on In2O3 Nanobricks at Low Temperature. *Sens. Actuators B Chem.* **2018**, *262*, 655–663. https://doi.org/10.1016/j.snb.2018.02.052.

(7) Deng, X.; Zhang, L.; Guo, J.; Chen, Q.; Ma, J. ZnO Enhanced NiO-Based Gas Sensors towards Ethanol. *Mater. Res. Bull.* **2017**, *90*, 170–174. https://doi.org/10.1016/j.materresbull.2017.02.040.

(8) Wang, F.; Hu, K.; Liu, H.; Zhao, Q.; Wang, K.; Zhang, Y. Low Temperature and Fast Response Hydrogen Gas Sensor with Pd Coated SnO2 Nanofiber Rods. *Int. J. Hydrog. Energy* **2020**, *45* (11), 7234–7242. https://doi.org/10.1016/j.ijhydene.2019.12.152.

(9) Li, Y.; Chen, N.; Deng, D.; Xing, X.; Xiao, X.; Wang, Y. Formaldehyde Detection: SnO2 Microspheres for Formaldehyde Gas Sensor with High Sensitivity, Fast Response/Recovery and Good Selectivity. *Sens. Actuators B Chem.* **2017**, *238*, 264–273. https://doi.org/10.1016/j.snb.2016.07.051.

(10) Xiao, L.; Xu, S.; Yu, G.; Liu, S. Efficient Hierarchical Mixed Pd/SnO2 Porous Architecture Deposited Microheater for Low Power Ethanol Gas Sensor. *Sens. Actuators B Chem.* **2018**, *255*, 2002–2010. https://doi.org/10.1016/j.snb.2017.08.216.

(11) Liu, D.; Lin, L.; Chen, Q.; Zhou, H.; Wu, J. Low Power Consumption Gas Sensor Created from Silicon Nanowires/TiO $_2$ Core–Shell Heterojunctions. *ACS Sens.* **2017**, *2* (10), 1491–1497. https://doi.org/10.1021/acssensors.7b00459.

(12) Bag, A.; Lee, N.-E. Gas Sensing with Heterostructures Based on Two-Dimensional Nanostructured Materials: A Review. *J. Mater. Chem. C* **2019**, *7* (43), 13367–13383. https://doi.org/10.1039/C9TC04132J.

(13) Kumar, R.; Al-Dossary, O.; Kumar, G.; Umar, A. Zinc Oxide Nanostructures for NO2 Gas–Sensor Applications: A Review. *Nano-Micro Lett.* **2015**, *7* (2), 97–120. https://doi.org/10.1007/s40820-014-0023-3.

(14) Li, H.; Mu, X.; Yang, Y.; Mason, A. J. Low Power Multimode Electrochemical Gas Sensor Array System for Wearable Health and Safety Monitoring. *IEEE Sens. J.* **2014**, *14* (10), 3391–3399. https://doi.org/10.1109/JSEN.2014.2332278.

(15) Bogue, R. Detecting Gases with Light: A Review of Optical Gas Sensor Technologies. *Sens. Rev.* **2015**, *35* (2), 133–140. https://doi.org/10.1108/SR-09-2014-696.

(16) Hodgkinson, J.; Tatam, R. P. Optical Gas Sensing: A Review. *Meas. Sci. Technol.* **2013**, *24* (1), 012004. https://doi.org/10.1088/0957-0233/24/1/012004.

(17) Kim, S.; Lee, Y.-I.; Choi, Y.-M.; Lim, H.-R.; Lim, J.-H.; Myung, N. V.; Choa, Y.-H. Thermochemical Hydrogen Sensor Based on Chalcogenide Nanowire Arrays. *Nanotechnology* **2015**, *26* (14), 145503. https://doi.org/10.1088/0957-4484/26/14/145503.

(18) Yu, J.; Yu, X.; Zhang, L.; Zeng, H. Ammonia Gas Sensor Based on Pentacene Organic Field-Effect Transistor. *Sens. Actuators B Chem.* **2012**, *173*, 133–138. https://doi.org/10.1016/j.snb.2012.06.060.

(19) Han, J.-W.; Rim, T.; Baek, C.-K.; Meyyappan, M. Chemical Gated Field Effect Transistor by Hybrid Integration of One-Dimensional Silicon Nanowire and Two-Dimensional Tin Oxide Thin Film for Low Power Gas Sensor. *ACS Appl. Mater. Interfaces* **2015**, *7* (38), 21263–21269. https://doi.org/10.1021/acsami.5b05479.

(20) Gautschi, G. Piezoelectric Sensors. In *Piezoelectric Sensorics*; Springer Berlin Heidelberg: Berlin, Heidelberg, 2002; pp 73–91. https://doi.org/10.1007/978-3-662-04732-3_5.

(21) Germain, M. E.; Knapp, M. J. Optical Explosives Detection: From Color Changes to Fluorescence Turn-On. *Chem. Soc. Rev.* **2009**, *38* (9), 2543. https://doi.org/10.1039/b809631g.

(22) Salinas, Y.; Martínez-Máñez, R.; Marcos, M. D.; Sancenón, F.; Costero, A. M.; Parra, M.; Gil, S. Optical Chemosensors and Reagents to Detect Explosives. *Chem Soc Rev* **2012**, *41* (3), 1261–1296. https://doi.org/10.1039/C1CS15173H.

(23) Sun, X.; Wang, Y.; Lei, Y. Fluorescence Based Explosive Detection: From Mechanisms to Sensory Materials. *Chem. Soc. Rev.* **2015**, *44* (22), 8019–8061. https://doi.org/10.1039/C5CS00496A.

(24) Janzen, M. C.; Ponder, J. B.; Bailey, D. P.; Ingison, C. K.; Suslick, K. S. Colorimetric Sensor Arrays for Volatile Organic Compounds. *Anal. Chem.* **2006**, *78* (11), 3591–3600. https://doi.org/10.1021/ac052111s.

(25) Rakow, N. A.; Suslick, K. S. A Colorimetric Sensor Array for Odour Visualization. *Nature* **2000**, *406* (6797), 710–713. https://doi.org/10.1038/35021028.

(26) Thomas, S. W.; Joly, G. D.; Swager, T. M. Chemical Sensors Based on Amplifying Fluorescent Conjugated Polymers. *Chem. Rev.* **2007**, *107* (4), 1339–1386. https://doi.org/10.1021/cr0501339.

(27) Shi, B.; Li, W.; Qin, P.; Zhao, X.-X.; Qi, X.-N.; Chai, Y.; Yang, H.-H.; Qu, W.-J.; Yao, H.; Zhang, Y.-M.; Wei, T.-B.; Lin, Q. A Selective and Stable Vapochromic System Constructed by Pillar[5]Arene-Based Host–Guest Interactions. *Dyes Pigments* **2022**, *197*, 109885. https://doi.org/10.1016/j.dyepig.2021.109885.

(28) Martini, G.; Martinelli, E.; Ruggeri, G.; Galli, G.; Pucci, A. Julolidine Fluorescent Molecular Rotors as Vapour Sensing Probes in Polystyrene Films. *Dyes Pigments* **2015**, *113*, 47–54. https://doi.org/10.1016/j.dyepig.2014.07.025.

(29) Ahmad, M.; Platonova, I.; Battisti, A.; Minei, P.; Brancato, G.; Pucci, A. Highly Selective Vapochromic Fluorescence of Polycarbonate Films Doped with an ICT-Based Solvatochromic Probe. *J. Polym. Sci. Part B Polym. Phys.* **2017**, *55* (15), 1171–1180. https://doi.org/10.1002/polb.24367.

(30) Minei, P.; Koenig, M.; Battisti, A.; Ahmad, M.; Barone, V.; Torres, T.; Guldi, D. M.; Brancato, G.; Bottari, G.; Pucci, A. Reversible Vapochromic Response of Polymer Films Doped with a Highly Emissive Molecular Rotor. *J Mater Chem C* **2014**, *2* (43), 9224–9232. https://doi.org/10.1039/C4TC01737D.

(31) Minei, P.; Pucci, A. Fluorescent Vapochromism in Synthetic Polymers. *Polym. Int.* **2016**, *65* (6), 609–620. https://doi.org/10.1002/pi.5105.

(32) Sorgi, C.; Martinelli, E.; Galli, G.; Pucci, A. Julolidine-Labelled Fluorinated Block Copolymers for the Development of Two-Layer Films with Highly Sensitive Vapochromic Response. *Sci. China Chem.* **2018**, *61* (8), 947–956. https://doi.org/10.1007/s11426-018-9302-6.

(33) Hong, Y.; Lam, J. W. Y.; Tang, B. Z. Aggregation-Induced Emission. *Chem. Soc. Rev.* **2011**, *40* (11), 5361. https://doi.org/10.1039/c1cs15113d.

(34) Lova, P.; Bastianini, C.; Giusto, P.; Patrini, M.; Rizzo, P.; Guerra, G.; Iodice, M.; Soci, C.; Comoretto, D. Label-Free Vapor Selectivity in Poly(*p* -Phenylene Oxide) Photonic Crystal Sensors. *ACS Appl. Mater. Interfaces* **2016**, *8* (46), 31941–31950. https://doi.org/10.1021/acsami.6b10809.

(35) Lionte, C. Lethal Complications after Poisoning with Chloroform — Case Report and Literature Review. *Hum. Exp. Toxicol.* **2010**, *29* (7), 615–622. https://doi.org/10.1177/0960327109357142.

(36) Zhang, X.-P.; Yuan, Q.; Qi, Y.-L.; Zheng, D.-J.; Liu, Q.-X.; Wang, B.-Z.; Yang, Y.-S.; Zhu, H.-L. An Umbelliferone-Derivated Fluorescent Sensor for Selective Detection of Palladium(II) from Palladium(0) in Living Cells. *Spectrochim. Acta. A. Mol. Biomol. Spectrosc.* **2019**, *220*, 117134. https://doi.org/10.1016/j.saa.2019.05.039.

(37) Liu, M.; Chen, L.; Shan, P.; lian, C.; Zhang, Z.; Zhang, Y.; Tao, Z.; Xiao, X. Pyridine Detection Using Supramolecular Organic Frameworks Incorporating Cucurbit[10]Uril. *ACS Appl. Mater. Interfaces* **2021**, *13* (6), 7434–7442. https://doi.org/10.1021/acsami.0c20292.

(38) Che, S.; Shou, Q.; Fan, Y.; Peng, X.; Zhou, C.; Fu, H.; She, Y. Fluorescent Ionic Liquid Membranes Based on Coumarin for the Real-Time and Visual Detection of Gaseous SO $_2$. *ACS Sustain. Chem. Eng.* **2022**, *10* (8), 2784–2792. https://doi.org/10.1021/acssuschemeng.1c08119.

(39) Krauter, C. M.; Möhring, J.; Buckup, T.; Pernpointner, M.; Motzkus, M. Ultrafast Branching in the Excited State of Coumarin and Umbelliferone. *Phys. Chem. Chem. Phys.* **2013**, *15* (41), 17846. https://doi.org/10.1039/c3cp52719k.

(40) Nagendra, B.; Cozzolino, A.; Daniel, C.; Rizzo, P.; Guerra, G.; Auriemma, F.; De Rosa, C.; D'Alterio, M. C.; Tarallo, O.; Nuzzo, A. Two Nanoporous Crystalline Forms of Poly(2,6-Dimethyl-1,4-Phenylene)Oxide and Related Co-Crystalline Forms. *Macromolecules* **2019**, *52* (24), 9646–9656. https://doi.org/10.1021/acs.macromol.9b01911.

(41) Rizzo, P.; Gallo, C.; Vitale, V.; Tarallo, O.; Guerra, G. Nanoporous-Crystalline Films of PPO with Parallel and Perpendicular Polymer Chain Orientations. *Polymer* **2019**, *167*, 193–201. https://doi.org/10.1016/j.polymer.2019.01.073.

(42) Perel'son, M. E.; Sheinker, Yu. N. Spectra and Structure of Hydroxycoumarin and Hydroxyfurocoumarin Salts. *J. Appl. Spectrosc.* **1966**, *5* (1), 78–82. https://doi.org/10.1007/BF00604656.

(43) Cozzolino, A.; Monaco, G.; Daniel, C.; Rizzo, P.; Guerra, G. Monomeric and Dimeric Carboxylic Acid in Crystalline Cavities and Channels of Delta and Epsilon Forms of Syndiotactic Polystyrene. *Polymers* **2021**, *13* (19), 3330. https://doi.org/10.3390/polym13193330.

(44) Hamilton, G.; Sanabria, H. Multiparameter Fluorescence Spectroscopy of Single Molecules. In *Spectroscopy and Dynamics of Single Molecules*; Elsevier, 2019; pp 269–333. https://doi.org/10.1016/B978-0-12-816463-1.00006-7.

(45) Alekseev, A. S.; Konforkina, T. V.; Savransky, V. V.; Kovalenko, M. F.; Jutila, A.; Lemmetyinen, H. Langmuir-Blodgett Films of a Rigidified 7-Aminocoumarin Derivative and

Their Absorption and Emission Properties. *Langmuir* **1993**, *9* (2), 376–380. https://doi.org/10.1021/la00026a003.

(46) Nizomov, N.; Kholov, A. U.; Ishchenko, A. A.; Ishchenko, V. V.; Khilya, V. P. Electronic Structure and Spectral Fluorescence Properties of Umbelliferone and Herniarin. *J. Appl. Spectrosc.* **2007**, *74* (5), 626–634. https://doi.org/10.1007/s10812-007-0102-z.

(47) Allen, F. H.; Wood, P. A.; Galek, P. T. A. Role of Chloroform and Dichloromethane Solvent Molecules in Crystal Packing: An Interaction Propensity Study. *Acta Crystallogr. Sect. B Struct. Sci. Cryst. Eng. Mater.* **2013**, *69* (4), 379–388. https://doi.org/10.1107/S2052519213015078.

(48) Huila, M. F. G.; Parussulo, A. L. A.; Armas, L. E. G.; Peres, H. E. M.; Seabra, A. C.; Ramirez-Fernandez, F. J.; Araki, K.; Toma, H. E. Laser Patterning a Chem-FET Like Device on a V_2O_5 Xerogel Film. *IEEE Sens. J.* **2018**, *18* (4), 1358–1363. https://doi.org/10.1109/JSEN.2017.2786082.

(49) Ingle, N.; Sayyad, P.; Bodkhe, G.; Mahadik, M.; AL-Gahouari, T.; Shirsat, S.; Shirsat, M. D. ChemFET Sensor: Nanorods of Nickel-Substituted Metal–Organic Framework for Detection of SO2. *Appl. Phys. A* **2020**, *126* (9), 723. https://doi.org/10.1007/s00339-020-03907-6.

(50) Qi, J.; Xu, X.; Liu, X.; Lau, K. T. Fabrication of Textile Based Conductometric Polyaniline Gas Sensor. *Sens. Actuators B Chem.* **2014**, *202*, 732–740. https://doi.org/10.1016/j.snb.2014.05.138.

(51) Korotcenkov, G.; Han, S. H.; Cho, B. K. Material Design for Metal Oxide Chemiresistive Gas Sensors. *J. Sens. Sci. Technol.* **2013**, *22* (1), 1–17. https://doi.org/10.5369/JSST.2013.22.1.1.

(52) Joshi, N.; Hayasaka, T.; Liu, Y.; Liu, H.; Oliveira, O. N.; Lin, L. A Review on Chemiresistive Room Temperature Gas Sensors Based on Metal Oxide Nanostructures, Graphene and 2D Transition Metal Dichalcogenides. *Microchim. Acta* **2018**, *185* (4), 213. https://doi.org/10.1007/s00604-018-2750-5.

(53) Yang, B.; Myung, N. V.; Tran, T. 1D Metal Oxide Semiconductor Materials for Chemiresistive Gas Sensors: A Review. *Adv. Electron. Mater.* **2021**, *7* (9), 2100271. https://doi.org/10.1002/aelm.202100271.

(54) Rao, B. M.; Roy, S. C. Chemi-Capacitive Gas Sensors Based on TiO_2 and $BaTiO_3$ Nanotube Arrays. *Sens. Lett.* **2018**, *16* (2), 100–104. https://doi.org/10.1166/sl.2018.3922.

(55) Dissanayake, S.; Vanlangenberg, C.; Patel, S. V.; Mlsna, T. Conducting Absorbent Composite for Parallel Plate Chemicapacitive Microsensors with Improved Selectivity. *Sens. Actuators B Chem.* **2015**, *206*, 548–554. https://doi.org/10.1016/j.snb.2014.09.069.

(56) Chowdhury, N. K.; Bhowmik, B. Micro/Nanostructured Gas Sensors: The Physics behind the Nanostructure Growth, Sensing and Selectivity Mechanisms. *Nanoscale Adv.* **2021**, *3* (1), 73–93. https://doi.org/10.1039/D0NA00552E.

(57) Ghosh, S.; Rajan, L. Zinc Oxide Thin-Film Transistor with Catalytic Electrodes for Hydrogen Sensing at Room Temperature. *IEEE Trans. Nanotechnol.* **2021**, *20*, 303–310. https://doi.org/10.1109/TNANO.2021.3068994.

(58) Bhowmik, B. Comparative Study of Thin-Film-Based Planar and Vertical Devices Towards Isopropyl Alcohol Sensing. *J. Electron. Mater.* **2019**, *48* (11), 7292–7301. https://doi.org/10.1007/s11664-019-07554-3.

(59) Samnakay, R.; Jiang, C.; Rumyantsev, S. L.; Shur, M. S.; Balandin, A. A. Selective Chemical Vapor Sensing with Few-Layer MoS $_2$ Thin-Film Transistors: Comparison with Graphene Devices. *Appl. Phys. Lett.* **2015**, *106* (2), 023115. https://doi.org/10.1063/1.4905694.

(60) Agarwal, M.; Balachandran, M. D.; Shrestha, S.; Varahramyan, K. SnO $_2$ Nanoparticle-Based Passive Capacitive Sensor for Ethylene Detection. *J. Nanomater.* **2012**, *2012*, 1–5. https://doi.org/10.1155/2012/145406.

(61) Zhang, Y.; Musselman, I. H.; Ferraris, J. P.; Balkus, K. J. Gas Permeability Properties of Matrimid® Membranes Containing the Metal-Organic Framework Cu–BPY–HFS. *J. Membr. Sci.* **2008**, *313* (1–2), 170–181. https://doi.org/10.1016/j.memsci.2008.01.005.

(62) Tsuchitani, S.; Sugawara, T.; Kinjo, N.; Ohara, S.; Tsunoda, T. A Humidity Sensor Using Ionic Copolymer and Its Application to a Humidity-Temperature Sensor Module. *Sens. Actuators* **1988**, *15* (4), 375–386. https://doi.org/10.1016/0250-6874(88)81507-5.

(63) Shibata, H.; Ito, M.; Asakursa, M.; Watanabe, K. A Digital Hygrometer Using a Polyimide Film Relative Humidity Sensor. *IEEE Trans. Instrum. Meas.* **1996**, *45* (2), 564–569. https://doi.org/10.1109/19.492788.

(64) Ong, K.; Grimes, C. A Carbon Nanotube-Based Sensor for CO2 Monitoring. *Sensors* **2001**, *1* (6), 193–205. https://doi.org/10.3390/s10600193.

(65) Liu, X.; Cheng, S.; Liu, H.; Hu, S.; Zhang, D.; Ning, H. A Survey on Gas Sensing Technology. *Sensors* **2012**, *12* (7), 9635–9665. https://doi.org/10.3390/s120709635.

(66) Zhou, X.; Lee, S.; Xu, Z.; Yoon, J. Recent Progress on the Development of Chemosensors for Gases. *Chem. Rev.* **2015**, *115* (15), 7944–8000. https://doi.org/10.1021/cr500567r.

(67) Patel, S. V.; Mlsna, T. E.; Fruhberger, B.; Klaassen, E.; Cemalovic, S.; Baselt, D. R. Chemicapacitive Microsensors for Volatile Organic Compound Detection. *Sens. Actuators B Chem.* **2003**, *96* (3), 541–553. https://doi.org/10.1016/S0925-4005(03)00637-3.

(68) Chowdhury, N. K.; Bhowmik, B. Au/TiO $_2$ Nanotube/Ti Chemicapacitive Devices: An Approach for Optimal Gas Sensing. *IEEE Trans. Nanotechnol.* **2022**, *21*, 143–150. https://doi.org/10.1109/TNANO.2022.3154590.

(69) Daniel, C.; Rizzo, P.; Nagendra, B.; Cozzolino, A.; Guerra, G. High Diffusivity Dense Films of a Nanoporous-Crystalline Polymer. *Polymer* **2021**, *229*, 124005. https://doi.org/10.1016/j.polymer.2021.124005.

(70) Cozzolino, A.; Nagendra, B.; Rizzo, P.; Daniel, C.; Guerra, G. Fast Uptake of Organic Pollutants from Dilute Aqueous Solutions by Nanoporous-Crystalline PPO Films with c-Perpendicular Orientation. *Eur. Polym. J.* **2021**, *161*, 110864. https://doi.org/10.1016/j.eurpolymj.2021.110864.

(71) Unsal, V.; Cicek, M.; Sabancilar, İ. Toxicity of Carbon Tetrachloride, Free Radicals and Role of Antioxidants. *Rev. Environ. Health* **2021**, *36* (2), 279–295. https://doi.org/10.1515/reveh-2020-0048.

(72) Chae, Y.; Cui, R.; Moon, J.; An, Y.-J. Ecological Hazard Assessment of Methyl Ethyl Ketone Using the Species Sensitivity Distribution Approach in a Soil Ecosystem. *J. Hazard. Mater.* **2018**, *360*, 490–497. https://doi.org/10.1016/j.jhazmat.2018.08.026.

(73) Chen, L. F.; Ong, C. K.; Neo, C. P.; Varadan, V. V.; Varadan, V. K. *Microwave Electronics: Measurement and Materials Characterization*, 1st ed.; Wiley, 2004. https://doi.org/10.1002/0470020466.

(74) Savchenko, V. V.; Levin, V. V.; Shakhparonov, M. I. Dielectric Properties of Methyl Ethyl Ketone-Chloroform Solutions. *J. Struct. Chem.* **1972**, *12* (6), 999–1002. https://doi.org/10.1007/BF00744173.

(75) Sengwa, R. J.; Khatri, V.; Sankhla, S. Static Dielectric Constants and Kirkwood Correlation Factor of the Binary Mixtures of N-Methylformamide with Formamide, N,N-Dimethylformamide and N,N-Dimethylacetamide. *J. Solut. Chem.* **2009**, *38* (6), 763–769. https://doi.org/10.1007/s10953-009-9408-1.

CONCLUDING REMARKS

In this section, the formation of two well-separated NC forms of PPO, named α and β, has been explained. The NC α and β forms not only exhibit different chain packing but also slightly different chain conformations (***c*** = 5.28 and 5.47 Å, respectively).

WAXD and FTIR measurements have shown that most of the guest molecules lead only to α or β CC (and related NC) forms, independently of the crystallization procedure (solution casting and solvent-induced crystallization of amorphous films). Only for few guest molecules (i.e., methyl benzoate and acetone) α or β CC and NC forms are obtained depending on the crystallization conditions.

Additionally, independently of the two considered crystallization methods, the α-form is favored by hydrophobic (with solubility lower than 0.11 mmol per 100 mL of water) and bulky guest molecules (with molecular volumes higher than 230 $Å^3$) while the β-form (being characterized by a higher chain periodicity) is favored by hydrophilic (with solubility higher than 2 mmol per 100 mL of water) and small guest molecules (with molecular volumes lower than 149 $Å^3$).

Another important aspect which has been point out is the strong influence on guest diffusivity due to the kind of orientation of NC PPO α phases, with respect to the film plane. In particular, NC PPO films exhibit diffusivity of the pollutant perchloroethylene from vapors as well as from aqueous solutions, when the orientation of NC phases is preferentially perpendicular to the film plane ($c_\perp$ orientation), diffusivity values are higher than for films with $c_{//}$ orientation and much higher than NC sPS films.

Moreover, guest uptakes for NC $c_\perp$ PPO films, when expressed as mass of guest per polymer volume, are also much higher than for NC PPO powders and aerogels. This advantage becomes very important considering that for most purification processes the limiting factor is the volume of the absorbent material.

An additional remarkable advantage of NC forms of PPO with respect NC forms of sPS is their much higher thermal stability. In fact, both NC forms of sPS transform into the dense γ-form after thermal treatments at temperatures higher than 80–90 °C while both NC forms of PPO are stable at least up to 150–180 °C. This allows thermal regeneration of the NC PPO forms, for most absorbed guests.

Furthermore, it has been found that guest diffusivity values in the high surface area NC PPO films (up to 620 $m^2\ g^{-1}$) are much higher even than for the $c_\perp$ oriented NC PPO films, for sorption both from vapor phase and from diluted aqueous solutions. Although the present analysis is confined to PCE, the above conclusions can be considered general for many organic pollutants like, e.g., aliphatic and aromatic hydrocarbons or other halogenated hydrocarbons.

These features make PPO films (especially with high surface area) very suitable for air and water purification.

In addition, preliminary results about potential gas sensors based on PPO films/coatings have been reported. Two approaches have been proposed based on the transduction methods: electrical and optical.

About electrical approach, a potential gas sensor based on a metal insulator semiconductor has been proposed. This device has been realized depositing a PPO coating (≈1μm) as dielectric material between two metal contacts (i.e., gold), in order to form a capacitor, the principal working element of the device itself. When it is exposed to different gases (i.e., methyl ethyl ketone and carbon tetrachloride), a diverse response pattern has been achieved, therefore a discrimination among volatile chemicals seems to be possible.

As concern optical approach, PPO films (≈40μm) containing 1–2 wt% of the fluorophore umbelliferone has been tested in saturated chloroform vapours. Once exposed to these vapours, fluorescence rapidly turned on within the first minutes thanks to the solvation effect provided by the polar vapours. Such fluorescence response has appeared also to be reversible for many cycles.

The whole set of data, about these gas sensors mechanisms, has suggested that PPO films/coatings can be very suitable for developing new advanced indicators for detection of harmful volatile organic compound vapours.

PART II

Results and Discussion about advances in the study on syndiotactic Polystyrene

CHAPTER 4

Co-crystalline forms of sPS with carboxylic acids

In this chapter, NC axially oriented sPS films with δ cavities and ε channels have been prepared and sorption of carboxylic acids has been studied. The aim of this work is to investigate the possibility to form co-crystalline (CC) forms with carboxylic acids and the interactions involved in these CC forms. In particular, the analysis started with the monocarboxylic hexanoic acid (HA), a molecule with six carbon atoms in the aliphatic chain which it is suitable to be absorbed by both crystalline phases. Then, it moved to explore longer aliphatic chains, i.e., lauric acid (LA, 12 C) and stearic acid (SA, 18 C) as well as the dicarboxylic adipic acid (AA, 6C), in order to verify if they are appropriate to be accommodated especially in ε channels. Finally, the study ended with the investigation on benzoic acid (BA), the simplest carboxylic aromatic acid.

The reported results mainly refer to axially stretched sPS films (with a draw ratio of 4 and degree of crystallinity in the range 25–30%), because they allow to obtain WAXD fiber patterns and polarized FTIR spectra, which are the most suitable techniques to establish the possible formation of polymer CC phases.[1] Data has been collected also considering the (denser) crystalline gamma (γ) and mesomorphic phases, where the sorption is allowed only in their amorphous phase. Guest uptakes from these semicrystalline sPS films were evaluated by FTIR spectra[2] as calibrated by TGA analyses.

4.1 Sorption of Hexanoic Acid (HA)

HA is the simplest aliphatic carboxylic acid considered in this study; it has six carbon atoms with one carbonyl group and one hydroxyl group. Moreover, it shows an antimicrobial activity against *E. coli* and *S. aureus*,[3] as well as an antifungal activity on *Botrytis cinerea*.[4]

4.1.1 FTIR analysis of CC sPS/HA

FTIR spectra of a 50 μm axially stretched γ-form film, after sorption of HA in different conditions, are shown in Figure 4.1. The uptake of HA, as evaluated based on the intensity of the carbonyl stretching peak at 1709 cm^{-1} (Figure 4.1c), after 12h of film immersion in liquid HA at 70 °C, is about 2 wt% (Figure 4.1a). The temperature of 70 °C was needed to have a stronger experimental condition, because the sorption at room temperature (≈20 °C) also for long time was negligible. HA uptake can be increased by immersion of the film in solutions of the acid in volatile carrier solvents. For instance, after 12h of film immersion in HA 40 wt% acetone solution at room temperature, followed by acetone desorption at 60 °C for 60 min, the HA uptake in the film is of 3.3 wt% (Figure 4.1b). It is worth noting that HA uptake from γ form films provides information on the HA uptake in the amorphous phase. In fact, γ-form (differently from δ and ε forms) is a dense form, and sorption of HA molecules is allowed only in the amorphous phase.

FTIR spectra of a 60 μm axially oriented δ-form film, after sorption of HA in two different conditions, are shown in Figure 4.2. The most relevant feature of these spectra is that two additional guest peaks clearly appear: a carbonyl stretching at 1751 cm^{-1}, as well as a O−H stretching peak at 3443 cm^{-1}, which is in the typical region of carboxylic acids at low concentration.[5] Both peaks are broad and barely detectable for the HA molecules absorbed in the amorphous phase. Based on an analogy with other carboxylic acids,[6–11] and in agreement with a report from Kaneko and co-workers,[2] these new peaks can be attributed to isolated guest molecules, while the peak at 1709 cm^{-1} can be attributed to hydrogen-bonded guest molecules.

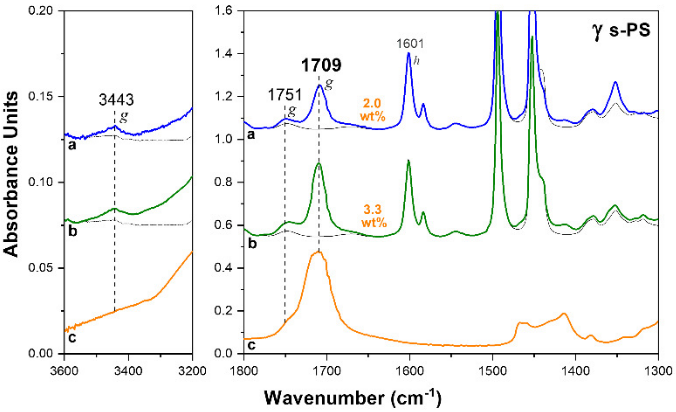

Figure 4.1 FTIR spectra of an axially oriented γ-form sPS film after immersion in: (a) HA at 70 °C for 12h; (b) 40 wt% solution of HA in acetone at room temperature for 12h, followed by acetone desorption at 60 °C for 1h. The uptake of HA in the film (expressed as wt%) is indicated close to the spectra. The FTIR spectrum of liquid HA is shown for comparison in (c).

In this framework, it is reasonable to assume that isolated and hydrogen-bonded HA molecules (with carbonyl peak at 1751 cm^{-1} and 1709 cm^{-1}) are mainly enclosed as guests in the crystalline cavities and in the amorphous phase of the δ-form film, respectively.

The HA uptake by the NC δ-form film (Figure 4.2) is much higher than for the γ-form film (Figure 4.1). In fact, by considering the intensity of both carbonyl stretching peaks, after 12h of immersion in the liquid at 70 °C, the HA uptake is 7.1 wt% (Figure 4.2a), i.e., ≈4 times higher than for the γ-form film, while, after immersion in HA solution in acetone at room temperature, the HA uptake is 7.7 wt% (Figure 4.2b), i.e., ≈2.5 times higher than for the γ-form film subjected to a similar treatment.

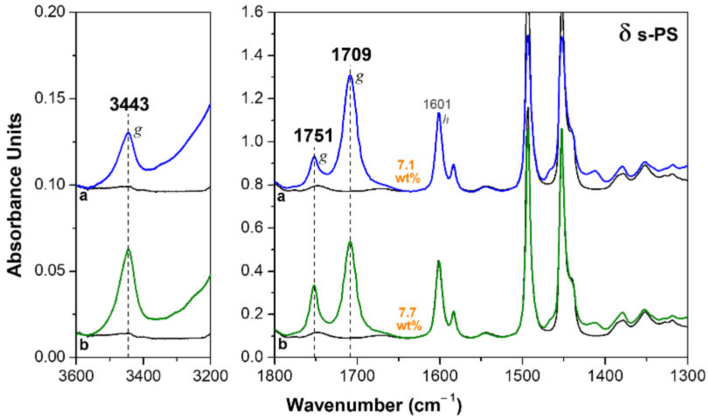

Figure 4.2 FTIR spectra of an axially oriented δ-form sPS film, after immersion in: (a) HA at 70 °C for 12h; (b) 40 wt% solution of HA in acetone at room temperature for 12h, followed by acetone desorption at 60 °C for 1h. The uptake of HA in the film (expressed as wt%) is indicated close to the spectra.

The HA sorption from NC films exhibiting the ε-form is much faster, as shown in Figure 4.3, due to the presence of empty space organized as channels.[12–15] As an example, only 10 min of immersion of a 120 μm thick film in a 40 wt% solution of HA in acetone, at room temperature, are sufficient to reach a HA uptake of 3.2 wt% (Figure 4.3a). After 2h of immersion, the HA uptake is higher than 12 wt%.

It is worth adding that the spectra of ε-form films (Figure 4.3), even in the absence of thermal treatments, do not exhibit absorbance peaks of acetone. The γ and δ form films, on the contrary, exhibit an intense acetone absorbance carbonyl peak at 1718 cm^{-1} (not shown here) before acetone removal by suitable thermal treatments (at 60 °C, as reported above for spectra of Figures 4.1 and 4.2). Hence, in the crystalline channels of the ε-form, the fast HA sorption does not allow significant sorption of acetone carrier molecules.

As already observed for the δ-form films (Figure 4.2), for the ε-form film the uptake of the HA generates the additional carbonyl peak at 1751 cm^{-1} and hydroxyl peak at 3443 cm^{-1}, which correspond to isolated HA molecules being enclosed in the empty space of the NC ε phase (Figure 4.3). Quantitative information on the amount of acid present as a monomer or dimer has been obtained by peak fitting, coupled with DFT calculations of molar extinction coefficients of the carbonyl signals.

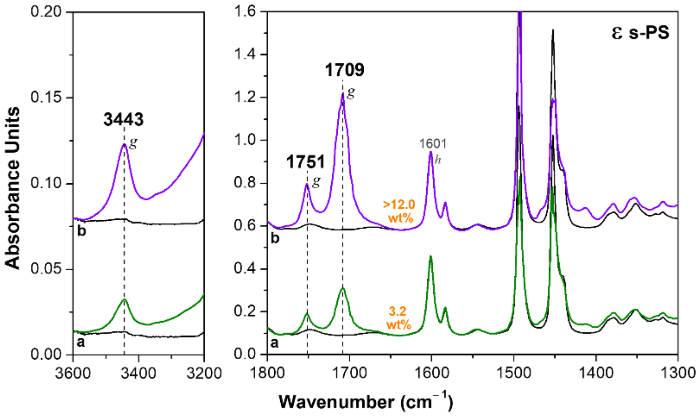

Figure 4.3 FTIR spectra of an axially oriented ε-form sPS film, after immersion in a 40 wt% solution of HA in acetone at room temperature: (a) for 10 min; (b) for 2h. The uptake of HA in the film (expressed as wt%) is indicated close to the spectra.

Calculations give access to a molar extinction coefficient, and then it is possible to compute the ratio $\frac{\varepsilon^{dim}_{1709}}{\varepsilon^{mon}_{1751}} = 2.43$, larger than the value of 2 expected for two uncoupled carbonyl groups. A fitting as a sum of Lorentzian peaks was performed on the FTIR spectra recorded with unpolarized light on the samples of Figures 4.2b and 4.3a for δ and ε films, respectively, as well as on the NC sPS forms (without HA guest). In the region of absorption of the monomer (1800–1750 cm^{-1}), a feeble peak of the host polymer is present (small band located at 1748 cm^{-1}). Then, spectral subtraction was performed, taking care of the different thicknesses of the films, as estimated by the integrated absorbance of the 1601 cm^{-1} peak. Eventually, the percentages of acid absorbed as monomer are estimated from the ratio of integrated absorbances of the peaks at 1751 and 1709 cm^{-1}, corrected for host absorption and the DFT-derived ratio of molar extinction, as the following formula:

$$r_{\text{mon}} = \frac{\frac{1}{2}\frac{\varepsilon^{dim}_{1709}}{\varepsilon^{mon}_{1751}}\left(I^{p+\text{HA}}_{1751} - I^{p}_{1751}\frac{I^{p+\text{HA}}_{1601}}{I^{p}_{1601}}\right)}{I^{p+\text{HA}}_{1709}} \qquad (4.1)$$

where the superscript p stands for either δ or ε sPS phases.

The molar fraction can be computed as follows: $x_{\text{mon}} = {}^{r_{\text{mon}}}/_{1+r_{\text{mon}}}$.

Results are present in Table 4.1. It is apparent that there is a higher amount of HA isolated guest molecules (almost 3 times higher) in the δ phase, i.e., the NC phase presenting isolated cavities, with respect to that absorbed in ε phase, in which the empty space is organized as channels and hence it seems to be more suitable to absorb hydrogen-bonded HA molecules than isolated guests.

Table 4.1 Integrated absorbances (in cm^{-1}) obtained by non-linear least square fitting of the spectra as sum of Lorentzian peaks, and the derived percentage of isolated guest HA molecules.

Form	I_{1601}	I_{1709}	I_{1751}	%mon
δ	17.8	-	2.0	
δ + HA	15.2	30.7	12.7	43
ε	29.2	-	6.3	
ε + HA	33.2	35.6	11.2	14

Polarized FTIR spectra for 3600−3200 cm^{-1} and 1800−1500 cm^{-1} regions of axially oriented γ, δ and ε sPS films, which exhibit similar intensity of the guest peak at 1709 cm^{-1}, are shown in Figure 4.4. The HA uptake is close to 3.5 wt% for the γ-form film while it is close to 7 wt% for both δ and ε form films.

The intensity differences between peaks collected with polarization planes parallel or perpendicular to the film-stretching direction (blue and red spectra, respectively) clearly show the presence of dichroism of the peaks of the host polymer. The orientation factor S_p, as evaluated on the basis of the dichroism of the crystalline peak at 572 cm^{-1}, is for the three films in the range 0.83−0.88.

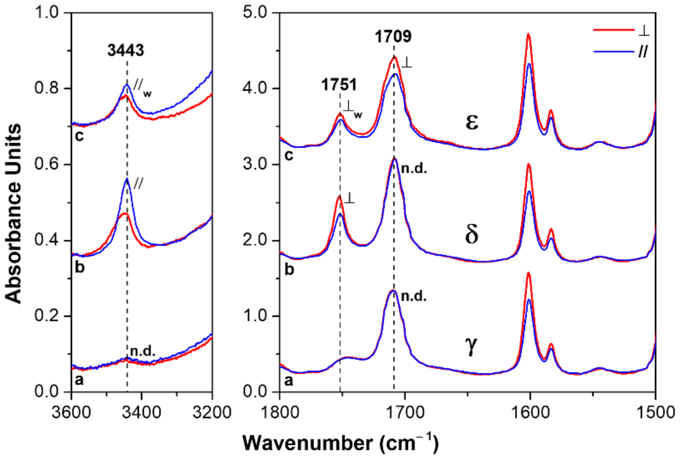

Figure 4.4 Polarized FTIR spectra as taken with polarization plane parallel (blue lines) and perpendicular (red lines) to the film-stretching direction, for two spectral ranges (3600–3200 cm^{-1} and 1800–1500 cm^{-1}), for axially oriented sPS semicrystalline films exhibiting different crystalline phases, after comparable uptake of HA guest molecules: (a) γ-form; (b) δ-form: (c) ε-form.

As for the HA guest peaks, dependent on the polymer crystalline form, some dichroism can be observed for the carbonyl stretching peaks at 1751 and 1709 cm^{-1}, as well as for the hydroxyl peak at 3443 cm^{-1}. In particular, the dichroism is absent for molecules absorbed by the γ-form film (Figure 4.4a), thus confirming that HA molecules are not absorbed by the dense γ phase, but only absorbed in the poorly oriented amorphous phase. As for the δ-form film (Figure 4.4b), significant dichroism is observed for the vibrational peaks corresponding to isolated HA molecules ($S_{m,1751,\delta} = -0.11$ and $S_{m,3443,\delta} = +0.24$), while no dichroism is observed for the hydrogen-bonded HA molecules. This confirms the previous hypothesis that isolated HA molecules are guests of the more oriented crystalline phase, while hydrogen-bonded HA molecules are guests of the less oriented amorphous phase.[16,17]

The dichroic behavior of peaks of HA guest molecules absorbed in the NC ε-form films is completely different (Figure 4.4c). In fact, the dichroism of the carbonyl peak of hydrogen-bonded HA molecules ($S_{d,1709,\varepsilon} = -0.06$) is similar to those of the peaks corresponding to isolated guest molecules ($S_{m,1751,\varepsilon} = -0.07$ and $S_{m,3443,\varepsilon} = +0.10$). These data can be rationalized by assuming that the structural channels of the ε-form are able to host not only isolated HA molecules but also HA dimers.

The sorption of HA, both as a monomer and dimer, in the crystalline channels of the ε-form can also rationalize the exceptionally high and fast HA uptake from these semicrystalline films.

It is worth noting that the dichroism of the O−H stretching for HA isolated guest in both δ and ε phases is positive, indicating a preferential orientation of the O−H bond parallel to the crystalline polymer chain axis, independent of the kind of NC phase. Moreover, the dichroism of the C=O stretching for the isolated HA guest in the δ-form, and for both isolated and dimeric HA guests in the ε-form, are always negative, indicating a preferential orientation of the C=O bond perpendicular to the crystalline polymer chain axis.

These orientations of the O–H and C=O groups, preferentially parallel and perpendicular to the polymer chain axis, respectively, can be easily rationalized for HA guest molecules in the crystalline channels of the ε-form. In fact, these preferential orientations can be anticipated on the basis of two obvious structural features: (i) parallelism of the aliphatic chains (in their trans-planar conformation) with respect to the chain axes of the polymer crystalline phase; (ii) minimum energy conformation of aliphatic carboxylic acids, which exhibit the double bonded carboxyl-oxygen atom in an eclipsed position with respect to the β carbon atom.[18] This is shown for monomeric and dimeric HA species in the crystalline channels of the ε-form by the schematic drawings of Figure 4.5A and 4.5B, respectively.

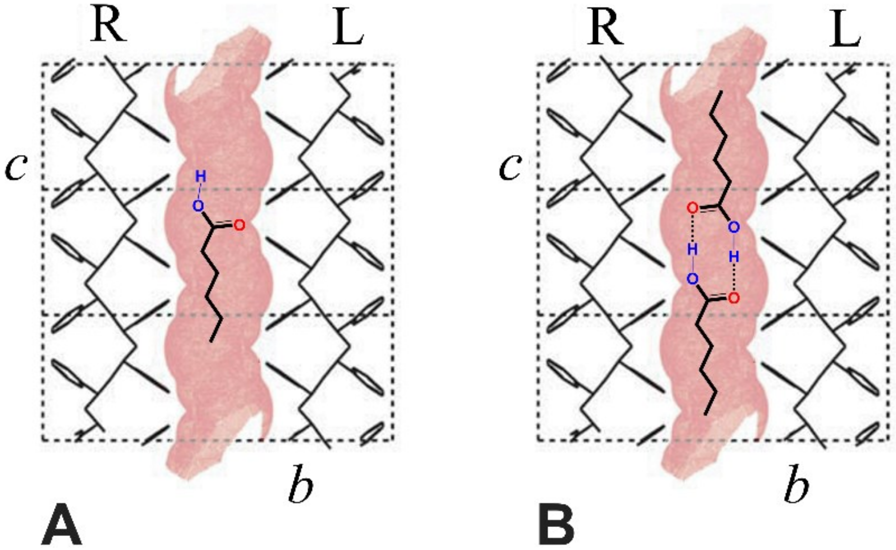

Figure 4.5 Schematic presentation of isolated (A) and dimeric (B) HA species in the crystalline channels of the ε-form. The parallelism of the aliphatic chain with respect to the chain axis and the minimum energy conformation of the carboxylic groups (C=O eclipsed) are able to rationalize the orientations of O−H and C=O groups, preferentially parallel and perpendicular to the polymer chain crystalline axes, respectively, as established by FTIR linear dichroism measurements.

Additional relevant information comes by studies of HA desorption from CC sPS films, e.g., at room temperature in air. In fact, the ratio between the two peaks corresponding to isolated and hydrogen-bonded HA molecules (I_{1751}/I_{1709}) increases with desorption time. This phenomenon, which occurs for both δ and ε form films, is shown for the ε-form film (left scale in Figure 4.6) and can easily be rationalized by guest desorption from amorphous sPS phases occurring faster than from CC phases.[1,19,20]

The increase in the dichroic ratio of the 1709 cm^{-1} peak (right scale in Figure 4.6), with guest desorption time, for the ε-form film is also interesting. This phenomenon can, again, be rationalized by the easier desorption of hydrogen-bonded HA from the less-oriented amorphous phase with respect to hydrogen-bonded HA dimer from the more oriented ε phase.

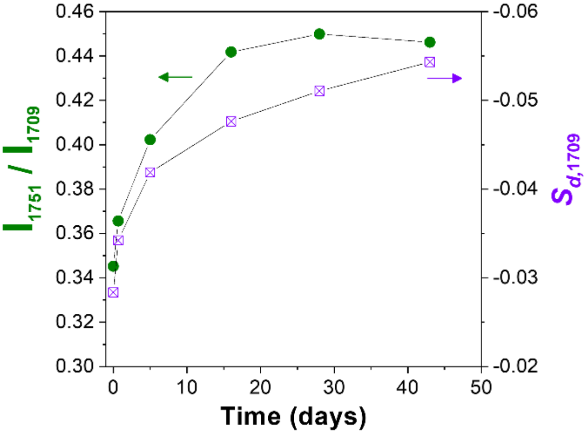

Figure 4.6 Intensity ratio of the two carbonyl peaks I_{1751}/I_{1709}, corresponding to isolated and hydrogen bonded HA guest molecules (left scale and green circles), and dichroism of the 1709 cm^{-1} peak (right scale and violet squares) versus the guest desorption time, for the ε-form film.

4.1.2 WAXD characterization of CC sPS/HA

In this section, the sorption of HA in sPS films exhibiting the dense γ-form or the NC δ and ε forms are characterized by WAXD analysis.

The WAXD patterns of axially sPS films that exhibit γ, δ and ε crystalline phases, are shown in Figure 4.7A–C, respectively.

Patterns A and A' (mainly the equatorial peaks at $2\theta_{CuK\alpha}$ = 9.3° and 10.4°) indicate the presence of the γ phase.[21] Patterns B and B' (mainly the equatorial peak at $2\theta_{CuK\alpha}$ = 8.7° and the shoulder at $2\theta_{CuK\alpha} \approx 10°$) indicate the presence of the triclinic NC δ phase.[22] Patterns C and C′ (mainly the equatorial peaks at $2\theta_{CuK\alpha}$ = 6.9° and at $2\theta_{CuK\alpha}$ = 8.2°) indicate the presence of the orthorhombic NC ε phase.[12]

HA sorption in the γ-form film does not change the diffraction patterns shown in Figure 4.7A and 4.7A′, confirming that (as generally observed for semicrystalline polymers) guest molecules are only absorbed by amorphous phases. Remarkable changes are instead observed for the WAXD patterns of the NC δ and ε forms, which indicate the formation of CC phases, as a consequence of HA sorption from 40 wt% acetone solution at room temperature for 12h. For instance, a comparison between WAXD patterns of the axially oriented δ and ε films of Figure 4.7, before and after sorption of HA from 40 wt% solution in acetone, with a guest content of nearly 7 and 12 wt%, respectively, is shown in Figure 4.8.

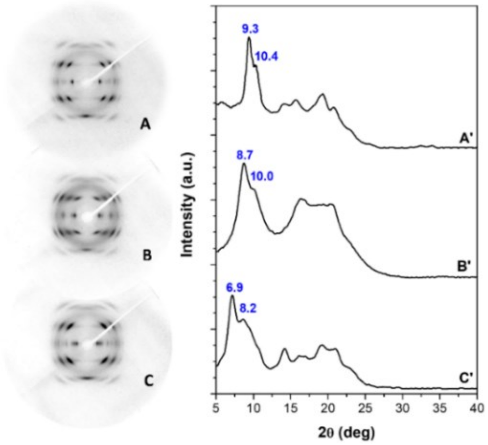

Figure 4.7 WAXD patterns of axially stretched sPS films with a draw ratio of 4, exhibiting γ (A, A′), δ (B, B′) and ε (C, C′) crystalline phases: (A–C) 2D patterns; (A′–C′) equatorial profiles of the 2D patterns.

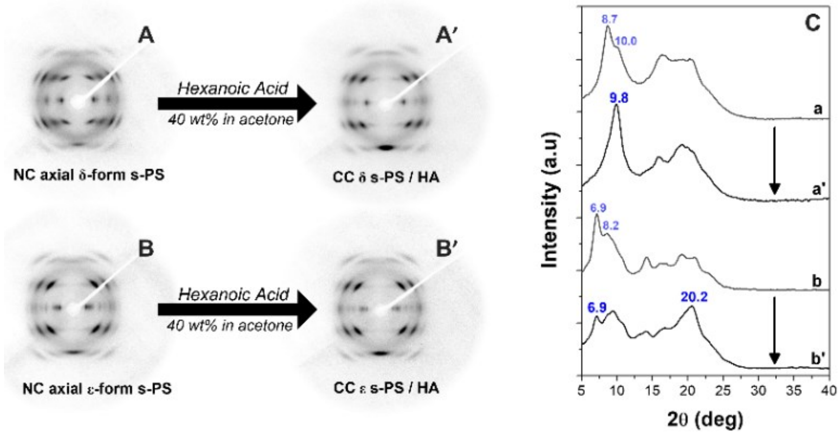

Figure 4.8 WAXD patterns of axially stretched sPS films exhibiting the NC δ-form before (A) and after HA sorption (A′) and the NC ε-form before (B) and after HA sorption (B′). The equatorial profiles of these 2D patterns are shown in (C) (a, a′, b, b′).

In particular, for the δ-form film, the equatorial peak at $2\theta_{CuK\alpha} = 8.7°$ and the shoulder at $2\theta_{CuK\alpha} \approx 10°$ of the triclinic NC δ phase are replaced by a single diffraction peak at $2\theta_{CuK\alpha} = 9.8°$, typical of the disordered CC form.[23] Analogously, for the ε form film, the intensity of the equatorial (110) and (020) peaks at $2\theta_{CuK\alpha} = 6.9°$ and 8.2°, respectively, is markedly decreased with respect to the intensity of the first-layer line reflections (mainly that one at $2\theta_{CuK\alpha} \approx 20.2°$), as is typical of CC ε-form films.[12,13]

Additionally, WAXD patterns of Figure 4.8 confirm that HA guest molecules are not only absorbed by the amorphous sPS phase but also included in the crystalline cavities of both δ and ε NC phases, leading to the formation of corresponding CC phases.

4.2 Sorption of long aliphatic chain carboxylic acids and Adipic Acid

In the previous section, the achievement of CC forms of sPS with an antimicrobial carboxylic acid (hexanoic acid, HA), by guest sorption in both δ and ε NC films was described.[24]

It was found that HA uptake is faster for ε-form films that exhibit crystalline channels, but it also occurs for δ-form films that exhibit crystalline cavities. This phenomenon was rationalized by polarized FTIR spectra, showing the inclusion of monomeric (isolated) HA molecules in the crystalline cavities of the δ-form and the inclusion in the crystalline channels of the ε-form of both isolated and dimeric HA species.[24]

In the present section, the possible formation of CC phases of sPS with longer aliphatic carboxylic acids: i.e., LA with 12 C atoms (Scheme 4.9A) and SA with 18 C atoms (Scheme 4.9B) is explored. The aim is to establish if the crystalline channels of ε sPS phases, especially, are able to accommodate carboxylic acids much longer than HA. This study is also focused on a dicarboxylic acid (adipic acid, AA, Scheme 4.9C), aiming to explore the possible formation of polymeric hydrogen bonded aggregations in the CC phases of sPS crystalline channels.

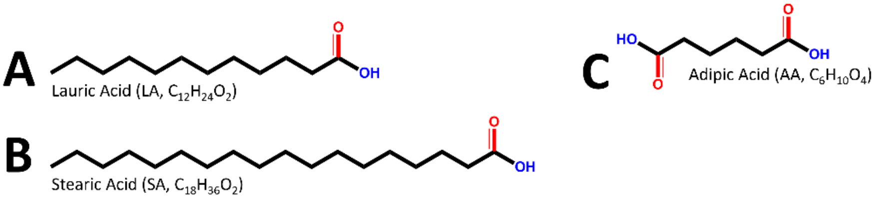

Scheme 4.9 Aliphatic carboxylic acids suitable to be guests of the NC ε-form of sPS, exhibiting crystalline channels: A) lauric; B) stearic; C) adipic.

4.2.1 FTIR analysis of CC sPS phases

FTIR spectra of sPS films, with thickness in the range 100–120 μm, after immersion in a 15 wt% LA solution in acetone for 15 min at room temperature, after acetone desorption at room temperature for 7–10 days are shown in Figure 4.9. The carbonyl region clearly shows that the LA uptake from the γ-form film is negligible (Figure 4.10C).

Both hydroxyl (3500–2400 cm^{-1}) and carbonyl (1800–1650 cm^{-1}) regions clearly show LA uptake for both δ (Figure 4.10B) and ε (Figure 4.10A) form films. LA uptake is definitely higher for the ε-form film (4.8 wt% vs 1.9 wt%).

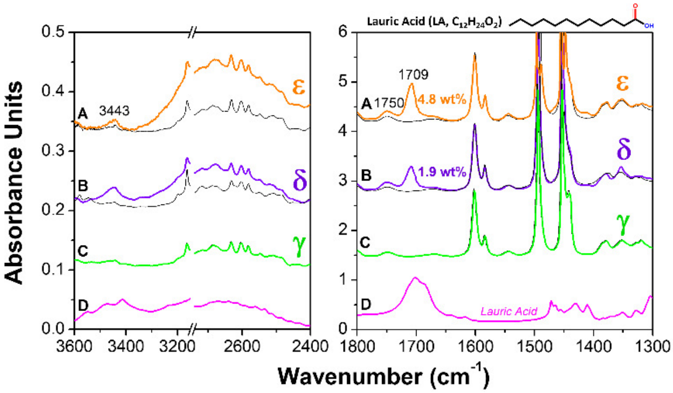

Figure 4.10 FTIR spectra of sPS films, with thickness in the range 100–120 μm, before and after immersion in a 15 wt% LA solution in acetone for 15 min: A) ε-form; B) δ-form; C) γ-form. A FTIR spectrum of solid LA is shown in D.

For both NC forms, the hydroxyl (at 3443 cm^{-1}) and carbonyl (at 1750 cm^{-1}) peaks, corresponding to isolated LA molecules, are weaker than those of the hydroxyl very broad band (in the range 3400–2400 cm^{-1}) and the carbonyl peak (at 1709 cm^{-1}), corresponding to hydrogen-bonded LA molecules. For instance, the carbonyl peak corresponding to isolated LA molecules is weak for the δ-form film [$(I_{1750}/I_{1709})_{\delta,LA} \approx 0.18$] and even weaker for the ε-form film [$(I_{1750}/I_{1709})_{\varepsilon,LA} \approx 0.13$]. These peaks of isolated acid molecules are much weaker than for the shorter HA guest [$(I_{1750}/I_{1709})_{\delta,HA} \approx 0.5$ and $(I_{1750}/I_{1709})_{\varepsilon,HA} \approx 0.36$].[24]

Highly informative are also polarized FTIR spectra of axially stretched sPS films, after longer times of immersion in a 15 wt% LA solution in acetone. In fact, after long term (12h) immersion, LA uptake is similar for δ-form (Figure 4.11B) and γ-form films (Figure 4.11C) and not far from 2 wt%. Moreover, for both films, all guest peaks are not dichroic. This clearly indicates that for both δ and γ form films, LA molecules are only included in the poorly oriented amorphous phase. This result is not surprising because the molecular volume of lauric acid (>0.3 nm^3)[25] is definitely larger than the bulkiest guest molecules of the CC δ forms (always lower than 0.2 nm^3).[13]

Completely different are polarized FTIR spectra of axially stretched ε-form sPS films, after immersion in a 15 wt% LA solution in acetone. In fact, after only 30 min of immersion, LA uptake is higher than 5 wt%. Moreover, both hydrogen-bonded carbonyl peak (at 1709 cm^{-1}) and the broad hydroxyl band corresponding to aggregated acid molecules (in the 3400−3200 cm^{-1} range) are markedly dichroic ($S_{g,1709} = -0.13$; $S_{g,2650} = +0.25$). This clearly indicates that, in ε-form sPS films, LA molecules are instead mainly included in the highly oriented crystalline channels, as dimeric hydrogen bonded aggregates.

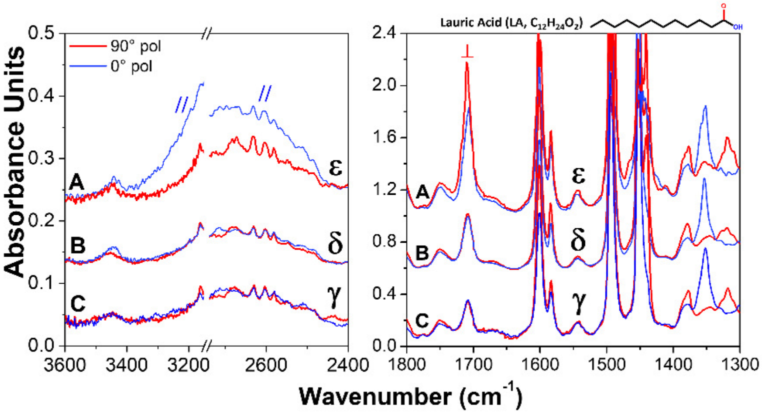

Figure 4.11 Polarized FTIR spectra of axially oriented sPS films with three different crystalline phases, after sorption of LA at room temperature from a 15 wt% acetone solution: A) NC ε, with crystalline channels (0.5h of sorption); B) NC δ, with crystalline cavities (12h of sorption); C) dense γ (12h of sorption). Red and blue lines correspond to polarization plane perpendicular and parallel to the stretching direction, respectively.

The uptake from sPS films of SA (18 C atoms) is much slower than the uptake of LA (12 C atoms).

Film immersion procedures at room temperature, like those used for collection of the spectra of Figures 4.10 and 4.11, lead to negligible SA uptake. Relevant SA uptakes can be instead achieved by immersion temperatures close to the boiling temperature of the acetone carrier (≈60 °C).

For instance, FTIR spectra of sPS films, with thickness in the range 100−120 μm, after 30 min of immersion in a 15 wt% SA solution in acetone in a closed vial placed on a heating plate at temperature of 60 °C, are shown in Figure 4.12. The spectra clearly show that SA uptake from γ-form (Figure 4.11C) and δ-form (Figure 4.12B) films is negligible. SA peaks are instead well apparent for the NC channeled ε-form film, for both hydroxyl and carbonyl regions (Figure 4.12A) and correspond to a SA uptake of nearly 5 wt%. As already observed for LA, more intense are the hydroxyl very broad band (in the range 3400−2400 cm^{-1}) and the carbonyl peak (at 1709 cm^{-1}), corresponding to hydrogen-bonded LA molecules with respect to the peaks (at 3443 cm^{-1} and 1750 cm^{-1}) corresponding to isolated acid molecules: $(I_{1750}/I_{1709})_{\varepsilon,SA} \approx 0.16$.

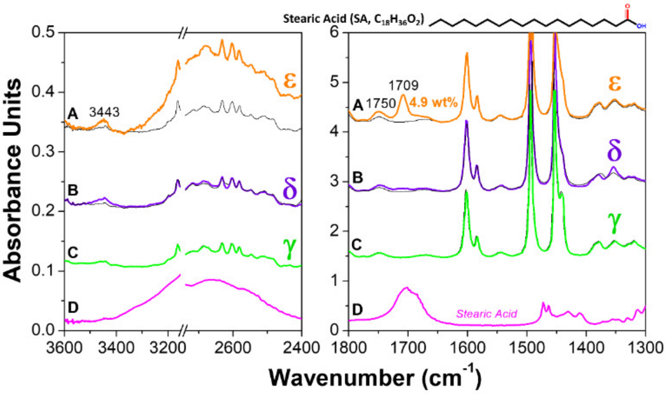

Figure 4.12 FTIR spectra of sPS films, with thickness in the range 100–120 μm, after immersion in a 15 wt% SA solution in acetone for 30 min at nearly 60°C: A) ε-form; B) δ-form; C) γ-form. A FTIR spectrum of solid SA is shown in D.

Again, highly informative are polarized FTIR spectra of axially stretched sPS films (Figure 4.13). In fact, after long term (12h) immersion in a 15 wt% SA solution in acetone at T ≈ 60°C, SA uptake for δ-form films (Figure 4.13B), is not far from 4 wt%, with both hydrogen-bonded carbonyl peak (at 1709 cm^{-1}) and aggregated hydroxyl band (in the 3400–2400 cm^{-1} range) being not dichroic. These data clearly indicate that for δ-form films SA molecules (just like LA molecules) are only included in the poorly oriented amorphous phase. Again, this is not surprising because the molecular volume of stearic acid (>0.5 nm^3)[25] is definitely higher than the volume of the bulkiest guest molecules of the CC δ-forms (always lower than 0.2 nm^3).[13]

Polarized FTIR spectra of an axially stretched ε-form sPS film, after only 30 min of immersion in a 15 wt% SA solution in acetone nearly at 60 °C, show a SA uptake higher than 5 wt% (Figure 4.13A). Moreover, both hydrogen-bonded carbonyl peak (at 1709 cm) and the broad hydroxyl band corresponding to aggregated acid molecules (in the 3400−2400 cm^{-1} range) are markedly dichroic ($S_{g,1709}$ = −0.13; $S_{g,2650}$ = +0.20). This clearly indicates that, in ε-form sPS films, SA molecules just like the shorter LA are prevailingly included in the highly oriented channels of the crystalline phase, as hydrogen bonded aggregates.

Sorption of AA from acetone solutions is negligible not only for sPS films exhibiting the dense γ phase but also for those exhibiting the NC δ-form, even for sorption experiments close to the acetone boiling temperature. As a consequence, only data relative to the sorption of AA in ε-form sPS films are reported. AA sorption from for sPS films exhibiting the NC ε-form is high and comparable with sorption of monocarboxylic acids like LA.

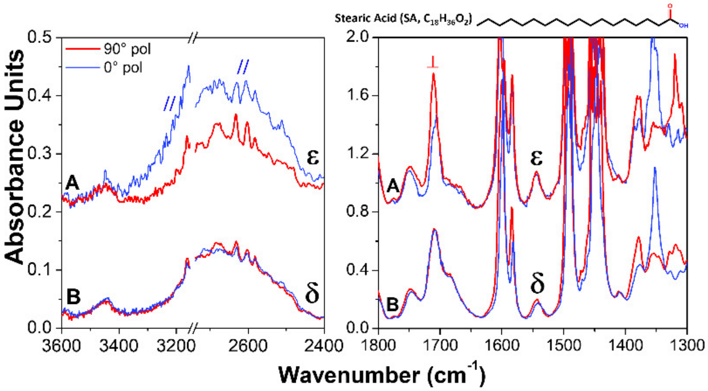

Figure 4.13 Polarized FTIR spectra of axially oriented sPS films with different NC crystalline phases, after sorption of SA at ≈60 °C from a 15 wt% acetone solution: A) ε, with crystalline channels (0.5h of sorption); B) δ, with crystalline cavities (12h of sorption). Red and blue lines correspond to polarization plane perpendicular and parallel to the stretching direction, respectively. Linear dichroism of guest peaks only occurs for the ε form film, indicating the presence of hydrogen-bonded SA aggregates in the crystalline channels.

This is shown, for instance, by FTIR spectra of a ε-form sPS film, with thickness in the range 100–120 μm, after immersion at room temperature in a 15 wt% AA solution in acetone, in Figure 4.14. Immersion procedures of 30 min and 120 min at room temperature lead to AA uptake of 1.7 wt% and 3.8 wt%, respectively. Sorption experiments at higher temperature (≈60°C) and with longer times (up to 12h) lead to a SA uptake of 4.5 wt%.

Polarized FTIR spectra of an axially stretched ε-form sPS film, after only 30 min of immersion in a 15 wt% AA solution in acetone at room temperature, with an AA uptake close to 1.5 wt%, are shown in Figure 4.15. Both hydrogen-bonded carbonyl peak (at 1709 cm^{-1}) and the broad hydroxyl band corresponding to aggregated acid molecules (in the 3400–2400 cm^{-1} range) are markedly dichroic ($S_{g,1709} = -0.13$; $S_{g,2650} = +0.32$). This clearly indicates that, in ε-form sPS films, AA molecules (just like the monocarboxylic acids HA, LA and SA) are prevailingly included in the highly oriented channels of the crystalline phase. Due to the very low intensity of the hydroxyl (at ≈ 3443 cm^{-1}) and carbonyl (at ≈1750 cm^{-1}) peaks corresponding to isolated acidic groups, it can be assumed that the dicarboxylic acid is present in the crystalline channels mainly as polymeric hydrogen bonded aggregates.

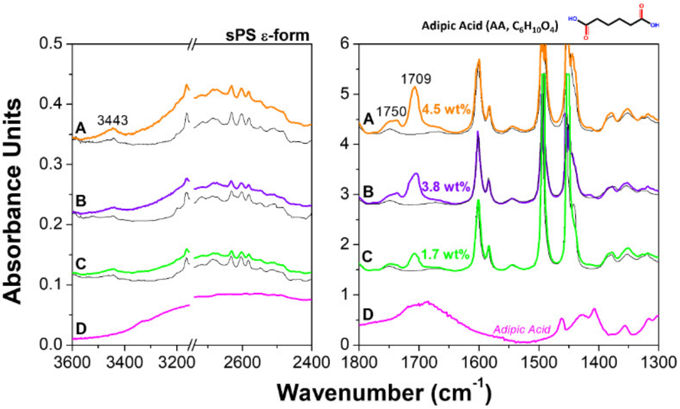

Figure 4.14 FTIR spectra of ε-form sPS films, with thickness in the range 100–120 μm, before and after immersion in a 15 wt% AA solution in acetone: A) for 12h at 60°C; B) for 120 min at room temperature; C) for 30 min at room temperature. A FTIR spectrum of solid AA is shown in D.

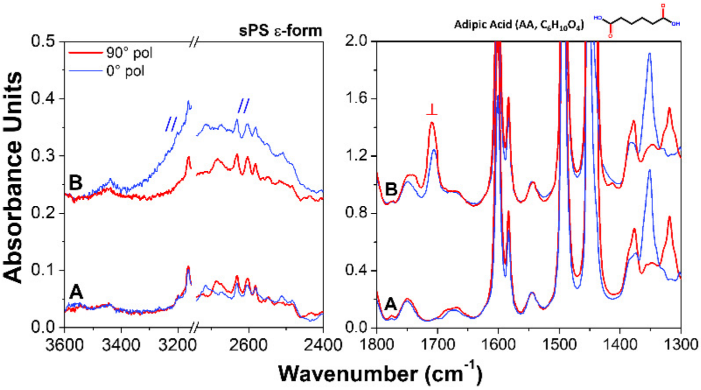

Figure 4.15 Polarized FTIR spectra of an ε-form axially oriented film before (A) and after sorption of AA at room temperature from a 15 wt% acetone solution (B). Red and blue lines correspond to polarization plane perpendicular and parallel to the stretching direction, respectively.

This final sentence of the section refers to all the considered acids (LA, SA and AA). The dichroism of the C=O stretching for dimeric guests in the ε-form is negative (Figures 4.11, 4.13 and 4.15). This indicates that C=O bonds, in the crystalline channels, are oriented preferentially perpendicular to the stretching direction (and hence to the chain axes of the host polymer crystalline phase).[24]

The same result has been found for HA molecules included in the ε channel of sPS films (Figure 4.4c, section 4.2.1).

4.2.2 WAXD characterization of CC sPS phases

Additional information on the possible inclusion of the carboxylic acids of Scheme 4.1, from sPS semicrystalline films exhibiting the dense γ phase or the NC δ or ε phases, can be obtained by comparisons of WAXD patterns of the axially oriented films, before and after guest uptake.

In particular, WAXD patterns (and corresponding equatorial diffraction profiles) as collected after sorption of LA, SA and AA are shown in Figures 4.16, 4.17 and 4.18, respectively. For AA only patterns of the ε-form are reported, because of the nearly negligible guest uptake from δ-form films.

The 2D patterns of Figures 4.16–4.18 show that both degree of crystallinity and orientation of the NC phases are essentially maintained after guest uptakes. In fact, the intensity of the amorphous halo as well as the width of the reflection arcs remain essentially unaltered.

Particularly informative are the equatorial profiles of Figures 4.16–4.18. Because of sorption of both LA (Figure 4.15) and SA (Figure 4.16), the 010 peak of the monoclinic δ-form located at $2\theta_{CuK\alpha}$ = 8.4° becomes broader and shifts its maximum in the range 9.8°–10.0°. A strictly similar phenomenon was already observed for sorption of HA, with the 010 peak of the triclinic δ- form located at $2\theta_{CuK\alpha}$ = 8.7° shifting its maximum up to 9.8° (Figure 4.8A,A′ section 4.1.2).[24] Hence, the treatment of NC δ-form films with carboxylic acid acetone solutions leads to the formation of the axially oriented disordered crystalline phase.[23]

This phenomenon occurs, although guest uptakes from these films are poor (in the range 2–4 wt%) and although LA and SA molecules are preferably located in the amorphous phase (as discussed previously).

The equatorial profiles of Figures 4.16–4.18 are also informative for sorption of guest molecules in the NC ε-form films. In fact, as already observed for sorption HA (Figure 4.8B,B′ section 4.1.2) and as typical of inclusion of guest molecules in the NC ε-form films,[12,13] because of sorption of LA (Figure 4.16), SA (Figure 4.17) and AA (Figure 4.18), the lower angle (110) and (020) diffraction peaks reduce their intensity with respect to the higher angle diffraction peaks.

It is worth adding that, because of sorption of all the considered guests, also a peak at $2\theta_{CuK\alpha}$ in the range 9.3°–9.5° appears, which becomes prominent for SA (Figure 4.17) and AA (Figure 4.18) sorption.

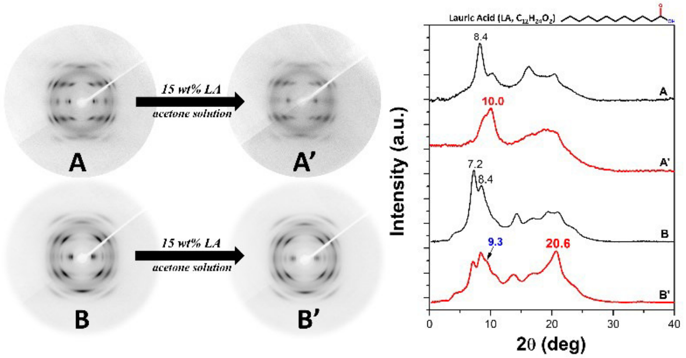

Figure 4.16 WAXD patterns of axially oriented sPS films exhibiting NC (monoclinic δ and orthorhombic ε) forms, before (A, B) and after (A′, B′) LA uptake from 15wt% acetone solution. Equatorial intensity profiles of the 2-D patterns are shown on the right part of the Figure.

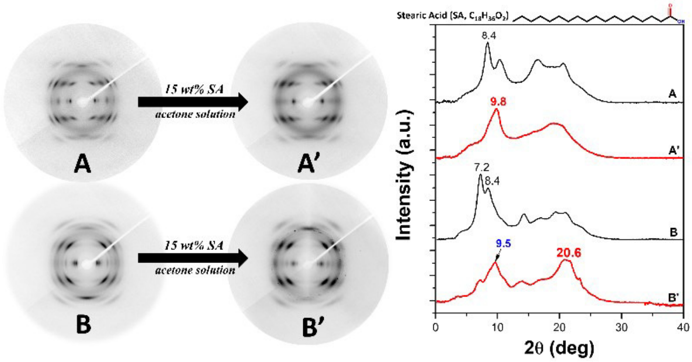

Figure 4.17 WAXD patterns of axially oriented sPS films exhibiting NC (monoclinic δ and orthorhombic ε) forms, before (A, B) and after (A′, B′) SA uptake from 15wt% acetone solution. Equatorial intensity profiles of the 2-D patterns are shown on the right part of the Figure.

This indicated that, mainly for SA and AA, a partial transformation of the starting NC ε-form in a NC disordered phase probably occurred. Both polarized FTIR spectra and WAXD patterns analysis of the ε-form of sPS indicate that LA, SA and AA guest molecules are present in the crystalline channels mainly as hydrogen bonded aggregates. The distribution of the empty space in the crystalline channels of the ε-form, [12,13] requires the formation of linear hydrogen bonded dimers for LA and SA (as schematically shown for SA in Figure 4.19A) as well as of linear hydrogen bonded oligomers (and even polymers) for AA, as schematically shown in Figure 4.19B.

The models of Figure 4.19, and simple considerations relative to the van der Waals encumbrance of aliphatic carboxylic acids, clearly suggest that these guest molecules, although too bulky to accommodate in the cavity of the δ-form, can easily enter in the empty channels of the ε-form by assuming their extended zig-zag planar conformation.

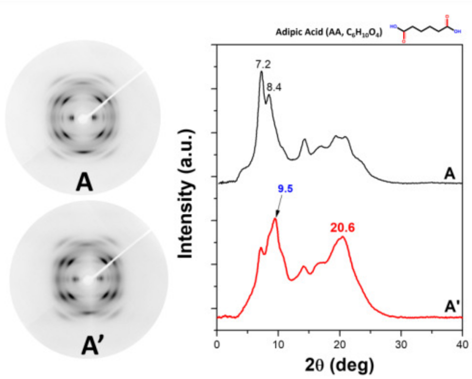

Figure 4.18 WAXD patterns of axially oriented sPS films exhibiting NC ε-form, before (A) and after (A') AA uptake from 15wt% acetone solution. Equatorial intensity profiles of both 2-D patterns are shown on the right part of the Figure.

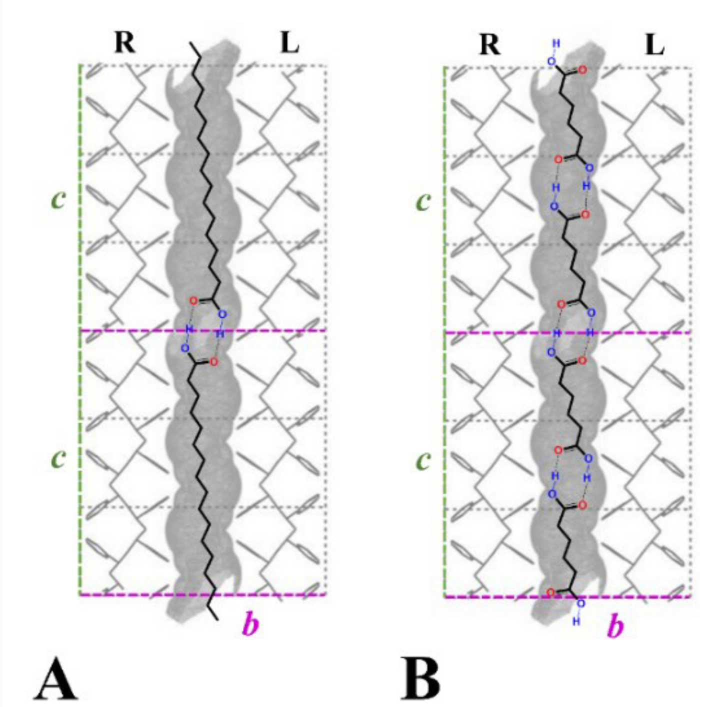

Figure 4.19 View perpendicular to the *bc* plane of the ε-form of sPS, showing its empty channels (gray regions). Schematic view of intermolecular hydrogen bonds between carboxylic groups in the crystalline channels: (A) linear dimers of SA guest molecules; (B) linear polymers of AA guest molecules.

The minimum energy conformations, of all carboxylic groups shown in Figure 4.19, exhibit the C=O groups eclipsed with respect to the β carbon atom.[18] These models well agree with the indication, obtained by linear dichroism of carbonyl stretching, that in the crystalline channels C=O bonds are oriented preferentially perpendicular to the chain axes of the host polymer crystalline phase.

This guest conformation and guest orientation with respect to the crystalline channel is clearly suitable for formation of intermolecular hydrogen bonds between carboxylic groups, leading to linear dimeric (Figure 4.19A) and linear polymeric (Figure 4.19B) guest aggregates.

It is worth adding that inclusion of the aliphatic carboxylic acids in the empty crystalline channels of the ε-form and formation of intermolecular hydrogen bonds between carboxylic guest groups could be the molecular origin of the observed uptakes of the carboxylic acids, being much higher and faster for ε-form than for δ-form sPS films.

4.3 Sorption of Benzoic Acid (BA)

Benzoic acid (BA) and its derivatives are very attractive for their pharmacological properties such as antioxidant, radical-regulating, antiviral, antitumor, anti-inflammatory, antimicrobial and antifungal.[26–28] These low toxicity compounds are widely used in medicine and can be found in various cosmetic products, medications and food as additives and preservatives to certain approved concentrations.[29,30] In fact, many literature studies report on release of BA and derivatives.[31–36]

In this section, sPS axially films including BA molecules in their amorphous and crystalline phases are described. In addition. a comparison with axially oriented PPO films is also reported.

4.3.1 FTIR and WAXD characterization of CC sPS/BA

Sorption of BA in axially oriented sPS films was conducted at room temperature, by using concentrated acetone solutions (30wt% of BA). The BA guest uptake after 14h of room temperature treatment is low for films exhibiting the dense γ phase (lower than 1 wt%) while is much higher for films being zig-zag planar mesomorphic (axially stretched amorphous) or exhibiting the NC δ and NC ε phases (4.1, 5.1 and 6.8 wt%, respectively). FTIR spectra of axially oriented sPS films being zig-zag planar mesomorphic or exhibiting NC δ and ε phases, before (black lines) and after 14h of BA sorption (colored lines), are shown in Figure 4.20. The FTIR peaks of the BA molecules of the zig-zag planar mesomorphic film (Figure 4.20A) and of the CC sPS/BA ε-form film (Figure 4.20B) are similar and essentially correspond to peaks of BA dimers (labeled by green numbers in Figure 4.20). These peak positions are listed in the 3rd column of Table 4.2

and are compared with the list of the BA dimer peaks, as observed for solid BA: from KBr pellets (1st column in Table 4.2)[37] as well as from mull (2nd column of Table 4.2)[38]. Both spectra of mesomorphic and CC ε films, besides vibrational peaks of BA dimer, show additional weak peaks (labeled with orange numbers in Figure 4.19: at 3443 cm^{-1}, 1738 cm^{-1}, and 632 cm^{-1}), which can be attributed to isolated BA molecules.

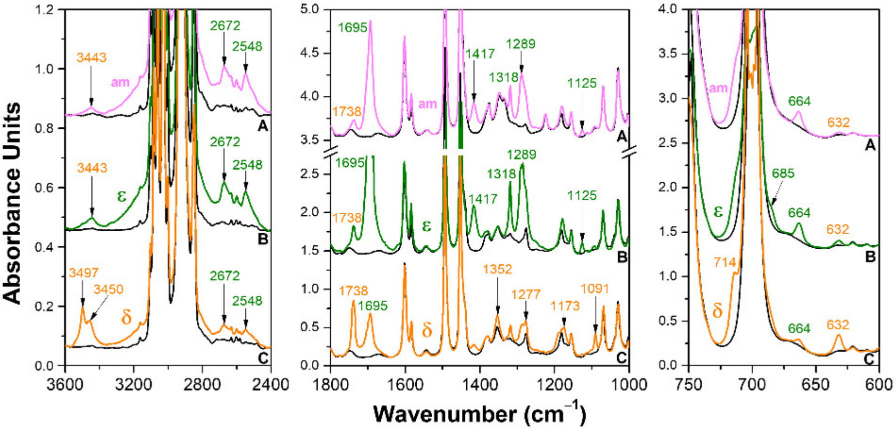

Figure 4.20 FTIR spectra, for three spectral ranges (3600–3200 cm^{-1}, 1800–1000 cm^{-1} and 750–600 cm^{-1}) of axially oriented sPS films before (black lines) and after BA sorption (colored lines): (A) zig-zag planar mesomorphic; (B) NC ε-form; (C) NC δ-form. Peaks due to isolated and dimeric BA molecules are labeled by orange and green numbers, respectively.

The percentages of BA molecules as monomer are estimated from the ratio of integrated absorbances of the 1738/1695 cm^{-1} pair of peaks for both mesomorphic and CC δ-form films, and of the 664/632 cm^{-1} pair of peaks for CC ε film (due to saturation of the signal at 1695 cm^{-1}), by using the formula (4.1).

The obtained results indicate that a low percentage (<20%) of BA is present as isolated molecules, for both the mesomorphic film (and consequently for its amorphous phase) and for the CC ε film.

It is not surprising because BA is prevailingly present as dimers even in dilute organic solutions.[38]

A completely different behavior is observed for FTIR spectra of CC sPS/BA δ-form films (Figure 4.20C). In fact, main BA peaks are of isolated BA (monomer) and are indicated as orange numbers in Figure 4.20. These peaks are listed in the third column of Table 4.3 and compared with the list of the peaks of BA monomer as obtained in Ar matrices (1st column in Table 4.3)[39] as well as for high temperature vapor of BA (2nd column of Table 4.3).[38]

Besides vibrational peaks of BA monomer, additional peaks (labeled with green numbers in Figure 4.19: at 2672 cm^{-1}, 2548 cm^{-1}, 1695 cm^{-1} and 664 cm^{-1}) are present, which can be attributed to BA dimers.

Quantitative evaluations indicate that approximately 50% of BA is present as isolated molecules, for the CC δ film.

Linear dichroism of dimeric and monomeric guest peaks of Tables 4.2 and 4.3, respectively, was studied by polarized FTIR spectra of axially oriented mesomorphic and CC (δ or ε) sPS films (Figure 4.21). The parallelism of the zig-zag planar chains of the dense mesomorphic phase with respect to the stretching direction is nearly complete (orientation factor, as evaluated from the 1222 cm^{-1} peak $S_{p,meso} > 0.95$). The orientation factor of the host helical crystalline polymer phases, exhibiting ***s***(2/1)2 helices, is also high and was evaluated based on the polymer host peak at 572 cm^{-1} : $S_{p,\delta} = 0.85$ and $S_{p,\varepsilon} = 0.80$.

The polarized spectra of Figure 4.21 show that many guest peaks are dichroic, not only for CC films that absorb BA molecules both in their amorphous and crystalline phases, but also for the mesomorphic film that absorbs BA molecules only in its amorphous phases.

In particular, labels // and ⊥ indicate that peak absorbance is higher for spectra with polarization parallel or perpendicular to the film stretching direction, respectively. These // and ⊥ labels are colored in green and in orange when the guest vibrational peak is of dimeric and of isolated BA molecules, respectively. This information relative to dichroism of peaks of dimeric and isolated BA was also inserted in Tables 4.2 and 4.3, respectively.

For the polarized spectra of the CC δ-form film (Figure 4.21C), the peaks of isolated BA molecules exhibit very intense dichroism. For instance, the orientation factor of peaks of the monomeric guest is $S_{m,1738,\delta} = -0.36$; $S_{m,1090,\delta} = -0.33$; $S_{m,632,\delta} = -0.36$, i.e., not far to the limit value of −0.5 corresponding to a perfect orientation of all BA guest molecules. Particularly informative is the carbonyl region, where the sign of dichroism of the carbonyl stretching of the isolated molecule (at 1738 cm^{-1}) is negative (⊥), so it can be assumed that the BA guest molecules of the δ-form are preferentially perpendicular to the stretching direction, as already observed for many aromatic guest molecules of the δ-form of sPS.[40–42]

Table 4.2 FTIR peaks (and related assignment) of BA dimers as observed for solid BA (KBr pellets[37] or mull[38]) and for BA guest molecules in axially stretched ε-form sPS and α-form PPO films.

Solid BA[37]		***Solid BA[38]*** s = strong m = medium w = weak vw = very weak	***BA in mesomorphic or in CC ε sPS***	***BA in CC α PPO***
Infrared peak (cm^{-1})	***Assignment***			
552	$\delta(CC) + \nu(O\cdots O)$	552 vw	na	547 //
668	$\delta(CC)_{rings} + \delta(COOH)$	664 vw	664 //	664 //
685	$\gamma(CC)_{rings} + \gamma(CC)$	682 vw	685 ⊥	685 ⊥
708	$\gamma(CC)_{rings} + \gamma(CC)$	707 s	712 ⊥	712 ⊥
- -		800 vw	797 //	797 //
806	$\nu(CC)_{rings} + \delta(COOH)$	807 vw	808 nd	808 nd
936	$\gamma(OH)$	932 w	936 nd	936 nd
1026	$\nu(CC)_{rings} + \delta(CH)$	1023 vw	na	na
1073	$\nu(CC)_{rings} + \delta(CH)$	1070 vw	na	1070
1129	$\nu(Ph\text{–}COOH) + \nu(CC)_{rings} + \delta(CH)$	1125 vw	1125 nd	1125
1181	$\nu(CC)_{rings} + \delta(CH)$	1184 vw	na	na
1294	$\nu(CC)_{rings} + \delta(OH) + \delta(CH)$	1290 m	1289 //	na
1327	$\nu(CC)_{rings} + \delta(CH)$	1323 m	1318 nd	na
1426	$\delta(OH)$	1420 w	1417 //	na
1454	$\delta(OH)$	1450 w	na	na
1497	$\delta(CH)$	1495 vw	na	na
1584	$\nu(CC)_{rings} + \delta(CH)$	1580 vw	na	na
1688	$\nu(C{=}O) + \delta(OH)$	1685 s	1695 //	1695 nd
- -		2560 vw	2548 //	2548 //
- -		2603 vw	2600 //	2600 //
- -		2670 vw	2672 //	2672 //
3012	$\nu(OH)$	3005 vw	na	na
3073	$\nu(CH)_{rings}$	3078 vw	na	na

Notes: ν = stretching; δ = in-plane bending; γ = out-of-plane bending; na = not accessible; nd= not dichroic; // and ⊥, dichroic peak with $A_{//} > A_{\perp}$ and $A_{//} < A_{\perp}$, respectively.

Also informative is the region of the O–H stretching of isolated BA molecules in CC δ-form film (Figure 4.21C). In fact, beside a poorly dichroic peak at 3450 cm^{-1} corresponding to isolated BA molecules in amorphous sPS phases, also a highly dichroic peak at 3497 cm^{-1} corresponding to isolated BA molecules in the cavities of the δ-form is observed.

For the polarized spectra of the mesomorphic film (Figure 4.21A) and of the CC ε film (Figure 4.21B), the kind of dichroism (// or ⊥) is the same for all the observed peaks. The dichroism of the largely prevailing BA dimers is opposite with respect to those observed for the minor content of BA dimers included in the δ-form film (see, e.g., dichroism of the peaks at 2672 cm^{-1}, 2548 cm^{-1} and 1695 cm^{-1}).

Table 4.3 FTIR peaks (and related assignment) of isolated BA as taken in Argon matrix,[39] as observed in vapor phase spectra (at 433 K)[38] and in an axially stretched δ-form sPS film.

isolated BA in Argon[39]		*BA vapour*[38] s = strong m = medium w = weak vw = very weak	*BA in CC δ sPS*
Infrared peak (cm^{-1})	*Assignment*		
565	C–O bend	575 vw	na
628	OH oop	632 vw	632 ⊥
711	CH oop	715 w	714 //
- -		817 vw	808 nd
937	CH oop	- -	936 nd
1027	ring str + ring bend	1010 vw	na
1066	ring str + CH bend	- -	na
1086	C-O str + ring bend	1084 m	1091 ⊥
1169	OH bend + CH bend	- -	1173 ⊥
1185	CH bend + OH bend	1184 m	1189 ⊥
1275	ring str	1290 vw	1277
1347	CH bend + ring str	1370 vw	1352
1606	ring str	1600 vw	na
1752	C=O str	1765 s	1738 ⊥
3567	OH str	3500 vw	3450 //
		3575 m	3497 ⊥

Notes: str = stretching; bend = bending; oop = out-of-plane; na = not accessible; nd= not dichroic; // and ⊥, dichroic peak with $A_{//} > A_{\perp}$ and $A_{//} < A_{\perp}$, respectively.

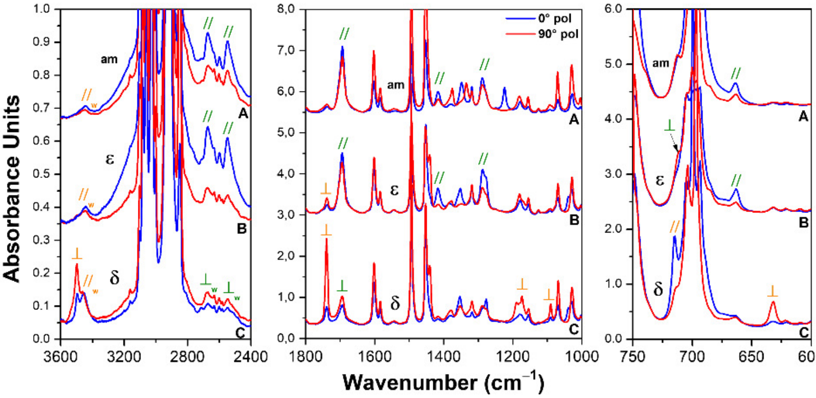

Figure 4.21 Polarized FTIR spectra as taken with polarization plane parallel (blue lines) and perpendicular (red lines) to the film stretching direction, in three spectral ranges (3600−2400 cm^{-1}, 1800−1000 cm^{-1} and 750−600 cm^{-1}), of axially oriented sPS films: (A) zig-zag planar mesomorphic; (B) CC ε-form; (C) CC δ-form. Labels // and ⊥ indicate that guest peak absorbance is higher for spectra with polarization parallel and perpendicular to the film stretching direction, respectively. Green and orange labels indicate peaks corresponding to dimeric and isolated BA, respectively.

This indicates that, both in the oriented amorphous phase as well as in the crystalline channels of the CC ε phase, probably the phenyl rings of BA dimers are preferentially parallel to the film stretching direction. This can be easily rationalized by the expected preferential axial orientation of long axes of the hydrogen bonded BA dimers. Moreover, the higher dichroism intensity for the CC ε film ($S_{d,2672,am}$ = +0.36; $S_{d,2672,\varepsilon}$ = + 0.55; $S_{d,1417,am}$ = +0.23; $S_{d,1417,\varepsilon}$ = +0.56; $S_{d,664,am}$ = +0.29 ; $S_{d,664,\varepsilon}$ = +0.40) clearly indicates the occurrence of an higher degree of orientation of the dimeric guest molecules in the channels of the CC ε phase.

It is worth adding that the sign of dichroism of the 1738 cm^{-1} peak is the same for CC ε and CC δ films ($S_{m,1738,\varepsilon}$ = −0.17, $S_{m,1738,\delta}$ = −0.36). This can indicate that, also for both CC δ and CC ε phases, the orientation of the isolated BA guest plane is preferentially perpendicular to the stretching direction.

To summarize, FTIR spectra of Figures 4.20 and 4.21 show that BA molecules are prevailingly present as dimers, preferentially parallel to the film stretching direction, both in amorphous and CC ε phases of sPS. BA molecules, on the contrary, are prevailingly present as isolated molecules and preferentially perpendicular to the film stretching direction, in CC δ phases of sPS. A schematic representation of BA guest molecules as monomer in crystalline cavities of the δ-form and as dimer in the crystalline channels of the ε-form is reported in Figure 4.22A and B, respectively.

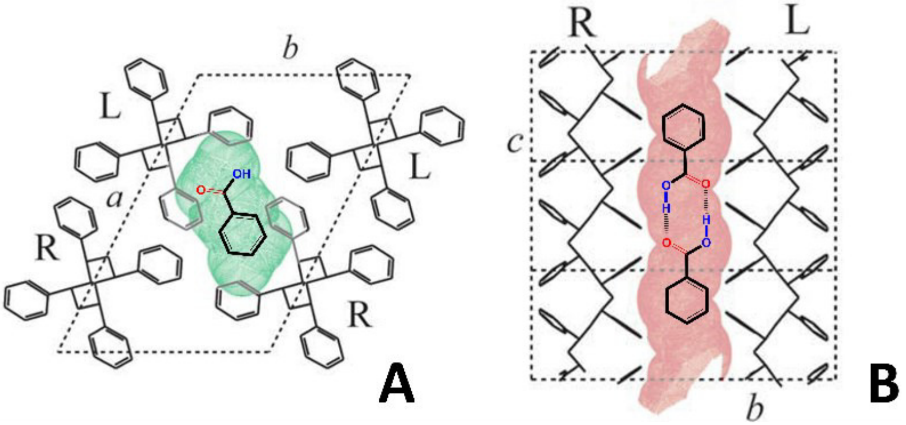

Figure 4.22 Schematic views of preferential aggregation and orientation of BA guest molecules in CC phases of sPS: (A) *ab* projection of CC δ-form with isolated BA molecules and guest molecular plane preferentially perpendicular to the helical chain axes; (B) *bc* projection of CC ε phase with dimeric BA molecules and guest molecular planes preferentially parallel to the helical chain axes.

WAXD fiber patterns, taken with a two-dimensional diffractometer (on the left) and corresponding equatorial diffraction profiles (on the right) for sPS axially stretched films, exhibiting the NC δ and ε phases, before and after sorption of BA, are shown in Figure

4.23. The WAXD patterns of the NC δ film (Figure 4.23A) present 010 and $\bar{2}10$ reflections (at $2\theta_{CuK\alpha} = 8.4°$ and 10.3°, respectively) typical of NC monoclinic δ phase;[41] after sorption of BA, the WAXD patterns shows shift of 010 and $\bar{2}10$ diffraction peaks to $2\theta_{CuK\alpha} = 8.1°$ and 10.1° (Figure 4.23A′) as well as a reduced intensity of the 010 peak, as typical of CC monoclinic δ phases.[22,43]

WAXD patterns of the NC ε film (Figure 4.23B) present 110 and 020 reflections (at $2\theta_{CuK\alpha} = 6.9°$ and 8.2°, respectively) typical of NC orthorhombic ε phase;[44] after sorption of BA, the intensity of these equatorial peaks is markedly decreased with respect to the intensity of first-layer line reflections (mainly at $2\theta_{CuK\alpha} = 20.2°$), as typical of CC ε phases (Figure 4.23B′).[40,44] No change in diffraction profiles for dense mesomorphic film after BA uptake can be observed.

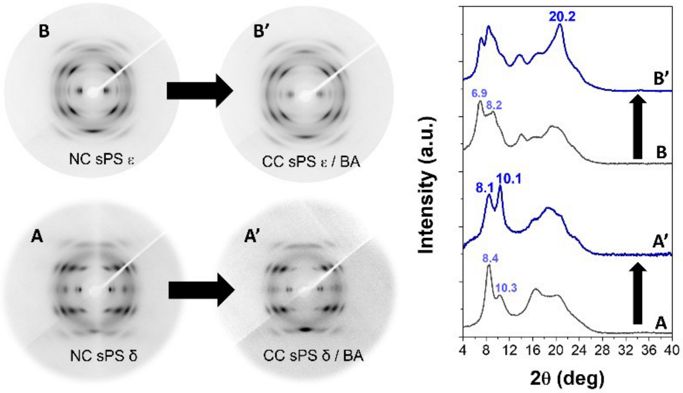

Figure 4.23 WAXD patterns and corresponding equatorial intensity profiles of sPS films presenting NC and CC δ (A, A′) and ε (B, B′) phases. Diffraction angles of relevant reflections of NC and CC phases are indicated.

4.3.2 Comparison with CC PPO/BA

Sorption of BA molecules in axially stretched PPO film, exhibiting the α phase, from 30 wt% BA/acetone solution for 2 hours and after subsequent acetone desorption, was also performed and characterized by polarized FTIR and WAXD analysis.

Polarized FTIR spectra of axially oriented α PPO films before and after before and after sorption of BA (8 wt%) are shown in Figure 4.24. In agreement with literature reports[17,45] the FTIR peaks (at 773, 756, 495 and 414 cm^{-1}) typical of the α NC host phase are dichroic (e.g., $S_{p,495} = +0.33$).

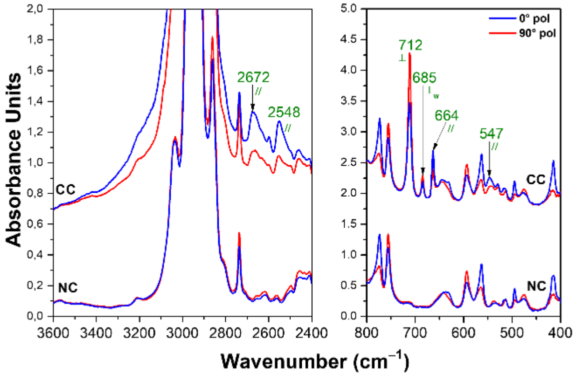

Figure 4.24 Polarized FTIR spectra as taken with polarization plane parallel (blue lines) and perpendicular (red lines) to the film stretching direction, for two spectral ranges (3600–2400 cm^{-1} and 800–400 cm^{-1}), for an axially oriented PPO film exhibiting the NC α phase, before and after BA sorption leading to the corresponding CC phase.

Positions of the guest peaks as well as their possible dichroism (⊥ or //) are listed in the 4th column of Table 4.2 (section 4.3.1). It is worth noting that, in the accessible spectral regions with low absorbance of the host polymer, positions and dichroism of all guest peaks are coincident with those of BA dimers being guest of the sPS ε-form film (3rd column of Table 4.2).

It is also worth noting the absence of FTIR peaks (e.g., at nearly 3500 cm^{-1}) of isolated BA guest molecules, which (although weak) occur for BA molecules in amorphous and CC ε phases of sPS. This indicated that, both in the high free-volume amorphous phase of PPO as well as in the large intrahelical channels of the α form of PPO,[46] BA molecules essentially are only present as dimers.

These data also confirm that the empty space in the NC form of PPO is distributed as channels (as occurs for the ε phase of sPS) rather than as isolated cavities (as occurs for the δ phase of sPS).

WAXD fiber patterns, taken with a two-dimensional diffractometer (on the left) and corresponding equatorial diffraction profiles (on the right) for a NC α phase PPO axially stretched film, before and after sorption of BA (8 wt%) are shown in Figure 4.24. WAXD patterns of the NC α film (Figure 4.25A) present typical diffraction peaks at $2\theta_{CuK\alpha} \approx 4.5°$, 7.1°, 11.3° and 15.0° corresponding to (100), (010), (210) and (310) crystal planes. After sorption of BA molecules, the pattern shows a reduced intensity of 100, 010 reflection as well as an increased intensity of the 310 reflection, clearly indicating the formation of α CC phase[47] (see, e.g., Figure 1.2 of section 1.1.1).

Both polarized FTIR spectra and WAXD patterns clearly indicate that BA molecules are present in the crystalline (and amorphous) PPO phases only as hydrogen bonded aggregates.

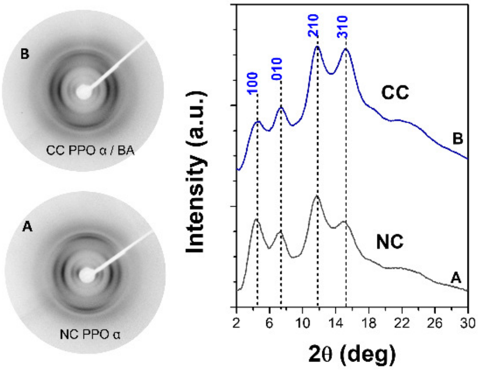

Figure 4.25 WAXD patterns and corresponding equatorial intensity profiles of axially oriented PPO films presenting: (A,A′) NC α-form; (B,B′) CC α-form with BA. Miller indexes of relevant equatorial reflections of the CC phase are indicated.

4.4 Conclusions

In this chapter, sorption of carboxylic acids in NC phases of axially oriented sPS phases has been described.

Primarily, the sorption of HA is definitely higher and faster in sPS films with NC δ and ε phases than for sPS films with the dense γ phase. HA sorption is particularly fast for ε-form films exhibiting crystalline empty channels.

The sorption of HA in sPS films with NC δ and ε phases leads to guest uptake not only in their amorphous phases, but also in the cavities and channels of their crystalline phases, respectively. In fact, the formation of CC δ and ε sPS/HA phases is shown by changes in reflection intensities in WAXD fiber patterns.

The appearance of two dichroic FTIR peaks (a carbonyl and a hydroxyl stretching at 1751 cm^{-1} and 3443 cm^{-1}, respectively) indicate that both δ and ε NC phases are able to include HA as isolated guest molecules. The dichroism of the carbonyl peak corresponding to hydrogen-bonded molecules (at 1709 cm^{-1}), observed only for ε-form films, indicates that HA dimers are also included in the crystalline channels of the ε phase. Moreover, the sign of dichroism of the O−H stretching and C=O stretching peaks indicates that the orientations of O−H and C=O bonds are preferentially parallel and perpendicular to the crystalline polymer chain axes, respectively. These functional group orientations can easily be rationalized for both monomeric and dimeric HA guest molecules in the crystalline channels of the ε form.

The inclusion of HA molecules in the channels of the ε phase, not only as isolated molecules, but also as dimers, is possibly the molecular origin of the much faster HA uptake from ε-form sPS films. As this phenomenon occurs in the NC ε-form, exhibiting continuous crystalline channels parallel to the polymer chain axis, these results suggest the possibility of inclusion in these channels of continuous molecular chains formed by hydrogen bonded dicarboxylic acids.

For this reason, sorption of long aliphatic monocarboxylic acids (LA with 12 C atoms, SA with 18 C atoms) as well as of the dicarboxylic acid AA (6 C atoms) has been also investigated.

Particularly, sorption of LA and SA is much faster for ε-form films that exhibit crystalline channels rather than for δ-form films that exhibit crystalline cavities. These phenomena are due to the fact that these aliphatic carboxylic acid molecules are included in the ε-form crystalline channels by assuming their zig-zag planar conformation and by establishing intermolecular hydrogen bonds between carboxylic groups of adjacent guest molecules. The same acid molecules are instead too big to be accommodated in the cavities of the NC δ-form films.

Polarized FTIR spectra show that, in the crystalline channels of the ε-form, mainly dimeric aggregates of LA and SA and mainly oligomeric aggregates of AA are present, and they exhibit the same orientation shown for the shorter HA guest molecules, whose amounts of isolated and dimeric species are comparable.

WAXD patterns of axially oriented ε-form sPS films, after sorption of LA, SA and AA, show a reduced intensity of the low angle (110) and (020) diffraction peaks with respect to the higher angle equatorial diffraction peaks, as found for HA sorption.

Thus, it has been established that the crystalline channels of the sPS ε-form are able to host: i) very long carboxylic acids prevailingly as hydrogen bonded linear dimers; ii) dicarboxylic acids prevailingly as hydrogen bonded linear polymers.

Sorption of the aromatic carboxylic acid BA is in line with results observed for aliphatic carboxylic acids. Particularly, Polarized FTIR spectra show that, in amorphous and CC ε phases of sPS, BA molecules are prevailingly present as dimers. In CC δ phases of sPS, on the contrary, BA molecules are prevailingly present as isolated molecules. Consequently, only the NC δ-form of sPS is able to isolate BA guest molecules even disrupting their strong intermolecular hydrogen bonds, which are present not only in BA crystals but also in diluted solutions. For BA molecules the δ sPS form plays a crucial role, not only avoiding additive aggregation but even leading to separation of dimeric molecules. This segregation of molecules allows spectroscopic characterization of isolated molecules already at room temperature, avoiding use of more difficult procedures such as Argon gas matrix maintained at 17 K onto a cooled optic CsI substrate.

Polarized FTIR spectra also show that, both in the high free-volume amorphous phase of PPO as well as in the large intrahelical channels of the α form of PPO, BA molecules are essentially present only as dimers. Moreover, sorption studies in PPO films were conducted also for the aliphatic carboxylic acids LA, SA and AA (not shown here because FTIR spectra were poorly informative) and the results were analogous: molecules present in PPO phases are essentially dimers/oligomers. These data thus confirm that the empty space in the NC form of PPO is distributed as channels (as occurs for the ε phase of sPS) rather than as isolated cavities (as occurs for the δ phase of sPS).

Moreover, considering $c_{\perp}$ orientated sPS (and PPO) films hosting hydrogen-bonded "linear polymers", the formation of isolated semiconductive channels perpendicular to the plane of insulating sPS films could be possible.

This can open new perspectives in the use of CC polymer films as functional materials.

REFERENCES

(1) Guerra, G.; Daniel, C.; Rizzo, P.; Tarallo, O. Advanced Materials Based on Polymer Cocrystalline Forms. *J. Polym. Sci. Part B Polym. Phys.* **2012**, *50* (5), 305–322. https://doi.org/10.1002/polb.23035.

(2) Sato, S.; Kawaguchi, T.; Kaneko, F. ATR FTIR Spectroscopic Study on Complexation of Sydiotactic Polystyrene with N-Alkyl Carboxylic Acids. *Macromol. Symp.* **2016**, *369* (1), 114–118. https://doi.org/10.1002/masy.201600052.

(3) Hismiogullari, S. E.; Hismiogullari, A. A.; Sahin, F.; Oner, E. T.; Yenice, S. M.; Karasartova, D. Investigation of Antibacterial and Cytotoxic Effects of Organic Acids Including Ascorbic Acid, Lactic Acid and Acetic Acids on Mammalian Cells. *J. Anim. Vet. Adv.* **2008**, *7*, 681–684.

(4) Leyva, M. O.; Vicedo, B.; Finiti, I.; Flors, V.; Del Amo, G.; Real, M. D.; García-Agustín, P.; González-Bosch, C. Preventive and Post-Infection Control of *Botrytis Cinerea* in Tomato Plants by Hexanoic Acid. *Plant Pathol.* **2008**, *57* (6), 1038–1046. https://doi.org/10.1111/j.1365-3059.2008.01891.x.

(5) Tammer, M. G. Sokrates: Infrared and Raman Characteristic Group Frequencies: Tables and Charts: Wiley, Chichester. *Colloid Polym. Sci.* **2004**, *283* (2), 235–235. https://doi.org/10.1007/s00396-004-1164-6.

(6) Creager, S. E.; Steiger, C. M. Conformational Rigidity in a Self-Assembled Monolayer of 4-Mercaptobenzoic Acid on Gold. *Langmuir* **1995**, *11* (6), 1852–1854. https://doi.org/10.1021/la00006a004.

(7) Halupka, M.; Sander, W. A Simple Method for the Matrix Isolation of Monomeric and Dimeric Carboxylic Acids. *Spectrochim. Acta. A. Mol. Biomol. Spectrosc.* **1998**, *54* (3), 495–500. https://doi.org/10.1016/S1386-1425(97)00248-5.

(8) Yamamoto, M.; Iwai, Y.; Nakajima, T.; Arai, Y. Fourier Transform Infrared Study on Hydrogen Bonding Species of Carboxylic Acids in Supercritical Carbon Dioxide with Ethanol. *J. Phys. Chem. A* **1999**, *103* (18), 3525–3529. https://doi.org/10.1021/jp984604p.

(9) Eliason, T. L.; Havey, D. K.; Vaida, V. Gas Phase Infrared Spectroscopic Observation of the Organic Acid Dimers (CH3(CH2)6COOH)2, (CH3(CH2)7COOH)2, and (CH3(CH2)8COOH)2. *Chem. Phys. Lett.* **2005**, *402* (1–3), 239–244. https://doi.org/10.1016/j.cplett.2004.12.021.

(10) Maçôas, E. M. S.; Myllyperkiö, P.; Kunttu, H.; Pettersson, M. Vibrational Relaxation of Matrix-Isolated Carboxylic Acid Dimers and Monomers. *J. Phys. Chem. A* **2009**, *113* (26), 7227–7234. https://doi.org/10.1021/jp8099384.

(11) Meyer, K. A. E.; Suhm, M. A. Vibrational Exciton Coupling in Homo and Hetero Dimers of Carboxylic Acids Studied by Linear Infrared and Raman Jet Spectroscopy. *J. Chem. Phys.* **2018**, *149* (10), 104307. https://doi.org/10.1063/1.5043400.

(12) Petraccone, V.; Ruiz de Ballesteros, O.; Tarallo, O.; Rizzo, P.; Guerra, G. Nanoporous Polymer Crystals with Cavities and Channels. *Chem. Mater.* **2008**, *20* (11), 3663–3668. https://doi.org/10.1021/cm800462h.

(13) Tarallo, O.; Schiavone, M. M.; Petraccone, V.; Daniel, C.; Rizzo, P.; Guerra, G. Channel Clathrate of Syndiotactic Polystyrene with *p* -Nitroaniline. *Macromolecules* **2010**, *43* (3), 1455–1466. https://doi.org/10.1021/ma902502f.

(14) Itagaki, H.; Sano, T.; Okabe, T.; Sano, S.; Ebihara, H.; Tomono, F.; Dohra, H. Polymerization of Aniline in Tubular Cavities of the Crystalline Phase of Syndiotactic Polystyrene: Proposal of a Preparation Method of Sophisticated Polymer Composites. *ACS Macro Lett.* **2017**, *6* (10), 1099–1103. https://doi.org/10.1021/acsmacrolett.7b00661.

(15) Sano, T.; Ebihara, H.; Sano, S.; Okabe, T.; Itagaki, H. The Ways of Connecting Crystalline Phases Having Tubular Cavities like Stringing Beads: New Conductive Polymer Composites Prepared by the Polymerization of Aniline in Highly Oriented ε Crystalline Phase of Syndiotactic Polystyrene. *Eur. Polym. J.* **2020**, *138*, 109975. https://doi.org/10.1016/j.eurpolymj.2020.109975.

(16) Albunia, A. R.; Di Masi, S.; Rizzo, P.; Milano, G.; Musto, P.; Guerra, G. Chlorinated Guest Orientation and Mobility in Clathrate Structures Formed with Syndiotactic Polystyrene. *Macromolecules* **2003**, *36* (23), 8695–8703. https://doi.org/10.1021/ma034964x.

(17) Golla, M.; Nagendra, B.; Fierro, F.; Rizzo, P.; Daniel, C.; Guerra, G. Axially Oriented Nanoporous Crystalline Phases of Poly(2,6-Dimethyl-1,4-Phenylene)Oxide. *ACS Appl. Polym. Mater.* **2020**, *2* (8), 3518–3524. https://doi.org/10.1021/acsapm.0c00532.

(18) Kanters, J. A.; Kroon, J.; Peerdeman, A. F.; Schoone, J. C. Conformation of Some Carboxylic Acids and Their Derivatives. *Tetrahedron* **1967**, *23* (10), 4027–4033. https://doi.org/10.1016/S0040-4020(01)97912-8.

(19) Rizzo, P.; Cozzolino, A.; Guerra, G. Chemical Stabilization of Hexanal Molecules by Inclusion as Guests of Nanoporous-Crystalline Syndiotactic Polystyrene Crystals. *Macromolecules* **2019**, *52* (6), 2255–2264. https://doi.org/10.1021/acs.macromol.8b02168.

(20) Golla, M.; Nagendra, B.; Daniel, C.; Rizzo, P.; Guerra, G. Isolated and Aggregated Carvacrol Guest Molecules in Cocrystalline Poly(2,6-Dimethyl-1,4-Phenylene)Oxide Films. *Polym. J.* **2021**, *53* (10), 1093–1100. https://doi.org/10.1038/s41428-021-00511-0.

(21) Immirzi, A.; de Candia, F.; Iannelli, P.; Zambelli, A.; Vittoria, V. Solvent-Induced Polymorphism in Syndiotactic Polystyrene. *Makromol. Chem. Rapid Commun.* **1988**, *9* (11), 761–764. https://doi.org/10.1002/marc.1988.030091108.

(22) Acocella, M. R.; Rizzo, P.; Daniel, C.; Tarallo, O.; Guerra, G. Nanoporous Triclinic δ Modification of Syndiotactic Polystyrene. *Polymer* **2015**, *63*, 230–236. https://doi.org/10.1016/j.polymer.2015.02.058.

(23) Cozzolino, A.; Rizzo, P.; Gallo, C.; Bianchi, R.; Daniel, C.; Guerra, G. Axially Oriented Guest Induced Crystallization in Syndiotactic Polystyrene Unstretched Fibers. *Polymer* **2021**, *228*, 123908. https://doi.org/10.1016/j.polymer.2021.123908.

(24) Cozzolino, A.; Monaco, G.; Daniel, C.; Rizzo, P.; Guerra, G. Monomeric and Dimeric Carboxylic Acid in Crystalline Cavities and Channels of Delta and Epsilon Forms of Syndiotactic Polystyrene. *Polymers* **2021**, *13* (19), 3330. https://doi.org/10.3390/polym13193330.

(25) Ayranci, E.; Akgul, G. Apparent Molar Volumes and Viscosities of Lauric, Palmitic, and Stearic Acids in 2-Butanol at (20, 30, 40, and 60) °C. *J. Chem. Eng. Data* **2003**, *48* (1), 56–60. https://doi.org/10.1021/je025538u.

(26) Gadgoli, C.; Mishra, S. H. Antihepatotoxic Activity of P-Methoxy Benzoic Acid from Capparis Spinosa. *J. Ethnopharmacol.* **1999**, *66* (2), 187–192. https://doi.org/10.1016/S0378-8741(98)00229-3.

(27) Park, E.-S.; Moon, W.-S.; Song, M.-J.; Kim, M.-N.; Chung, K.-H.; Yoon, J.-S. Antimicrobial Activity of Phenol and Benzoic Acid Derivatives. *Int. Biodeterior. Biodegrad.* **2001**, *47* (4), 209–214. https://doi.org/10.1016/S0964-8305(01)00058-0.

(28) Amborabé, B.-E.; Fleurat-Lessard, P.; Chollet, J.-F.; Roblin, G. Antifungal Effects of Salicylic Acid and Other Benzoic Acid Derivatives towards Eutypa Lata: Structure–Activity Relationship. *Plant Physiol. Biochem.* **2002**, *40* (12), 1051–1060. https://doi.org/10.1016/S0981-9428(02)01470-5.

(29) *Benzoic Acid and Sodium Benzoate: IPCS, International Programm on Chemical Safety (IPCS)*; Wibbertmann, A., International Programme on Chemical Safety, Eds.; Concise international chemical assessment document; World Health Organization: Geneva, 2000.

(30) Johnson, W.; Bergfeld, W. F.; Belsito, D. V.; Hill, R. A.; Klaassen, C. D.; Liebler, D. C.; Marks, J. G.; Shank, R. C.; Slaga, T. J.; Snyder, P. W.; Andersen, F. A. Safety Assessment of Benzyl Alcohol, Benzoic Acid and Its Salts, and Benzyl Benzoate. *Int. J. Toxicol.* **2017**, *36* (3_suppl), 5S-30S. https://doi.org/10.1177/1091581817728996.

(31) Rao, K. V. R.; Devi, K. P.; Buri, P. Influence of Molecular Size and Water Solubility of the Solute on Its Release from Swelling and Erosion Controlled Polymeric Matrices. *J. Controlled Release* **1990**, *12* (2), 133–141. https://doi.org/10.1016/0168-3659(90)90089-C.

(32) Böttcher, H.; Jagota, C.; Trepte, J.; Kallies, K.-H.; Haufe, H. Sol–Gel Composite Films with Controlled Release of Biocides. *J. Controlled Release* **1999**, *60* (1), 57–65. https://doi.org/10.1016/S0168-3659(99)00053-X.

(33) Byrne, R. S.; Deasy, P. B. Use of Commercial Porous Ceramic Particles for Sustained Drug Delivery. *Int. J. Pharm.* **2002**, *246* (1–2), 61–73. https://doi.org/10.1016/S0378-5173(02)00357-5.

(34) López-Periago, A.; Argemí, A.; Andanson, J. M.; Fernández, V.; García-González, C. A.; Kazarian, S. G.; Saurina, J.; Domingo, C. Impregnation of a Biocompatible Polymer Aided by Supercritical CO2: Evaluation of Drug Stability and Drug–Matrix Interactions. *J. Supercrit. Fluids* **2009**, *48* (1), 56–63. https://doi.org/10.1016/j.supflu.2008.09.015.

(35) Sruthi, R.; Balagangadharan, K.; Selvamurugan, N. Polycaprolactone/Polyvinylpyrrolidone Coaxial Electrospun Fibers Containing Veratric Acid-Loaded Chitosan Nanoparticles for Bone Regeneration. *Colloids Surf. B Biointerfaces* **2020**, *193*, 111110. https://doi.org/10.1016/j.colsurfb.2020.111110.

(36) Biswal, A. K.; Thodikayil, A. T.; Saha, S. PH-Sensitive Acetalated Dextran/PLGA-Based Double-Layered Microparticles and Their Application in Food Preservation. *ACS Appl. Bio Mater.* **2021**, *4* (3), 2429–2441. https://doi.org/10.1021/acsabm.0c01361.

(37) Boczar, M.; Szczeponek, K.; Wójcik, M. J.; Paluszkiewicz, C. Theoretical Modeling of Infrared Spectra of Benzoic Acid and Its Deuterated Derivative. *J. Mol. Struct.* **2004**, *700* (1–3), 39–48. https://doi.org/10.1016/j.molstruc.2004.03.024.

(38) Linstrom, P. NIST Chemistry WebBook, NIST Standard Reference Database 69, 1997. https://doi.org/10.18434/T4D303.

(39) Stepanian, S. G.; Reva, I. D.; Radchenko, E. D.; Sheina, G. G. Infrared Spectra of Benzoic Acid Monomers and Dimers in Argon Matrix. *Vib. Spectrosc.* **1996**, *11* (2), 123–133. https://doi.org/10.1016/0924-2031(95)00068-2.

(40) Guerra, G.; Daniel, C.; Rizzo, P.; Tarallo, O. Advanced Materials Based on Polymer Cocrystalline Forms. *J. Polym. Sci. Part B Polym. Phys.* **2012**, *50* (5), 305–322. https://doi.org/10.1002/polb.23035.

(41) De Rosa, C.; Guerra, G.; Petraccone, V.; Pirozzi, B. Crystal Structure of the Emptied Clathrate Form (δ_eForm) of Syndiotactic Polystyrene. *Macromolecules* **1997**, *30* (14), 4147–4152. https://doi.org/10.1021/ma970061q.

(42) Chatani, Y.; Shimane, Y.; Inagaki, T.; Ijitsu, T.; Yukinari, T.; Shikuma, H. Structural Study on Syndiotactic Polystyrene: 2. Crystal Structure of Molecular Compound with Toluene. *Polymer* **1993**, *34* (8), 1620–1624. https://doi.org/10.1016/0032-3861(93)90318-5.

(43) Tarallo, O.; Petraccone, V.; R. Albunia, A.; Daniel, C.; Guerra, G. Monoclinic and Triclinic δ-Clathrates of Syndiotactic Polystyrene. *Macromolecules* **2010**, *43* (20), 8549–8558. https://doi.org/10.1021/ma1013513.

(44) Petraccone, V.; Ruiz de Ballesteros, O.; Tarallo, O.; Rizzo, P.; Guerra, G. Nanoporous Polymer Crystals with Cavities and Channels. *Chem. Mater.* **2008**, *20* (11), 3663–3668. https://doi.org/10.1021/cm800462h.

(45) Golla, M.; Nagendra, B.; Daniel, C.; Rizzo, P.; Guerra, G. Axial Orientation of Co-Crystalline Phases of Poly(2,6-Dimethyl-1,4-Phenylene)Oxide Films. *Polymers* **2020**, *12* (10), 2394. https://doi.org/10.3390/polym12102394.

(46) Auriemma, F.; Daniel, C.; Golla, M.; Nagendra, B.; Rizzo, P.; Tarallo, O.; Guerra, G. Polymorphism of Poly(2,6-Dimethyl-1,4-Phenylene) Oxide (PPO): Co-Crystalline and Nanoporous-Crystalline Phases. *Polymer* **2022**, *258*, 125290. https://doi.org/10.1016/j.polymer.2022.125290.

(47) Nagendra, B.; Cozzolino, A.; Daniel, C.; Rizzo, P.; Guerra, G.; Auriemma, F.; De Rosa, C.; D'Alterio, M. C.; Tarallo, O.; Nuzzo, A. Two Nanoporous Crystalline Forms of Poly(2,6-Dimethyl-1,4-Phenylene)Oxide and Related Co-Crystalline Forms. *Macromolecules* **2019**, *52* (24), 9646–9656. https://doi.org/10.1021/acs.macromol.9b01911.

CHAPTER 5
Co-crystalline axially oriented sPS fibers

This chapter gives details about a very unusual phenomenon of both crystallization as well as axial orientation in sPS unstretched fibers by different guests. Moreover, some of these guests shows antimicrobial activity. So, in addition, the release of these antimicrobials (i.e.. eugenol, and the phenolic isomers carvacrol and thymol) from these axially oriented co-crystalline (CC) sPS fibers has been also investigated.

5.1 Guest-induced axial orientation in sPS fibers

Crystalline phase orientations, axial and planar, can be generally obtained for polymers by axial and biaxial stretching, respectively.[1–5]

For CC phases between polymer hosts and low-molecular-mass molecules, different kinds of planar orientations can be easily prepared, even in the absence of mechanical stretching.

For sPS films, especially, different kinds of uniplanar orientations, i.e. of preferential orientation of a crystalline plane with respect to the film plane, have been obtained depending on the film preparation procedure as well as on the chemical nature of the guest.[6–12]

Uniplanar orientations of sPS can be maintained[9] not only after guest-exchange[13] but also after suitable guest removal procedures leading to NC phases.[14]

It is also worth adding that for sPS by combining axial or unbalanced biaxial stretching with co-crystallization procedures, as induced by selected guest molecules, two different kinds of uniplanar-axial orientations have also been achieved.[15] These orientations exhibit the polymer chain axis (***c***-axis) parallel to the main draw direction and a crystal plane parallel or perpendicular to the film plane.

Moreover, high degrees of axial orientation can be obtained for CC, NC and dense crystalline (α, β, γ) phases of sPS by usual axial stretching procedures on polymer films and fibers as well as by high-speed melt spinning processes.[16]

In this section, guest-induced crystallization and at the same time axial orientation in essentially unoriented amorphous melt-spun fibers is reported.

5.1.1 WAXD and Birefringence characterization

For a 35 μm melt-spun sPS fiber (as obtained by a melt spinning process with a take-up speed of 80 m/min), a WAXD pattern and the corresponding radial $2\theta_{CuK\alpha}$ scan are shown in Figures 5.1a and a′, respectively. The broad halos occurring in the $2\theta_{CuK\alpha}$ scan (Figure 5.1a′) indicate that the fibers are fully amorphous while the uniform rings of the 2D pattern (Figure 5.1a) indicate that the spinning procedure does not lead to appreciable axial orientation. It is worth adding that melt-spun sPS fiber of similar diameter, but obtained by a take-up speed of 2000 m/min, exhibit WAXD patterns very similar to those of Figure 5.1a,a′.

The occurrence of very low axial orientations can be however established by optical birefringence measurements. In fact, in agreement with data reported in Figure 3 of Ref.[16], birefringence ($\Delta n = n_{//} - n_{\perp}$) of sPS amorphous fibers, as obtained with take-up speeds of 80m/min and 2000m/min, are –0.007 ± 0.001 and –0.014 ± 0.002, respectively.

Nearly negligible orientation also characterizes both kinds of fibers after their thermal crystallization in the α-form as induced by annealing at 200 °C.[20,21] In fact, uniform diffraction rings, at $2\theta_{CuK\alpha} \approx 6.8°$, 11.8°, 13.5° and 20.5°, corresponding to (110), (300), (220) and (211) reflections, typical of the α′-form are observed.[21] Correspondingly, the birefringence of these α′-form fibers remains nearly unchanged with respect to those of the starting amorphous films.

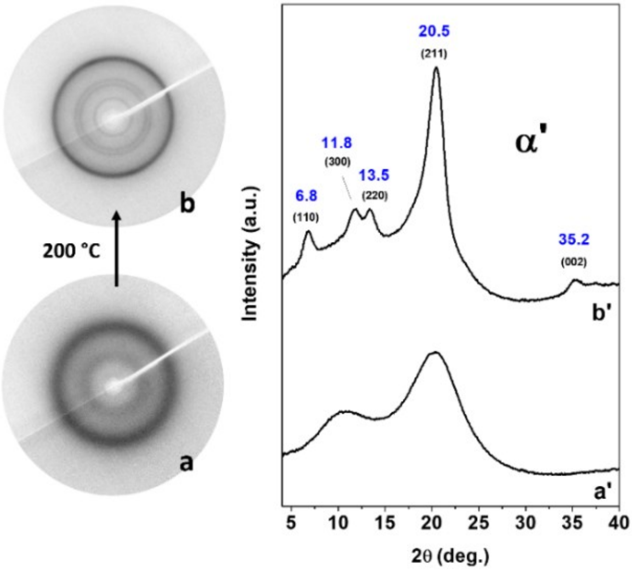

Figure 5.1 WAXD patterns of sPS amorphous fibers, as obtained by melt-spinning at take-up velocity of 80 m/min, before (a,a′) and after thermal crystallization (in α′-form) by annealing at 200 °C (b,b′). (a,b) 2D patterns; (a′,b′) radial intensity scans vs the diffraction angle $2\theta_{CuK\alpha}$.

Completely different behavior is observed for guest-induced crystallization of these amorphous unstretched fibers. In fact, the 2D patterns of amorphous fibers (Figure 5.1a,a′), after guest-induced crystallization, show the presence of diffraction arcs rather than of uniform diffraction rings (Figure 5.2), thus indicating the achievement of axial orientation of the crystalline phases, already in the absence of mechanical stretching.

WAXD patterns of the 35 μm amorphous sPS fiber after room temperature sorption of liquid dichloromethane (DCM), dimethyl naphthalene (DMN) and eugenol, with guest content close to 15, 34 and 35 wt% are shown in Figures 5.2a-c, respectively.

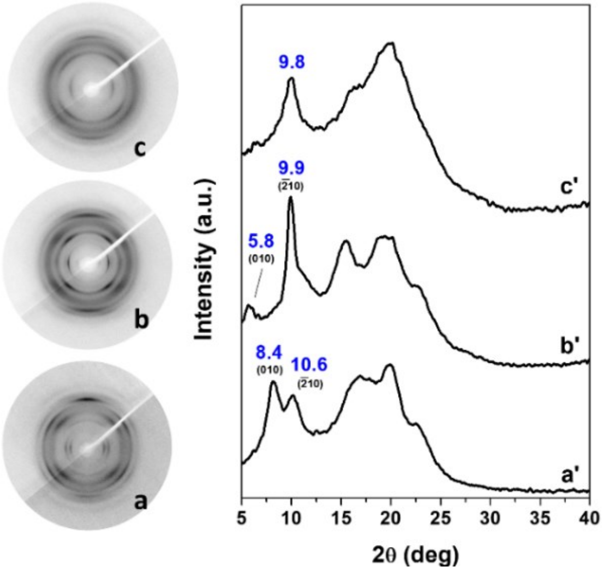

Figure 5.2 WAXD patterns of sPS amorphous melt-spun fibers after crystallization as induced by liquid guest sorption: (a,a′) DCM, leading to a monoclinic δ-clathrate phase; (b,b′) DMN, leading to a δ-intercalate phase; (c,c′) eugenol, leading to a disordered crystalline form. (a-c) 2D patterns; (a′-c′) equatorial intensity scans vs the diffraction angle $2\theta_{CuK\alpha}$.

The patterns of Figure 5.2a,a′ show the presence of two intense equatorial reflection arcs at $2\theta_{CuK\alpha} \approx 8.4°$ and 10.6°, corresponding to 010 and $\bar{2}10$ reflections, respectively,[22] as typical of monoclinic δ-clathrate phases[23] with DCM.[24] The observed reflections are collected in the left part of Table 5.1.

WAXD patterns of the amorphous sPS fiber after room temperature sorption of liquid DMN show the presence of the intercalate sPS/DMN phase,[25] with equatorial peaks at $2\theta_{CuK\alpha} \approx 5.8°$ and 9.9° corresponding to 010 and $\bar{2}10$ reflections (Figure 5.2b’). The observed reflections are collected in the central part of Table 5.1.

WAXD patterns of the amorphous sPS fiber after sorption of eugenol (Figure 5.2 c,c') only exhibits few diffraction peaks: mainly an equatorial reflection (with $2\theta_{CuK\alpha} \approx 9.8°$, $d = 0.90_0$ nm, i.e. intermediate between those of the 010 and $\bar{2}10$ reflections of monoclinic δ-form); a meridional reflection ($2\theta_{CuK\alpha} \approx 22.7°$, $d = 0.39_1$ nm); two broad reflections on the first layer line (at $2\theta_{CuK\alpha} \approx 16.2°$ and $2\theta \approx 19.7°$). The observed reflections are collected in the right part of Table 5.1. This indicates the occurrence of a disordered crystalline phase including, as the clathrate and intercalate CC phases of Figure 5.2a and b, ***s***(2/1)2 helical chains with typical periodicity of 0.78 nm. The presence of only one equatorial reflection suggests a hexagonal packing of the helical polymer chains axes, with $a = 1.05$ nm. Similar WAXD patterns corresponding to disordered crystalline phases are obtained by guest induced crystallization with many other guests, like methylethylketone, ethylacetate or methylacetate.[26]

The degree of axial orientation, as obtained by guest induced crystallization, is always high ($f_c \approx 0.75$) and is particularly high for the intercalate sPS/DMN phase ($f_c = 0.85$, Figure 5.2b).

Similarly, birefringence increases up to $\Delta n = -0.026 \pm 0.002$, nearly independently of the considered take-up speed range (80–2000 m/min) as well as of the crystallization inducing guest. Definitely higher is birefringence of the intercalate sPS/DMN phase ($\Delta n = -0.069 \pm 0.002$).

After guest removal from the fibers of Figure 5.2 (by ACN sorption/desorption at room temperature) WAXD patterns of Figure 5.3 are observed. In particular, after DCM guest removal from the δ-clathrate fiber, WAXD patterns (Figure 5.3a,a′) show an intense 010 reflection at $2\theta_{CuK\alpha} \approx 8.4°$ and very low intensity of the $\bar{2}10$ reflection at $2\theta_{CuK\alpha} \approx 10°$, which indicate the formation of the monoclinic NC δ-form.[23]

After DMN guest removal from the δ-intercalate fiber, WAXD patterns (Figure 5.3b,b′) are very similar to those of the disordered crystalline phase, as obtained by eugenol induced crystallization (Figure 5.2c,c′). It is worth adding that the 2D pattern of Figure 5.3b is a fiber pattern of the disordered NC form that was already obtained in unstretched samples, by guest removal from intercalate sPS/DMN phases.[26]

WAXD patterns of the crystalline fiber as crystallized by eugenol sorption, after eugenol removal, are only slightly changed. In fact WAXD patterns of Figure 5.3c,c′ are very similar to those of Figures 5.2c,c′ with only a minor shift of the equatorial peak from 9.8° to 9.7°.

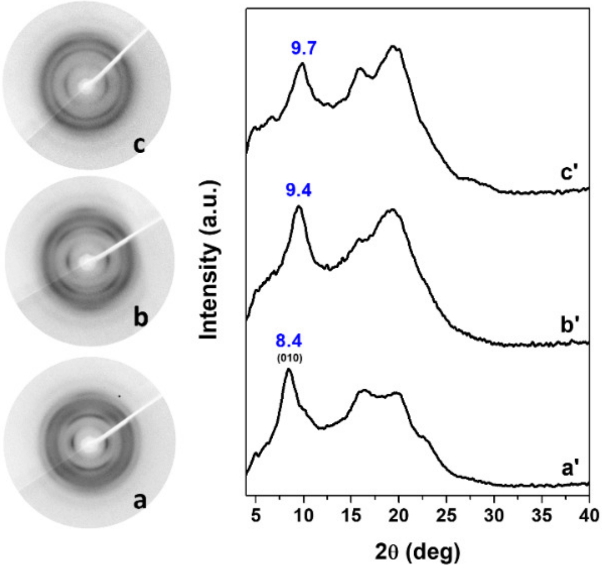

Figure 5.3 WAXD patterns of sPS amorphous melt-spun fibers after guest induced crystallization followed by complete guest desorption: (a,a′) sorption/desorption of DCM, leading to the monoclinic δ-form; (b,b′) sorption/desorption of DMN, leading to a disordered crystalline form; (c,c′) sorption/desorption of eugenol, leading to a disordered crystalline form. (a–c) 2D patterns; (a′–c′) equatorial intensity scans vs the diffraction angle $2\theta_{CuK\alpha}$.

This guest-induced axially oriented crystallization not only occurs by guest sorption by fiber immersion in pure liquid but can also occur by sorption of the guest from diluted aqueous solutions. This is shown, for instance, by WAXD patterns of sPS amorphous fibers, after equilibrium eugenol uptake from 0.1% aqueous solution, 1% aqueous emulsion (water solubility of 2460 mg/L at 25 °C) and liquid eugenol which are shown by patterns a,a′, b,b′ and cc′ in Figure 5.4, respectively. The eugenol content evaluated by TGA measurements is of 3, 34 and 35 wt% for 0.1% aqueous solution, 1% aqueous emulsion and liquid eugenol treatments, respectively.

It is worth adding that the result obtained for a dilute eugenol aqueous solution (Figure 5.4a,a′) is particularly relevant for a possible industrial production. In fact, immersion of amorphous sPS fibers, (as produced by industrial melt-spinning plants), in an eco-friendly dilute aqueous solution is sufficient to get, beside large uptake of the antimicrobial guest, crystallization as well as remarkable axial orientation.

A plausible mechanism to rationalize the spontaneous axial orientation of crystallites of unstretched sPS fibers upon co-crystallization with organic guest molecules could be based on co-crystalline fibril formation in confined space. In fact, CC phase formation can occur only behind the advancing guest penetration front, which moves radially toward the fiber axis. The nano-confinement of crystalline fibrils in the cylindrical crown of the fiber could favor their orientation parallel rather than perpendicular to the fiber axis.

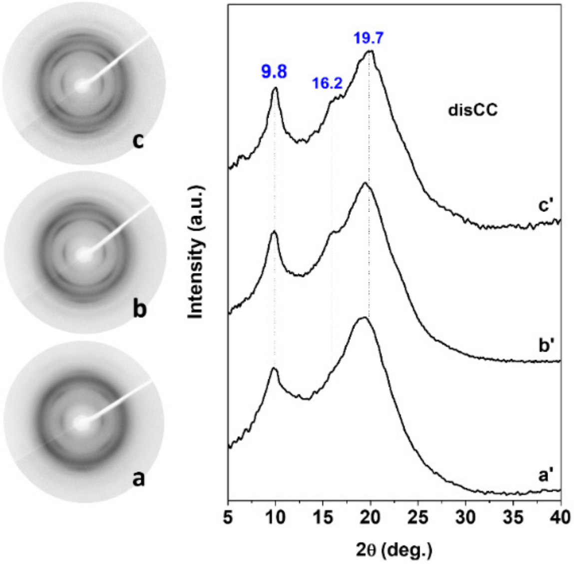

Figure 5.4 WAXD patterns of sPS amorphous melt-spun fibers after crystallization as induced by eugenol sorption from 0.1 wt% aqueous solution (a,a′); 1 wt% aqueous emulsion (b,b′); liquid eugenol (c,c′). (a–c) 2D patterns; (a′–c′) equatorial intensity scans vs the diffraction angle $2\theta_{CuK\alpha}$.

Table 5.1 Diffraction angles ($2\theta_{CuK\alpha}$), Bragg distances (*d*) and relative intensities (I) of the reflections on the layer lines (*l*) of WAXD patterns of axially-oriented δ-clathrate with DCM, δ-intercalate with DMN and disordered crystalline form with eugenol. Miller indexes (*hkl*) of the reflections of clathrate and intercalate phases are also indicated.

l	*δ-clathate sPS/DCM*				*δ-intercalate sPS/DMN*				*Disordered crystalline sPS with eugenol*		
	$2\theta_{CuK\alpha}$ (deg)	***d (nm)***	***I***	***hkl***	***$2\theta_{CuK\alpha}$ (deg)***	***d (nm)***	***I***	***hkl***	***$2\theta_{CuK\alpha}$ (deg)***	***d (nm)***	***I***
0	8.4	1.049	s	(010)	5.8	1.522	w	(010)			
0	10.6	0.833	ms	$(\bar{2}10)$	9.9	0.890	s	$(\bar{2}10)$	9.8	0.900	s
0					11.5	0.768	vvw	(020)			
0					15.4	0.57_4	br	$(\bar{2}30)$			
0					20.0	0.44_2	br	$(\bar{2}40)$			
1	13.5	0.654	vvw	(101) $(\bar{1}11)$	12.7	0.696	vw	$(\bar{1}11)$			
1	17.4	0.508	vs	(111)	14.9	0.593	vs	$(\bar{1}21)$	16.2	0.547	vs
1	20.8	0.426	s	$(\bar{3}21)$ (211) (301)	19.1	0.46_5	br	(301) (121) $(\bar{3}31)$ $(\bar{3}21)$	19.7	0.45_1	br
1	23.6	0.376	w	$(\bar{4}11)$ $(\bar{4}21)$							
2	22.8	0.389	s	(002)	22.7	0.391	s	(002)	22.7	0.391	s

5.1.2 Thermal treatments

The high degrees of axial orientation, as obtained by guest induced crystallizations on amorphous sPS fibers (Figure 5.2), are also maintained after thermal treatments leading to crystal-to-crystal transitions, even associated with relevant changes of polymer chain conformation. This is shown, for instance, for a disordered CC fiber as crystallized and axially oriented by sorption of liquid eugenol, whose WAXD patterns before and after annealing at 200 °C are shown in Figure 5.5a,a′ and b,b′, respectively. In fact, the WAXD pattern of Figure 5.5b shows the presence of reflections arcs typical of the α′-form, with a high degree of orientation (f_c = 0.84). This high degree of orientation is observed irrespective of the drastic conformational change of the polymer chain, from helical ***s***(2/1)2 to zig-zag planar.[20]

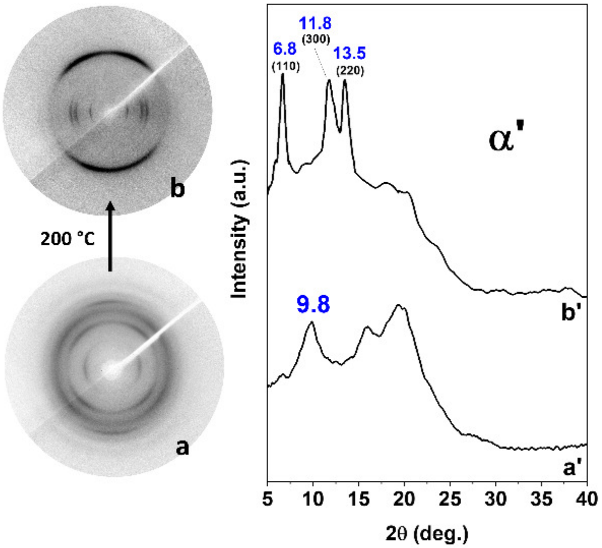

Figure 5.5 WAXD patterns of an amorphous sPS fiber, after crystallization and orientation as induced by liquid eugenol sorption leading to a disordered CC phase (a,a′) and after subsequent thermal treatment at 200°C leading to the α′-form (b,b′). (a,b) 2D patterns; (a′,b′) equatorial intensity scans vs the diffraction angle $2\theta_{CuK\alpha}$.

Birefringence measured for the axially oriented fiber of Figure 5.5a, exhibiting a disordered NC form and hence ***s***(2/1)2 helical chains,[26] is Δn = –0.026 while birefringence measured for the axially oriented fiber of Figure 5.5b, exhibiting the α′-form and hence zig-zag planar chains,[20] is markedly higher Δn = –0.14.

As already observed for axially stretched sPS films,[27] although orientation factors of crystalline phases with helical and zig-zag planar crystalline phases are similar, birefringence values are largely different. This has been rationalized on the basis of the orientation of the phenyl rings of the crystalline chains with respect to the chain axis, being completely different for the two polymer conformations.[27]

5.2 Antimicrobial guest release from CC axially oriented sPS fibers

Relevant antimicrobial properties have been described for phenolic components (such as thymol, carvacrol and eugenol) of essential oils (EOs), i.e., of aromatic oily liquids obtained from plant materials (flowers, seeds, leaves, herbs, wood, fruits and roots). In addition to antibacterial properties[28], these phenolic compounds exhibit antiviral[29], antimycotic[30], antitoxigenic[31], antiparasitic[32], and insecticidal[33] properties.

It is worth noting that the use of natural antimicrobial agents, such as EOs, is considered as a valid alternative therapeutic strategy to conventional synthetic drugs that are commonly used nowadays in medicine, agriculture, cosmetics and food industry.[34] In recent years, the combination of EOs with engineered materials has emerged as a promising approach for several applications.

In fact, since EOs are naturally found in plants, they have the added advantage of being relatively inexpensive and biodegradable and, therefore bioaccumulation is not a concern. There is, hence, a significant interest in developing carrier systems of these natural antimicrobial compounds, trying to manage the control of their release in the environment. In this regard, various materials in different morphologies, including micro/nanofibers[35–40], films[41], nano/microparticles[37,42–44], surface coatings[45], and hydrogels[46], are being developed as carrier or matrices for incorporating EOs in material complexes especially for biomedical applications. Also polymers have been explored as materials for microcapsule shells, such as chitosan and cellulose, but the encapsulation efficiency achieved ranged from 20–75% and a burst release was observed in the early stages.[47–51]

It is well known that the release of guest molecules from CC sPS phases is generally slower from the crystalline phases than from the corresponding amorphous phase[52]; the kinetic release can be further maximized controlling the orientation of the host crystalline phase.[6,53–57]

In this section, the solvent-induced crystallization as well as axial orientation of sPS unstretched fibers by using eugenol is explored similarly for other natural antimicrobials, i.e. the phenolic isomers carvacrol and thymol. Their release in air during time from sPS fibers is also investigated.

5.2.1 Release of eugenol from CC sPS oriented fibers

Eugenol sorption in amorphous unstreched sPS fibers leds to crystallization as well as axial orientation.[58]

This axial orientation as well as crystallization not only occurs by sorption of pure liquid but can also happen by sorption of the guest from diluted aqueous solutions. This phenomenon was clearly shown, in the previous section (5.1), by WAXD patterns of sPS amorphous fibers, after equilibrium eugenol uptake from 0.1% aqueous solution, 1% aqueous emulsion and liquid eugenol (patterns a,a′, b,b′ and c,c′ in Figure 5.4, respectively). The eugenol content in the axially oriented CC sPS fibers, evaluated by thermogravimetric measurements, after immersion in 0.1% aqueous solution, 1% aqueous emulsion and liquid eugenol, is almost 3, 34 and 35 wt%, respectively. It is worth noting that the eugenol uptake after treatment with 1% aqueous emulsion and liquid eugenol is nearly the same (34-35 wt%). The action induced by pure liquid eugenol seems to be equal to that induced by eugenol 1% aqueous emulsion.

sPS fibers after treatments by 0.1% aqueous solutions and 1% aqueous emulsion have also been characterized by FTIR analysis by DRIFT method (Figure 5.6). The spectral region 3150–3750 cm^{-1} shows a broad band centered at 3447 cm^{-1} and a sharper band located at 3527 cm^{-1} (Figure 5.6b,c), these FTIR bands are present also in the FTIR spectrum of pure eugenol (Figure 5.6, pink line).

Moreover, FTIR spectra particularly for the axially oriented CC sPS fibers after immersion in 1% aqueous emulsion (Figure 5.6c) show the presence of other peaks related to eugenol (i.e. 649, 794, 819 and 995 cm^{-1}) as well as the sharp peak at 571 cm^{-1} due to the crystallization of sPS fibers in ***s***(2/1)2 helical conformation[59]. FTIR peaks of eugenol absorbed in the CC sPS fibers after immersion in 0.1% aqueous solution reported in Figure 5.6b are almost negligible due to the low amount (3 wt%).

The desorption kinetic of eugenol from these axially oriented CC sPS fibers are reported in Figure 5.7.

For the axially oriented CC sPS fibers with an initial content close to 34 wt%, after treatment with 1% aqueous emulsion (red squares in Figure 5.7A), a fast initial desorption (up to 200 days) is apparent followed by a slower release.

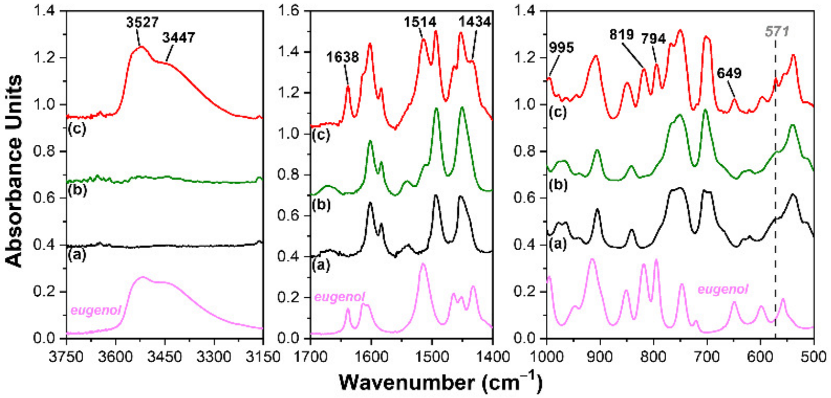

Figure 5.6. FTIR spectra in the ranges 500–1000, 1400–1700 and 3150–3750 cm^{-1} of sPS amorphous fibers (a) before and after crystallization as induced by (b) 0.1% eugenol aqueous solution and (c) 1% eugenol aqueous solution. FTIR spectra of pure liquid eugenol is also reported in the bottom (pink line).

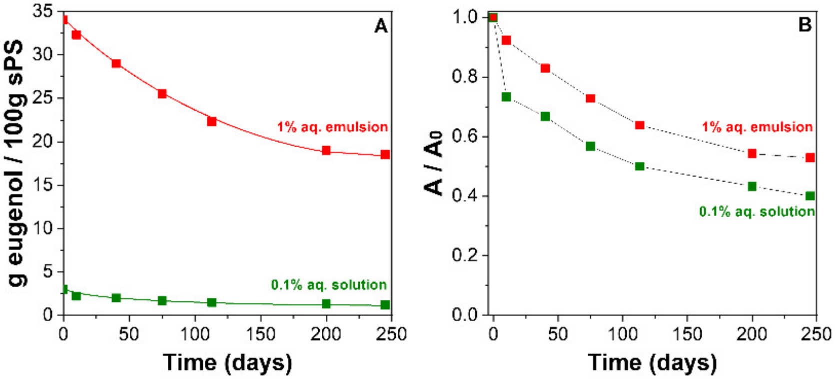

Figure 5.7 Eugenol desorption as at room temperature (A) as grams of guest per 100 grams of polymer and (B) as reduction absorbance of eugenol spectral bands, from sPS fibers with: (red squares) eugenol initial content of 34 wt% as obtained by immersion in 1% eugenol aqueous emulsion; (green squares) eugenol initial content of 3 wt% as obtained by immersion in 0.1% eugenol aqueous solution.

As for the axially oriented CC sPS fibers after treatment with 0.1% aqueous solution (green squares in Figure 5.7A), the initial content of 3 wt% slowly decreases reaching a loss of nearly 50% after 120 days.

It is well known that the initial kinetic desorption of the guest in sPS samples is fast and occurs prevailingly by the amorphous phase while a slower guest desorption involves the CC phases.[60] Also in this case, a same phenomenon occurs for both axially oriented CC sPS fibers with eugenol and it seems more evident for CC sPS fibers after treatment with 1% aqueous emulsion due to a large guest uptake (34 wt%, red squares, Figure 5.7A).

The quantitative evaluation of the guest desorption was also performed considering the absorbance ratio A/A_0, where A_0 is the peak absorbance in the spectrum of the freshly prepared CC fibers while *A* is the peak absorbance at a certain desorption time. This absorbance ratio is reported versus the desorption time (Figure 5.7B).

Comparing the eugenol desorption kinetics from both axially oriented CC sPS fibers (Figure 5.7B), it is clearly evident that both kinetics are identical, a slightly difference is only at the beginning (up to 12 days), where the release seems to be higher for the CC sPS fibers after treatment with 0.1% aqueous solution (green squares in Figure 5.7B).

This is probably due to a lower degree of crystallinity of CC sPS fibers with eugenol initial content of 3 wt%, as shown also by WAXD patterns of Figure 5.4a,a′ (diffraction arcs less intense compared to those of Figure 5.4b,b′ for CC sPS fibers with eugenol initial content of 34 wt%).

It is worth adding that this slow release can ensure long-term antimicrobial effect of the sPS fibers (or a fabric made with them) which can be involved in different applications, especially for biomedical practices where the inhibition of microorganisms' growth is very crucial. Additionally, the procedure to get fibers with antimicrobial property is very easy, considering that a simple aqueous solution with 0.1% of eugenol is needed.

5.2.2 Release of phenolic isomers from CC sPS oriented fibers

Carvacrol and thymol molecules have been recognized as the principal active compounds extracted from thyme (*Thymus vulgaris*).[61] Both molecules show not only excellent antibacterial[62–65] and fungicidal activities,[66,67] but also they were found to be active against viral particles[68,69] as well as larvae and adult insects.[70,71]

Their schematics are reported in Figure 5.8a and b, respectively. Carvacrol is liquid while thymol is solid at room temperature, and they are structural isomers presenting the hydroxyl group (–OH) in different positions in the aromatic ring.[72]

A WAXD pattern of sPS fibers with a diameter of 35 μm, as obtained by a melt spinning process, is shown in Figure 5.9a′ and the presence of broad halos indicates that fibers are fully amorphous. These amorphous sPS fibers are immersed for 10 minutes in pure liquid carvacrol as well as in a 30 wt% thymol methyl acetate (MA) solution and their WAXD patterns are shown in Figure 5.9b,c. The presence of diffraction arcs is apparent, indicating the occurrence of crystallization associated to a development of axial orientation. The same phenomenon, which occurs also for the antimicrobial eugenol, as shown in the previous section (5.1), is here confirmed likewise for these phenolic isomers. The degree of axial orientation (f_c), evaluated via the Herman's orientation function (according to ref [58]), is ~0.75.

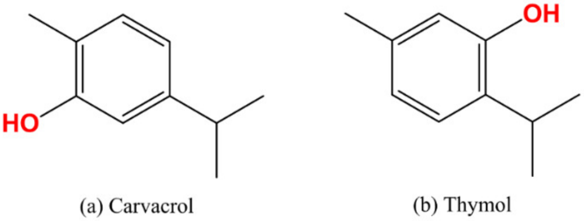

Figure 5.8 Schematic of (a) Carvacrol and (b) Thymol molecular structures.

2D-patterns in Figure 5.9b′,c′ exhibit one single equatorial peak located at $2\theta_{\mathrm{CuK\alpha}}$ value of ≈ 9.8°, due to the presence of the crystalline disordered phase which is a modification formed of small bundles of ***s***(2/1)2 helical chain with typical periodicity of 0.78 nm.[26,58]

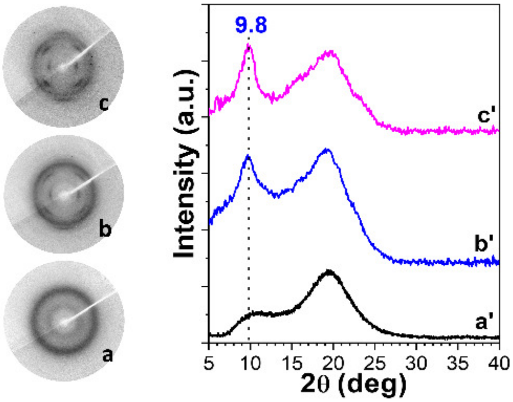

Figure 5.9 WAXD patterns of sPS amorphous fibers, as obtained by melt-spinning (a,a′) before and after crystallization as induced by (b,b′) thymol/MA solution and (c,c′) liquid carvacrol sorption. (a-c) 2D patterns; (a′-c′) radial intensity scans vs the diffraction angle $2\theta_{\mathrm{CuK\alpha}}$.

sPS fibers after treatments by pure carvacrol or thymol/MA solution have also been characterized by FTIR analysis using DRIFT method (Figure 5.10). Particularly informative is the spectral region 3150–3750 cm^{-1} showing a broad band centered at c.a. 3400 cm^{-1} present in pure carvacrol and thymol and a new sharp band located at 3540 cm^{-1} for thymol CC sample (curve b) and 3552 cm^{-1} for carvacrol CC sample (curve c). Moreover, FTIR spectra show the presence of other peaks related to the guests (i.e. 637, 813, 865, 939 and 993 cm^{-1} for carvacrol and 809, 851 and 944 cm^{-1} for thymol) as well as to the sharp peak at 571 cm^{-1} due to the crystallization of sPS fibers in ***s***(2/1)2 helical conformation.[59]

Carvacrol and thymol amount, determined by TGA measurements, is nearly 28 and 16 wt% for fibers immersed in carvacrol and thymol/MA solution, respectively.

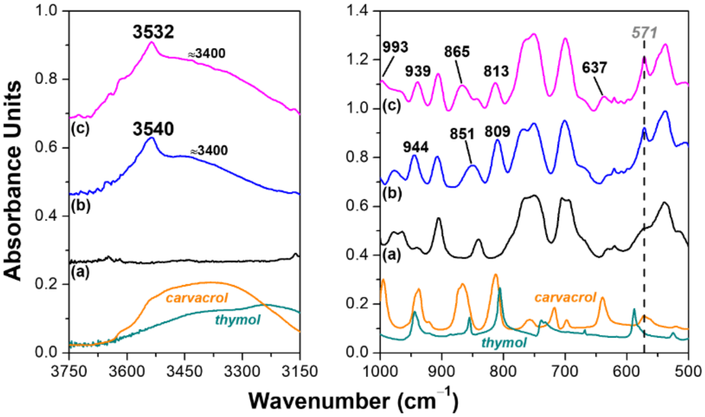

Figure 5.10 FTIR spectra in the ranges 500–1000 and 3150–3750 cm^{-1} of sPS amorphous fibers (a) before and after crystallization as induced by (b) thymol/MA solution and (c) liquid carvacrol sorption. FTIR spectra of pure liquid carvacrol and thymol are also reported in the bottom (orange and green lines, respectively).

An useful tool to understand the host-guest interactions in a polymer matrix, in particular the presence of new extra FTIR peaks, are polarized FTIR measurements.[73,74] Polarized FTIR analysis of axially oriented sPS δ-form films before and after immersion in carvacrol and in thymol/MA solution overnight at room temperature have been also performed and shown in Figures 5.11 and 5.12, respectively.

FTIR peaks located at 813, 858, 993, 1115, 1174, 1228, 1254 cm^{-1} related to carvacrol molecules[75] in sPS film are apparent and, as shown, they are poorly dichroic (Figure 5.11, curve b). More informative is the spectral region 3200–3600 cm^{-1} (Figure 5.11), in which a dichroic narrow peak at 3532 cm^{-1} is present. A similar behavior is displayed also for axially oriented sPS δ-form film after immersion in the thymol/MA solution overnight at room temperature. In Figure 5.12 FTIR peaks of thymol[75] located at 808, 1087 and 1290 cm^{-1} are poorly dichroic while the peak at 3540 cm^{-1} shows a high dichroism (Figure 5.12, curve c). FTIR peaks related to the carrier MA are visible and dichroic too (Figure 5.12, curve b).

The OH stretching region in FTIR spectra (3200–3600 cm^{-1}) can be used to discriminate between guest molecules included into the crystalline phase and molecules dissolved in the amorphous phase,[18,73,76–80] as shown also in chapter 4. In particular, the peak located at 3532 or 3540 cm^{-1} is related to the OH groups of isolated guest molecules included in the crystalline phase while the broad band centered at c.a. 3400 cm^{-1} corresponds to molecules simply dissolved in the amorphous phase. The broadness of the OH stretching band is indeed due to hydrogen bonding between molecules.[81]

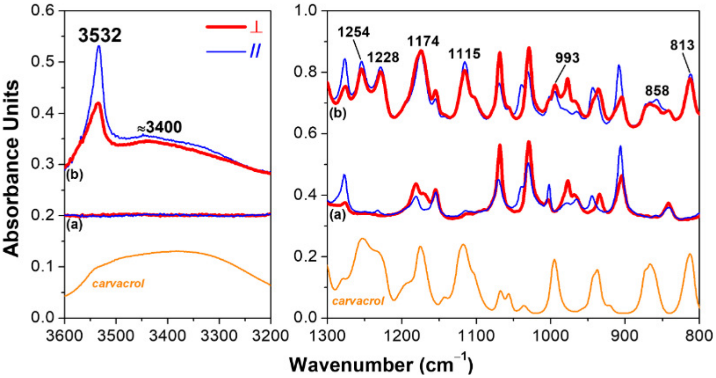

Figure 5.11 Polarized FTIR spectra, in the wavenumber ranges 800–1300 and 3200–3600 cm^{-1}, taken with polarization plane parallel (thin blue lines) and perpendicular (thick red lines) to the draw direction, for an axially oriented sPS δ-form film (a) before and (b) after immersion in pure liquid carvacrol. FTIR spectrum of pure liquid carvacrol is also reported in the bottom (orange line).

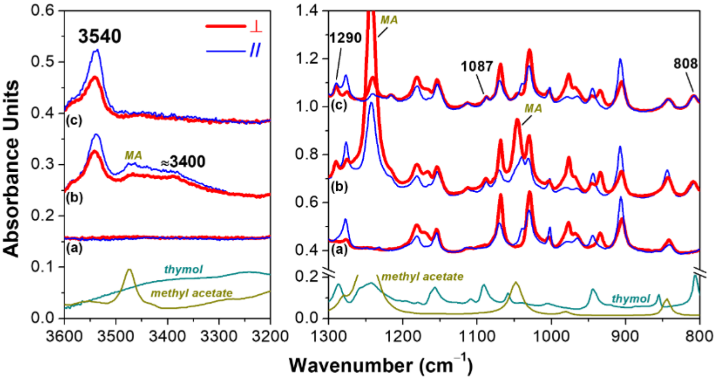

Figure 5.12 Polarized FTIR spectra, in the wavenumber ranges 800–1300 and 3200–3600 cm^{-1}, taken with polarization plane parallel (thin blue lines) and perpendicular (thick red lines) to the draw direction, for an axially oriented sPS δ-form film: (a) before; (b) after immersion in thymol/MA solution; (c) after 21 days of desorption in air. FTIR spectrum of pure MA (dark yellow line) and thymol (green line) are also reported in the bottom.

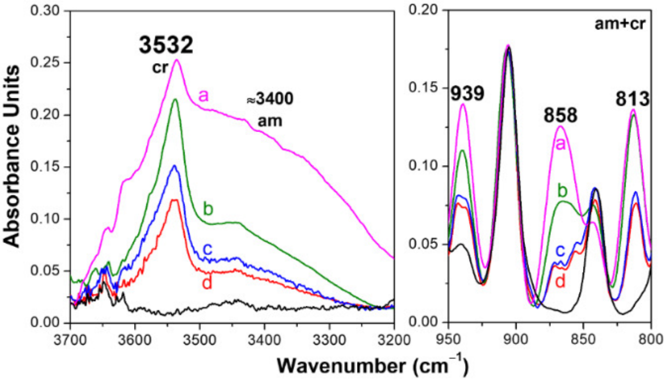

Figure 5.13 FTIR spectra in the range 800–950 cm^{-1} and 3200–3700 cm^{-1} of sPS/carvacrol CC fibers, with an initial carvacrol content close to 28 wt%, as collected at various desorption times (up to 250 days): (a) t=0; (b) 9 days; (c) 145 days; (d) 250 days.

Other FTIR peaks of guest molecules are poorly dichroic, and they can be related to molecules in both phases (crystalline and amorphous) of sPS films. The guest amount in the films, as determined by TGA measurements, is ≈8 wt% and ≈7 wt% for carvacrol and thymol, respectively.

FTIR spectra of sPS fibers, crystallized using carvacrol or thymol/MA solution, as prepared and after different desorption times in air at room temperature are shown in Figure 5.13 and in Figure 5.14, respectively.

As for carvacrol guest molecules, all FTIR peaks located at 813, 858, 993, ≈3400, 3532 cm^{-1} decrease during time (Figure 5.13) indicating the desorption of carvacrol molecules from both the amorphous as well as the CC phase.

Considering CC sPS fibers with thymol, while the desorption in air of the carrier MA occurs (shown by the decrease of intensity of FTIR peak located at 1236 cm^{-1}) an increase of the absorbances of the OH stretching thymol peak located at 3540 cm^{-1} (labeled cr) and a contemporary decrease of the band at ≈3400 cm^{-1} (labeled am) are apparent (Figure 5.14). These data can be easily rationalized by assuming that, while the carrier MA desorbs, the crystalline cavities, initially occupied by the carrier molecules, are progressively filled by the thymol molecules, which mostly move from the amorphous toward the crystalline phase. The desorption kinetics of carvacrol and thymol molecules being dissolved in the amorphous as well as in the crystalline phase are reported in Figure 5.15. It is clearly apparent that the reduction of intensity of the broad band at ≈3400 cm^{-1} (labeled as am), due to the guest molecules in the polymer amorphous phase, is much faster than the reduction of the peak at 3532 (carvacrol) and at 3540 (thymol) cm^{-1} (labeled as cr), due to molecules in the polymer co-crystalline phases.

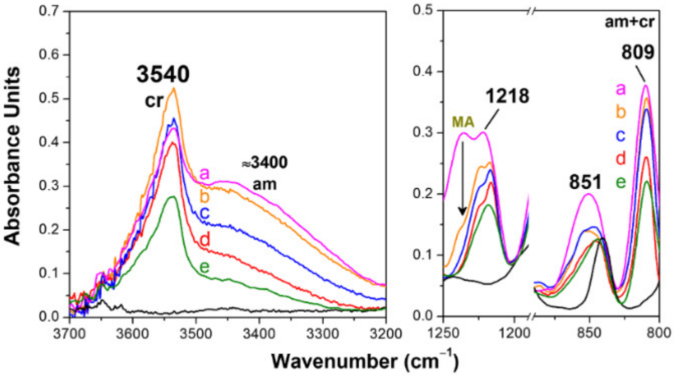

Figure 5.14 FTIR spectra in the range 800–1250 cm^{-1} and 3200–3700 cm^{-1} of sPS/thymol CC fibers, with an initial thymol content close to 16 wt%, as collected at various desorption times (up to 150 days): (a) t=0; (b) 1 hour; (c) 1 days; (d) 4 days; (e) 150 days.

As expected, the reduction of intensity of FTIR peaks of guest molecules (i.e., 939 cm^{-1} carvacrol and 809 cm^{-1} thymol) absorbed in both amorphous and crystalline polymer phases, is intermediate (magenta curves of Figures 5.15B, D). The overall amounts of carvacrol and thymol in sPS fibers evaluated by thermogravimetric measurements are reported in Figure 5.15B,D right scale, respectively.

As for carvacrol, the initial content is close to 28 wt%, a fast initial desorption (up to 50 days) is apparent followed by a slower kinetic desorption. After ~200 days the carvacrol is completely released from the amorphous phase (see red squares in Figure 5.15A) and the residual amount of nearly 3 wt% (shown in Figure 5.15B) is prevailingly related to the guest molecules included in the crystalline phase.

As for thymol, the initial content is close to 16 wt%. This uptake is smaller respect to carvacrol due to different experimental conditions: pure liquid and MA solution for carvacrol and thymol, respectively. MA performs as a carrier, and it enables the absorption of molecules by the crystalline phase. After 24 hours the carrier MA is completely desorbed (stars in figure 5.15C), the thymol in the amorphous phase (evaluated on the basis of the intensity of the band at 3400 cm^{-1}) decrease of ~65% and the amount of thymol in the crystalline cavities (evaluated on the basis of the intensity of the peak at 3540 cm^{-1}) reached a maximum (squares in Figure 5.15C), suggesting that a fraction of thymol molecules moves from the amorphous toward the crystalline phase. After ~250 days the thymol amount in sPS fibers is close to 10 wt% (shown in Figure 5.15D) prevailingly related to the guest molecules included in the crystalline phase (Figure 5.15C).

Curves of Figure 5.15 highlight a slower carvacrol and thymol guest desorption from CC phase and a faster desorption from amorphous phase (similar for eugenol, Figure 5.7 in section 5.2.1). The plot also indicates that a much faster desorption of carvacrol guest molecules from CC sPS fibers occurs compared to thymol guest release. This slower thymol release from sPS fibers is possibly due to a larger fraction of guest molecules hosted in the crystalline phase respect to carvacrol as well as to the solid-state nature of the molecules which affects its desorption in air.

As discussed for the antimicrobial eugenol, also here a slow release for both molecules is evident and it can ensure long-term antimicrobial effect of the sPS fibers (or a fabric made with them) especially for medical practices.

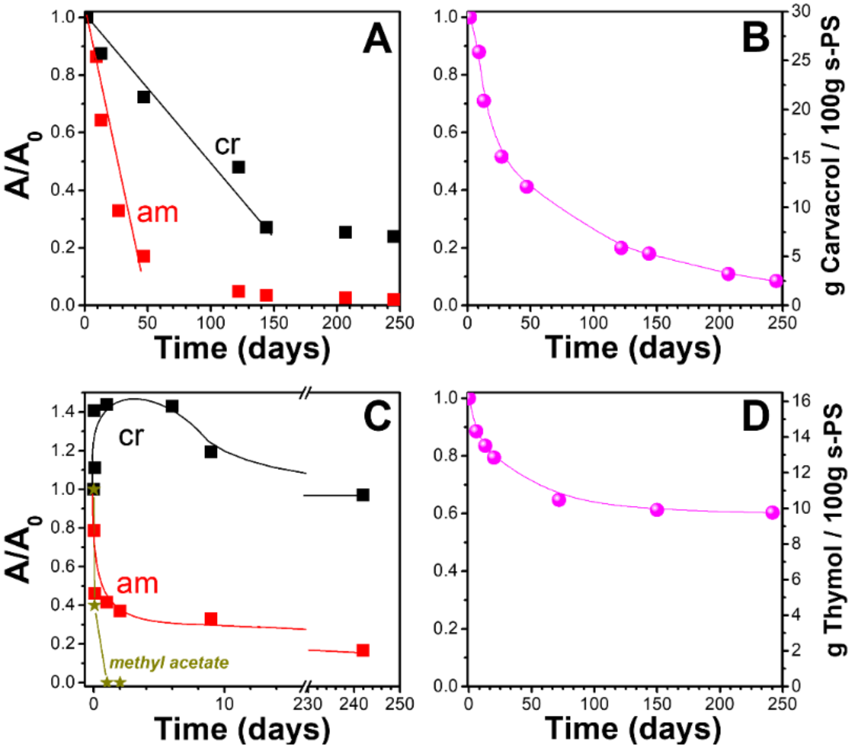

Figure 5.15 (A) Reduced absorbance of carvacrol infrared bands of guest molecules only in the crystalline (black squares, cr label, 3532 cm^{-1}) or only in the amorphous (red squares, am label, ≈3400 cm^{-1}) versus desorption time. (B) Carvacrol desorption (grams of guest per 100 grams of polymer) at room temperature from sPS fibers with a carvacrol initial content of 28 wt% (magenta circles, 939 cm^{-1}). (C) Reduced absorbance of thymol infrared bands of guest molecules only in the crystalline (black squares, cr label, 3540 cm^{-1}) or only in the amorphous (red squares, am label, ≈3400 cm^{-1}) and desorption of MA in air (stars) versus desorption time. (D) Thymol desorption (grams of guest per 100 grams of polymer) at room temperature from sPS fibers with a thymol initial content of 16 wt% (magenta circles, 809 cm^{-1}).

5.3 Conclusions

Guest-induced crystallization of amorphous unstretched sPS fibers leads to high degrees of axial orientation of CC phases and of derived NC phases, already in the absence of mechanical stretching. In particular, for all the prepared NC fibers, degrees of axial orientation are in the range $0.7 < f_c < 0.8$ with birefringence $\Delta n = -0.026 \pm 0.002$, nearly independently of the considered take-up speed range (80–2000 m/min) of the starting amorphous fibers as well as of the crystallization inducing guest.

This phenomenon is unique for polymer fiber crystallization, and it has been observed for all guest induced crystallizations of sPS. In particular, sorption of DCM, DMN and eugenol in unstretched sPS fibers leads to axially oriented fibers exhibiting clathrate δ-form, intercalate δ-form and disordered crystalline form, respectively. In the case of eugenol, the induced crystallization and orientation can be also obtained by guest sorption from aqueous emulsions as well as from dilute aqueous solutions.

Maintenance of axial orientations is also observed for α-form fibers as obtained by high temperature treatments of CC (or NC) fibers.

For the disordered NC form, fiber patterns only exhibit few diffraction peaks that can be rationalized by ***s***(2/1)2 helical chains (with typical periodicity of 0.78 nm) with a hexagonal packing of their chains axes (***a*** = 1.05 nm).

However, the most relevant achievement of this study is that by simple guest sorption procedures in amorphous sPS fibers (as produced in pilot industrial plants) not only it is possible to obtain CC forms with active guests (suitable, e.g., for antimicrobial release) but also to get axial orientation that improves mechanical properties of fiber.

This could be particularly interesting for CC fibers with active guests (suitable, e.g., for antimicrobial release).

CC sPS fibers as well with carvacrol and thymol, relevant natural antimicrobial molecules, have been also prepared by sorption of pure carvacrol and thymol/MA solution on amorphous sPS fibers, leading to high degrees of axial orientation of CC phases.

Eugenol, Carvacrol and Thymol guests release from sPS fibers in air at room temperature has been also analysed. The preparation of CC sPS fibers with antimicrobial molecules, being prevailingly present as guest of the crystalline phase, assures slow antimicrobial release and hence long-term antimicrobial properties.

As for carvacrol and thymol, very informative are FTIR spectra, especially the OH stretching region. In fact, this spectral region shows a narrow peak as well as a broad band corresponding to carvacrol and thymol molecules being isolated guests into the CC phase or simply dissolved in the amorphous phase, respectively. This interpretation has been confirmed by polarized FTIR spectra of axially oriented sPS films.

The release of antimicrobial guest molecules from fibers or fabrics can ensure a long-term antimicrobial effect usable for months, especially for biomedical applications where the inhibition of microorganisms' growth is crucial.

REFERENCES

(1) Heffelfinger, C. J.; Burton, R. L. X-Ray Determination of the Crystallite Orientation Distributions of Polyethylene Terephthalate Films. *J. Polym. Sci.* **1960**, *47* (149), 289–306. https://doi.org/10.1002/pol.1960.1204714926.

(2) Uejo, H.; Hoshino, S. Structure of Biaxially Oriented Polypropylene Film. *J. Appl. Polym. Sci.* **1970**, *14* (2), 317–328. https://doi.org/10.1002/app.1970.070140206.

(3) Gohil, R. M. Morphology-Permeability Relationships in Biaxially Oriented Pet Films: A Relationship between Oxygen Permeability and PROF. *J. Appl. Polym. Sci.* **1993**, *48* (9), 1649–1664. https://doi.org/10.1002/app.1993.070480916.

(4) Saraf, R. F. Planar and Fibre Textures Induced in Isotactic Polypropylene on Equibiaxial Hydrostatic Deformation. *Polymer* **1994**, *35* (7), 1359–1368. https://doi.org/10.1016/0032-3861(94)90334-4.

(5) McGonigle, E.-A.; Liggat, J. J.; Pethrick, R. A.; Jenkins, S. D.; Daly, J. H.; Hayward, D. Permeability of N 2 , Ar, He, O 2 and CO 2 through Biaxially Oriented Polyester Films — Dependence on Free Volume. *Polymer* **2001**, *42* (6), 2413–2426. https://doi.org/10.1016/S0032-3861(00)00615-7.

(6) Rizzo, P.; Albunia, A. R.; Milano, G.; Venditto, V.; Guerra, G.; Mensitieri, G.; Di Maio, L. Crystalline Orientation and Molecular Transport Properties in Nanoporous Sndiotactic Polystyrene Films. *Macromol. Symp.* **2002**, *185*, 65–75.

(7) Rizzo, P.; Costabile, A.; Guerra, G. Perpendicular Orientation of Host Polymer Chains in Clathrate Thick Films. *Macromolecules* **2004**, *37* (8), 3071–3076. https://doi.org/10.1021/ma035698q.

(8) Rizzo, P.; Della Guardia, S.; Guerra, G. Perpendicular Chain Axis Orientation in S-PS Films: Achievement by Guest-Induced Clathrate Formation and Maintenance after Transitions toward Helical and Trans-Planar Polymorphic Forms. *Macromolecules* **2004**, *37* (21), 8043–8049. https://doi.org/10.1021/ma049616p.

(9) Rizzo, P.; Spatola, A.; De Girolamo Del Mauro, A.; Guerra, G. Polymeric Films with Three Different Uniplanar Crystalline Phase Orientations. *Macromolecules* **2005**, *38* (24), 10089–10094. https://doi.org/10.1021/ma051247p.

(10) Albunia, A. R.; Rizzo, P.; Tarallo, O.; Petraccone, V.; Guerra, G. Layers of Close-Packed Alternated Enantiomorphous Helices and the Three Different Uniplanar Orientations of Syndiotactic Polystyrene. *Macromolecules* **2008**, *41* (22), 8632–8642. https://doi.org/10.1021/ma801180b.

(11) Itagaki, H.; Sago, T.; Uematsu, M.; Yoshioka, G.; Correa, A.; Venditto, V.; Guerra, G. Guest Orientation in Uniplanar-Axial Polymer Host Films and in Co-Crystal Unit-Cell, Determined by Angular Distributions of Polarized Guest Fluorescence. *Macromolecules* **2008**, *41* (23), 9156–9164. https://doi.org/10.1021/ma801849b.

(12) Albunia, A. R.; Rizzo, P.; Guerra, G. Polymeric Films with Three Different Orientations of Crystalline-Phase Empty Channels. *Chem. Mater.* **2009**, *21* (14), 3370–3375. https://doi.org/10.1021/cm900968c.

(13) Yoshioka, A.; Tashiro, K. Polymer−Solvent Interactions in Crystalline δ Form of Syndiotactic Polystyrene Viewed from the Solvent-Exchange Process in the δ Form and the Solvent Evaporation Phenomenon in the Thermally Induced Δ−γ Phase Transition. *Macromolecules* **2003**, *36* (10), 3593–3600. https://doi.org/10.1021/ma021774y.

(14) Petraccone, V.; Ruiz de Ballesteros, O.; Tarallo, O.; Rizzo, P.; Guerra, G. Nanoporous Polymer Crystals with Cavities and Channels. *Chem. Mater.* **2008**, *20* (11), 3663–3668. https://doi.org/10.1021/cm800462h.

(15) Albunia, A. R.; Rizzo, P.; Guerra, G. Two Different Uniplanar–Axial Orientations of Syndiotactic Polystyrene Films. *Macromolecules* **2011**, *44* (14), 5671–5681. https://doi.org/10.1021/ma200806x.

(16) Hada, Y.; Shikuma, H.; Ito, H.; Kikutani, T. Structure and Properties of Syndiotactic Polystyrene Fibers Prepared in High-Speed Melt Spinning Process. *Fibers Polym* **2005**, *6*, 19–27.

(17) D'Aniello, C.; Rizzo, P.; Guerra, G. Polymorphism and Mechanical Properties of Syndiotactic Polystyrene Films. *Polymer* **2005**, *46* (25), 11435–11441. https://doi.org/10.1016/j.polymer.2005.09.052.

(18) Albunia, A. R.; Rizzo, P.; Ianniello, G.; Rufolo, C.; Guerra, G. Syndiotactic Polystyrene Films with a Cocrystalline Phase Including Carvacrol Guest Molecules. *J. Polym. Sci. Part B Polym. Phys.* **2014**, *52* (9), 657–665. https://doi.org/10.1002/polb.23464.

(19) Rizzo, P.; Cozzolino, A.; Guerra, G. Chemical Stabilization of Hexanal Molecules by Inclusion as Guests of Nanoporous-Crystalline Syndiotactic Polystyrene Crystals. *Macromolecules* **2019**, *52* (6), 2255–2264. https://doi.org/10.1021/acs.macromol.8b02168.

(20) Guerra, G.; Vitagliano, V. M.; De Rosa, C.; Petraccone, V.; Corradini, P. Polymorphism in Melt Crystallized Syndiotactic Polystyrene Samples. *Macromolecules* **1990**, *23* (5), 1539–1544. https://doi.org/10.1021/ma00207a050.

(21) De Rosa, C. Crystal Structure of the Trigonal Modification (α Form) of Syndiotactic Polystyrene. *Macromolecules* **1996**, *29* (26), 8460–8465. https://doi.org/10.1021/ma960905q.

(22) Chatani, Y.; Inagaki, T.; Shimane, Y.; Shikuma, H. Structural Study on Syndiotactic Polystyrene: 4. Formation and Crystal Structure of Molecular Compound with Iodine. *Polymer* **1993**, *34* (23), 4841–4845. https://doi.org/10.1016/0032-3861(93)90007-W.

(23) De Rosa, C.; Guerra, G.; Petraccone, V.; Pirozzi, B. Crystal Structure of the Emptied Clathrate Form (δ_eForm) of Syndiotactic Polystyrene. *Macromolecules* **1997**, *30* (14), 4147–4152. https://doi.org/10.1021/ma970061q.

(24) Immirzi, A.; de Candia, F.; Iannelli, P.; Zambelli, A.; Vittoria, V. Solvent-Induced Polymorphism in Syndiotactic Polystyrene. *Makromol. Chem. Rapid Commun.* **1988**, *9* (11), 761–764. https://doi.org/10.1002/marc.1988.030091108.

(25) Tarallo, O.; Petraccone, V.; Venditto, V.; Guerra, G. Crystalline Structures of Intercalate Molecular Complexes of Syndiotactic Polystyrene with Two Fluorescent Guests: 1,3,5-Trimethyl-Benzene and 1,4-Dimethyl-Naphthalene. *Polymer* **2006**, *47* (7), 2402–2410. https://doi.org/10.1016/j.polymer.2006.01.056.

(26) Rizzo, P.; Ianniello, G.; Albunia, A. R.; Acocella, M. R.; Guerra, G. Disordered Nanoporous Crystalline Modifications of Syndiotactic Polystyrene. *J. Solut. Chem.* **2014**, *43* (1), 158–171. https://doi.org/10.1007/s10953-013-0118-3.

(27) Rizzo, P.; Albunia, A. R.; Guerra, G. Negatively Birefringent Polymer Films: Negatively Birefringent Polymer Films. *Macromol. Chem. Phys.* **2009**, *210* (24), 2148–2152. https://doi.org/10.1002/macp.200900451.

(28) Mourey, A.; Canillac, N. Anti-Listeria Monocytogenes Activity of Essential Oils Components of Conifers. *Food Control* **2002**, *13* (4–5), 289–292. https://doi.org/10.1016/S0956-7135(02)00026-9.

(29) Bishop, C. D. Antiviral Activity of the Essential Oil of *Melaleuca Alternifolia* (Maiden Amp; Betche) Cheel (Tea Tree) Against Tobacco Mosaic Virus. *J. Essent. Oil Res.* **1995**, *7* (6), 641–644. https://doi.org/10.1080/10412905.1995.9700519.

(30) Mari, M.; Bertolini, P.; Pratella, G. C. Non-Conventional Methods for the Control of Post-Harvest Pear Diseases. *J. Appl. Microbiol.* **2003**, *94* (5), 761–766. https://doi.org/10.1046/j.1365-2672.2003.01920.x.

(31) Juglal, S.; Govinden, R.; Odhav, B. Spice Oils for the Control of Co-Occurring Mycotoxin-Producing Fungi. *J. Food Prot.* **2002**, *65* (4), 683–687. https://doi.org/10.4315/0362-028X-65.4.683.

(32) Pessoa, L. M.; Morais, S. M.; Bevilaqua, C. M. L.; Luciano, J. H. S. Anthelmintic Activity of Essential Oil of Ocimum Gratissimum Linn. and Eugenol against Haemonchus Contortus. *Vet. Parasitol.* **2002**, *109* (1–2), 59–63. https://doi.org/10.1016/S0304-4017(02)00253-4.

(33) Karpouhtsis, I.; Pardali, E.; Feggou, E.; Kokkini, S.; Scouras, Z. G.; Mavragani-Tsipidou, P. Insecticidal and Genotoxic Activities of Oregano Essential Oils. *J. Agric. Food Chem.* **1998**, *46* (3), 1111–1115. https://doi.org/10.1021/jf970822o.

(34) Shabnum, S.; Wagay, M. G. Essential Oil Composition of Thymus Vulgaris L. and Their Uses. **2011**, *11*, 12.

(35) Rafiq, M.; Hussain, T.; Abid, S.; Nazir, A.; Masood, R. Development of Sodium Alginate/PVA Antibacterial Nanofibers by the Incorporation of Essential Oils. *Mater. Res. Express* **2018**, *5* (3), 035007. https://doi.org/10.1088/2053-1591/aab0b4.

(36) Unalan, I.; Endlein, S. J.; Slavik, B.; Buettner, A.; Goldmann, W. H.; Detsch, R.; Boccaccini, A. R. Evaluation of Electrospun Poly(ε-Caprolactone)/Gelatin Nanofiber Mats Containing Clove Essential Oil for Antibacterial Wound Dressing. *Pharmaceutics* **2019**, *11* (11), 570. https://doi.org/10.3390/pharmaceutics11110570.

(37) Sahal, G.; Nasseri, B.; Ebrahimi, A.; Bilkay, I. S. Electrospun Essential Oil-Polycaprolactone Nanofibers as Antibiofilm Surfaces against Clinical Candida Tropicalis Isolates. *Biotechnol. Lett.* **2019**, *41* (4–5), 511–522. https://doi.org/10.1007/s10529-019-02660-y.

(38) Unalan, I.; Slavik, B.; Buettner, A.; Goldmann, W. H.; Frank, G.; Boccaccini, A. R. Physical and Antibacterial Properties of Peppermint Essential Oil Loaded Poly (ε-Caprolactone) (PCL) Electrospun Fiber Mats for Wound Healing. *Front. Bioeng. Biotechnol.* **2019**, *7*, 346. https://doi.org/10.3389/fbioe.2019.00346.

(39) Kossyvaki, D.; Suarato, G.; Summa, M.; Gennari, A.; Francini, N.; Gounaki, I.; Venieri, D.; Tirelli, N.; Bertorelli, R.; Athanassiou, A.; Papadopoulou, E. L. Keratin–Cinnamon Essential Oil Biocomposite Fibrous Patches for Skin Burn Care. *Mater. Adv.* **2020**, *1* (6), 1805–1816. https://doi.org/10.1039/D0MA00416B.

(40) Suganya Bharathi, B.; Stalin, T. Cerium Oxide and Peppermint Oil Loaded Polyethylene Oxide/Graphene Oxide Electrospun Nanofibrous Mats as Antibacterial Wound Dressings. *Mater. Today Commun.* **2019**, *21*, 100664. https://doi.org/10.1016/j.mtcomm.2019.100664.

(41) Valizadeh, S.; Naseri, M.; Babaei, S.; Hosseini, S. M. H.; Imani, A. Development of Bioactive Composite Films from Chitosan and Carboxymethyl Cellulose Using Glutaraldehyde, Cinnamon Essential Oil and Oleic Acid. *Int. J. Biol. Macromol.* **2019**, *134*, 604–612. https://doi.org/10.1016/j.ijbiomac.2019.05.071.

(42) Shetta, A.; Kegere, J.; Mamdouh, W. Comparative Study of Encapsulated Peppermint and Green Tea Essential Oils in Chitosan Nanoparticles: Encapsulation, Thermal Stability, in-Vitro Release, Antioxidant and Antibacterial Activities. *Int. J. Biol. Macromol.* **2019**, *126*, 731–742. https://doi.org/10.1016/j.ijbiomac.2018.12.161.

(43) Badea, M. L.; Iconaru, S. L.; Groza, A.; Chifiriuc, M. C.; Beuran, M.; Predoi, D. Peppermint Essential Oil-Doped Hydroxyapatite Nanoparticles with Antimicrobial Properties. *Molecules* **2019**, *24* (11), 2169. https://doi.org/10.3390/molecules24112169.

(44) Liakos, I. L.; Iordache, F.; Carzino, R.; Scarpellini, A.; Oneto, M.; Bianchini, P.; Grumezescu, A. M.; Holban, A. M. Cellulose Acetate - Essential Oil Nanocapsules with Antimicrobial Activity for Biomedical Applications. *Colloids Surf. B Biointerfaces* **2018**, *172*, 471–479. https://doi.org/10.1016/j.colsurfb.2018.08.069.

(45) Cazzola, M.; Ferraris, S.; Allizond, V.; Bertea, C. M.; Novara, C.; Cochis, A.; Geobaldo, F.; Bistolfi, A.; Cuffini, A. M.; Rimondini, L.; Banche, G.; Spriano, S. Grafting of the Peppermint Essential Oil to a Chemically Treated Ti6Al4V Alloy to Counteract the Bacterial

Adhesion. *Surf. Coat. Technol.* **2019**, *378*, 125011. https://doi.org/10.1016/j.surfcoat.2019.125011.

(46) Li, Y.; Liu, J.; He, X.; Kong, D.; Zhou, C.; Wu, H.; Yang, Z.; Yang, Z.; Hu, Y. Preparation of Cinnamon Oil-Loaded Antibacterial Composite Microcapsules by In Situ Polymerization of Pickering Emulsion Templates. *Macromol. Mater. Eng.* **2020**, *305* (3), 1900851. https://doi.org/10.1002/mame.201900851.

(47) Martins, I. M.; Rodrigues, S. N.; Barreiro, M. F.; Rodrigues, A. E. Release of Thyme Oil from Polylactide Microcapsules. *Ind. Eng. Chem. Res.* **2011**, *50* (24), 13752–13761. https://doi.org/10.1021/ie200791r.

(48) Vishwakarma, G. S.; Gautam, N.; Babu, J. N.; Mittal, S.; Jaitak, V. Polymeric Encapsulates of Essential Oils and Their Constituents: A Review of Preparation Techniques, Characterization, and Sustainable Release Mechanisms. *Polym. Rev.* **2016**, *56* (4), 668–701. https://doi.org/10.1080/15583724.2015.1123725.

(49) Bhalerao, Y. P.; Wagh, S. J. A Review on Thymol Encapsulation and Its Controlled Release through Biodegradable Polymer Shells. *Int. J. Pharm. Sci. Res.* **2018**, *9*, 11.

(50) Zhu, Z.; Min, T.; Zhang, X.; Wen, Y. Microencapsulation of Thymol in Poly(Lactide-Co-Glycolide) (PLGA): Physical and Antibacterial Properties. *Materials* **2019**, *12* (7), 1133. https://doi.org/10.3390/ma12071133.

(51) Cai, C.; Ma, R.; Duan, M.; Lu, D. Preparation and Antimicrobial Activity of Thyme Essential Oil Microcapsules Prepared with Gum Arabic. *RSC Adv.* **2019**, *9* (34), 19740–19747. https://doi.org/10.1039/C9RA03323H.

(52) Annunziata, L.; Albunia, A. R.; Venditto, V.; Mensitieri, G.; Guerra, G. Polymer/Gas Clathrates for Gas Storage and Controlled Release. *Macromolecules* **2006**, *39* (26), 9166–9170. https://doi.org/10.1021/ma0618878.

(53) Albunia, A. R.; Rizzo, P.; Guerra, G. Control of Guest Transport in Polymer Films by Structure and Orientation of Nanoporous-Crystalline Phases. *Polymer* **2013**, *54* (6), 1671–1678. https://doi.org/10.1016/j.polymer.2013.01.027.

(54) Rizzo, P.; Gallo, C.; Vitale, V.; Tarallo, O.; Guerra, G. Nanoporous-Crystalline Films of PPO with Parallel and Perpendicular Polymer Chain Orientations. *Polymer* **2019**, *167*, 193–201. https://doi.org/10.1016/j.polymer.2019.01.073.

(55) Daniel, C.; Rizzo, P.; Nagendra, B.; Cozzolino, A.; Guerra, G. High Diffusivity Dense Films of a Nanoporous-Crystalline Polymer. *Polymer* **2021**, *229*, 124005. https://doi.org/10.1016/j.polymer.2021.124005.

(56) Cozzolino, A.; Nagendra, B.; Rizzo, P.; Daniel, C.; Guerra, G. Fast Uptake of Organic Pollutants from Dilute Aqueous Solutions by Nanoporous-Crystalline PPO Films with c-Perpendicular Orientation. *Eur. Polym. J.* **2021**, *161*, 110864. https://doi.org/10.1016/j.eurpolymj.2021.110864.

(57) Nagendra, B.; Mondrone, G.; Daniel, C.; Rizzo, P.; Guerra, G. Control of Guest Thermal Release by Crystalline Host Orientation. *ACS Appl. Polym. Mater.* **2021**, *3* (2), 949–955. https://doi.org/10.1021/acsapm.0c01246.

(58) Cozzolino, A.; Rizzo, P.; Gallo, C.; Bianchi, R.; Daniel, C.; Guerra, G. Axially Oriented Guest Induced Crystallization in Syndiotactic Polystyrene Unstretched Fibers. *Polymer* **2021**, *228*, 123908. https://doi.org/10.1016/j.polymer.2021.123908.

(59) Torres, F. J.; Civalleri, B.; Meyer, A.; Musto, P.; Albunia, A. R.; Rizzo, P.; Guerra, G. Normal Vibrational Analysis of the Syndiotactic Polystyrene s(2/1)2 Helix. *J. Phys. Chem. B* **2009**, *113* (15), 5059–5071. https://doi.org/10.1021/jp809043w.

(60) Venditto, V.; De Girolamo Del Mauro, A.; Mensitieri, G.; Milano, G.; Musto, P.; Rizzo, P.; Guerra, G. Anisotropic Guest Diffusion in the δ Crystalline Host Phase of Syndiotactic Polystyrene: Transport Kinetics in Films with Three Different Uniplanar Orientations of the Host Phase. *Chem. Mater.* **2006**, *18* (9), 2205–2210. https://doi.org/10.1021/cm051657s.

(61) Antih, J.; Houdkova, M.; Urbanova, K.; Kokoska, L. Antibacterial Activity of Thymus Vulgaris L. Essential Oil Vapours and Their GC/MS Analysis Using Solid-Phase Microextraction and Syringe Headspace Sampling Techniques. *Molecules* **2021**, *26* (21), 6553. https://doi.org/10.3390/molecules26216553.

(62) Zheng, L.; Bae, Y.-M.; Jung, K.-S.; Heu, S.; Lee, S.-Y. Antimicrobial Activity of Natural Antimicrobial Substances against Spoilage Bacteria Isolated from Fresh Produce. *Food Control* **2013**, *32* (2), 665–672. https://doi.org/10.1016/j.foodcont.2013.01.009.

(63) Gutiérrez-Larraínzar, M.; Rúa, J.; Caro, I.; de Castro, C.; de Arriaga, D.; García-Armesto, M. R.; del Valle, P. Evaluation of Antimicrobial and Antioxidant Activities of Natural Phenolic Compounds against Foodborne Pathogens and Spoilage Bacteria. *Food Control* **2012**, *26* (2), 555–563. https://doi.org/10.1016/j.foodcont.2012.02.025.

(64) Hui, X.; Yan, G.; Tian, F.-L.; Li, H.; Gao, W.-Y. Antimicrobial Mechanism of the Major Active Essential Oil Compounds and Their Structure–Activity Relationship. *Med. Chem. Res.* **2017**, *26* (2), 442–449. https://doi.org/10.1007/s00044-016-1762-0.

(65) Marchese, A.; Arciola, C. R.; Coppo, E.; Barbieri, R.; Barreca, D.; Chebaibi, S.; Sobarzo-Sánchez, E.; Nabavi, S. F.; Nabavi, S. M.; Daglia, M. The Natural Plant Compound Carvacrol as an Antimicrobial and Anti-Biofilm Agent: Mechanisms, Synergies and Bio-Inspired Anti-Infective Materials. *Biofouling* **2018**, *34* (6), 630–656. https://doi.org/10.1080/08927014.2018.1480756.

(66) Ahmad, A.; Khan, A.; Akhtar, F.; Yousuf, S.; Xess, I.; Khan, L. A.; Manzoor, N. Fungicidal Activity of Thymol and Carvacrol by Disrupting Ergosterol Biosynthesis and Membrane Integrity against Candida. *Eur. J. Clin. Microbiol. Infect. Dis.* **2011**, *30* (1), 41–50. https://doi.org/10.1007/s10096-010-1050-8.

(67) Abbaszadeh, S.; Sharifzadeh, A.; Shokri, H.; Khosravi, A. R.; Abbaszadeh, A. Antifungal Efficacy of Thymol, Carvacrol, Eugenol and Menthol as Alternative Agents to Control the Growth of Food-Relevant Fungi. *J. Mycol. Médicale* **2014**, *24* (2), e51–e56. https://doi.org/10.1016/j.mycmed.2014.01.063.

(68) Gilling, D. H.; Kitajima, M.; Torrey, J. R.; Bright, K. R. Antiviral Efficacy and Mechanisms of Action of Oregano Essential Oil and Its Primary Component Carvacrol against Murine Norovirus. *J. Appl. Microbiol.* **2014**, *116* (5), 1149–1163. https://doi.org/10.1111/jam.12453.

(69) Toujani, M. M.; Rittà, M.; Civra, A.; Genovese, S.; Epifano, F.; Ghram, A.; Lembo, D.; Donalisio, M. Inhibition of HSV-2 Infection by Pure Compounds from *Thymus Capitatus* Extract *in Vitro*: Anti-HSV-2 Compounds from Thymus Capitatus Extract. *Phytother. Res.* **2018**, *32* (8), 1555–1563. https://doi.org/10.1002/ptr.6084.

(70) Sedy, K. A.; Koschier, E. H. Bioactivity of Carvacrol and Thymol against Frankliniella Occidentalis and Thrips Tabaci. *J. Appl. Entomol.* **2003**, *127* (6), 313–316. https://doi.org/10.1046/j.1439-0418.2003.00767.x.

(71) Cetin, H.; Erler, F.; Yanikoglu, A. A Comparative Evaluation OfOriganum Onites Essential Oil and Its Four Major Components as Larvicides against the Pine Processionary Moth,Thaumetopoea Wilkinsoni Tams. *Pest Manag. Sci.* **2007**, *63* (8), 830–833. https://doi.org/10.1002/ps.1401.

(72) Ben Arfa, A.; Combes, S.; Preziosi-Belloy, L.; Gontard, N.; Chalier, P. Antimicrobial Activity of Carvacrol Related to Its Chemical Structure. *Lett. Appl. Microbiol.* **2006**, *43* (2), 149–154. https://doi.org/10.1111/j.1472-765X.2006.01938.x.

(73) Cozzolino, A.; Monaco, G.; Daniel, C.; Rizzo, P.; Guerra, G. Monomeric and Dimeric Carboxylic Acid in Crystalline Cavities and Channels of Delta and Epsilon Forms of Syndiotactic Polystyrene. *Polymers* **2021**, *13* (19), 3330. https://doi.org/10.3390/polym13193330.

(74) Albunia, A. R.; Guerra, G. Spectroscopic Investigation of Guest–Guest Interactions in the Nanoporous-Crystalline δ and ε Forms of Syndiotactic Polystyrene. *J. Phys. Chem. C* **2014**, *118* (22), 11774–11783. https://doi.org/10.1021/jp502679d.

(75) Rajkumar, P.; Selvaraj, S.; Suganya, R.; Velmurugan, D.; Gunasekaran, S.; Kumaresan, S. Vibrational and Electronic Spectral Analysis of Thymol an Isomer of Carvacrol Isolated from Trachyspermum Ammi Seed: A Combined Experimental and Theoretical Study. *Chem. Data Collect.* **2018**, *15–16*, 10–31. https://doi.org/10.1016/j.cdc.2018.03.003.

(76) Furukawa, K.; Nakaoki, T. Comparison of Absorption Kinetics of Ethanol and Butanol into Different Size Nanopores Present in Syndiotactic Polystyrene and Poly(*P* -Methylstyrene). *Soft Mater.* **2011**, *9* (2–3), 141–153. https://doi.org/10.1080/1539445X.2011.552351.

(77) Sato, S.; Kawaguchi, T.; Kaneko, F. ATR FTIR Spectroscopic Study on Complexation of Sydiotactic Polystyrene with N-Alkyl Carboxylic Acids. *Macromol. Symp.* **2016**, *369* (1), 114–118. https://doi.org/10.1002/masy.201600052.

(78) Uda, Y.; Kaneko, F.; Kawaguchi, T. Guest Exchange Mechanism in the Clathrate Phase of Syndiotactic Polystyrene. *Macromolecules* **2005**, *38* (8), 3380–3385. https://doi.org/10.1021/ma047567a.

(79) Kaneko, F.; Radulescu, A.; Ute, K. Time-Resolved Small-Angle Neutron Scattering Study on Guest-Exchange Processes in Co-Crystals of Syndiotactic Polystyrene. *J. Appl. Crystallogr.* **2014**, *47* (1), 6–13. https://doi.org/10.1107/S1600576713030343.

(80) Golla, M.; Nagendra, B.; Daniel, C.; Rizzo, P.; Guerra, G. Isolated and Aggregated Carvacrol Guest Molecules in Cocrystalline Poly(2,6-Dimethyl-1,4-Phenylene)Oxide Films. *Polym. J.* **2021**, *53* (10), 1093–1100. https://doi.org/10.1038/s41428-021-00511-0.

(81) Kristiansson, O. Investigation of the OH Stretching Vibration of CD3OH in CCl4. *J. Mol. Struct.* **1999**, *477* (1–3), 105–111. https://doi.org/10.1016/S0022-2860(98)00591-2.

CONCLUDING REMARKS

In these chapters (fourth and fifth), sorption of carboxylic acids in NC phases of axially oriented sPS phases has been described.

Firstly, it has been established that the ε crystalline channels can host:

i) carboxylic acids (i.e., 6 C atoms HA, 12 C atoms LA, 18 C atoms HA) prevailingly as hydrogen-bonded linear dimers;

ii) dicarboxylic acids (i.e., AA 6 C atoms) prevailingly as hydrogen-bonded linear polymers.

This sorption occurs with a very fast kinetic, probably due to intermolecular hydrogen bonds between carboxylic groups of adjacent guest molecules, so the uptake could be very ease. Moreover, the sign of dichroism of the O−H stretching and C=O stretching peaks indicates that the orientations of O−H and C=O bonds are preferentially parallel and perpendicular to the crystalline polymer chain axes, respectively.

The formation of hydrogen bonded linear polymers in the crystalline channels of the NC ε phase could be particularly useful for films exhibiting the $c_{\perp}$ orientation, in which the crystalline channels and hence the hydrogen-bonded "linear polymers" are preferentially perpendicular to the film plane. In this field, could be very interesting the possible formation of hydrogen bonded linear polymers of fully conjugated dicarboxylic acids (like, e.g. *trans-trans* muconic acid) to be explored. This procedure could possibly lead to formation of isolated semiconductive linear polymers perpendicular to the plane of insulating sPS membranes.

Furthermore, sorption of the aromatic BA in amorphous as well as in CC ε phases of sPS (where BA molecules are prevailingly present as dimers) has been examined. The main result find is that the NC δ-form of sPS is able to isolate BA guest molecules, even disrupting their strong intermolecular hydrogen bonds, which are present not only in BA crystals but also in diluted solutions.

The δ sPS phase plays a crucial role not only avoiding additive aggregation but even leading to separation of dimeric BA guest molecules. This segregation of molecules by NC δ phases of sPS allows spectroscopic characterization of isolated molecules already at room temperature, avoiding use of more difficult procedures such as Ar gas matrix maintained at 17 K onto a cooled optic CsI substrate.

Another important aspect reported in these chapters has been the study of guest-induced crystallization of amorphous unstretched sPS fibers.

Guest treatments (as pure solvent or in aqueous diluted solutions) have been performed on amorphous unstretched sPS fibers leading not only to crystallization phenomenon but also to induction of high degrees of axial orientation of CC phases (in the range $0.7 < f_c < 0.8$), in totally absence of mechanical stretching.

This phenomenon has been observed for all guest induced crystallizations as for instance dichloromethane, dimethyl naphthalene and eugenol.

Maintenance of axial orientations is also observed after removing guests from CC phases, leading to axially oriented NC fibers, as well as after thermal treatment and subsequent crystal-to-crystal transition.

The most relevant achievement of this study is that by simple guest sorption procedures in amorphous sPS fibers (as produced in pilot industrial plants) not only it is possible to obtain CC forms with active guests (suitable, e.g., for antimicrobial release) but also to get axial orientation that improves fiber properties, without applying mechanical stretching.

Finally, CC sPS fibers, presenting high degrees of axial orientation of CC phases including eugenol, carvacrol and thymol, relevant natural antimicrobial molecules, have been prepared and characterized, and their release in air at room temperature has been analysed during time. The release of antimicrobial guest molecules from fibers starts quickly, due to release from both amorphous and crystalline phases, then it becomes slower when it happens mainly from the crystalline phase.

The location of most antimicrobial molecules in the crystalline phases assures a decrease of desorption diffusivity and hence long-term antimicrobial releasing fibers, making them usable for months in many biomedical applications where the inhibition of microorganisms’ growth is crucial.

EXPERIMENTAL SECTION

Materials

Poly(2,6-dimethyl-1,4-phenylene)oxide (PPO) used in this study was kindly supplied by SABIC. Its molecular weight is $M_w = 350$ kg mol^{-1} (Ultra High P6130 grade).

Syndiotactic polystyrene (sPS), with the trademark Xarec 90ZC, was provided by Idemitsu. The content of syndiotactic triads, evaluated by ^{13}C nuclear magnetic resonance, is higher than 98%. The mass average molar mass, determined by gel permeation chromatography in trichlorobenzene at 145 °C, is $M_w = 140$ Kg mol^{-1}, and the polydispersity index is $M_w/M_n = 2.0$.

Poly(2,6-diphenyl-1,4-phenylene)oxide powder (Tenax, TA 60–80 mesh), with surface area of 18 m^2 g^{-1}, was purchased from Sigma Aldrich.

All solvents were provided by Sigma Aldrich too and used without further purification.

Film preparation: NC sPS/PPO films were obtained by casting procedure from 1.0–1.5 wt% solution with a specific solvent at room temperature or higher temperature, using a Petri dish with a diameter in the range 4–9 cm, after solvent extraction by acetonitrile guest sorption/desorption at room temperature or by supercritical carbon dioxide. All the NC films have a thickness in the range 20–100 μm, measured using a caliper.

Amorphous PPO films were obtained from 1.0–1.5 wt% $CHCl_3$ solution casting at T = 60 °C using a Petri dish, as described for NC films. Immersion of amorphous PPO films in a suitable solvent (i.e., liquid carvone), followed by guest extraction, leads to the formation of NC PPO films with orientation of the main chain axes preferentially perpendicular to the film plane. Tenax films were prepared by casting from 1.5 wt% chloroform solution at T = 60 °C and then immersion in acetonitrile to remove the chloroform.

Aerogel preparation: sPS/PPO gels were prepared in hermetically sealed test tubes by heating the polymer solvent mixtures, with a polymer concentration $C_{pol} = 10$ wt%, until complete dissolution of the polymer and appearance of a transparent homogeneous solution. Then the hot solution was cooled to room temperature where gelation occurred. sPS/PPO aerogels were obtained by solvent extraction from the gels by a supercritical carbon dioxide extractor at the following conditions: T = 40 °C, P = 200 bar, extraction time t = 3h. The obtained aerogels are monolithic with a regular cylindrical shape.

Axially oriented films: Axially oriented sPS films were prepared by axial stretching of sPS amorphous films with a dynamometer INSTRON 4301 at 105 °C, up to a draw ratio of 4.0 by using elongation rate of 10 mm/min. Amorphous sPS films were obtained by a blown extrusion process using a melt temperature of 290 °C. Axially oriented sPS films with the NC δ-form were obtained by immersion of axially stretched amorphous films in dichloromethane at room temperature for 1 night, followed by guest removal by acetonitrile sorption for 3 h. Axially oriented sPS films with the dense γ-form were obtained by annealing of δ-form films at 170 °C for 1 h. Axially oriented sPS films with the NC ε-form were obtained by immersion of the axially oriented γ-form film for 1 h in chloroform and then in acetonitrile at room temperature.

Films exhibiting axial orientation of α NC phases were obtained by immersion of axially stretched amorphous films in limonene at room temperature for 1 night, followed by limonene removal by acetonitrile sorption for 3 h. Film stretching experiments were conducted by a dynamometer INSTRON 4301, at 220 °C, up to a draw ratio of 4.0 by using elongation rate of 10 mm/min.

Fibers preparation: Amorphous sPS fibers with diameter of 35 μm were obtained by melt spinning with extruding temperature of 290 °C, by using two different take-up speeds (80 m/min and 2000 m/min).

These amorphous sPS fibers were co-crystallized by immersion in liquid guests (or aqueous solutions/emulsions) for 10 min at room temperature. To obtain sPS fibers with NC phases, guest molecules were removed by sorption/desorption of acetonitrile at room temperature.

Methods

Birefringence: Birefringence measurements were conducted by using a *Leitz* polarizing microscope, with Ehringhaus rotary compensator of 5 and 10 orders. The occurrence of negative birefringence, i.e. refractive index parallel to the stretching direction lower than refractive index perpendicular to the stretching direction, has been well established for axially oriented sPS fibers.

Capacitance: Capacitance values (C_p) with parallel-equivalent circuit model were measured using a E4980A Precision LCR Meter by Agilent with a voltage $\Delta V = 100mV$ and a frequency of 100 Hz at room temperature (≈20 °C).

Degree of orientation: The degree of orientation (f_c) has been evaluated on a quantitative numerical basis using the Hermans' orientation function described in literature:[1]

$$f_c = \chi_{(hkl)} = (3\,\overline{\cos^2\gamma} - 1)/2 \qquad \text{(M.1)}$$

where $\overline{\cos^2\gamma}$ has been determined by azimuthal distribution of *hkl* reflection intensities of the sample. In these assumptions, $f_c = 0$ corresponds to random crystallite orientation while $f_c = 1$ or -0.5 indicate that ***c*** axes of all crystallites are perfectly parallel or perpendicular to the film plane (or the fiber axis), respectively.

For PPO films presenting chain axis orientation of the crystalline phases preferentially parallel and perpendicular to the film plane (named $c_{//}$ and $c_{\perp}$ orientations, respectively), $f_c = \chi_{(001)}$, and it was evaluated by azimuthal scans of the 001 reflection of the α form (at $2\theta_{CuK\alpha} = 16.8°$). The degree of orientation for axially oriented sPS fibers was evaluated by using azimuthal scans of the 002 reflection (for all crystalline phases, both with helical and with zig-zag planar polymer).

Degrees of crystallinity: Degrees of crystallinity (X_c) of NC PPO samples was evaluated by DSC measurements and based on the following formula:[2]

$$X_{c,DSC} = \Delta H_f / \Delta H_f^o \qquad \text{(M.2)}$$

where ΔH_f is the enthalpy of fusion and ΔH_f^o is the enthalpy of fusion of a totally crystalline PPO polymer (42 ± 3 J/g).[3]

The degree of crystallinity of sPS films, instead, was evaluated by the FTIR method described in literature as following:[4]

$$X_{c,FTIR} = 1 - K\,(L'/L) \qquad \text{(M.3)}$$

where K is the subtraction coefficient applied to reduce the amorphous phase contribution to the baseline, L and L' are the thickness of the sample and of an amorphous reference film, respectively. The ratio L/L' can be estimated spectroscopically from the absorbance ratio of a conformationally insensitive peak (i.e., at 1601 cm^{-1}).

Density: Density of amorphous PPO (higher than 1 g/cm^3) and NC PPO (lower than 1 g/cm^3) films was evaluated by the classical floatation method, by using aqueous solutions of $CaCl_2$ and methanol at room temperature, respectively.

Differential Scanning Calorimetry: DSC measurements were conducted by TA Q2000 equipment from TA Instruments in the temperature range from 25 °C to 300 °C and at heating rate of 10 °C/min. To avoid sample degradation, DSC experiments were conducted under nitrogen atmosphere.

DFT calculations: FTIR spectra have been fitted as sums of Lorentzian peaks, as described in ref[5]. In order to obtain percentage of monomer and dimers, integrated areas obtained by the fitting have been corrected by molar extinction coefficients estimated by a quantum mechanical computation on monomer and dimer in gas phase in the harmonic approximation at the APFD[6]/6-311+G** level, using Gaussian16.[7]

Diffusivity coefficient: In view of the Fickian behavior of sorption kinetics, the diffusivity coefficient (D) was estimated from experimental sorption data in the transient stage by using the following equation:[8]

$$\frac{d(M_t/M_\infty)}{d(t^{1/2})} = \left(\frac{16D}{L^2\pi}\right)^{1/2} \qquad \text{(M.4)}$$

where M_t and M_∞ are the masses of penetrant absorbed at the time t and at equilibrium conditions, respectively. Film thickness (L) was evaluated by using a digital micrometer, with an accuracy of ±0.5 μm. Use of this equation requires constant film thickness during guest sorption. This assumption is safe for all the samples.

Fluorescence: Fluorescence spectra were measured at room temperature on a Horiba Jobin-Yvon Fluorolog®-3 spectrofluorometer and equipped with a 450W xenon arc lamp, double-grating excitation, and single-grating emission monochromators.

Fourier transform infrared spectroscopy: FTIR spectra were obtained at a 2.0 cm^{-1} resolution with a Vertex70 spectrometer from Bruker. It is equipped with a deuterated triglycine sulfate detector and a Ge/KBr beam splitter. A total of 32 scans were averaged to reduce the spectral noise. Polarized infrared spectra of films were recorded by using a SPECAC 12000 wire grid polarizer, while FTIR spectra of the fibers were collected in the diffuse reflectance infrared Fourier transform mode (DRIFT) by using an Easy Diff accessory benchmark from Pike Technologies.

Guest extraction by $scCO_2$: The guest extraction procedure for the sample used in these studies was conducted by using $scCO_2$ at a temperature of 40 °C and pressure of 250 bar.

Guest molecular volume: The guest molecular volume was calculated from the following equation:[9]

$$V_{guest} = M / \rho N_A \qquad (M.5)$$

where M and ρ are the molecular mass and density of the guest molecules, respectively. N_A is the Avogadro's number (6.02×10^{23} molecules/mol).

Order parameter: The order parameter of the polymer crystalline phases (S_p) was calculated by the formula:[10]

$$S_p = \frac{R_p - 1}{R_p + 2} \qquad (M.6)$$

where $R = A_{//}/A_{\perp}$ is the dichroic ratio, and $A_{//}$ and $A_{\perp}$ are the measured absorbance for polarization plane parallel and perpendicular to the draw direction, respectively. This orientation factor is equal to zero for random crystallite orientation, while it is equal to +1 and −0.5 for orientation of all polymer chain axes of the crystallites, being parallel and perpendicular to the stretching direction, respectively. Polarized FTIR spectra of CC films also allow an analogous evaluation of the order parameter of monomeric and dimeric guest molecules (S_m and S_d, respectively), with respect to the film stretching direction:

$$S_m = \frac{R_m - 1}{R_m + 2} \quad ; \quad S_d = \frac{R_d - 1}{R_d + 2} \qquad (M.7)$$

where R_m and R_d are the dichroic ratios, as evaluated for monomeric and dimeric vibrational peaks.

Porosity: Total porosity of the monolithic aerogels with regular cylindrical shape was evaluated as:

$$P = 100 \left[1 - \frac{\rho_a}{\rho_p}\right] \qquad (M.8)$$

where ρ_p is the density of the polymer matrix and ρ_a is the aerogel apparent density calculated from the mass/volume ratio of monolithic cylindrical aerogels.

Quantum yield: The absolute quantum yield (Φ_F) of umbelliferone-doped PPO films was determined by using a 152 mm diameter Quanta-phi integrating sphere, coated in Spectralon® and positioned on the optical path of the spectrofluorometer, placing the detector in right-angle mode (RA).

Scanning electron microscopy: The surface morphology of the PPO polymer sample was analyzed by scanning electron microscopy (Carl Zeiss SMT AG). Before imaging, all PPO polymer samples were coated with gold (Agar Auto Sputter Coater model 108 A) at 30 mA for 5 min.

Sorption analysis: Vapour sorption measurements were carried out at 35 °C with a VTI-SA symmetrical vapour sorption analyzer from TA Instruments. PCE absorption tests in polymer films from water were conducted using 50 ppm aqueous solutions, kept homogeneous by a magnetic stirrer, at room temperature (≈20 °C). Then, PCE uptake was evaluated by the intensity of the isolated PCE FTIR peak at 800 cm^{-1}.

Spin coating: PPO thin coating (1–8 µm thickened) on gold/silicon support were prepared by using the Spin Coater Spin 150 (SPS-Europe) setting 2000 rpm/sec, 1000 rpm and 30 seconds.

Surface area: Specific surface area of samples was obtained by N_2 adsorption measurements carried out at 77 K on a Nova Quantachrome 4200e instrument and was calculated by using the Brunauer–Emmet–Teller method in the $0.05 < p/p_0 < 0.2$ pressure range.

Thermogravimetric analysis: Guest amount in all samples was determined by thermogravimetric measurements (TGA), as performed with a TG 209 F1 equipment from *Netzsch*.

UV–Vis absorption spectroscopy: Spectroscopy by UV–Vis absorption was carried out by means of a Cary 5000 (Agilent) equipped with a solid sample holder.

X-ray diffraction patterns: WAXD patterns were performed using a D8 QUEST Bruker diffractometer (CuK*α* radiation) by sending the X-ray beam parallel or perpendicular to the film surface (with the normal to the film surface horizontal); the collected two-dimensional (2D) patterns were named EDGE and THROUGH, respectively. Equatorial and meridional profiles were collected along equatorial and meridional directions of the 2D patterns.

REFERENCES

(1) Alexander, L. E. *X-Ray Diffraction Methods in Polymer Science*; Krieger: Huntington, N.Y, 1979.

(2) Kong, Y.; Hay, J. N. The Enthalpy of Fusion and Degree of Crystallinity of Polymers as Measured by DSC. *Eur. Polym. J.* **2003**, *39* (8), 1721–1727. https://doi.org/10.1016/S0014-3057(03)00054-5.

(3) F. E. Karasz; J. M. O'Reilly; H. E. Bair; R. A. Kluge. In *Analytical Calorimetry, Vol.1, R. S. Porter and J. E. Johnson*; Plenum Press, NY: NY, 1968; p 59.

(4) Musto, P.; Mensitieri, G.; Cotugno, S.; Guerra, G.; Venditto, V. Probing by Time-Resolved FTIR Spectroscopy Mass Transport, Molecular Interactions, and Conformational Ordering in the System Chloroform−Syndiotactic Polystyrene. *Macromolecules* **2002**, *35* (6), 2296–2304. https://doi.org/10.1021/ma011684d.

(5) Monaco, G.; Aquino, F.; Zanasi, R.; Herrebout, W.; Bultinck, P.; Massa, A. Model-Averaging of Ab Initio Spectra for the Absolute Configuration Assignment via Vibrational Circular Dichroism. *Phys Chem Chem Phys* **2017**, *19* (41), 28028–28036. https://doi.org/10.1039/C7CP05358D.

(6) Austin, A.; Petersson, G. A.; Frisch, M. J.; Dobek, F. J.; Scalmani, G.; Throssell, K. A Density Functional with Spherical Atom Dispersion Terms. *J. Chem. Theory Comput.* **2012**, *8* (12), 4989–5007. https://doi.org/10.1021/ct300778e.

(7) Frisch, M. J.; Trucks, G. W.; Schlegel, H. B.; Scuseria, G. E.; Robb, M. A.; Cheeseman, J. R. Gaussian 16 Rev. A.03. *Gaussian 16 Rev. A.03* **2016**.

(8) Coulson, C. A. The Mathematics of Diffusion, Clarendon Press. *Math. Gaz.* **1958**, *42* (340), 165–165. https://doi.org/10.2307/3609455.

(9) Nagendra, B.; Golla, M.; Gallo, C.; Daniel, C.; Rizzo, P.; Guerra, G.; Baldino, L.; Reverchon, E. Mechanisms Determining Different Planar Orientations in PPO Films Crystallized by Guest Sorption. *Polymer* **2021**, *235*, 124242. https://doi.org/10.1016/j.polymer.2021.124242.

(10) Torres, F. J.; Civalleri, B.; Meyer, A.; Musto, P.; Albunia, A. R.; Rizzo, P.; Guerra, G. Normal Vibrational Analysis of the Syndiotactic Polystyrene s(2/1)2 Helix. *J. Phys. Chem. B* **2009**, *113* (15), 5059–5071. https://doi.org/10.1021/jp809043w.

LIST OF ABBREVIATIONS AND SYMBOLS

Δn : birefringence (optical property of the material)

$2\theta_{\mathrm{CuK}\alpha}$: degree of a peak position in an X-ray diffraction pattern at the CuKα radiation wavelength (1.5418 Å)

$A_{//}$: peak absorbance taken with polarization of light parallel to the film stretching direction

$a_{//}c_{//}$: orientation of the *ac* layers of alternated enantiomorphous helices being preferentially parallel to the film plane

$A_{\perp}$: peak absorbance taken with polarization of light perpendicular to the film stretching direction

AA : adipic acid

ACN : acetonitrile

Ar : Argon

Au : Gold

BA : benzoic acid

BE : benzyl ether

BET : Brunauer-Emmett-Teller method

$c_{//}$: polymer chain axes oriented preferentially parallel to the film plane

C=O : carbonyl group

$c_{\perp}$: polymer chain axes oriented preferentially perpendicular to the film plane

$CaCl_2$: calcium chloride

CB : chlorobenzene

CC : co-crystalline

CCl_4 : carbon tetrachloride

$CHCl_3$: chloroform

C_p : capacitance value for a parallel-plate capacitor

CsI : cesium iodide

D_{abs} : diffusivity coefficient during absorption (by Fick's II law)

DCE : 1,2-dichloroethane

DCM : dichloromethane

DFT : Discrete Fourier Transform

DMN : 1,4-dimethylnaphthalene

DSC : Differential Scanning Calorimetry

EOs : essential oils obtained from plant

FTIR : Fourier transform infrared

GIC: guest induced crystallization on amorphous film

HA : hexanoic acid

High-SA: high values of surface area

LA : lauric acid

MA : methyl acetate

MB : methyl benzoate

MEK : methyl ethyl ketone

MIS : metal insulator semiconductor

MOS : metal oxide semiconductor

$n_{\perp}$: refractive index of light propagating perpendicular to the optic axis

$n_{//}$: refractive index of light propagating parallel to the optic axis

NC : nanoporous crystalline

o-DCB : *orto*-dichrolobenzene

O−H : hydroxyl group

p/p_0 : relative pressure

PCE : perchloroethylene

PCL : polycaprolactone

PLA : poly lactic acid

PLGA : polylactic-co-glycolic acid

ppm : parts per million

PPO : poly(2,6-dimethyl-1,4-phenylene oxide)

rpm : revolutions per minute

SA : stearic acid

SA_{BET} : surface area by BET method

$scCO_2$: carbon dioxide in supercritical conditions

SEM : Scanning Electron Microscope

sPS : syndiotactic polystyrene

TCA : 1,1,1-trichloroethane

TCB : 1,2,4-trichlorobenzene

TCE : 1,1,2-trichloroethylene

TGA : Thermogravimetric analysis

T_{GIC} : temperature of guest inducing crystallization of amorphous films

TOL : toluene

UV–Vis : ultraviolet-visible spectroscopy

VOCs : volatile organic compounds

WAXD : wide-angle X-ray diffraction

wt% : wight percentage

X_c : degree of crystallinity

α : alfa crystalline phase

β : beta crystalline phase

γ : gamma crystalline phase

δ : delta crystalline phase

δ : Hildebrand solubility parameter

ε : epsilon crystalline phase

ε_r : relative dielectric permittivity

θ : (teta) diffraction angle

λ_{exc} : (lambda) excitation wavelength

Φ_F : fluorescent quantum yield

ACHIEVEMENTS

Publications:

1. Baku Nagendra, Antonietta Cozzolino, Christophe Daniel, Paola Rizzo, Gaetano Guerra, Finizia Auriemma, Claudio De Rosa, Massimo Christian D'Alterio, Oreste Tarallo, Anna Nuzzo, Two Nanoporous Crystalline Forms of Poly(2,6-dimethyl-1,4-phenylene)oxide and Related Co-Crystalline Forms,
   Macromolecules **2019**, 52, 9646−9656,
   DOI: 10.1021/acs.macromol.9b01911;
2. Baku Nagendra, Antonietta Cozzolino, Manohar Golla, Christophe Daniel, Paola Rizzo, Gaetano Guerra, Guest induced transition from β to α nanoporous crystalline forms of PPO,
   Polymer **2020**, 187, 122083,
   DOI: 10.1016/j.polymer.2019.122083;
3. Antonietta Cozzolino, Paola Rizzo, Chiara Gallo, Riccardo Bianchi, Christophe Daniel, Gaetano Guerra, Axially oriented guest induced crystallization in syndiotactic polystyrene unstretched fibers,
   Polymer **2021**, 228, 123908,
   DOI: 10.1016/j.polymer.2021.123908;
4. Christophe Daniel, Paola Rizzo, Baku Nagendra, Antonietta Cozzolino, Gaetano Guerra, High diffusivity dense films of a nanoporous-crystalline polymer,
   Polymer **2021**, 229, 124005,
   DOI: 10.1016/j.polymer.2021.124005;
5. Nicola Coscia, Antonietta Cozzolino, Manohar Golla, Paola Rizzo, Absorption and Isomerization of Azobenzene Guest Molecules in Polymeric Nanoporous Crystalline Phases,
   Chemistry **2021**, 3, 1074–1088,
   DOI: 10.3390/chemistry3030078;
6. Antonietta Cozzolino, Guglielmo Monaco, Christophe Daniel, Paola Rizzo, Gaetano Guerra, Monomeric and Dimeric Carboxylic Acid in Crystalline

Cavities and Channels of Delta and Epsilon Forms of Syndiotactic Polystyrene,
Polymers **2021**, 13, 3330,
DOI: 10.3390/polym13193330;

7. Antonietta Cozzolino, Baku Nagendra, Paola Rizzo, Christophe Daniel, Gaetano Guerra, Fast uptake of organic pollutants from dilute aqueous solutions by nanoporous-crystalline PPO films with c-perpendicular orientation,
   European Polymer Journal **2021**, 161, 110864,
   DOI: 10.1016/j.eurpolymj.2021.110864;
8. Manohar Golla, Antonietta Cozzolino, Baku Nagendra, Emanuele Vignola, Christophe Daniel, Paola Rizzo, Gaetano Guerra, Finizia Auriemma, Massimo Christian D'Alterio, Molecular Features Behind Formation of α or β Co-Crystalline and Nanoporous-Crystalline Phases of PPO,
   Frontiers in Chemistry **2022**, 9, 809850,
   DOI: 10.3389/fchem.2021.809850;
9. Baku Nagendra, Antonietta Cozzolino, Christophe Daniel, Paola Rizzo, Gaetano Guerra, High Surface Area Nanoporous-Crystalline Polymer Films,
   Macromolecules **2022**, 55, 2983-2990,
   DOI: 10.1021/acs.macromol.2c00271;
10. Paola Rizzo, Chiara Gallo, Antonietta Cozzolino, Nicola Coscia, Cosimo Micheletti, Francesco Ventura, Pierpaolo Minei, Andrea Pucci, Nanoporous-crystalline and amorphous films of PPO including off-on vapochromic fluorescent 7-hydroxy coumarin guests,
    Polymer **2022**, 249, 124833,
    DOI: 10.1016/j.polymer.2022.124833;
11. Antonietta Cozzolino, Simone Pappalardo, Paola Rizzo, Gaetano Guerra, Linear hydrogen bonded aggregates of carboxylic acids in crystalline channels of syndiotactic polystyrene,
    Polymer **2022**, 262, 125484,
    DOI: 10.1016/j.polymer.2022.125484;
12. Antonietta Cozzolino, Guglielmo Monaco, Paola Rizzo, Gaetano Guerra, Segregation of benzoic acid in polymer crystalline cavities,

Polymers **2023**, 15, 177,
DOI: 10.3390/polym15010177;

13. Antonietta Cozzolino, Chiara Botta, Christophe Daniel, Paola Rizzo, Thymol and Carvacrol: phenolic monoterpenes extracted from the essential oil of Thymus vulgaris as natural antimicrobial guests of nanoporous crystalline syndiotactic polystyrene fibers,
Macromolecular Symposia **2023**, in press.

Presentations:

1. MACROGIOVANI-Digital Edition (AIM 2020)
Oral Presentation
Nanoporous-crystalline polymers for air and water purification by A. Cozzolino, P. Rizzo, B. Nagendra, C. Daniel and G. Guerra;
2. XXVII Congresso Nazionale della Società Chimica Italiana (SCI 2021, online edition)
Oral Presentation
Axially oriented guest induced crystallization in syndiotactic polystyrene unstretched fibers by A. Cozzolino, P. Rizzo, C. Gallo, C. Daniel and G. Guerra;
3. POLYSOLVAT-13 2021 (online congress)
Poster Presentation
Axially oriented guest induced crystallization in syndiotactic polystyrene unstretched fibers by A. Cozzolino, P. Rizzo, C. Gallo, C. Daniel and G. Guerra;
4. XXIV Convegno Nazionale dell'Associazione Italiana di Scienza e Tecnologia delle Macromolecole (AIM 2022)
Oral Presentation
Innovative polymeric membrane for environmental applications by A. Cozzolino, B. Nagendra, C. Daniel, P. Rizzo and G. Guerra;
5. Workshop "Polymers, Health and Sustainability" (MoDEST 2022)
Oral Presentation
Vapochromic fluorescent sensors based on nanoporous crystalline polymer for environmental applications by A. Cozzolino, P. Rizzo and A. Pucci;

6. POLYSOLVAT-14 2022

   Oral Presentation

   H-bonded carboxylic acids in crystalline nanoporous of syndiotactic polystyrene by A. Cozzolino, P. Rizzo, G. Monaco, C. Daniel and G. Guerra.